

Interface damage mechanism between concrete layers under temperature loads

Von der
Fakultät für Bauingenieurwesen und Geodäsie
der Gottfried Wilhelm Leibniz Universität Hannover
zur Erlangung des akademischen Grades
Doktor-Ingenieur (Dr.-Ing.)
genehmigte

DISSERTATION

von
M.Sc. Sisi Zhang

2021

Betreuer und Referent: Prof. Dr.-Ing. Steffen Marx

Korreferentin: Prof. Dr.-Ing. Daniele Waldmann

Tag der Promotion: 26. März 2021

Kurzfassung

Beton-Beton-Verbundfugen werden in Baukonstruktionen häufig verwendet, beispielsweise zwischen Betonfertigteilen und Ortbetonelementen oder zwischen alten und neuen Betonelementen. Betonelemente erfahren Temperaturschwankungen sowie Kriech- und Schwindenverformungen, welche aufgrund der durch die Beton-Beton-Verbundfugen ausgeübten Beschränkungen zu Spannungen führen. Hohe Scher- und Zugspannungen an den Kanten von Trägern oder Platten führen zum Versagen der Verbundfuge. Dieses Phänomen tritt beispielsweise in der Festen Fahrbahn im Eisenbahnwesen auf. An der Grenzfläche zwischen der Betonfertigteileplatte und der Mörtelfüllschicht entstehen mitunter Risse und Lücken. Dieses Phänomen verringert die Dauerhaftigkeit der Struktur, erhöht die Wartungskosten und verursacht Sicherheitsrisiken. Daher ist eine theoretische Untersuchung des Versagensmechanismus in der Verbundfugen für den praktischen Entwurf erforderlich.

Ziel dieser Arbeit ist es, den Versagensmechanismus von Beton-Beton-Verbundfugen unter Temperatureinwirkungen zu untersuchen. Als Grundlage dient das Beispiel des kontinuierlichen Festen Fahrbahn Systems der Firma Max Bögl. Es wird ein experimentelles Programm in Kombination mit einer inversen Analyse entwickelt, um die Bruchzustände von Grenzflächen zwischen Beton und Zement-Asphalt-Mörtel (CAM) zu erhalten. Für die inverse Analyse werden hierzu Finite Element Modellen (FEM) erstellt. Zentrische Zugversuche für Modus I und Scherversuche für Modus II werden durchgeführt. Aufgrund des ungleichmäßigen Spannungszustands an der Verbundfuge wird die inverse Analyse verwendet, um die Experimente zu kalibrieren. Mit dessen Hilfe werden die Spannungs- und Verschiebungsbeziehungen in Modus I und Modus II ermittelt, die das konstitutive Modell der Verbundfuge bilden.

Anschließend wird das Verhalten der Verbundfuge in Längsrichtung unter konstanter Temperaturänderung und in Vertikalrichtung unter linear veränderlichem Temperaturgradient mittels analytischer Lösungen in einer Dimension (1D) und Finite-Elemente-Lösungen in zwei (2D) und drei Dimensionen (3D) mit Federelementen oder kontaktbasierten Kohäsionszonenmodell (CZM) erforscht. Die analytischen Modelle werden mit dem 1D FE Modell validiert. Es hat sich gezeigt, dass die analytische Lösung für das Verhalten der Verbundfuge in Längsrichtung bei konstanter Temperaturveränderung im Vergleich zur FEM die ungünstigsten Ergebnisse hinsichtlich des Verbundversagens liefert. Die Ergebnisunterschiede zwischen verschiedener Modelle werden kleiner, wenn Schäden an der Verbundfuge auftreten. Im Gegensatz hierzu kann für die Verhalten der Verbundfugen in Vertikalrichtung unter linear veränderlichem Temperaturgradient ein äquivalentes 3D-Modell auf der Basis einer analytischen Lösung entwickelt werden, das ähnliche Ergebnisse wie die 3D-FEM liefert.

Schließlich werden die Einflüsse verschiedener Verbundparameter der Fuge wie Haftfestigkeit und Steifigkeit auf die Fugenschädigung untersucht. Um geeignete Empfehlungen für den Entwurf der Verbundfugen zu geben, werden geometrische Parameter der Platte (z. B. Plattenlänge, -breite und -dicke) sowie Verbundparameter der Fuge für die Grenzzustandsstudien zur Gebrauchstauglichkeit implementiert. In diesem Fall bleibt die Verbundfuge in linear elastische Phase ohne Verbundversagen unter extremen Temperatureinwirkungen.

Schlüsselwörter: Beton-Beton-Verbundfugen, Verbund-Versagensmechanismus, Spannungs-Verschiebungs-Beziehung, Temperatureinwirkungen, analytische Lösungen, Kohäsionszonenmodell

Abstract

Interface between concrete layers is widely used in composite constructions in practical engineering, such as between precast concrete elements and cast-in-situ elements, or between old and new concrete elements. Massive concrete elements subjected to temperature variations, creep and shrinkage differences arouse volume changes, which results in stresses due to the restraint exerted by the bond of concrete-to-concrete interface. High shear and tensile stresses at the edges of beams or slabs lead to interface failure. This phenomenon occurs, for example in the slab track systems. Cracks and gaps occur at interface between the prefabricated concrete slab and mortar filling layer. This incident reduces the durability of the structure, increases the maintenance costs and also causes safety risks. Thus, theoretical study of interface debonding mechanism is needed for practical design in the future.

This thesis aims to explore the interface damage mechanism between concrete layers under temperature loads. The example of continuous slab track system (i.e. Bögl system) was taken. An experimental program was developed combined with an inverse analysis based on finite element model (FEM) to obtain the interface fracture properties between concrete and cement-asphalt mortar (CAM). Direct tensile tests for mode I and push-off tests for mode II were implemented. Due to the non-uniform stress-state at interface, an inverse analysis was employed to calibrate the experiments, so that the interface constitutive model, i.e. bond-slip relationship in mode I and mode II were obtained.

Afterwards, the longitudinal interface behavior under uniform temperature variations and vertical interface behavior under temperature gradient variations were studied by means of analytical solutions in one dimension (1D) and finite element solutions in two (2D) and three dimensions (3D) with connector elements or cohesive zone model (CZM). The analytical models were validated by 1D FEM. It's shown that the analytical solution for the longitudinal interface behavior under uniform temperature variations gives the most unfavorable results with respect to interface damage compared to other FEM. The result differences between various models become smaller when damage at interface occurs. What's more, an equivalent 3D model based on analytical solution could be developed for vertical interface behavior under temperature gradient variations, which produces similar results with 3D FEM.

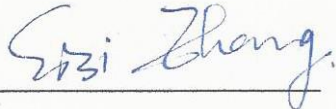
Finally, the influences of different interface parameters such as bonding strength and stiffness on the interface damage were investigated. In order to give proper recommendations for the interface design in the future, geometric parameters of the slab (e.g. slab length, width and thickness) as well as interface bonding parameters for the serviceability limit state studies were implemented, in which case the interface stays in elastic phase without damage under extreme temperature loads.

Keywords: concrete-to-concrete interface, debonding mechanism, bond-slip relationship, temperature loads, analytical solution, cohesive zone model

Eigenständigkeitserklärung

Hiermit bestätige ich,

1. die Regeln der geltenden Promotionsordnung zu kennen und eingehalten zu haben und mit einer Prüfung nach den Bestimmungen der Promotionsordnung einverstanden zu sein;
2. die Dissertation selbst verfasst zu haben, keine Textabschnitte von Dritten oder eigener Prüfungsarbeiten ohne Kennzeichnung übernommen und alle von mir benutzten Hilfsmittel und Quellen in meiner Arbeit angegeben zu haben;
3. Dritten weder unmittelbar noch mittelbar geldwerte Leistungen für Vermittlungstätigkeiten oder für die inhaltliche Ausarbeitung der Dissertation erbracht zu haben;
4. die Dissertation noch nicht als Prüfungsarbeit für eine staatliche oder andere wissenschaftliche Prüfung eingereicht zu haben;
5. die gleiche oder eine in wesentlichen Teilen ähnliche Arbeit nicht bei einer anderen Hochschule als Dissertation eingereicht zu haben; Auch eine andere Abhandlung wurde nicht als Dissertation bei einer Hochschule eingereicht

Hannover den 26.12.2020, 

Acknowledgements

The research presented in this thesis was carried out at the Institute of Structural Concrete, Leibniz University Hannover, Germany.

I am in particular grateful to my supervisor Prof. Dr.-Ing. Steffen Marx for providing me the opportunity to conduct my PhD studies at the Institute of Structural Concrete as well as for his comprehensive supports on my work in the institute. I would also like to thank Prof. Dr.-Ing. Daniele Waldmann for her interest in reviewing my thesis. Meanwhile thank Prof. Dr.-Ing. Nabil A. Fouad to be the co-examiner and Prof. Dr.-Ing. Martin Achmus to take over the chair of my doctoral examination committee. My thanks also go to Prof. Dr.-Ing. Volker Slowik for his suggestions on my experiment part and analytical solution, which inspired me a lot.

Moreover, thank all the colleagues, technicians and student research assistants in the Institute for their supports and willingness to discuss.

Finally, I am indebted to my family, they have always been supporting and motivating me to overcome all the difficulties.

Hannover, December 2020

Table of Content

Kurzfassung.....	i
Abstract.....	ii
Eigenständigkeitserklärung.....	iii
Acknowledgements.....	iv
Table of Content.....	v
Nomenclature.....	viii
1. Introduction.....	1
1.1 Background of the research.....	1
1.2 Objectives and scope of the research.....	3
1.3 Structure of the dissertation.....	3
2. State of the Art.....	6
2.1 Mechanical behavior of concrete-to-concrete interface.....	7
2.1.1 Shear transfer strength of concrete interface.....	7
2.1.2 Existing technologies for characterization of concrete surface roughness.....	11
2.1.3 Bond-slip relationship of concrete interface.....	15
2.1.4 Experiment methods of concrete-to-concrete interface.....	17
2.2 Fracture modelling approaches.....	18
2.2.1 Fundamental theory of fracture mechanics.....	19
2.2.2 Elastic-plastic damage model.....	27
2.2.3 Fractural modelling for concrete-to-concrete interface.....	28
2.2.4 Concept of degree of restraint.....	30
3. Fundamentals of numerical simulation.....	32
3.1 Basic concept of FEM.....	32
3.2 Nonlinear FEM.....	33
3.3 Modelling in ABAQUS.....	36
3.3.1 Connector elements.....	38
3.3.2 Cohesive elements.....	40
3.3.3 Contact interaction.....	43
4. Experimental determination of interface fracture parameters.....	53
4.1 Objectives of the interface experiments.....	53
4.2 Preparation of the material and specimens.....	54
4.3 Direct tensile test.....	56

4.3.1	Testing setup and instrumentation.....	56
4.3.2	Testing results	57
4.4	Push-off test.....	59
4.4.1	Test setup and instrumentation.....	59
4.4.2	Testing results	59
4.5	Simulation of the experiments.....	61
4.5.1	Material parameters and FE discretization.....	62
4.5.2	Direct tensile test.....	64
4.5.3	Push-off test.....	68
4.6	Summary	71
5.	Longitudinal interface behavior under uniform temperature variations	73
5.1	Analytical models.....	74
5.1.1	Linear longitudinal interface behavior.....	74
5.1.2	Longitudinal interface with pure friction resistance	77
5.1.3	Trilinear longitudinal Interface behavior.....	79
5.1.4	Calculation algorithms with Matlab	82
5.2	Finite element models.....	83
5.2.1	1D models.....	84
5.2.2	2D models.....	87
5.2.3	3D models.....	89
5.3	Parameter study	90
5.3.1	Interface parameter study.....	91
5.3.2	Limit value study	93
5.4	Summary	94
6.	Vertical interface behavior under temperature gradients.....	98
6.1	Analytical models.....	98
6.1.1	Interface as Winkler's foundation.....	98
6.1.2	Winkler's foundation with damage	102
6.1.3	Bilinear vertical interface behavior	106
6.1.4	Trilinear vertical interface behavior	108
6.1.5	Calculation algorithms with Matlab	111
6.2	Finite element models.....	112
6.2.1	1D models.....	112

Table of Content

- 6.2.2 2D models..... 113
- 6.2.3 3D models..... 115
- 6.3 Parameter study 116
 - 6.3.1 Interface parameter study..... 116
 - 6.3.2 Limit value study 119
- 6.4 Summary 122
- 7. Conclusion and outlook..... 126
 - 7.1 Conclusion..... 126
 - 7.2 Outlook 130
- Bibliography..... 132
- Lebenslauf 141

Nomenclature

The most important abbreviations and formula symbols are listed below. Unlisted symbols are explained in the text.

Abbreviations

1/2/3D	One- /Two- /Three- dimensional
ACI	American Concrete Institute
ASTM	American Society for Testing and Materials
BC	Boundary condition
CAD	Computer-aided design
CAM	Cement-asphalt mortar
CMOD	Crack mouth opening displacement
CORM	Components of relative motions
CPM	Compensation plane method
CRTS	China Railway Track System
CST	Continuous slab track
CTOD	Crack tip opening displacement
CZM	Cohesive zone model
DAfStb	Deutscher Ausschuss für Stahlbeton
DOF	Degree of freedom
ESF	Extended shear friction theory
FEA/FEM	Finite Element Analysis/-Method
FPZ	Fracture process zone
HPW	High-pressure water jetting
JSCE	Japan Society of Civil Engineers
LEFM	Linear elastic fracture model
LVDT	Linear variable displacement transducer
MC1990	<i>fib</i> Model Code 1990
MC2010	<i>fib</i> Model Code 2010
MPC	Multi-Point Constraint
MSF	Modified shear friction theory
MTD	Mean texture depth
NLFM	Nonlinear fracture model

RC	Reinforced concrete
SF	Shear friction theory
VCCT	Virtual crack closure technique
XFEM	Extended finite element method

Lower-case Latin letters

a_c	Critical crack length
a_e	Interface length of elastic phase
a_d	Interface length of damage phase
a_u	Interface length of friction phase or unrestraint phase
b	Width of the slab
f_t	Tensile strength
\mathcal{G}	Energy release rate
\mathcal{G}_c	Critical energy release rate
\mathcal{G}_R	Crack extension resistance in terms of energy release rate
k	Spring stiffness
k_d	Slope of damage evolution
k_e	Elastic stiffness in the interface resistance
k_p	Penalty stiffness
t	Thickness of the slab
t_n	Normal traction
t_s	Slip traction
t_t	Tear traction
\bar{t}	Traction stress predicted by elastic traction-separation behavior for current separations without damage
t^0	Traction at damage initiation
t^{max}	Traction corresponding with maximum value of effective separation during loading history
u	Displacement
ν	Poisson's ratio

Upper-case Latin letters

D	Damage variable
E	Young's modulus or the modulus of elasticity in tension

Nomenclature

E_c	Interface elasticity
E_a	Adhesive material elasticity
F	Force
G_f	Fracture energy
I	Second moment of area
K_c	Interface stiffness in compression
$K_{nn}/K_{ss}/K_{tt}$	Stress intensity factor in fracture mode I/II/III
K_{Norm}	Stiffness of the linear normal behavior in contact interaction in ABAQUS
K_R	Crack extension resistance in terms of stress intensity factor
L	Length of the slab
M	Bending moment
S_{surf}	Absorbed surface energy associated with a crack
$S(x)$	Interface shear slip along the slab length (in longitudinal direction)
S_e	Maximum interface elastic slip in longitudinal direction or slip at damage initiation
S_u	Maximum interface damage slip in longitudinal direction or slip at complete bonding failure
T_c	Adhesive material geometrical thickness
T_0	Original thickness/ constitutive thickness of the cohesive elements
$U(x)$	Longitudinal deformation of the slab
W^*	Strain energy per unit volume
W	Total released strain energy

Greek letters

α	Exponential parameter for exponential damage evolution in CZM
α_T	Thermal expansion coefficient
δ_n	Normal separation
δ_s	Slip separation
δ_t	Tear separation
δ_m	Effective separation
δ_m^{max}	Maximum value of effective separation during loading history
δ_m^0	Effective separation at damage initiation
δ_m^f	Effective separation at complete failure
$\dot{\delta}_s$	Slip rate
ε	Strain

ε_n	Normal strain in cohesive element
ε_s	Slip strain in cohesive element
ε_t	Tear strain in cohesive element
ε^0	Strain in cohesive element at damage initiation
τ	Shear stress
τ_e	Maximum elastic shear stress at interface
τ_u	Residual frictional shear stress at interface
τ_{app}	Applied external shear stress
τ_{crit}	Critical shear stress
$\bar{\tau}_{max}$	Shear stress limit
σ	Normal stress
σ_{tmax}	Maximum tensile stress
μ	Coulomb friction coefficient
μ_s	Static friction coefficient
μ_k	Kinetic friction coefficient
$\bar{\rho}_c$	Density of the interface
ρ_c	Density of adhesive material
γ	Degree of restraint

Vector and Matrix in FEM

$\{C_u\}$	Vector of displacement correction
$[D]$	Material stiffness matrix
$[E]$	Material elasticity matrix
$\{I\}$	Vector of internal nodal forces
$[K]$	Global element stiffness matrix
$[K_T]$	Tangent stiffness matrix in Newton-Raphson iteration method
$\{P\}$	Vector of external nodal forces
$[\beta]$	Matrix of relationship between displacement and strain
$\{u\}$	Vector of nodal displacement
$\{\varepsilon\}$	Vector of nodal strain
$\{\sigma\}$	Vector of nodal stress
$\{t\}$	Vector of traction stress in traction-separation law
$\{\delta\}$	Vector of separation in traction-separation law

1. Introduction

1.1 Background of the research

Concrete-to-concrete interface exists widely in constructions such as prefabricated concrete connected with cast-in-situ concrete, or new concrete bonded with old concrete, see Figure 1.1. Following situations may become relevant in practice [1]:

- Repairing and strengthening existing reinforced concrete (RC) members with new concrete sections
- Supplementing precast elements by means of cast-in-situ concrete
- Construction joints between concrete sections cast-in-situ one after another
- Load transfer via concrete element (e.g. corbels) subsequently attached to existing members



Figure 1.1 Practical applications of concrete interface in constructions: (a) between old and new concrete for rehabilitation [2]; (b) between precast and cast-in-situ concrete in modular construction [3]; and (c) between concrete section cast-in-situ one after another [4]

There exist also many forms of concrete-to-concrete interface as connection joints in practical cases (see Figure 1.2): (a) floor-to-floor connections (i.e. cast-in-situ topping or cast-in-situ joints); (b) floor-to-beam connections; (c) beam-to-column connections; (d) column-to-foundation connections [5].

Despite the extensive applications of concrete-to-concrete interface in civil engineering, the damage mechanisms between concrete layers still remain unclear in many aspects. Massive concrete elements subjected to differential shrinkage, creep, and temperature variations arouse volume changes, which results in shear and tensile stresses due to the restraint from bonding of concrete-to-concrete interface. High shear and tensile stresses at the edges of the beams or slabs can cause the edge to lift, which in some cases leads to interface failure.

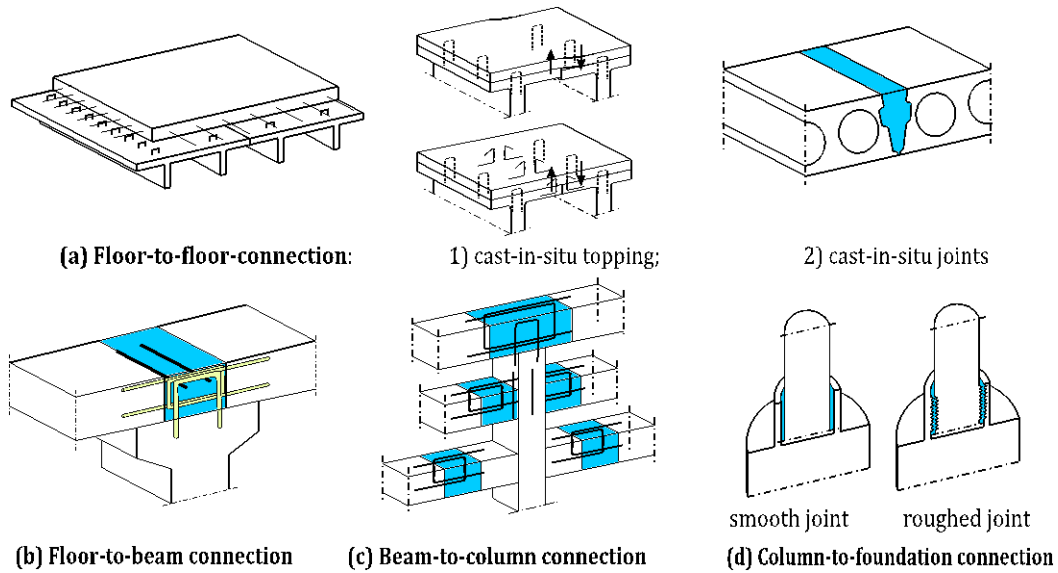


Figure 1.2 Concrete connection joints in precast structures

This interface damage phenomenon occurs, for example, in concrete slabs of Bögl slab track system in Germany or the continuous slab track systems (CST) in China, where cracks and gaps exist at the interface between the prefabricated concrete slab and mortar filling layer, see Figure 1.3. The cracks at interface could deteriorate the transfer strength of the interface joints, leading to safety risks or causing serious durability problems, since the cracks or gaps at interface allow water to enter, which also increases the maintenance costs. Thus, the study of interface damage mechanism between concrete layers brings significant importance for practical designs and maintenance.

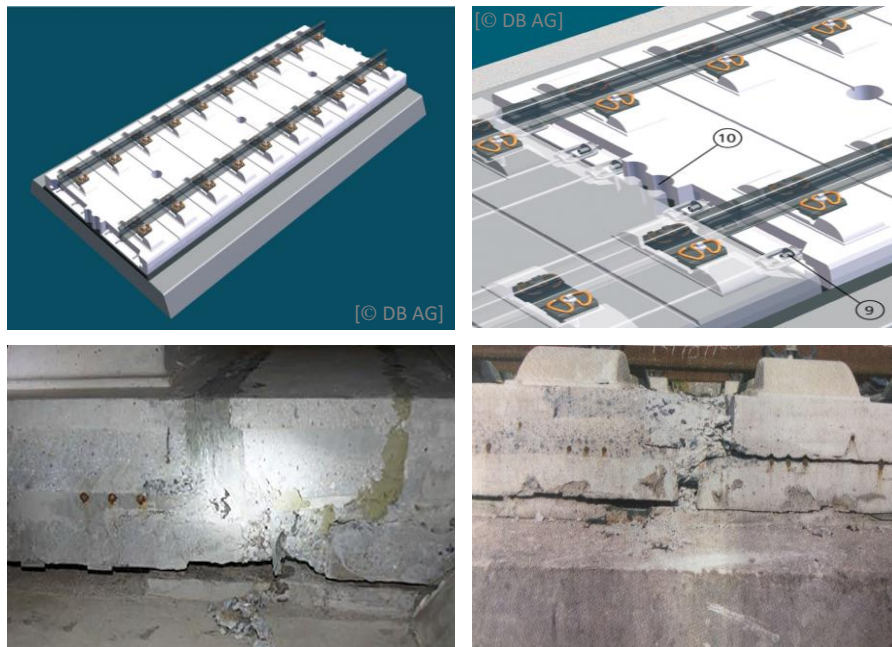


Figure 1.3 Interface damage at Bögl slab track system in high-speed railway line

1.2 Objectives and scope of the research

The aim of the thesis is to study the horizontal interface damage between concrete layers under temperature loads. The example of CST system is used in this thesis. The thesis focuses on the interface failure mechanisms. Thus, the linear elastic material properties are applied to concrete and cement-asphalt mortar (CAM). Only the degradation at interface would be considered. The main objectives of this study are summarized as follows:

- (1) to design and implement an experiment program for the determination of interface fracture parameters between concrete and CAM;
- (2) to propose analytical models for the analysis of interface restraint under temperature loads;
- (3) to develop finite element models (FEM) for the simulation of interface under temperature loads;
- (4) to come up with proper and practical recommendations for the design of slab track system regarding interface bonding behavior.

1.3 Structure of the dissertation

The thesis addresses the horizontal interface behavior in both longitudinal directions under uniform temperature variations and vertical direction under temperature gradients. Experiment testing results are combined with a manual iterative inverse analysis procedure based on FEM to obtain the interface fracture parameters. Analytical models combined with 2D and 3DFEMs are developed to investigate the interface behavior under temperature loads. The research can be thus considered as a combination of experiments, analytical and numerical studies. The contents of each chapter are summarized as follows:

Chapter 1: Introduction

The first introduction chapter gives a short overview of the background, aims and scope as well as the structure of the dissertation.

Chapter 2: State of the Art

The relevant current research on the concrete-to-concrete interface behavior including interface bond capability and experimental methods as well as fracture mechanical modelling approaches is summarized in this chapter.

Chapter 3: Fundamentals of numerical simulation

The fundamental theory of finite element analysis (FEA) in the software ABAQUS is introduced in this chapter. The modelling methods with connector elements, cohesive zone model (CZM) and contact interaction that will be used in later studies are also illustrated in this chapter.

Chapter 4: Experimental determination of interface fracture parameters

In this chapter, direct tensile tests and push-off tests are designed and implemented to obtain the interface fracture parameters in mode I and mode II. A manual iterative inverse analysis procedure based on FEM, which comprises 2D and 3D modellings varying from simple to complex idealization of the structure, is used to calibrate the interface bond-slip relationships according to testing results.

Chapter 5: Longitudinal interface behavior under uniform temperature variations

A uniform temperature variation could arouse an elongation or shortening of the structure. Thus, the longitudinal interface behavior is investigated under uniform temperature variations. In addition, the interface

restraint stresses along one edge of the slab produce also an eccentricity, leading to flexural deformation of the structure. In this chapter, the 1D analytical solutions under centric loading are firstly developed for linear, pure friction and trilinear interface behaviors. The analytical models are validated by the 1DFEMs under centric loading. What's more, 1DFEM under eccentric loading, 2DFEM and 3DFEM are then used for further studies. Finally, parameter studies are implemented to learn the influences of different interface parameters on the interface damage as well as to explore the limit state in longitudinal direction.

Chapter 6: Vertical interface behavior under temperature gradients

On the other hand, temperature gradients could lead to flexural deformation of the structure and the vertical interface behavior is thus studied under temperature gradients. In this case, the 1D analytical solutions are also developed for Winkler's foundation (i.e. linear vertical interface behavior), Winkler's foundation with damage, and bilinear and trilinear vertical interface behaviors. Similarly, the analytical models are validated by 1DFEM. In addition, 2DFEM and 3DFEM are further investigated followed by interface parameter studies and limit state studies in this chapter.

Chapter 7: Conclusion and outlook

The main discoveries of this thesis are summarized in this chapter along with further outlook on this topic.

An overview of the analysis paths of this thesis is visually summarized in the following Figure 1.4:

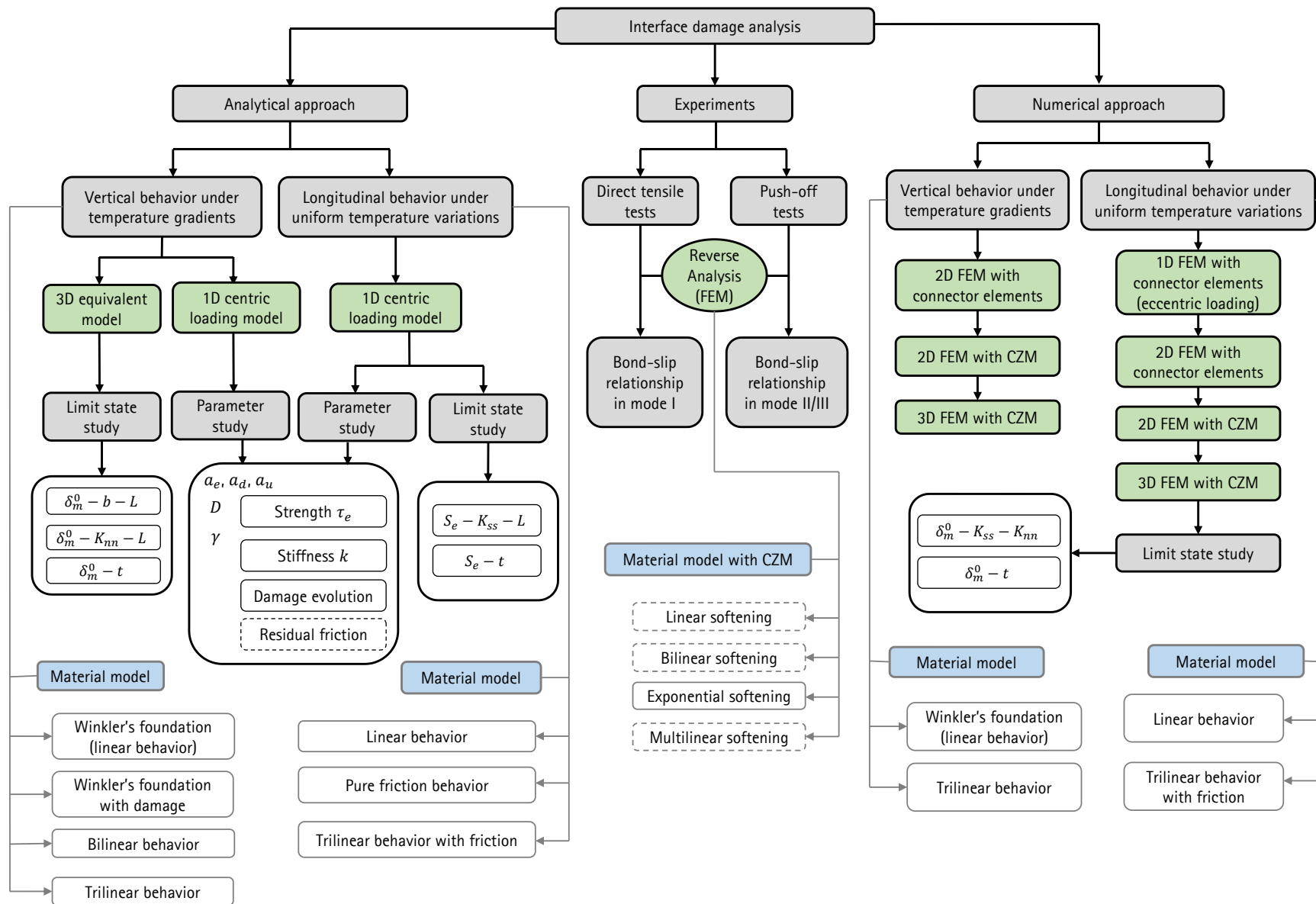


Figure 1.4 Flowchart of the analysis paths

2. State of the Art

The loadbearing capacity of the interface is firstly dependent on the location of interface in the construction components [6]. Two kinds of interface joints could be characterized:

- (1) Interface joints loaded with longitudinal shear stresses, where shear stresses at interface are parallel to structural axis or plane;
- (2) Interface joints loaded with bending shear stresses, where shear stresses are vertical to structural axis or plane.

Examples of the aforementioned interface joints are demonstrated in Figure 2.1. Within this thesis, concrete interface with longitudinal shear stresses is discussed.

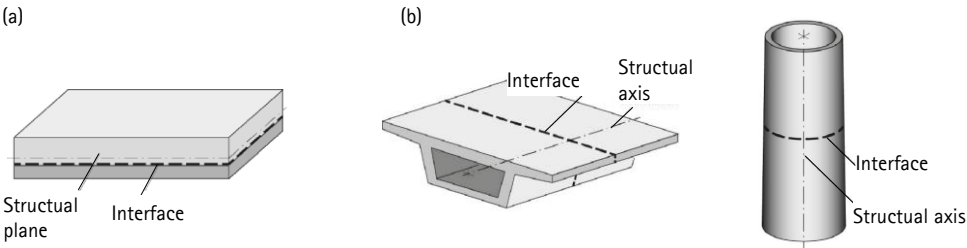


Figure 2.1 Interface joints location types: (a) shear stresses at interface parallel to structural plane as an example of precast component with cast-in-situ supplement; (b) shear stresses at interface vertical to structural axis as examples of prefabricated segment bridge and tower in segment constructions [7]

Guckenberger et. al. (1980) [8] have categorized the interface joints in their research on segment prefabricated bridges into the following types:

- (1) Filling joints with filling material from concrete or cement mortar;
- (2) Press joints with a thin intermediate layer (< 3 mm) from epoxy resin or cement mortar;
- (3) Dry joints without filling material or intermediate layer.

In DAfStb booklet 311 [8], five joint types are distinguished based on the typical thicknesses according to D.J. Lee [9] , see Figure 2.2.

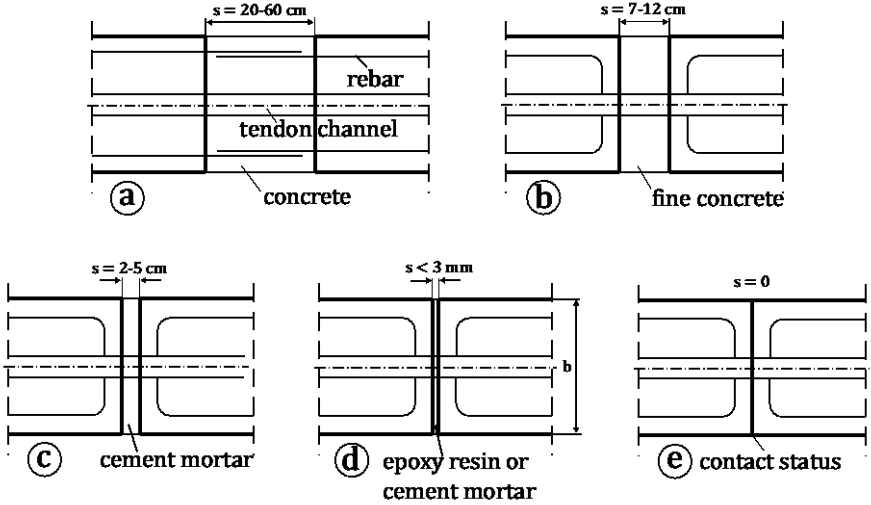


Figure 2.2 Joint types based on the typical thickness [8]

Type (a) to (c) belong to filling joints (or wet joints), whereas type (d) and (e) refer to press joints and dry joints respectively. Type (a) has the largest thickness of 20–60 cm with concrete filling material meanwhile longitudinal reinforcements from segments at two sides extend into the joint. Type (b) has a thickness of 7–12 cm filled with fine concrete and type (c) is filled with cement mortar for a thickness of 2–5 cm.

Since 1960s, various comprehensive research projects regarding the loadbearing capacity of concrete-to-concrete interface have been conducted all over the world, in order to make a conservative prediction of the bond strength for a quasi-monolithic behavior as well as give reliable recommendations for design and construction. Fundamental bonding mechanism and related influential factors, and current design approaches for strength and damage models for interface debonding will be discussed in chapter 2.1. What's more, diverse experiment methods for the concrete interface will also be reviewed.

2.1 Mechanical behavior of concrete-to-concrete interface

2.1.1 Shear transfer strength of concrete interface

The bonding mechanism of reinforced concrete shear joints can be explained most simply by the *shear-friction theory (SF)*, which was firstly developed by Birkeland in 1966 [10]. A simple saw tooth model was proposed, in which the shear stressing at joint causes not only tangential displacements but also normal displacements, leading to tensile stresses in the rebars crossing the interface. In turn, these create equalizing compressive stresses in the joint and produce frictional forces, see Figure 2.3 (a). Birkeland provided the simplest but very conservative equation for low clamping stresses, which gives unconservative results for high clamping stresses [11]. Mattock and Hawkins [12] came up with the *modified shear friction theory (MSF)* by taking the additive adhesion of the interface (assumed to be 1.38 MPa) and external normal forces into consideration. Loov [13] was the first to incorporate the influence of the concrete compressive strength. The full tensile yield strength of the steel rebar as the reaction force is assumed. Several standards and codes, e.g. Eurocode 2 [14] has adopted this approach routine. The next milestone was contributed by Walraven [15] in 1987. By assuming spherical aggregate particles, the aggregate interlock effect based on a statistical analysis of 88 push-off test results could be explained, see Figure 2.3 (b). This model was originally derived for cracked concrete interface and provides realistic predictions of shear friction capacity and shear-slip behavior of cracked concrete interface especially when normal stress or confinement force is known. The work from Tassios and Vintzeleou [16]; [17] provided a basis for the former Model Code 1990 (MC 1990) [18] regarding concrete-to-concrete interface shear transfer. Comprehensive studies on interface shear transfer have been conducted by Randl [19]–[21] since 1990s and proposed a design expression that explicitly includes the contribution from adhesion, friction and dowel action. Other recent studies [22]–[24] mainly focus on the investigation of the correlation between roughness parameters and bond strength. Thus, appropriate methods for identifying the topography of the surface in detail are important and prerequisite, which will be discussed in the following chapter 2.1.2.

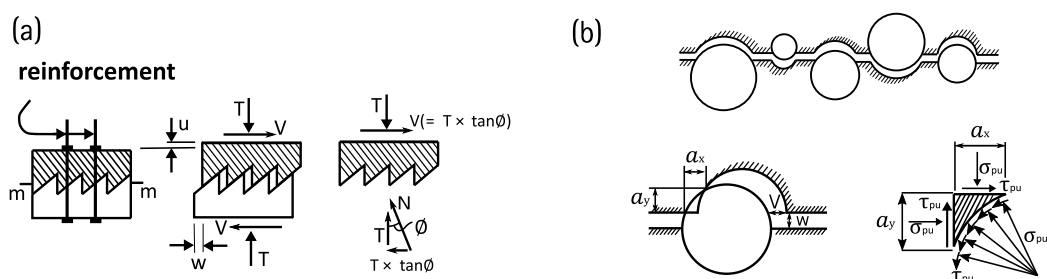


Figure 2.3 Concrete-to-concrete Interface bond models: (a) shear friction theory and saw tooth model by Birkeland (1966) [10]; (b) aggregate interlock model by Walraven (1981) [25]

In Germany, Franz [26] from Karlsruhe performed numerous experiment series regarding transverse force in filling joints and dry joints at end of 1950s. Zelger and Rüsç [27] in Munich University of Applied Science also implemented experiments on shear transfer in joints filled with mortar at beginning of 1960s. Substantial research on topic of concrete-to-concrete interface has been investigated since 1980s at Munich Technical University. Daschner and Kupfer (1986) [28] carried out a large number of experiments on the necessary shear reinforcements between prefabricated elements and cast in-situ concrete elements for various interface roughnesses. Nissen (1987) [29] developed saw-tooth models for the interlock of the concrete. Reinecke (2002) [30] investigated the adhesion and interlock of concrete interface without reinforcements. Müller (2008) [31] then explored the tension and shear properties of concrete interface in microscopic, mesoscopic and macroscopic levels. Lenz (2012) [32] researched the untapped potential of concrete-to-concrete bond I practice. Wagner (2016) [33] from Leipzig studied the bonding behavior (i.e. tension and shear strength as well as combined tension and shear tests) between strain hardening cement-based composites (SHCC) and concrete substrate.

The following Table 2.1 demonstrates important formulae of shear transfer at concrete interface proposed by different researchers chronologically. Meanwhile, design equations in the main standards and codes for RC structures around the world are presented in Table 2.2.

Table 2.1 Representative shear transfer expressions of concrete interface

Researcher	Year	Design expression
Birkeland [10]	1966	$\tau_{Rd} = \mu \rho f_y$
Mattock [12]	1972	$\tau_{Rd} = 1.38 + 0.8(\sigma_n + \rho f_y)$
Loov [13]	1978	$\tau_{Rd} = k \sqrt{f_c(\sigma_n + \rho f_y)}$
Walraven [15]	1987	$\tau_{Rd} = C_1(\rho f_y)^{C_2}$ with $C_1 = 0.822f_c^{0.406}$ and $C_2 = 0.159f_c^{0.303}$
Randl[19]	1997	$\tau_{Rd} = \tau_{coh} + \mu \cdot \sigma_n + \alpha \cdot \rho \sqrt{f_y f_c}$
Ali [34]	1999	$\tau_{Rd} = 1.47a f_c \sqrt{(\rho f_y + \sigma_n)/f_c}$
Papanicolaou [35]	2002	$\tau_{Rd} = 0.3(\sigma_n + \rho f_y) + 1.7\sqrt{f_{ct}}$ (smooth interface) $\tau_{Rd} = 0.45(\sigma_n + \rho f_y) + 1.4\sqrt{f_{ct}}$ (rough interface)
Santos[36]; [37]	2010	$\tau_{Rd} = c f_c$ (without shear reinforcements) $\tau_{Rd} = \mu(\rho f_y + \sigma_n)$ (with shear reinforcements)

In the equations, τ_{Rd} is the shear strength by unit area; V_n is the maximum shear force; μ is the friction coefficient (dependent on the interface roughness); μ_e is the effective coefficient of friction; ρ is the ratio of the area of reinforcement crossing the interface and the area of the interface; f_y is the reinforcement yield stress; σ_n and P_c are the external normal stress and force perpendicular to the interface (positive for compression); f_c is the concrete compressive strength; τ_{coh} is the cohesion due to aggregate interlock; α is the dowel action coefficient ($45^\circ \leq \alpha \leq 90^\circ$); θ refers to the inclination of the compressive struts; λ refers a factor related to the concrete density; ϕ_c and ϕ_s are the resistance factor for concrete and reinforcing bars respectively; c is the cohesion coefficient (dependent on the interface roughness); f_{cta} is the tensile strength of the weakest concrete; and k , C_1 , and C_2 are special parameters formulated by different researchers; A_{vf} and A_{cv} mean the cross section area of the reinforcements based on shear-friction theory and interface area;

A_{c1} , A_k and A_{sd} denote the areas of concrete interface, shear key bottom surface and reinforcements crossing interface respectively.

Table 2.2 Shear-friction provisions of design codes

Design code	Year	Design expression
CEB-FIB Model Code 1990 [18]	1990	$\tau_{Rd} = cf_{ctd} + \mu(\sigma_n + \rho f_y)$
AASHTO Standard Specifications for Highway Bridges [38]	1996	$\tau_{Rd} = \rho f_y (\mu \cdot \sin \alpha + \cos \alpha)$
DIN 1045-1 [39]	2001	$\tau_{Rd} = \rho f_y \cot \theta - \mu \sigma_n$
Eurocode 2 [14]	2004	$\tau_{Rd} = cf_{ctd} + \mu \sigma_n + \rho f_y (\mu \cdot \sin \alpha + \cos \alpha)$
PCI Design Handbook [40]	2004	$\tau_{Rd} = \phi \rho f_y \mu_e$, $(\mu_e = \frac{6.9 \lambda \mu}{\tau_{Rd}})$
CAN/CSA A23.3 [41]	2004	$\tau_{Rd} = \lambda \phi_c (c + \mu \sigma_n) + \phi_s \rho f_y \cos \alpha$
AASHTO LFRD Bridge Design Specifications [42]	2007	$V_n = c A_{cv} + \mu (A_{vf} f_y + P_c)$ or $\tau_{Rd} = c + \mu (\rho f_y + \sigma_n)$
DIN 1045-1 (reversed version) [43]	2008	$\tau_{Rd} = cf_{ctd} - \mu \sigma_n + 1.2 \rho f_y \mu$
ACI 318-08 [44]	2008	$V_n = \mu A_{vf} f_y$ or $\tau_{Rd} = \rho f_y (\mu \cdot \sin \alpha + \cos \alpha)$
fib Model Code 2010 [45]	2010	$\tau_{Rd} = c + \mu (\rho k f_y + \sigma_n) + a \rho \sqrt{f_y f_c}$
JGJ 1-2014 [46]	2014	$\tau_{Rd} = 0.07 f_c A_{c1} + 0.1 f_c A_k + 1.65 A_{sd} \sqrt{f_c f_y}$

The basic mechanisms contributing to shear resistance of the concrete interface with connectors or external compression perpendicular to shear plane could be divided as following:

- (1) **Adhesive bonding and mechanical interlock:** Adhesion bonding due to chemical (e.g. ionic bond, covalent bond and metallic bond) and physical (e.g. hydrogen bond and Van der Waals force) bonding has a big contribution to overall resistance when the shear slip is smaller than 0.05 mm. In this stage, the bond-slip behavior is very stiff. The failure slip at interface is very small when only the effect of adhesion is considered [19]. However, the mechanical interlocking still has important influence after adhesion failures at slip larger than 0.05 mm. The influence of aggregate interlocking is only observed along interfaces with strong and irregular roughness. The real surface contact area has a decisive influence on the adhesive bonding capacity, which could be described by a "modified Wenzel coefficient" [32]. A roughness factor can be defined in this context relating the real full contact area.
- (2) **Friction:** the friction forces occur when there are compression forces perpendicular to the interface and meanwhile the interface roughness exists. The compression forces could come from either external actions (e.g. self-weight, prestressing forces and confinement) or clamping effect caused by connectors or reinforcements crossing the interface. Interface joints without reinforcements and external compression only have a very stiff adhesion resistance.
- (3) **Dowel action** (or bending resistance) of reinforcements or connections crossing interface: relative shear slip at interface leads to a lateral displacement of upper and lower reinforcing bar or connector ends, which arouses bending stresses in these bars that are superimposed by axial tensile forces due to the opening of joints.

These mechanisms interact with each other but contribute to the total shear strength at different times. The 'rigid' bonding of adhesion and interlocking dominate the shear resistance at small slips, while the 'non-rigid' bonding of friction and dowel action contribute mainly at larger slips when adhesion and mechanical interlocking collapse. Most design recommendations did not take into account the aforementioned effects in an appropriate way [6]. However, in the *fib* Mode Code 2010 (MC 2010) [45], the interaction factors are defined to calculate the ultimate shear strength, since maximum contributions of different mechanisms occur at different slips, see Figure 2.4. The theory behind MC 2010 is also known as "extended shear friction theory" (ESF) [1].

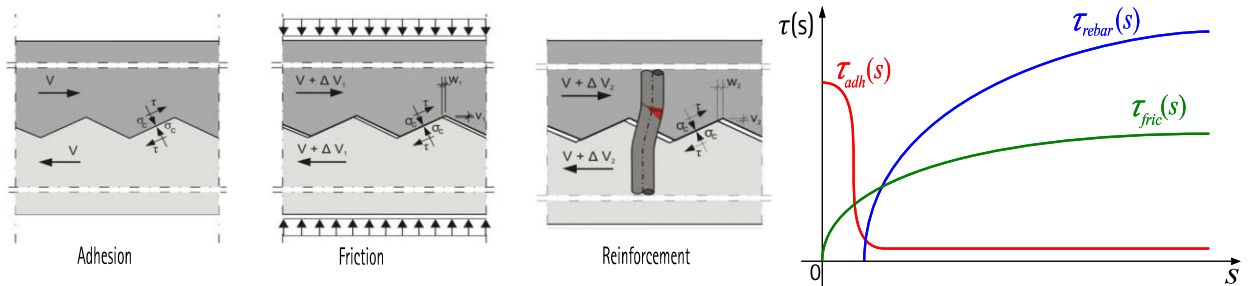


Figure 2.4 Schematic description of shear contribution from adhesion, friction and reinforcements at concrete interface [32]; [30]

For the adhesion bonding between old and new concrete, a variety of factors are determined. The influences of properties of hardened concrete (such as compressive strength and shrinkage) are significantly relevant. Müller (2009) [31] shows that the characteristics of fresh concrete also affect the bonding capacity. Thus, influences on concrete-to-concrete adhesion bonding could be divided into three groups: *characteristics of old concrete*, *characteristics of new concrete* and *compound conditions*, see Figure 2.5 [32].

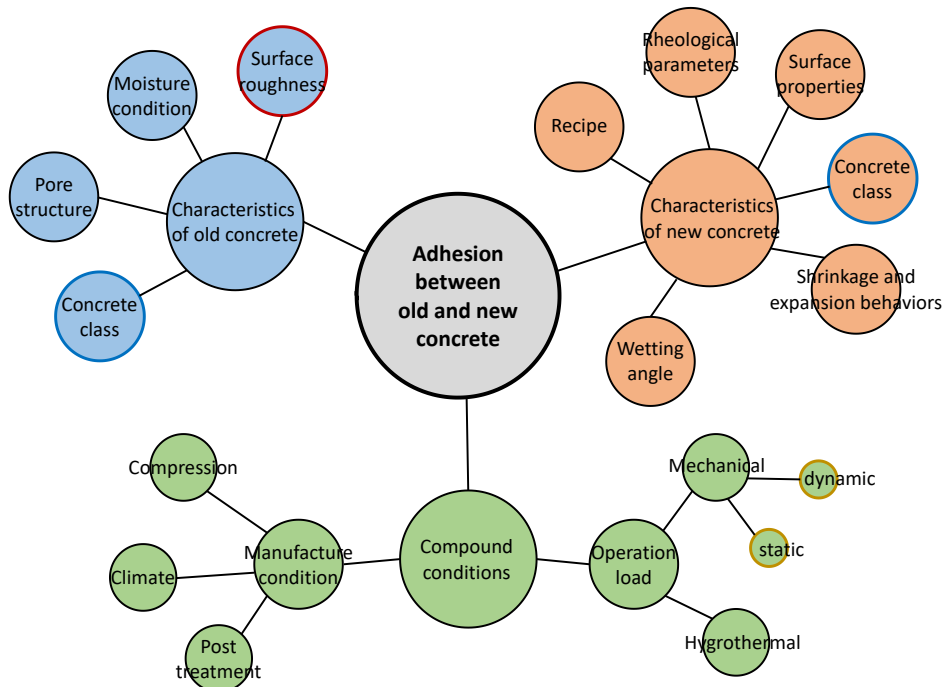


Figure 2.5 Basically influential aspects of concrete-to-concrete interface bonding [32]

The following aspects need to be considered in practice, which may reduce the bond between differently aged concrete elements [1]:

- Contamination of the concrete surface prior to casting of the overlay could significantly reduce the bond [47]; similarly, adverse climatic conditions (e.g. intense dry winds or solar radiation) can dry out the concrete surface and reduce bond strength;
- Inappropriate roughening methods may damage the top surface of the concrete (leading to micro-cracking, for instance)
- Inadequate quality of the new overlay concrete may cause significant constraint forces (e.g. due to shrinkage) and also reduce bonding;
- Edge zones (where significant internal tensile and shear stresses may occur due to constraint forces) have to be sufficiently secured.

2.1.2 Existing technologies for characterization of concrete surface roughness

As we mentioned above, surface roughness plays an important role in the bond of concrete interface. Reliable methods for the quantification of concrete surface roughness are in demand for both on site and laboratory measurements. The profile roughness parameters are defined by different standards associations in ISO 4287-1(1984) [48], BS 1134-1(1988) [49], DIN 4762 (1989) [50], DIN 4768 (1990) [51] and JIS B 0601(1994) [52]. DIN 4762 has identical notations for the same parameters with as EN ISO 4827. However, DIN 4768 may use the same notation but a different terminology. For example, The notation R_z in DIN 4768 refers to the terminology *Mean Peak-to-Valley Height*, while other mentioned standards use this notation for *Ten Points Height* parameter [53]; [54]. In order to differentiate the notation in different standards, the standard designation is added in subscript, such as $R_{z(ISO)}$ and $R_{z(DIN)}$.

The most commonly used parameter is the *Average Roughness* R_a , also known as *Center Line Average* or *Arithmetic Average*, which represents the average deviation of the profile from a mean line. It's determined as the mean value of profile heights along a certain length l_m

$$R_a = \frac{1}{l_m} \cdot \int_0^{l_m} y(x) dx \approx \frac{1}{n} \sum_{i=1}^n y_i \quad (2.1)$$

where l_m is the evaluation length and $y(x)$ is the profile height at position x .

Similar with the *Average Roughness* parameter is the *Root-Mean-Square Roughness* R_q , which is more sensitive to peaks and valleys and given by

$$R_q = \sqrt{\frac{1}{l_m} \cdot \int_0^{l_m} y(x)^2 dx} \approx \sqrt{\frac{1}{n} \sum_{i=1}^n y_i^2} \quad (2.2)$$

Another frequently used parameter is the *Mean Peak-to-Valley Height* $R_{z(DIN)}$, representing the average maximum valley-to-peak heights z_i within five different sampling lengths:

$$R_{z(DIN)} = \frac{1}{5} \sum_{i=1}^5 z_i \quad (2.3)$$

This parameter overcomes the limitation of Average Roughness R_a by taking into consideration the location and spacing between peaks and valleys, so that information of the surface topography is also included. Similar

with *Mean Peak-to-Valley Height* $R_{z(DIN)}$ are *Mean Peak Height* R_{pm} , *Mean Valley Depth* R_{vm} and *Ten Points Height* $R_{z(ISO)}$. The former two approaches are defined as average of maximum peak height and valley depth relative to the mean line within five different sampling lengths respectively. The *Ten Points Height* $R_{z(ISO)}$ is the sum of the five highest peaks p_i with five lowest valleys v_i within the entire evaluation length (see Figure 2.6) and given by

$$R_{z(ISO)} = \frac{1}{5} \left(\sum_{i=1}^5 p_i + \sum_{i=1}^5 v_i \right) \quad (2.4)$$

Since the five highest peaks and deepest valleys could be concentrated in a small area, this texture parameter is superior for use in very short evaluation lengths. Otherwise, the *Mean Peak-to-Valley Height* is a better choice.

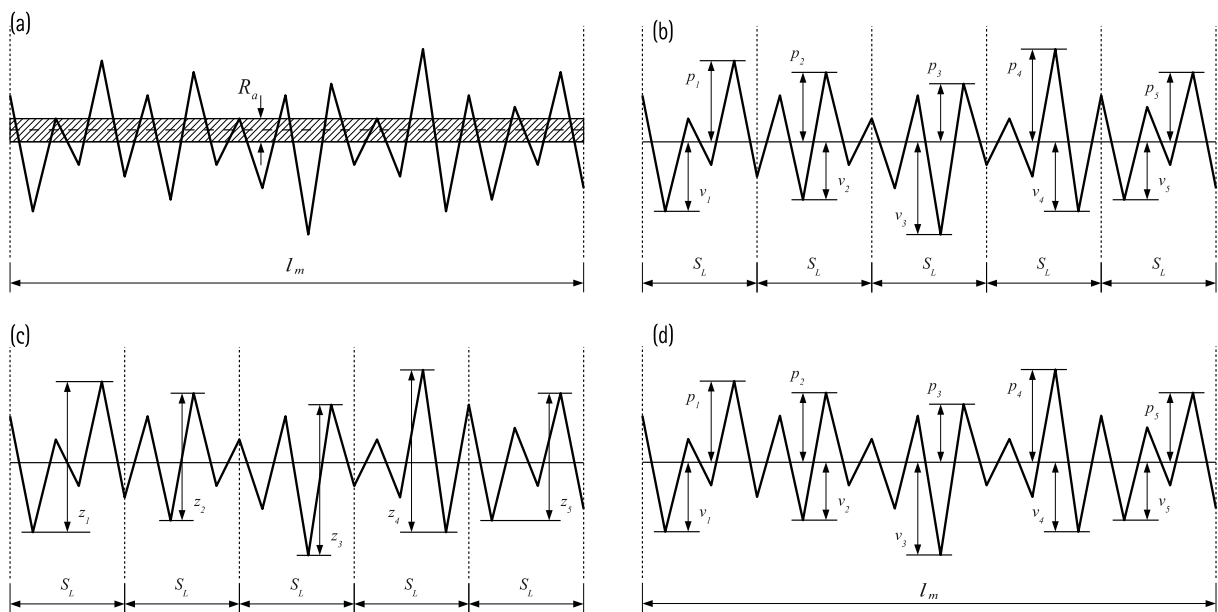


Figure 2.6 Surface texture parameters: (a) *Average Roughness* R_a ; (b) *Mean-Peak-Height* R_{pm} and *Mean Valley Depth* R_{vm} ; (c) *Mean Peak-to-Valley Height* $R_{z(DIN)}$; (d) *Ten Point Height* $R_{z(ISO)}$ [55]

Among all the measurement methods for surface roughness, the sand patch method proposed by Kaufmann 1971 [56] is most widely used on site due to its simplicity and quickness. A defined volume of fine sands is spread on the surface as a circle until the sands cover all the voids in this area. Depending on the diameter of the circle, the *Mean Texture Depth* (MTD) is determined to quantify the surface texture in EN 13036-1 [57]

$$MTD = R_t = \frac{4V}{\pi D^2} \quad (2.5)$$

where V is the volume of the sand and D is the diameter of the sand spread circle. Although *sand patch test* provides a quick, simple and cheap way to quantify the surface roughness, it's not very accurate and can only be used on horizontal or slightly inclined surfaces.

According to American National Standards Institute (ANSI) [58], methods for measuring roughness and surface texture can be classified into three types: *contacting methods*, *taper sectioning* and *optical (non-contact) methods*. Besides, these can also be divided as *qualitative methods* or *quantitative methods*, depending on whether the surface characterization is made by human assessment only or it's evaluated by a numerical value.

Finally, the approaches could also be catalogued as *non-destructive methods*, *partially destructive methods* and *destructive methods* [55].

Various methods have been developed over the years to characterize the surface roughness of concrete based on 2D profilometry and 3D surfometry techniques. The data obtained by these techniques allow a true quantitative evaluation of the surface profile using statistical parameters calculated from the total superficial profile [59] and from the filtered waviness (low frequency/macro roughness) and roughness (high frequency/micro roughness) [60]. Table 2.3 provides a comparison of the effectiveness, accuracy, consistency, and field applicability of several important roughness quantification methods.

Table 2.3 Comparison of various methods of concrete surface geometry characterization [61]

Roughness quantification method	Quantitative evaluation	Non-destructive	Cost	Portable	Work intensive	Contact with the surface
Concrete surface profile	No	Yes	Low	Yes	No	No
Sand patch test	Yes	Yes	Low	Yes	No	Yes
Outflow meter	Yes	Yes	Low	Yes	No	Yes
Mechanical stylus	Yes	No	Moderate	No	Yes	Yes
Circular track meter	Yes	Yes	Moderate	Yes	No	No
Digital surface roughness meter	Yes	Yes	Moderate	Yes	No	No
Microscopy	Yes	No	High	No	Yes	No
Ultrasonic method	No	Yes	Moderate	Yes	No	No
Slit-island method	Yes	No	Low	No	Yes	Yes
Roughness gradient method	Yes	No	Low	No	Yes	Yes
Photogrammetric method	Yes	Yes	Moderate	Yes	Yes	No
Shadow profilometry	Yes	Yes	Low	Yes	Yes	Yes
Air leakage method	No	Yes	Low	Yes	No	Yes
PDI method	Yes	No	Low	No	Yes	Yes
2D LRA method	Yes	Yes	Moderate	Yes	No	No
3D laser scanning method	Yes	Yes	High	Yes	No	No

The following techniques are analyzed on a comparative basis [62]:

- *Concrete surface profile*: in accordance with ICRI Guideline No. 310.2R-2013.
- *Sand patch test*: according to ASTM E965 (similar to EN 13036-1:2010) and EN 1766.
- *Mechanical profilometry*: in which a high-precision extensometer is moved over the entire surface to obtain a 3D map (with x , y and z coordinates) from which morphological parameters are computed.
- *Laser technique*: in this technique, the superficial elevation of each point (distance from the laser beam source to the object) is calculated based on the transit time of the laser beam.
- *Interferometric profilometry*: based on observation and analysis of the shadow resulting from the superficial roughness of the surface (moiré fringe pattern principle).

In order to have a quasi-monolithic behavior, the concrete-to-concrete interface is usually roughened by means of modern technologies. Several methods are available to remove the superficial layer of concrete, either for the removal of damaged concrete or to increase the surface roughness. According to ACI 555R [63],

the removal techniques could be grouped in four catalogues: a) *mechanical removal*; b) *paritcal impact removal*; c) *hydrodemolition*; and d) *chemical removal*.

Mechanical removal involves the use of manual or mechanized systems to remove the superficial layer of concrete. Typical techniques in the category are *chipping*, *wire-brushing* and *scarification* (also known as *milling*). These techniques are in general low cost with exception of scarification due to the cost of cutting wheels. However, reinforcement bars in the areas of reduced concrete cover can be damaged with this approach. Meanwhile the noise and dust produced in the process counts also as a disadvantage of mechanical removal methods.

Particle impact removal is designated as a process of roughening a surface by forcing solid particles across it at high speeds. The most used techniques are *shot-blasting* with metal particles and *sand-blasting* with sand particles. This could be used in both horizontal and vertical surfaces in a fast and effective way. In cases where the use of water is prohibited, this method is also suitable.

Hydrodemolition is also known as high-pressure water jetting (HPW), where high pressure water jets are used to remove the superficial layer of concrete. This method shows great advantage when the reinforcement bars will be reused, since it introduces no damage to the concrete members. What's more, some research [22] [64] [65] found that with HPW higher bond strength of interface could be obtained compared with other methods.

Chemical removal uses an acid solution on a concrete surface, allowing the acid to react with it and etch the concrete. This method is less popular than other methods, since some acid solutions are highly dangerous and may lead to severe injury.

In MC 2010, concrete surfaces are divided into four categories based on the roughness and representative mean values for the adhesive bond under appropriate measures (clean surface, appropriate roughening, good concrete quality, etc.). The coefficients of friction for concrete grades \leq C50/60 in the four categories are suggested in Table 2.4.

Table 2.4 Concrete surface categories for concrete grades \leq C50/60 [45]

Category	Average roughness R_a [mm]	Adhesive bond [N/mm ²]	Friction coefficient
Very smooth (e.g. cast against steel formwork)	not measurable		
Smooth (e.g. untreated, cast with wooden formwork)	< 1.5	0.5- 1.5	0.5 –0.7
Rough (e.g. sand blasted, high pressure water blasted, etc.)	\geq 1.5	1.5-2.5	0.7 –1.0
Very rough (e.g. HPW, indented)	\geq 3	2.5-3.5	1.0 –1.4

Since the average roughness R_a can't provide any information on the local variability of the surface profile, identical values of the same average roughness R_a might still lead to different shear resistances due to diverse actual surface topography. Engineering judgement is thus required when determining the appropriate roughness category.

Alternatively to the quantitative approaches with numerical values, qualitative methods based on visual inspection are proposed in several design codes such as EN 1992-1-1 [14], CEB-FIP Model Code 1990 [18] and ACI 318 [44]. Typical concrete surface profiles are demonstrated or described to make a visual classification. Different shear strengths could be obtained based on the surface roughness categories. The

following Table 2.5 gives the information of the surface roughness dependent parameters for evaluation of interface shear strength capacity in EN 1992-1-1 [14], DIN 1045-1 (2001) [39] and DIN 1045-1 (revised version 2008) [43].

Table 2.5 Parameters for concrete-to-concrete interface shear design based on surface roughness categories according to different design codes [6]

Surface category		EN 1992-1-1 (2004)		DIN 1045-1 (2001)		DIN 1045-1 (revised version 2008)			
		$c^{1)}$	$c^{2)}$	μ	β_{ct}	μ	c	μ	v
Indented	A surface with indentation complying with Fig. 6.9 in EN 1992-1-1 or Fig. 35 a) in DIN 1045-1 (revised version 2008)	0.5	0.5	0.9	2.4	1.0	0.5	0.9	0.7
Rough ³⁾	A surface with a least 3 mm roughness at about 40 mm spacing, achieved by raking, exposing of aggregate or other methods giving an equivalent behavior	0.45	0.4	0.7	2.0	0.7	0.4	0.7	0.5
Smooth	A slipformed or extruded surface, or a free surface left without further treatment after vibration	0.35	0.2	0.6	1.4	0.6	0.2	0.6	0.2
Very smooth	A surface cast against steel, plastic or specially prepared wooden moulds	0.25	0.025-0.1	0.5	0	0.5	0	0.5	0

¹⁾ values from EN 1992-1-1 (12.2004)

²⁾ newly corrected values from Maintenance Group of CEN/TC 250/SC 2 [66]

³⁾ different minimum roughness criterion based on the sand patch test of Kaufmann: $R_t > 0.9$ mm according to DIN 1045-1 (2001) [39] and DAFStb Booklet 525 [67] ; whereas $R_t > 1.5$ mm according to DIN 1045-1 (revised version 2008) [43]

2.1.3 Bond-slip relationship of concrete interface

As aforementioned the concrete shear resistance comes from three mechanisms: 1) adhesion and interlocking; 2) friction from external compressive action or clamping effect of reinforcements; and 3) dowel action from reinforcements crossing the interface. These effects interact with each other as a function of shear slip w and normal displacement v . The adhesion is fully effective when there is no shear slip at interface and dramatically decreases to zero once the slip occurs. After the failure of adhesive bond, the aggregate interlock effect also decreases quickly when protruding aggregates are crushed. The frictional resistance declines firstly and then increases due to the increasing clamping effects from reinforcements. The friction could be divided as static friction with static coefficient μ_s and kinetic friction with kinetic coefficient μ_k according to the values of the shear slip w . In comparison, the dowel action increases to approach a final value with the rise of slip, see Figure 2.7.

Ackemann and Bukhardt (1992) [68] have divided the bond-slip relationships in three phases dependent on the shear slip:

- Rigid ($0 \text{ mm} < w \leq 0.02 \text{ mm}$)
- Quasi-rigid ($0.02 \text{ mm} < w \leq 0.05 \text{ mm}$)
- Movable bond ($w > 0.05 \text{ mm}$)

The superposition of each load bearing component is then calculated with respect to the interface slip state. The adhesion model could then be simplified as a bilinear curve in rigid and quasi-rigid phases, meanwhile the original adhesion is related to tensile strength of the concrete. Based on the work of Vintzeleou, Tassion 1985 [16], a relationship between normal displacement (joint opening) v and tangential displacement w (joint slip) at interface could be described as

$$v = \alpha \cdot \sqrt[3]{w^2} \tag{2.6}$$

where α is a factor dependent on the surface roughness.

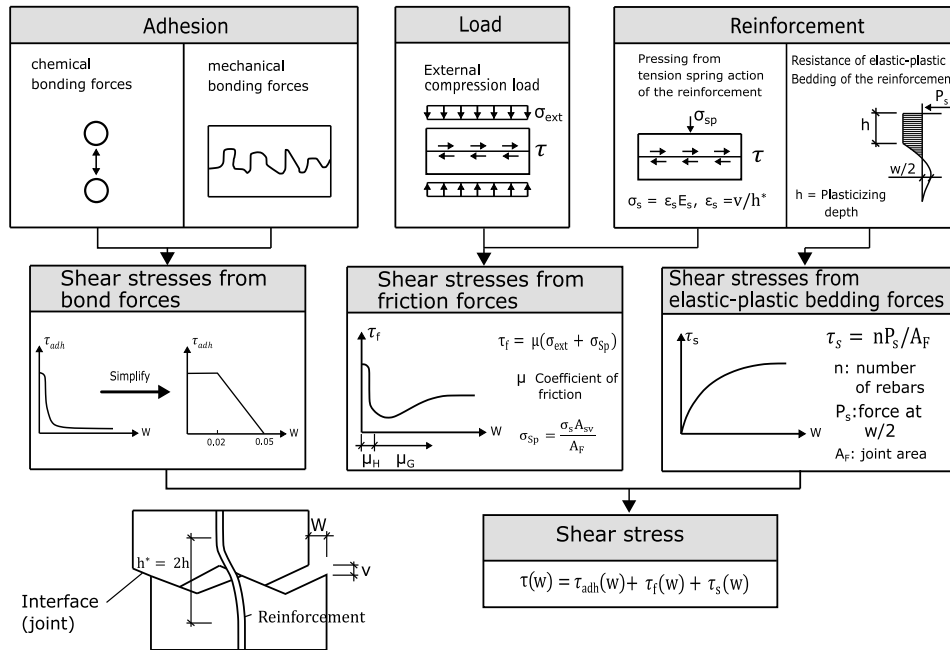


Figure 2.7 Schematic representation of the shear stress portions in unreinforced and reinforced concrete-to-concrete interface by consideration of mutual displacements [68]

The actual interaction of each mechanism is heavily dependent on the roughness category, quality of bond and amount of reinforcements crossing the interface, which in return also determine the possible shear slip of concrete interface at ultimate limit state. Typical shear-slip relationships of unreinforced concrete interface, reinforced rough interface and reinforced smooth interface are demonstrated in Figure 2.8 (a). When no reinforcement exists at interface or only a small amount of reinforcements crossing the interface is present, the behavior of the joint is quite brittle and failure typically occurs after the loss of adhesion at slip < 0.05 mm. On the other hand, reinforced joints exhibit a more ductile behavior and failure usually occurs at larger slips ranging from 0.5 mm – 1.5 mm. For smooth concrete interface joints with reinforcements, the dowel action plays a dominant role in the shear resistance, i.e. Figure 2.8 (b). On the other hand, rough reinforced joints have a big influence from friction and interlocking at small slip. The friction and interlocking effect declines, meanwhile dowel action increases and finally dominates the shear resistance with the rise of shear slip, i.e. Figure 2.8 (c).

With respect to the necessary reinforcements at concrete interface joints, it's suggested that the adhesion contribution in the total load bearing could be fully covered by reinforcements, so that a ductile bond-slip relationship could be obtained. Thus, the minimum reinforcement degree crossing interface could be determined [68].

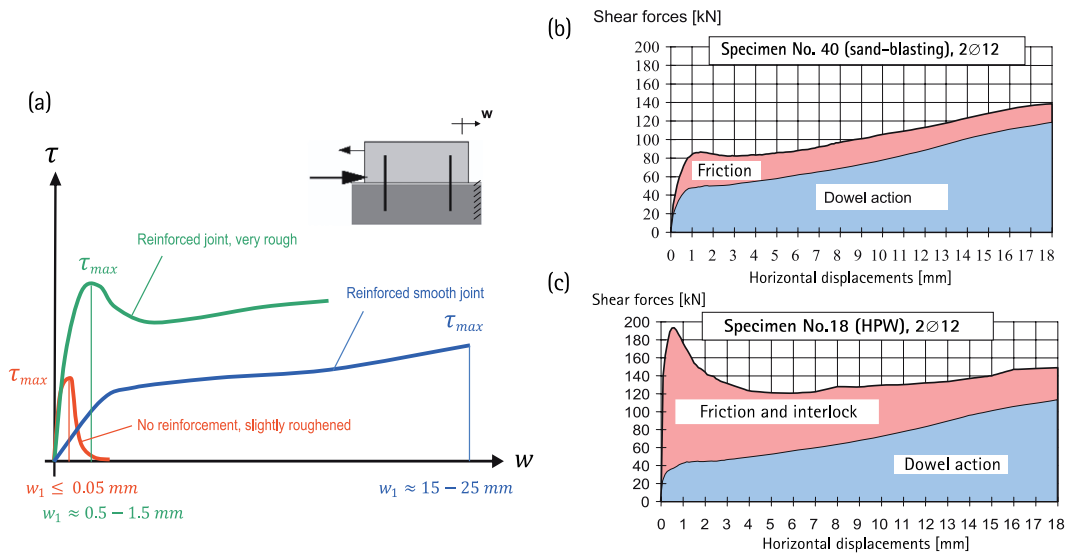


Figure 2.8 Bond-slip relationship: (a) shear stress-displacement relationship for selected specimens with unreinforced interface, reinforced smooth interface and reinforced rough interface; (b) Load-displacement diagram for a HPW specimen with depiction of different shear resistance contributions; (c) Load-displacement diagram for a sand-blasting specimen with depiction of different shear resistance contributions [6]

2.1.4 Experiment methods of concrete-to-concrete interface

The experimental specimens for concrete interface bonding could be divided into three categories [69]:

- Small scale specimens, including tension and shear experiments
- Slabs
- Beams

Unlike the large scale specimens such as slabs and beams, the small scale specimens allow extensive parameter studies easily to be conducted. The main parameters decisive for actual load bearing capacity observed in tests are [70]; [45]:

- Age differences (between prefabricated concrete elements and cast-in-situ concrete elements);
- Concrete strength (between prefabricated concrete elements and cast-in-situ concrete elements in compression and tension);
- Surface quality (e.g. roughness, moisture and cleanliness, etc.);
- Reinforcements (e.g. anchor, strength, form + location, amount);
- Consistency of the cast concrete
- Aggregates/ admixture/ additives
- Stresses (shear/ tension/ cyclic/ constraint, eccentricity/ inclination of shear force)
- Intermediate layer, i.e. filling layer
- Strong bond/ pre-cracking/ debonding before testing

As a result, the testing method is very important for determining of the characteristics of the interface. There is no standard method to test concrete-to-concrete bond strength. Beushausen (2005) [71] has reviewed different methods considering concrete overlay interface strength. Momayez (2005) [72] suggested that bonding tests could be divided into three categories according to the subjected stress state of interface: a) tension stress; b) shear stress; c) combination of shear and compression stress. Based on the large

investigations [71]; [73]; [55]; [72], a summary and classification of the concrete interface bonding tests is presented in Figure 2.9.

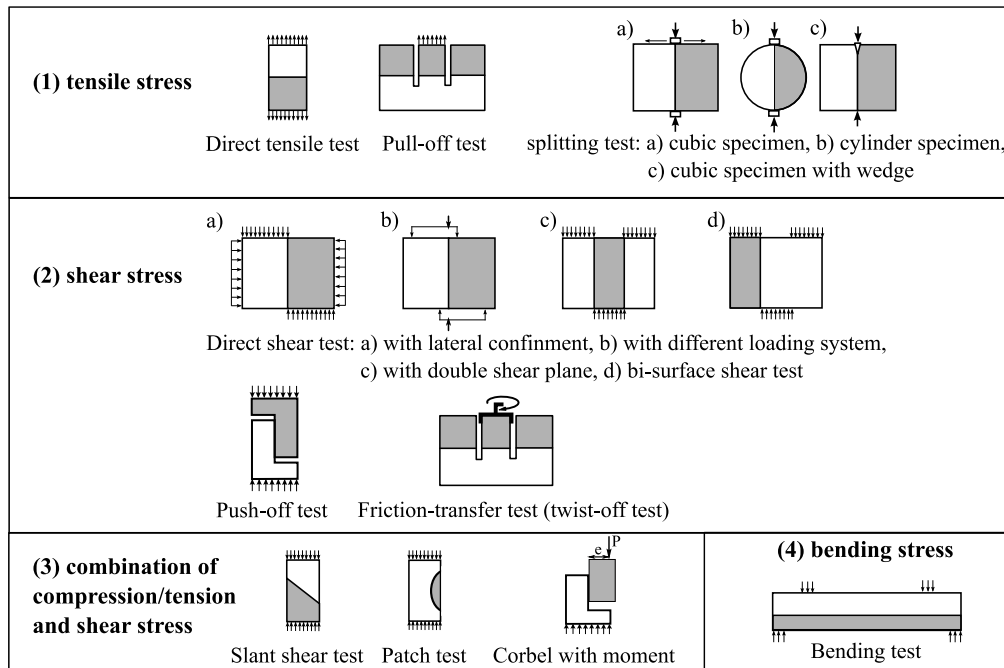


Figure 2.9 Schematic description of concrete interface bonding test methods [74]

Among the test methods, pull-off test is defined in EN 1542 (1999) [75] and ASTM C1583 (2013) [76]; splitting test is described in EN 12390-6 (2009) [77] and ASTM C496 (2017) [78]; and slant-shear test is also recorded in EN 12615 (1999) [79] and ASTM C822 (2018) [80]. Splitting test provides a method to get tensile strength in compression loading. This method is technically easy to implement, however it requires more interpretation, e. g. inverse analysis, to obtain the crack properties of the interface. On the other hand, direct tensile test has a high requirement on the testing equipment but could get a direct crack behavior under tension. It's found in previous experiments that the interface displacements under shear stresses depend significantly on whether the interface is under compression or not. The normal stresses perpendicular to the joint can be caused either by an external load or by the clamping effect of the reinforcements crossing the interface. In the case of not compressed and unreinforced interface joints, only the adhesive bond contributes to the transmission of shear forces. Thus, a brittle failure of bond would occur after comparatively slight relative displacements at interface (Figure 2.8) [70]. With respect to the implementation of direct shear tests, different variants could be designed to avoid tensile stresses at interface by inducing lateral confinement or symmetric loading. In practice, concrete interface is usually subjected to multi-stress state instead of single stress state. In order to obtain the full characteristics of interface, different bonding tests such as tensile test, shear test, and combined shear and compression/tensile test should be implemented together.

2.2 Fracture modelling approaches

Fracture and failure processes take place in all size scales. Structural engineers mainly prefer the macroscopic approach, while material scientists are more interested in the material structure in mesoscopic or the underlying microscopic processes. On the other hand, solid physicists primarily focus on the nanoscopic structure of atomic bonds. The modelling of cracks and defects at different observation levels could be implemented with molecular dynamics, micromechanics, damage mechanics and fracture mechanics, see Figure 2.10.

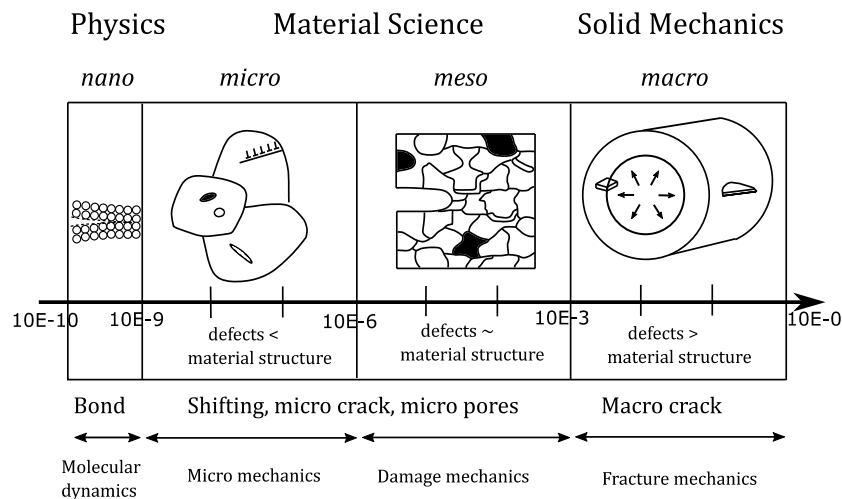


Figure 2.10 Fracture processes on different scales [81]

Structural design based on strength criterion could not fully demonstrate the true failure behavior. Thus, fracture mechanics approach is needed for a more accurate research. Five compelling reasons for developing fracture mechanics are stated [82]:

- (1) Energy required for crack formation;
- (2) Objectivity of calculations by considering strain-softening and avoiding of mesh size dependency;
- (3) Lack of yield plateau leading to stress reduction (softening) and especially overestimation of failure load for large size structure under strength criterion;
- (4) Energy absorption capability and ductility by considering the post-peak decline of the load and the dissipated energy in the process;
- (5) Size effect representing a dependence of nominal stress σ_n on the structure dimension and its influence on ductility.

Figure 2.11 shows a comparison between fracture mechanics approach and traditional material strength approach for structural design. In contrast to strength approach with two parameters where a material is assumed to be adequate when the strength is greater than the applied stress, the fracture mechanics approach combines the three variables of applied stress, flaw size and fracture toughness.

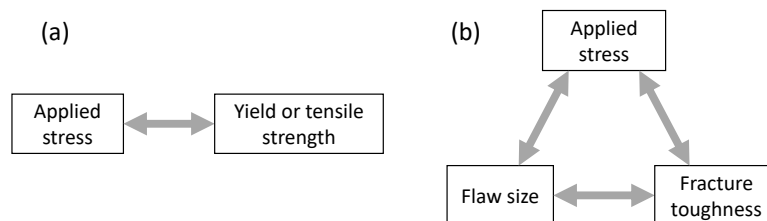


Figure 2.11 Comparison of design approaches based on material strength and fracture mechanics [83]

2.2.1 Fundamental theory of fracture mechanics

Fracture failure due to existing crack or flaw could be predicted and diagnosed by various models. For brittle materials (e.g. glass and ceramic) where the plastic zone around the crack tip is very small, the linear elastic fracture mechanics (LEFM) based on linear elastic assumption is applied. However, when significant plastic deformation precedes the crack failure (i.e. big crack tip plastic zone), LEFM is then no longer suitable. Nonlinear fracture mechanics (NLFM) should be used to describe a more ductile failure. Different concepts

were developed in last decades for LEFM such as Griffith's energy concept in 1920, Irwin's stress intensity concept in 1957 and R-curve (i.e. crack extension resistance curve) concept. On the other hand, equivalent crack model and cohesive crack model concepts were developed for NLFM.

A brief overview of fracture mechanics regarding the concepts and corresponding models is demonstrated in Figure 2.12.

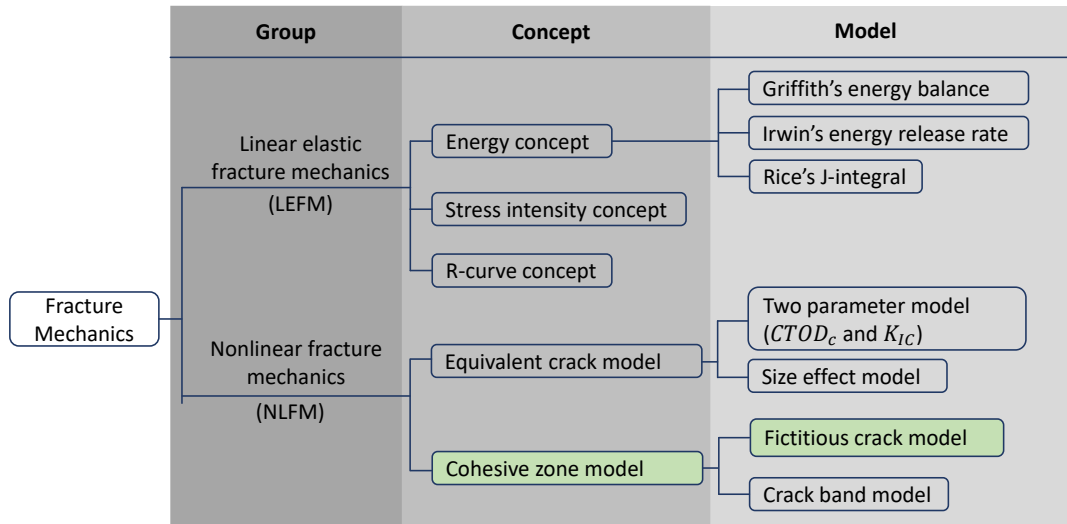


Figure 2.12 Overview of fracture mechanics [33]

2.2.1.1 Linear elastic fracture model

(1) Energy concept

Griffith (1920) [84] was the first to propose the energy criterion for fracture behavior of brittle materials such as glass. An energy-balance approach between the absorbed surface energy for initiation crack and released strain energy adjacent to crack was developed.

For linear material ($\sigma = E\varepsilon$), the strain energy per unit volume W^* is

$$W^* = \int \sigma d\varepsilon = \frac{E\varepsilon^2}{2} = \frac{\sigma^2}{2E} \quad (2.7)$$

When a crack occurs to a depth a (e.g. a plate with an edge-cracked length a subjected to a remote tensile stress), the region adjacent to the free surfaces is unloaded and its strain energy releases. A simple way to evaluate the released strain energy is to regard two triangular regions of width a and height β near the crack flanks as being completely unloaded, while the remaining material still sustains full stress. The parameter $\beta = \pi$ for plane stress loading based on the Inglis solution.

The total released strain energy W is then

$$W = -\frac{\sigma^2}{2E} \cdot \pi a^2 \quad (2.8)$$

On the other hand, requisite bond energy must be absorbed by the material to form a crack. The surface energy S_{surf} associated with a crack of length a is

$$S_{surf} = 2\gamma_e a \quad (2.9)$$

where γ_e is the surface energy per unit area and the factor 2 refers to two free surfaces that have been formed.

The total energy associated with the crack is then the sum of absorbed energy to create new free surfaces and the liberated strain energy near the crack flanks. Up to the critical crack length a_c , the crack will grow only if the stress increases. However, beyond that point, the system can lower its energy by letting crack grow longer and thus crack growth is spontaneous and catastrophic.

The critical crack length could be calculated by setting the derivation of the total energy $w + S_{surf}$ to zero

$$\frac{\partial(w + S_{surf})}{\partial a} = 2\gamma - \frac{\sigma_c^2}{E}\pi a = 0 \tag{2.10}$$

As a result, the critical stress for catastrophic crack could be determined as

$$\sigma_c = \sqrt{\frac{2E\gamma}{\pi a}} \tag{2.11}$$

Irwin (1956) [85] then modified Griffith's equation by employing the *strain energy release rate* G for ductile materials. It's suggested that the released strain energy was not only absorbed by creating new surfaces but also by energy dissipation due to plastic flow in the material near the crack tip. The uncontrolled fracture occurs when the strain energy is released at a rate sufficient to satisfy the needs of all these energy "sinks", thus the Griffith equation can then be rewritten as

$$\sigma_c = \sqrt{\frac{2G_c}{\pi a}} \tag{2.12}$$

where G_c denotes the *critical strain energy release rate*, which is also a measure of fracture toughness.

Rice (1968) [86] developed a line integral (path-independent) parameter around the crack tip, also called as J integral, so that Rice was able to generalize the energy release rate to nonlinear materials by idealizing plastic deformation as nonlinear elastic. The J integral can be viewed as nonlinear stress-intensity parameter as well as an energy release rate and it is also now implemented in many Finite-Element programs.

(2) Stress intensity concept

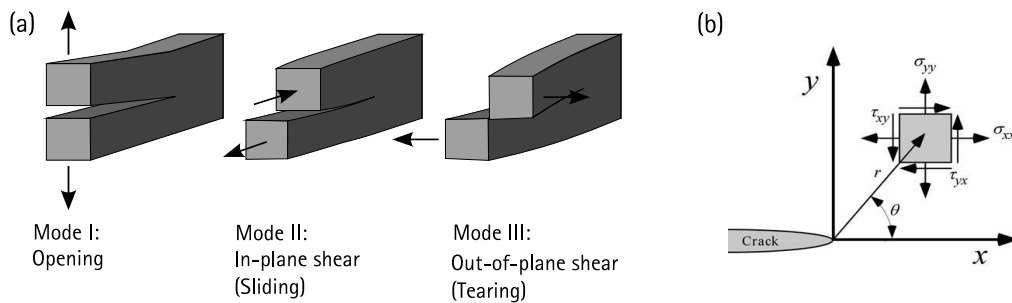


Figure 2.13 The stress intensity approach: (a) the fracture modes; (b) stresses near the tip of a crack in an elastic material [83]

Based on Westergaard (1939)'s [87] approach of a semi-inverse technique for analyzing stresses and displacements ahead of a sharp crack, Irwin (1957) [88] found that the stresses and displacements near the crack tip could be described by a single constant related to energy release rate, which is then known as *stress intensity factor*.

Three types of fracture modes are distinguished in classical fracture mechanics, see Figure 2.13, which are the opening mode (mode I), in-plane shear (mode II) and out-of-plane shear (mode III). The singular stress fields of all the three fracture modes could be described by their corresponding *stress intensity factor* that is only dependent on the geometry of the component, crack size as well as the external loads. For linear elastic material, the stress fields of the three modes could be superposed, so that the approximations of the stress state near the crack tip could be given as

$$\sigma_{ij}(r, \theta) = \frac{1}{\sqrt{2\pi r}} [K_I f_{ij}^I(\theta) + K_{II} f_{ij}^{II}(\theta) + K_{III} f_{ij}^{III}(\theta)] \quad (2.13)$$

and the displacement state around the crack tip could be expressed as

$$u_{ij}(r, \theta) = \frac{1}{2G} \sqrt{\frac{r}{2\pi}} [K_I g_{ij}^I(\theta) + K_{II} g_{ij}^{II}(\theta) + K_{III} g_{ij}^{III}(\theta)] \quad (2.14)$$

where $G = E/2(1 + \nu)$ is the shear modulus (ν is the Poisson's ratio); K_I , K_{II} and K_{III} are the stress-intensity factors of three fracture modes and f_{ij}^I , f_{ij}^{II} , f_{ij}^{III} , g_{ij}^I , g_{ij}^{II} and g_{ij}^{III} are the geometrical functions or weight functions, which are summarized in Table 2.6.

Table 2.6 Summarized geometrical functions [83]; [89]

	Mode I	Mode II	Mode III
f_{xx}	$\cos \frac{\theta}{2} \left(1 - \sin \frac{\theta}{2} \sin \frac{3\theta}{2}\right)$	$-\sin \frac{\theta}{2} \left(2 - \cos \frac{\theta}{2} \cos \frac{3\theta}{2}\right)$	0
f_{yy}	$\cos \frac{\theta}{2} \left(1 + \sin \frac{\theta}{2} \sin \frac{3\theta}{2}\right)$	$\sin \frac{\theta}{2} \cos \frac{\theta}{2} \cos \frac{3\theta}{2}$	0
f_{zz}	0 (plane stress) $2\nu \cdot \cos \frac{\theta}{2}$ (plane strain)	0 (plane stress) $-2\nu \cdot \sin \frac{\theta}{2}$ (plane strain)	0
f_{xy}	$\sin \frac{\theta}{2} \cos \frac{\theta}{2} \cos \frac{3\theta}{2}$	$\cos \frac{\theta}{2} \left(1 - \sin \frac{\theta}{2} \sin \frac{3\theta}{2}\right)$	0
f_{xz}	0	0	$-\sin \frac{\theta}{2}$
f_{yz}	0	0	$\cos \frac{\theta}{2}$
g_x	$\cos \frac{\theta}{2} \left[\kappa - 1 + 2\sin^2 \frac{\theta}{2}\right]$	$\sin \frac{\theta}{2} \left[\kappa + 1 + 2\cos^2 \frac{\theta}{2}\right]$	0
g_y	$\sin \frac{\theta}{2} \left[\kappa + 1 - 2\cos^2 \frac{\theta}{2}\right]$	$-\cos \frac{\theta}{2} \left[\kappa - 1 - 2\sin^2 \frac{\theta}{2}\right]$	0
g_z	0	0	$4\sin \frac{\theta}{2}$

Note: ν is Poisson's ratio, $\kappa = 3 - 4\nu$ (plane strain) and $\kappa = (3 - \nu)/(1 + \nu)$ (plane stress)

The equations (2.13) and (2.14)(5.50) are valid only near the crack tip, where the $1/\sqrt{r}$ singularity dominates the stress field, which is defined as *singularity-dominated zone*. The stress intensity factor defines the amplitude of the crack tip singularity, and stresses near crack tip increase in proportion to K .

$$\begin{cases} K_I \\ K_{II} \\ K_{III} \end{cases} = \lim_{r \rightarrow 0} \sqrt{2\pi r} \begin{cases} \sigma_{yy}(r, \theta = 0) \\ \sigma_{xy}(r, \theta = 0) \\ \sigma_{yz}(r, \theta = 0) \end{cases} = \lim_{r \rightarrow 0} \sqrt{\frac{2\pi}{r}} \begin{cases} \frac{1}{\kappa + 2} u_y(r, \theta = \pi) \\ \frac{1}{\kappa + 1} u_x(r, \theta = \pi) \\ \frac{1}{4} u_z(r, \theta = \pi) \end{cases} \quad (2.15)$$

The material can withstand crack tip stresses up to a critical value of stress intensity, denoted as *critical stress intensity factor* (K_{Ic} , K_{IIc} and K_{IIIc}), which is also a measure of fracture toughness. The stress intensity and energy concept are interrelated and their relationship could be demonstrated as

$$\begin{cases} K_{Ic}^2 = E G_c & (\text{plane stress}) \\ K_{Ic}^2 = E G_c (1 - \nu^2) & (\text{plane stress}) \end{cases} \quad (2.16)$$

(3) R-curve concept

Crack extension occurs when the applied energy release rate \mathcal{G} reaches the material's crack extension resistance \mathcal{G}_R . A plot of \mathcal{G}_R vs. crack extension is called a *resistance curve* or *R-curve*. The corresponding plot of \mathcal{G} vs. crack extension is the *driving force curve*. The relationship between the applied driving force curve and material's R-curve determines the stability of a given crack. The shape of R-curve depends mainly on material behavior but the configuration of the crack also plays a subordinate role. The R-curve for an ideally brittle material is flat due to the invariant material property of surface energy, whereas ductile fracture in metals usually exhibits a rising R-curve for the increase of plastic zone at crack tip. When a metal fails by cleavage, a failing R-curve occurs that is far less common. R-curve can alternatively be discussed in terms of stress intensity factor K_R and it's also a measure of fracture toughness.

2.2.1.2 Nonlinear elastic fracture model

LEFM is valid only when the nonlinear material deformation is confined to a small region surrounding the crack tip, which is not this case for most materials. For cementitious material, LEFM is only applied on very large sized specimens since in this case the nonlinearity in the vicinity of *fracture process zone* (FPZ) is so small as to be negligible compared to the specimen dimension. Otherwise, NLFM is used for normal size concrete components. There are mainly two approaches to model the fracture mechanism for cementitious material – the equivalent crack model and the cohesive zone model.

(1) Equivalent crack model

The two most important representatives of the equivalent crack model are the two-parameter model proposed by Jenq and Shah in 1985 [90] and the size effect model introduced by Bazant and Kazemi in 1990 [91]. Both models reflect only the maximum load-bearing capacity taking into account the current crack condition and do not allow any modelling of post-fracture behavior, and are different with the cohesive zone model based on softening functions that could simulate the local damage [33].

The equivalent crack model was originally based on LEFM and then extended to NLFM with additional size independent parameters, i.e. critical stress intensity factor K_{Ic} and critical crack tip opening displacement $CTOD_c$. With this model, the maximum bearing load for mode I failure of a given structure with an arbitrary geometry could be calculated.

The size effect model describes the transition from conventional strength criterion to the LEFM models. The strength criterion can only be used for small concrete components. In contrast, the LEFM can only be used for very large concrete components such as dams. The area in between is described by a continuous function: the size effect law, see Figure 2.14 (right).

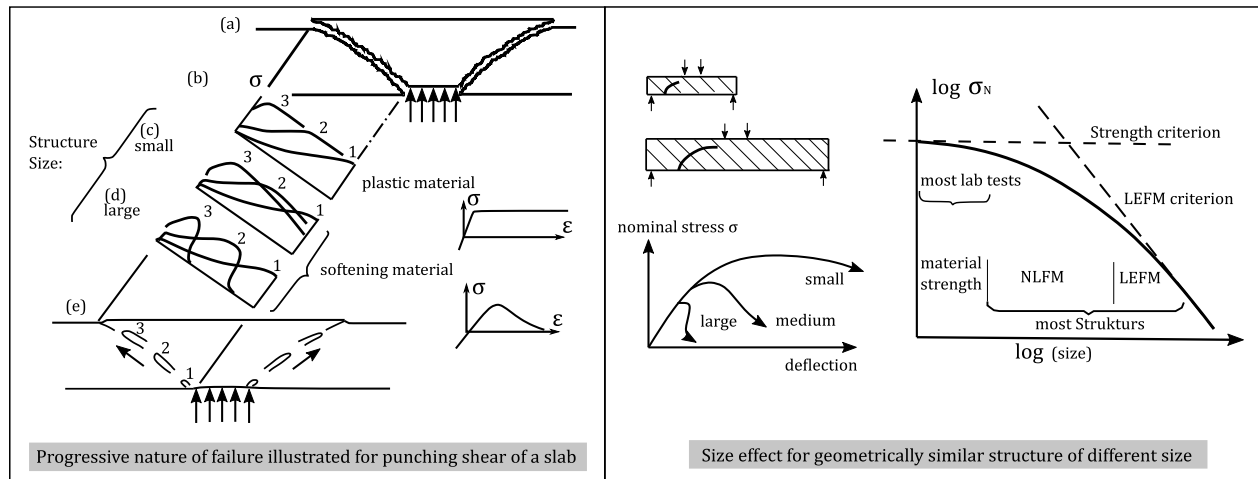


Figure 2.14 Nominal strength depending on the test specimen size according to Bazant [82]

A comparison of geometrically similar structures with different sizes is used to define the size effect, which is characterized in terms of the nominal stress σ_N at ultimate load P_u . The nominal stress doesn't present any actual stress in the structure but is defined as $\sigma_N = P_u/bd$ for 2D similarity and as $\sigma_N = P_u/d^2$ for 3D similarity, where b refers to thickness of 2D structure and d denotes the characteristic dimension of the structure such as depth of the beam or its span. Taking the punching shear failure for example, for cementitious materials, after fracture there exists a softening of the material rather than a plastic plateau, where the stress peak moves in the damage zone, leaving a reduced stress behind it (softening). The stress reduction is mild only if the structure is small, in which case the plastic limit analysis based on strength or yield criteria is not so far off. However, when the structure is large, the stress curve shows a steep stress drop behind the peak stress point, so that the limit analysis grossly overestimates the damage load, see Figure 2.14 (left). Very large specimens governed by LEFM exhibit a rather strong size effect. The actual situation of most concrete structures is a transitional behavior between strength criterion and LEFM criterion [82].

(2) Cohesive zone model

Due to the widespread use of finite element method (FEM), cohesive zone models (CZM) with the consideration of softening functions are increasingly used in the fracture analysis. The CZM was firstly proposed by Dugdale (1960) [92] for plastic material and Barenblatt (1962) [93] for brittle material to describe the nonlinear fracture processes and stress transfer across cracks in materials. A linear elastic behavior is assumed before the stress reaches the strength, followed by the application of a softening function dependent on the degree of damage. One of the advantages of CZM is that the fracture behavior of the cementitious material could be characterized with different post-peak behavior. A distinction between discrete and smeared crack formations is made based on how the softening function is described.

Hillerborg et al. (1976) [94] modified the CZM to relate the concrete fracture to a single crack surface, also known as fictitious crack model. In the case of fictitious crack model, the softening function is described as a stress-crack opening curve (also known as traction-separation law) by means of zero-thickness contact elements along the crack path in FEM. The area under the traction-separation curve corresponds to the fracture energy G_f . In this model, the crack propagation path should be known in advance. This prerequisite is given when analyzing bonding joints, which makes the fictitious crack model especially appropriate for this application. Although the use of fictitious crack model is also possible without prior knowledge of crack path nowadays due to the rapid developments of FEM, computationally expensive remeshing is required [95].

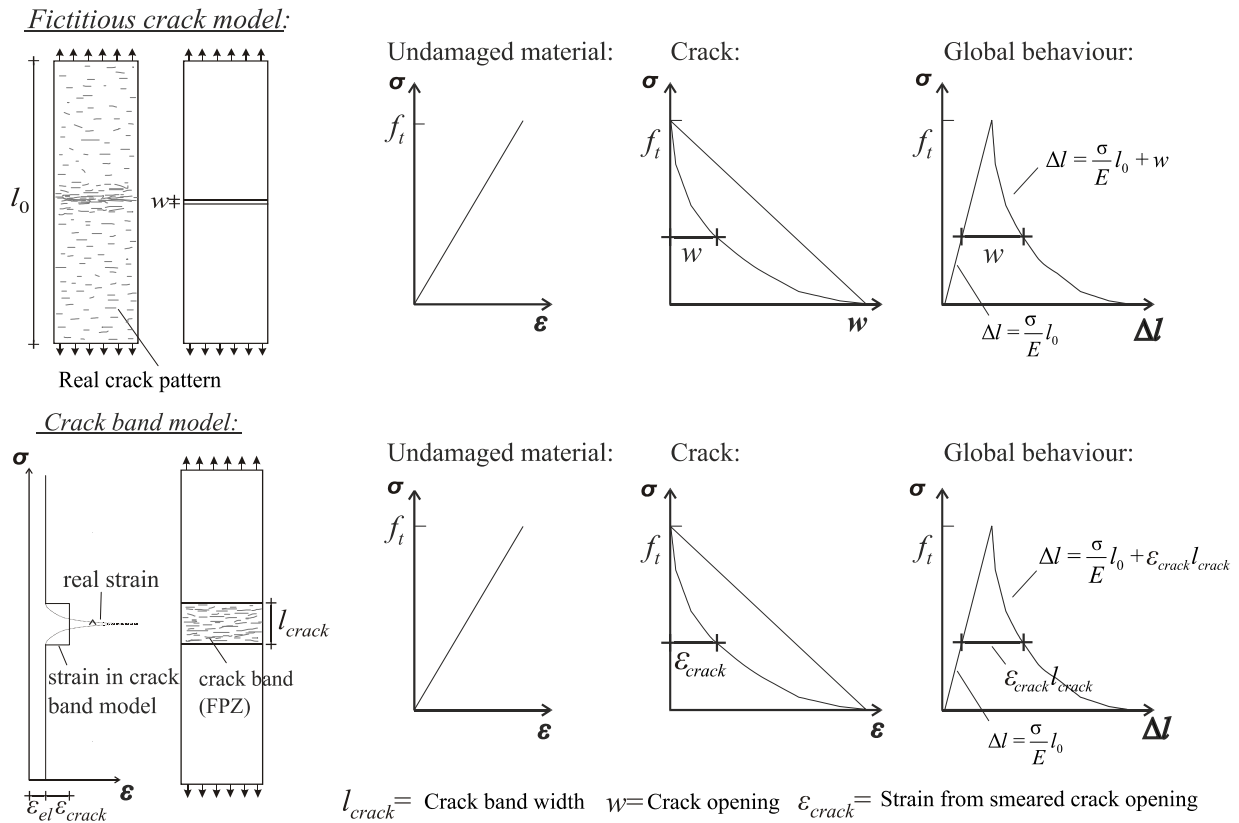


Figure 2.15 Comparison of fictitious crack model and crack band model [96]

In contrast, the crack band model developed by Bazant and Oh (1983) [97] mimics the fracture as a blunt smeared crack band, in which an equivalent material parameter - crack width (physically interpreted as the width of the FPZ) - should be defined. The constitutive law of the material is combined with the traction-separation law of a crack, so that an effective continuum stress-strain law for material could be used in the FEM. Once the crack initiates, the total strain is decomposed into continuum strain and an effective crack strain, which is computed by smearing the crack opening displacements over a prescribed band of material. A major advantage of the crack band model is that the crack path doesn't have to be known in advance in the calculation compared with fictitious crack, in which a prior knowledge of the crack growth path before computation is required. A comparison of the fictitious crack model and crack band model is demonstrated in the Figure 2.15.

2.2.1.3 Fracture models for concrete in FEM

In the macroscopical fracture analysis of quasi-brittle materials such as concrete within FEM, two approaches are generally in use [98]:

- Discrete crack approach
- Smeared crack approach

In the discrete crack approach, a crack is assumed as soon as the normal nodal forces exceed the tolerable tensile force. New degree of freedom would be created on the node and generate a geometric discontinuity at the original position. The discrete crack concept approach though reflects this phenomenon most closely, in which the crack is directly simulated via a displacement-discontinuity in an interface element that separates two solid elements [99]. There are two distinct disadvantages of this approach: (1) continuous remeshing is required which significantly slows down the efficiency; (2) the crack could only propagate along the mesh lines. Thus, to overcome the problem of remeshing, the smeared crack approach has been introduced

alternatively. A smeared crack concept imagines the cracked solid to be a continuum and permits a description in terms of stress-strain relationship, in which the underlying assumption of displacement continuity conflicts with the reality of a discontinuity.

There are three implemented material modules for the crack simulation based on smeared crack approach for (reinforced) concrete in Abaqus [100]:

- *Concrete smeared cracking model*
- *Cracking model for concrete*
- *Concrete damaged plasticity*

Table 2.7 Summary of fracture models for concrete based on smeared approach in Abaqus

Concrete smeared cracking	Cracking model for concrete	Concrete damage plasticity
<ul style="list-style-type: none"> • Concrete/ reinforced concrete • Linear elastic material in elastic stage • Isotropically hardening yield surface when stress is dominated in compression • "Crack detection surface" to detect crack • For application where relatively monotonic loadings are applied under fairly low confining pressures 	<ul style="list-style-type: none"> • Concrete/ reinforced concrete or other brittle material such as ceramics or brittle rocks • Linear elastic material in elastic stage • Compressive behavior always in linear elastic stage • Rankine criterion to detect crack • For application where behavior is dominated by tensile cracking 	<ul style="list-style-type: none"> • Concrete/ reinforced concrete and other quasi-brittle materials • Non-associated multi-hardening plasticity and isotropic damage elasticity • Failure determined by yield/failure surface, which is controlled by tensile and compressive equivalent plastic strains • For both tensile crack and compressive crushing • For concrete subjected to monotonic and cyclic loading

Concrete smeared crack model is intended as a model for the behavior of concrete under relatively monotonic loading at relatively low confining pressures (i.e. less than four to five times the magnitude of the largest stress that can be carried by the concrete in uniaxial compression). In this model, the individual "macro" cracks could not be tracked. Constitutive law of the material is calculated independently at each integration point of the finite element in the model. Cracking is assumed to occur when the stress reaches a failure surface (i.e. *cracking detection surface*), which has a linear relationship between the equivalent pressure stress and the Mises equivalent deviatoric stress. The model also performs the constitutive calculations independently at material point of finite element model and couldn't track the individual "macro" cracks. The presence of cracks affects the stress and material stiffness associated with the material point. Here, a simple Rankine criterion, which states a crack occurs when maximum principal tensile stress exceeds the tensile strength of the brittle material, is used to detect the crack initiation. *Concrete damaged plasticity* model is a continuum, plasticity-based damage model for concrete and other quasi-brittle materials in all types of structures, e.g. beams, trusses, shells, solids, etc. Both tensile crack and compressive crushing of the concrete could be simulated. The model consists of the combination of non-associated multi-hardening plasticity and isotropic damaged elasticity to describe the irreversible damage during fracture process. The failure of the material is determined by the yield/failure surface, which is controlled by tensile and compressive equivalent plastic strains. This model could be used for applications in which concrete is subjected to monotonic, cyclic, and/or dynamic

loading under low confining pressures. The stiffness recovery effects during cyclic load reversals as well as sensitivity of the straining rate could also be defined in this model. A summary and comparison of the three models are shown in the following Table 2.7.

The virtual crack closure technique (VCCT) based on LEM as well as cohesive contact element technique are otherwise available in FEM for a discrete approach simulation, where the propagation of interfacial cracks/debonding could be observed in the model. Extended finite element method (XFEM) was later developed by Belyschko and Black in 1999 [101] for the propagation of discrete crack along arbitrary, solution-dependent path without the requirement of remeshing, which allows the crack to be modeled independent of mesh. In this thesis, the cohesive element technique will mainly be used in the simulation and the concept of this model will be discussed in more detail in the chapter 3.3.

2.2.2 Elastic-plastic damage model

In continuum mechanics, elastic damage models or elastic plastic constitutive laws are generally the standard approach to describe concrete behavior. The former represents the progressive micro-cracking and strain softening by degradation of the elastic stiffness, while the latter describes the softening by means of irreversible plastic strain. However, pure elastic damage models or pure elastic plastic constitutive laws are not totally satisfactory to describe the concrete behavior, such as the unloading slopes in cyclic loading or permeability of damaged concrete [102]. Hence, coupling of these two effects is requisite in some cases dealing with concrete structures, see Figure 2.16.

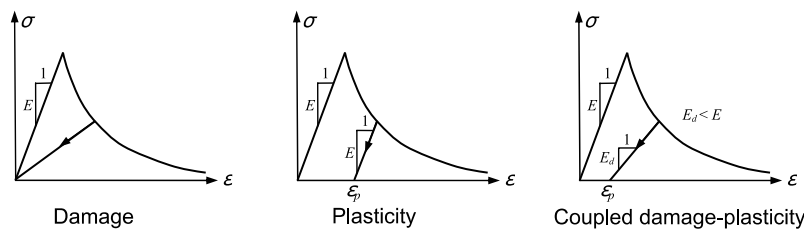


Figure 2.16 Uniaxial stress-strain behavior of constitutive models [103]

Once the limit of elasticity is reached, the plastic deformation occurs, which is defined by yield criterion. The plastic behavior of a material is observed through experiments. Metals demonstrate usually no volume change during plastic yield, whereas the volume changes could be observed in other nonmetallic materials such as concrete. The volume changes are caused by hydrostatic pressure, which indicates the contributions of both hydrostatic and deviatoric components to the concrete plastic behavior. Thus, the most common or classic yield criterion could be classified as [104]:

- **Independent on hydrostatic pressure:** Von-Mises Criteria, Tresca Criteria, Rankin Criteria, etc.;
- **Dependent on hydrostatic pressure:** Mohr-Coulomb Criteria, Drucker-Prager Criteria, Mises-Schleicher Criteria, etc.

Unlike fracture mechanics where the macroscopic cracks in materials are described, the damage mechanism is still based on classical strength theory. A material law is used for the formulation that integrates the distributed defects on a microscopic level, such as microcracks or micropores. The material damage is presented by defect proportion per volume with parameter "D" (i.e. damage scalar) [105]:

$$D = \frac{\text{volume of all micropores}}{\text{volume of whole volume elements}} \in [0,1] \quad (2.17)$$

The coupling of damage mechanism and plasticity could be implemented using the following methods [106]:

- (1) *Coupling in stress space* occurs by means of the concept of effective stress. This combination could be formulated according to a yield/ damage surface (Meschke, Lackner and Mang in 1998 [107]; Lee and Fenves in 1998 [108]) or one yield surface and one damage surface, i.e. two limit state surfaces (Yazdani and Schreyer in 1990 [109]).
- (2) *Coupling in strain space* is firstly introduced by Han and Chen (1986) [110]. The yield or damage surface is located in a strain space. Additional assumptions have to be made for the division of inelastic rates.
- (3) *Mix coupling of the two effects* exist by defining the two limit state surfaces in two spaces. Here the stress-based plasticity theory is coupled with the strain-based damage theory. This procedure was developed by Bazant and Kim (1979) [111]. It's carried out by an elaborate curve fitting using many material parameters, which ensures a high modelling quality.

2.2.3 Fractural modelling for concrete-to-concrete interface

The simplification of the fracture mechanics with the consideration of concrete-to-concrete interface joints comes from the nonlinear elastic fracture models described in chapter 2.2.1.2. Since the bond joint usually represents the weakest location of the composite structure, the application of fictitious crack model is thus very appropriate here to describe the stress transfer and crack propagation at interface joints [33].

Various models have been developed in recent decades for modelling the stress-displacement relationships of two crack flanks and associated dilatancy. These models can be divided as [33]

- (1) Empirical models
- (2) Physical models
- (3) Statistical models

The modelling of the interface joint behavior requires a closer examination of the interface characteristics. This primarily refers to the surface geometry, which produces mechanical interlocking. The concrete surface characteristics depend not only particularly on the type and intensity of the surface treatment, consistency and strength of cement matrix, but also on the shape, size and strength of aggregates [30]. Therefore, different surface sections of one component with homogeneous concrete and same surface treatment will always have similar surface characteristics in terms of macro and micro roughness. In contrast, two concretes with different aggregates but under otherwise identical conditions show diverse roughness properties.

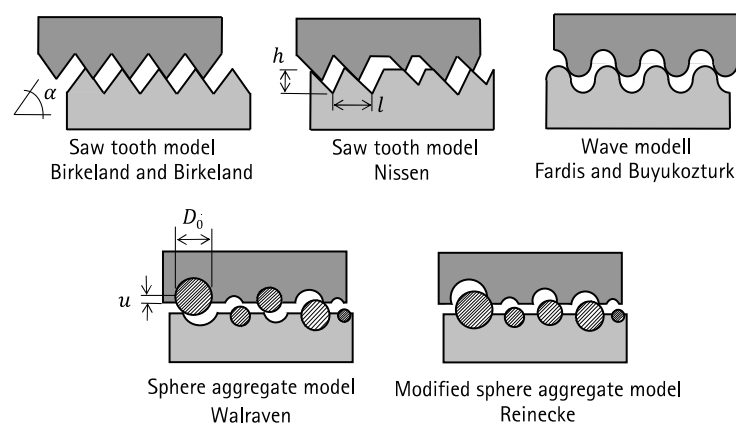


Figure 2.17 2D geometrical models from different researchers based on shear transfer theory [30]

Global similarity of the surface characteristics is expected for concrete with approximately the same homogeneous mixture and the same surface treatment. In order to describe the surface characteristics

reproducibly, different geometrical models are developed to explain the influence of roughness on the shear transfer, see Figure 2.17.

Birkeland (1966) [10] first proposed the saw tooth model in the late 1960s, where the surface roughness is simplified with regular isosceles triangular shaped teeth with a slop variable α depending on roughness parameters. From the geometry, the maximum transferable shear stress due to interlocking could be determined. Niessen(1988) [29] further developed the saw tooth model in 1988 and described the cracking laws with triangular teeth of different base length l and height h aligned arbitrarily against each other. The occurrence probability of these variables was then calculated with independent density functions. In the analytical expression of the fracture stress, a distinction was made between oblique and contact fractures of the individual teeth.

Another idea from Fardis and Buyukozturk (1980) [112] with the help of the wave model takes into account the roughened concrete surface by characterizing the surface with round peaks representing exposed round, cubic aggregates grains. The complex surface structure is in this case represented by a periodic sequence of waves of specific wavelength and amplitude [30] .

Walraven (1980) [113] modeled the roughness in a next step by assuming sphere aggregates of different size D_0 embedded in the concrete surface at different depth u . The frequency of size D_0 and u is calculated based on the grain size distribution. Reinecke (2004) [30] modified the Walraven's sphere aggregate model by setting the aggregates on one side of the surfaces instead of two sides for interface between old and new concrete, since there is no uniform distribution of aggregates on both sides. The calculation of occurrence probability of the surface texture is then omitted, since a determination of roughness was carried out before the cast of new concrete layer.

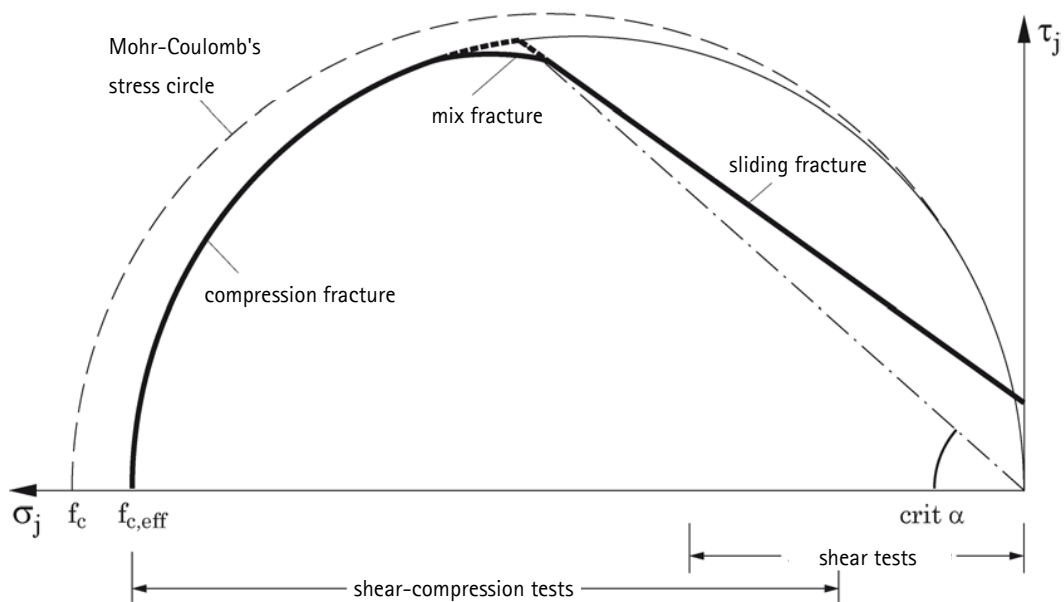


Figure 2.18 Limit relationship between the shear and normal stresses of interface joints at failure of specimens by Guckenberger et al. (1980) [8]

The cracking loads or stresses of reinforced and unreinforced interface joints could also be estimated with the help of plasticity theory. The Mohr-Coulomb criteria is usually employed to describe the interface behavior under combination of shear and normal stresses. Zelger and Rüsçh (1961) [27] modified the Mohr-Coulomb criteria to describe the slant shear test results. The shear and normal stress in the interface joint at failure is given in the shear-pressure diagram, see Figure 2.18.

The two different types of specimen failure could be observed from the shear–pressure diagram. If the joint inclination angle α of the specimen is smaller than the critical joint inclination angle α_{crit} , then a "compression fracture" occurs due to the concrete damage. In this case, the joint inclination angle α doesn't affect the load-bearing capacity. On the other side, if the joint inclination angle α of the specimen is greater than the critical joint inclination angle α_{crit} , a "sliding fracture" occurs due to the failure of the joint. In this case, the load-bearing capacity is influenced by the joint inclination angle and can be described by Mohr–Coulomb's failure criteria:

$$\tau_j = c + \mu \cdot \sigma_j \quad (2.18)$$

where τ_j and σ_j refer to the shear and normal stresses at joint and c denotes the friction coefficient.

Foster et al. (2017) [114] employed the upper-bound theory of plasticity for interface shear. The behavior predicted by the upper-bound theory is consistent with the modified push-off test results for an initially uncracked concrete interface joints subjected to combinations of shear and tension.

2.2.4 Concept of degree of restraint

In RILEM report [73], the stresses due to restrained movements can be described as:

$$\text{Stress} = \text{stiffness} \times \text{free strain} \times \text{degree of restraint}$$

The stiffness is dependent on modulus of elasticity but also on creep or relaxation. Thermal or moisture variations, shrinkage and creep, or any other internal or external source lead to volumetric change of the structure. The free strain here refers to the strain of completely free members caused by these volumetric variations. It's important to be aware that the bond between overlay and substrate does not necessarily cause complete restraint. The degree of restraint is defined as a ratio γ between the actual stresses generated in element σ_{real} , to the hypothetical stress at total restraint σ_{full} :

$$\gamma = \frac{\sigma_{real}}{\sigma_{full}} = 1 - \frac{\varepsilon_{real}}{\varepsilon_{free}} \in [0,1] \quad (2.19)$$

The degree of restraint could also be calculated according to the ratio between actual strain ε_{real} and the hypothetical strain at completely free deformation ε_{free} . The restraint for composite beam can be associated with two kinds of degree of freedom, i.e. axial and flexural degree of freedom. The incomplete restraint leads to substantial stress reduction. In addition, creep can also contribute to the reductions that limit the maximum tensile stress below the tensile strength.

Restraint sources could be [73]:

- **internal restraint** due to heterogeneous materials at micro level such as concrete aggregates restrained by cement paste deformation;
- **frictional forces** on the edge of slabs, which could be described by interface model with adapted Mohr–Coulomb models;
- **the flexural and axial stiffness of the substrate** on which an overlay is applied, in which case the degree of restraint of the overlay should be determined by considering the combined stiffness of the composite system;
- **dowels** as well as other combination of different layers;
- **reinforcement bars** or formworks;
- **the static system of a structure member** acting on different degree of freedom.

Lots of analytical models for the mechanical response of composite structure members under differential shrinkage have been studied. The existing analytical models can be classified on the basis of three main features [73]:

- considering of flexural degree of freedom (effect of curvature);
- considering of partial debonding;
- considering of viscoelastic behavior of overlay and substrate.

It's found [115]; [116] that, for the slender composite beam with a length to height ratio $L/H > 5$, the "prestress analogy" could be well adapted to simply represent a composite member with shrinkage of the overlay, in which concentrated forces at the free ends of a composite member to model the shrinkage effect are introduced as well as the Bernoulli's principle of plane sections remaining plane after stressed is applied. This theory is first presented by Birkeland [117] without the consideration of debonding and then developed by Silfwerbrand [118]; [119] with the consideration of debonding. However, for the deep composite elements with aspect ratio $L/H < 1$, Bernoulli's hypothesis is no longer suitable and thus the "prestress analogy" theory could not describe the behavior very well in this case based on the studies of Beushausen [120]–[123] with the testing of various specimen geometries.

With respect to the deep elements such as walls on slabs, the compensation plane method (CPM) is first introduced in Japan [124] and could be found in the Standard Specifications for Concrete Structures of Guidelines from JSCE [125]. In this approach, the total stress is assumed to consist of three components [126]:

- internal restraint;
- external restraint against axial deformations;
- external restraint against flexural deformations.

Based on the CPM, other methods for the determination of stress state in externally-restrained concrete elements are referred by Nilsson introduced in his licentiate thesis [127] and developed in further research [128], which could also be found in ACI Report 207 [129], EN 1992-3 [130] as well as I CIRIA C660 [131].

3. Fundamentals of numerical simulation

In this thesis, numerical computational analysis is based on software ABAQUS, which consists of the following five core software products [100] [132]:

1. Abaqus/CAE: it is a complete Abaqus environment including Abaqus/Viewer, which provides an easy-to-use environment to quickly and efficiently create, edit, monitor, diagnose and visualize advanced ABAQUS analysis.
2. Abaqus/Standard: a general purpose FEA that employs implicit integration scheme, which is ideal for static and low-speed dynamic events where highly accurate solutions are required.
3. Abaqus/Explicit: a special purpose FEA that employs explicit integration scheme to solve highly nonlinear systems, which is particularly well-suited to simulate brief transient dynamic events such as consumer electronic drop testing, automotive crashworthiness and ballistic impact.
4. Abaqus/CFD, CFD is an acronym of "Computational Fluid Dynamics", which could be used for advanced computational fluid dynamics capabilities with extensive support for pre-processing and post-processing provided in Abaqus/CAE.
5. Abaqus/Electromagnetic: it solves advanced computational electromagnetic problems.

An open-source scripting language called Python is utilized in Abaqus for scripting and customization. Considering the study scope of this thesis, Abaqus/CAE and Abaqus/Standard are mainly used for the numerical investigation.

3.1 Basic concept of FEM

Generally, engineering analysis can be classified into two types: classic method with analytical solution and numerical method with approximate solution. Complex structures could be analyzed by solving a partial differential equation, only a few of which have analytical solutions. Nevertheless, to find a sufficiently accurate result, the structure is divided into a network of non-uniform regions, i.e. finite elements that are connected with discrete nodes. For each typical element, an interpolation function is defined relative to the values of dependent variables describing their mechanical behavior, e.g. displacements, at associated nodes. The functions of all the elements are assembled into global matrix equation (governing algebraic equations) to present the studied object. After applying boundary condition (BC) by specifying the degree of freedom (DOF) at the nodes, the governing algebraic equations can be solved. Most FE programs apply the deformation method, which originate from unknown displacements and torsions. The strain and stress can be calculated based on the displacement of nodes associated with the element. The FEM is thus an approximation procedure, with which complicated realistic structures could be solved with sufficient accuracy [133].

Every complete FEA includes the following three stages, which also construct the main framework of available FEA software:

1. **Pre-processing:** in this step, the model is constructed with appropriate geometry, material, element type as well as certain BC, etc. The model is then divided (mesh) into a number of sub-regions (elements) connected with discrete nodes. It is worth mentioning that no unit is defined in a classical pre-processing stage in ABAQUS, thus the user should pay attention to the consistency of the units themselves. This step is provided by Abaqus/CAE or other compatible computer- aided design (CAD) software or even a text editor.
2. **Processing:** in this step, the finite element model is submitted to the solver as input in the finite element code. A series of linear or nonlinear equations will be solved with implicit or explicit integration schemes to generate numerical output results. Abaqus/Standard, Abaqus/Explicit or Abaqus/CFD are capable of accomplishing this stage.
3. **Post-processing:** This step provides a visualization environment for users to display the results in colored contours, animations, reports or other approaches that assist the users to get a better understanding of the results. This stage is also provided by Abaqus/CAE.

3.2 Nonlinear FEM

The aim of a FEA is to transfer a realistic structural problem into a mathematical computational model with its physical BC and then solve the model with sufficiently accurate approximate solution. In reality, the behavior of all physical structures are nonlinear. However, the response of a structure can be approximated as linear when the deformation is small meanwhile linear elastic material model is used. Nevertheless, the structure analysis should be considered as nonlinear problem in most practical cases [134]. The concept of mechanical equilibrium is:

$$\{P\} - \{I\} = 0 \quad (3.1)$$

where $\{P\}$ represents the externally applied loads and $\{I\}$ the internal forces due to stresses in the structure:

$$\{I\} = \int_V [\beta^T] \{\sigma\} dV \quad (3.2)$$

$[\beta]$ denotes the relationship between displacement $\{u\}$ and strain $\{\varepsilon\}$ increments:

$$\{\varepsilon\} = [\beta] \cdot \{u\} \quad (3.3)$$

Seen from equation (3.1) and (3.10), the general resources of nonlinearity come from:

- (1) **Geometric nonlinearity** caused by integration over current volume V and nonlinear relationship $[\beta]$ between displacement and strain increments. Effects such as stress-stiffening, bifurcation, buckling and collapse belong to this category.
- (2) **Material nonlinearity** due to dependence of stress $\{\sigma\}$ on current strain, which includes the effects of plasticity, viscoelasticity, damage, etc.
- (3) **Boundary nonlinearity** contributed from dependence of $\{P\}$ on current displacements that is produced by effects of contact, nonlinear external loads, etc.

To linearize the analysis, the linear FEM is based on Hooke's law and could be described as:

$$[K]\{u\} = \{P\} \quad (3.4)$$

where $[K]$ is the globe stiffness matrix and is expressed as:

$$[K] = \int_V [\beta^T][D][\beta] dV \quad (3.5)$$

in which $[D]$ is a constant material stiffness matrix. Thus, the relationship between node of stress $\{\sigma\}$ and strain $\{\varepsilon\}$ could be expressed as:

$$\{\sigma\} = [D]\{\varepsilon\} \quad (3.6)$$

In general, the equilibrium equation of nonlinear system is solved by dividing the total applied load into small time increments and an approximate solution is obtained for each load increment. There are two different approaches to solve the time-dependent ordinary and partial differential equations, which are implicit and explicit integration. Explicit methods calculate the state of a system at current time from previous system state, while implicit methods gain the solution by solving an equation involving both the current and previous states of system. To solve an equation in implicit approach involves inverting the stiffness matrix $[K]$, which means each iteration is computationally expensive and may cause a convergence problem. On the other hand,

explicit approach doesn't involve equation solution, which means no iteration is implemented and thus has no convergence problem. However, small time increments are required to keep the error in the result bounded. Thus, even it's more complex to solve an equation at each time step, it takes much less computational time to use implicit approach with larger steps. A comparison between these two methods are shown in Table 3.1.

Table 3.1 Comparison between explicit and implicit numerical methods

Numerical method	Stiffness matrix inversion	Iteration/Convergence problem	Element order	Numerical stability	Time increments
Explicit	No	No	Lower-order	Not stable	Very small
Implicit	Yes	Yes	any order	Stable	Any size

In this thesis, implicit approach with Abaqus/Standard is used to implement the simulation for its generally lower computational costs and higher numerical stability. Two robust iterative methods are Newton-Raphson technique and Quasi-Newton technique. With Newton-Raphson method, each iteration involves the formulation and solution of linearized equilibrium equations and the solutions should be smaller than a certain tolerance in order to obtain sufficient accuracy. However, the quasi-Newton method differs from the full Newton-Raphson method, since the stiffness matrix is not recalculated in every iteration and could provide substantial savings of computational efforts.

In Abaqus/Standard, Newton-Raphson method is used to find an equilibrium solution $\{u\}$, so that the residual $\{R(u)\}$ between external and internal forces at each degree of freedom is smaller than the tolerance value.

$$\{R(u)\} = \{P\} - \{I\} \quad (3.7)$$

A displacement $\{u_0\}$ is firstly assumed with $\{R(u_0)\} \neq \{0\}$. Displacement correction $\{C_u\}$ is found, so that $\{u + C_u\}$ is in equilibrium as:

$$\{R(u + C_u)\} = \left\{ R(u) + \frac{\partial R}{\partial u} \Big|_u \cdot C_u + \dots \right\} = \{0\} \quad (3.8)$$

Higher-order terms of a Taylor series could be neglected and the above equation is transferred as:

$$\underbrace{\frac{\partial R}{\partial u} \Big|_u}_{[K_T(u)]} \cdot \{C_u\} = -\{R(u)\} \quad (3.9)$$

$[K_T]$ is named in literature as tangential stiffness matrix. It could be seen that equation (3.9) is linear in $\{C_u\}$. Once $\{C_u\}$ is calculated, the $\{u\}$ is updated using:

$$\{u_{i+1}\} = \{u_i\} + \{C_{u_i}\} = \{u_i\} - [K_T(u_i)]^{-1} \{R(u_i)\} \quad (3.10)$$

In general, the iterative calculation of Newton-Raphson method is summarized in the following steps (also see Figure 3.1):

- 1) Calculate the residual $\{R(u_i)\}$;
- 2) Calculate the tangential stiffness matrix $[K_T(u_i)]$;
- 3) Solve the linear equation $[K_T(u_i)] \cdot \{C_{u_i}\} = -\{R(u_i)\}$ to get the displacement correction $\{C_{u_i}\}$;
- 4) Update the displacement $\{u_{i+1}\} = \{u_i\} + \{C_{u_i}\}$;

- 5) Calculate the residual $\{R(u_{i+1})\}$ and check if it is smaller than the tolerance value meanwhile the last displacement correction $\{C_{u_i}\}$ is less than a fraction (1% by default) of the incremental displacement, i.e. converged. If yes, then stop. If no, go to step 2).

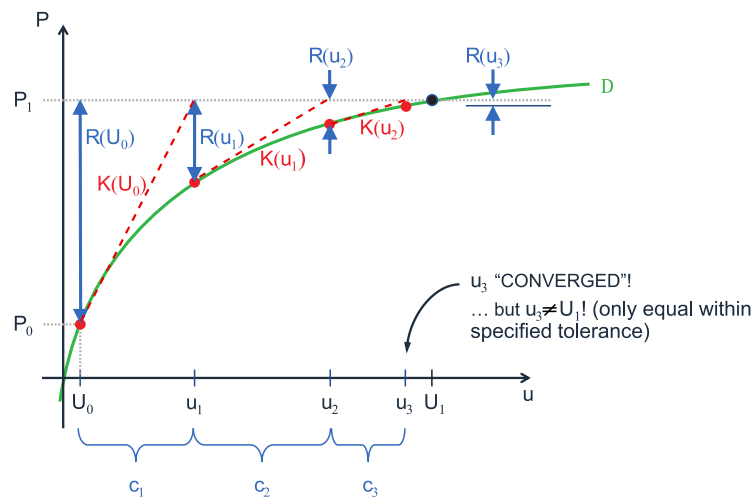


Figure 3.1 Schematic diagram of Newton-Raphson iterative method [134]

The reasons why a FEM based on Newton-Raphson method doesn't converge could be various, such as:

- **Numerical singularities**, which may indicate the rigid body motions are not fully constrained.
- **Zero pivots**, referring to the occurrence where a force term exists without corresponding stiffness term, which may be caused by the lack of constraints or overconstraints.
- **Negative eigenvalues**, indicating that the stiffness matrix is not positive defined associated with a loss of stiffness or a non-unique solution.
- **Excessive yielding**, when relatively large deformations occur in plastic material.
- **Element distortion**, when the volume at the integration point of an element becomes negative.
- **Hourglassing or shear locking**, which would be discussed later in chapter 3.3.

To solve the convergence problem in Abaqus/Standard, the following method could be used:

- **Alternative techniques** to the standard Newton method such as quasi-Newton method, Linear Complementarity Problem solution technique for frictionless contact.
- **Automatic incrementation control**, with which Abaqus/Standard automatically adjusts the size of time increments to solve nonlinear problems efficiently.
- **Automatic stabilization** of unstable problem through the automatic addition of volume-proportional damping to the model. The applied damping factors can be constant over the duration of a step or vary with time to account for changes over the course of a step. The latter is also called *adaptive approach* and typically preferred. The damping factor could be defined 1) based on *the dissipated energy fraction* for the calculation with a stable beginning, or 2) by *directly specifying the damping factor* when the initial increment is unstable or singular. Unfortunately, the damping factor depends not only on the amount of damping but also on mesh size and material behavior, making it quite difficult to have a reasonable estimation. Obtaining an optimal value for the damping factor is a manual process requiring trial and error until a converged solution is obtained and the dissipated stabilization energy is sufficiently small.

- **Viscous regularization** for damage stabilization, which creates a tangent stiffness matrix of the softening material to be positive for sufficiently small time increments. Using a small value of viscosity parameter usually helps improve the rate of convergence in softening regime without compromising results.
- **Nondefault solution controls**, with which customized solution controls could be used, such as 1) *avoiding premature cutbacks in difficult analyses for discontinuous problems*, 2) *activating the "line search" algorithm*, 3) *controlling the time incrementation scheme* and 4) *changing solution method* to quasi-Newton technique, etc. The solution controls are generally intended for experienced analysts and should be used with great care.

With regard to the automatic stabilization, the damping factor should be increased if the convergence behavior is problematic or decreased if it distorts the solution. Thus, the following points should be checked when using automatic stabilization:

- (1) For a damping factor defined by dissipated energy fraction, check the message file (.msg) at the end of the first increment to ensure a reasonable amount of damping. Unfortunately, the damping factor is problem dependent and an appropriate estimation must rely on experience from previous runs.
- (2) Compare the viscous forces (VF) with the overall forces in the analysis to ensure that the viscous forces are relatively small compared with the overall forces.
- (3) Compare the viscous damping energy (ALLSD) with the total strain energy (ALLIE) to ensure that the ratio doesn't exceed the dissipated energy fraction or any reasonable amount. The viscous damping energy may be large if the structure undergoes a large amount of motion.

3.3 Modelling in ABAQUS

Appropriate element types describing the main physical characteristics of structural components are crucial in the modelling of FEA. In general, finite element types could be divided into one dimensional (1D) elements, two dimensional (2D) elements and three dimensional (3D) elements [135]. 1D elements just connect two nodes, such as beam element and truss element. 2D planar elements could be triangular or quadrilateral in shape. Shell elements and membrane elements are typical 2D elements. 3D elements, also called solid elements, could be tetrahedral or brick in volume based on triangles or quads. Some commonly used element families in ABAQUS are shown in Figure 3.2.

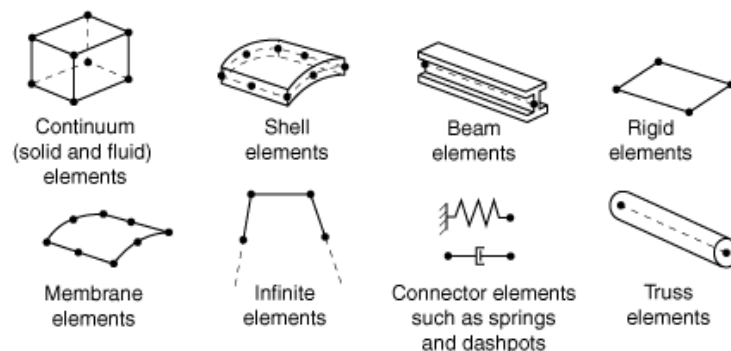


Figure 3.2 Commonly used element families in ABAQUS [100]

The choice of elements is based upon five aspects [100]: a) family; b) degree of freedom; c) number of nodes; d) formulation; e) integration. Element displacements are obtained by interpolating from nodal displacements, while the interpolation order is determined by number of nodes in the element. Linear interpolation is used for linear element (first-order element) with nodes only at the corners. Quadratic interpolation is utilized for quadratic element (second-order element) with midside nodes and modified second-order interpolation for

modified triangular or tetrahedral elements (modified second-order elements) with midside nodes, see Figure 3.3.

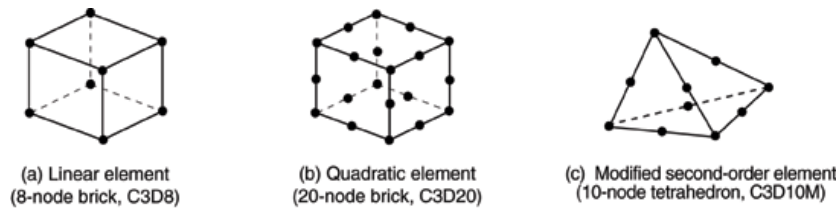


Figure 3.3 Linear brick, quadratic brick and modified tetrahedral elements in ABAQUS [100]

Numerical integration is necessary for calculation of stiffness matrix. Gaussian Quadrature method is employed in ABAQUS for integration of function (i.e. full integration), where a number of points are calculated and their positions are optimized. Reduced integration uses less points for calculation, which means it takes less time for computation but also has significant effect on the accuracy for a given problem, see Figure 3.4 (a). Displacement-based FE formulations always over-estimate the stiffness matrix and the use of fewer integration points could produce a less stiff element. What's more, fully integrated linear element could experience *shear locking* in bending, where spurious shear rather than bending stresses arise in a pure bending state due to the incapability of curve at the edge of element, see Figure 3.4 (b). In comparison, the quadratic elements don't have this problem, since their edges are able to curve. Nevertheless, fully integrated quadratic elements can also lock under complex states of stress. Therefore, reduced integration is actually advisable to be used in some cases such as plasticity and creep, considering the slight loss of accuracy counteracted by the improvement in approximation to real-life behavior. The fully integrated elements are however very useful for modelling areas where concentrated stresses are located.

However, special attention should be paid to the *hourglass phenomenon* when using reduced integration, where the deformation of the element could not be observed due to the lack of enough integration points. Considering a linear shell element, only one integration point instead of four points are used in reduced integration. The strain at the single integration point is zero, since the dotted lines remain the same in magnitude and angle under bending deformation, see Figure 3.4 (c). As a result, hourglass mode is also called zero energy mode that leads to excessive element distortion. This is a nonphysical energy mode that only happens in FEA and the hourglass energy contained in zero energy modes should not exceed 1% of the internal energy.

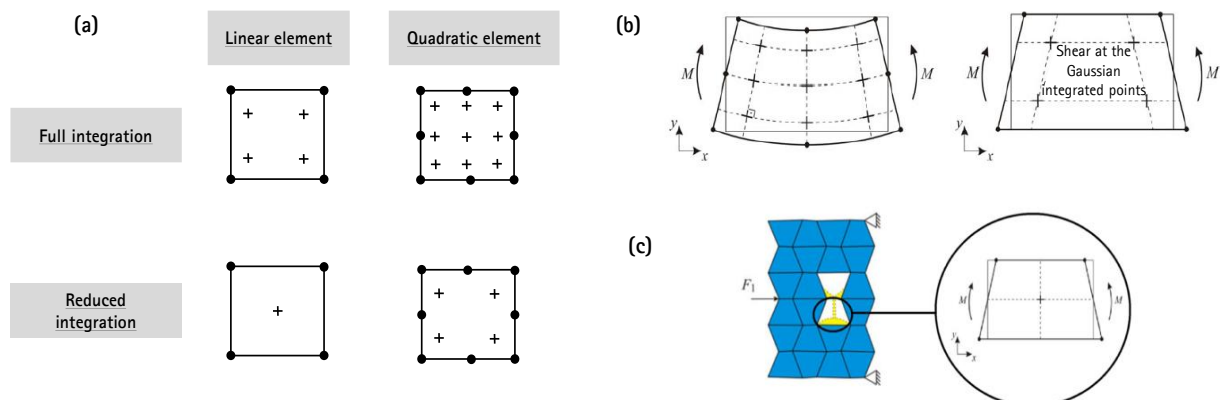


Figure 3.4 Element types and the probable phenomena in simulation: (a) nodes and integrations of elements; (b) shear locking for fully integrated linear elements; (c) hourglass phenomenon for reduced integrated elements [136]

To solve the hourglass problem, following solutions could be applied:

1. **Mesh refining;**
2. **Stabilization technology** such as providing arbitrary stiffness in the mode or using viscous damping;
3. **Dispensation of the load** (avoiding concentration load);
4. Application of **quadratic elements**. Although hourglass problem could theoretically happen in the quadratic elements, the risks are very small.

Quadratic reduced integrated elements are not susceptible to locking even when subjected to complicated states of stresses, meanwhile the risk of experiencing hourglass problem is also very small. Thus, these elements are generally the best choice for most general simulations except in simulations involving very large strains or in some types of contact analysis.

For composite materials, the crack growth at interface could be simulated in Abaqus by the application of:

- **Cohesive zone model (CZM)** based on traction-separation relationship
- **(Enhanced) virtual crack-closure technique (VCCT)** based on LFM
- **Extended finite element method (XFEM)**

In this thesis, the cohesive zone model was chosen for the crack simulation. The adhesive bond behavior between two materials could be simulated with connector elements or cohesive elements in Abaqus. The connector elements with a predefined force-deformation relationship could model discrete physical connections between two points. On the other hand, cohesive elements with a traction-separation relationship are able to model bond between two surfaces. Both methods could be used to simulate the progressive failure of adhesion or delamination in composites. However, connector elements discretely connect two parts and thus are dependent on the mesh size, whereas cohesive elements are mesh-independent surface connection. For negligibly small interface thickness, Abaqus provides a surface-based cohesive behavior with contact elements, in which the traction-separation constitutive model could also be implemented. In summary, three methods could be used to simulate the bonding behavior between concrete layers in Abaqus:

- connector elements
- cohesive elements
- contact interaction with cohesive behavior

3.3.1 Connector elements

With connector elements, relative displacements and rotations between two points, referred to as components of relative motions (CORM), could be modeled with appropriate definition of connection types, local connector directions and connector behaviors. The connection types contain translational basic, rotational basic and assembled connection components. Translational basic connectors affect translational DOFs at both nodes and may affect rotational DOFs at the first node of the connector element. Rotational basic connectors have an influence only on rotational DOFs at both nodes, while assembled connectors are a combination of translational and rotational basic connection components. For each kind of connection components, different types are available to customize various applications. For example, in the category of translational basic connection components, Axial connector provides a connection between two nodes that acts along the line connecting the nodes; Cartesian connector defines a connection between two nodes that allows independent behavior in three local Cartesian directions; Join connector joins the positions of two nodes. In the category of basic rotational connection components, Revolute connector affords a revolute connection between two nodes; Cardan connector produces a rotational connection parameterized by Cardan angles; Euler connector describes rotational connection parameterized by Euler angles. Assembled connectors are characterized by assorted combinations of two basic connections. The connector local directions are decided by a local

orientation or coordinate system. Not all connection types require the local directions, e.g. Link connector and in some cases default local directions are chosen, e.g. Cartesian connector. Local directions at the second node are ignored in some connection types, e.g. Slot connector. By defining connector behavior, different characteristics of connection could be simulated, such as linear or nonlinear response, elasticity, plasticity, friction, damage and failure. Summary of basic and assembled connection types are listed in Table 3.2 and Table 3.3.

Table 3.2 Summary of basic connection types [137]

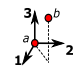
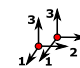

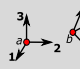
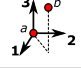
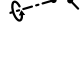
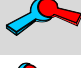
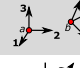







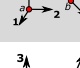

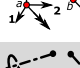
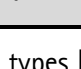
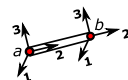
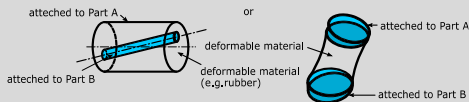

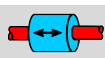

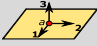
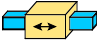


Translational basic connector	Local directions		Rotational basic connector	Local directions	
	1 st node	2 nd node		1 st node	2 nd node
Accelerometer 	Optional	Optional	Align 	Optional	Optional
Axial 	Optional	Optional	Cardan 	Required	Optional
Cartesian 	Optional	Ignored	Constant Velocity 	Required	Optional
Join 	Optional	Ignored	Euler 	Required	Optional
Link 	Ignored	Ignored	Flexion-Torsion 	Required	Optional
Projection Cartesian 	Optional	Optional	Projection flexion-torsion 	Required	Optional
Radial-Thrust 	Required	Ignored	Revolute 	Required	Optional
Slide-Plane 	Required	Ignored	Rotation 	Optional	Optional
Slot 	Required	Ignored	Rotation-accelerator 	Optional	Optional
			Universal 	Required	Optional

Table 3.3 Summary of assembled connection types [137]

Assembled connector	Local directions		Equivalent basic connection components (translational + rotational)	
	1 st node	2 nd node		
Beam 	Optional	Optional	Join	Align
Bushing 	Required	Optional	Projection Cartesian	Projection flexion-torsion
CVJoint 	Required	Optional	Join	Constant velocity
Cylindrical 	Required	Optional	Slot	Revolute
Hinge 	Required	Optional	Join	Revolute

Planar		Required	Optional	Slide-plane	Revolute
Translator		Required	Optional	Slot	Align
UJoint		Required	Optional	Join	Universal
Weld		Optional	Optional	Join	Align

3.3.2 Cohesive elements

In three cases, cohesive elements could be used for an appropriate modelling in Abaqus:

- Finite-thickness adhesives
- infinitesimally thin adhesive layers for interface debonding
- Gaskets or small adhesive patches

For finite-thickness adhesives as well as gaskets or small adhesive patches, the continuum macroscopic properties of this material could be used directly for modeling the constitutive response of the cohesive zone. The latter could be applied with material model for one-dimensional elements, since uniaxial stress state gives a good approximation for the state of these elements. However, for the applications of interface debonding with negligible thin adhesive layers, a traction-separation constitutive behavior should be defined. In the scope of this thesis, main focus will be discussed later with traction-separation behavior for debonding simulation. Cohesive elements must be constrained to other components. When the cohesive elements and their neighboring parts have matched meshes, cohesive elements share nodes with the adjacent components. More generally, when the two neighboring parts do not have matched meshes, the top and/or bottom surface of the cohesive layer could be tied to surrounding structures using tie constraints. For some applications e.g. gaskets, it's appropriate to define contact on one side of the cohesive elements, see Figure 3.5.

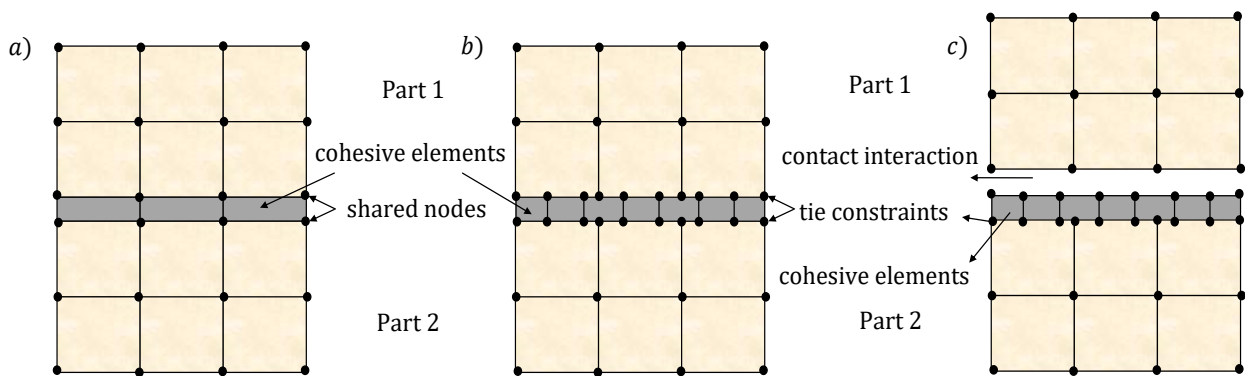


Figure 3.5 Connecting cohesive elements to other components: a) having shared nodes, b) independent meshes with tie constraints, c) contact interactions between cohesive elements and other components [100]

3.3.2.1 Linear elastic behavior

To define a traction-separation behavior for interface debonding in Abaqus, linear elastic behavior is assumed followed by the initiation and evolution of damage. The nominal traction stress vector \mathbf{t} consists of one normal traction t_n , sliding traction t_s and tearing traction t_t . The corresponding separations are denoted by δ_n , δ_s and δ_t . Denoting by T_0 original thickness of cohesive element (constitutive thickness), the nominal strains can be defined as:

$$\varepsilon_n = \frac{\delta_n}{T_0}, \quad \varepsilon_s = \frac{\delta_s}{T_0}, \quad \varepsilon_t = \frac{\delta_t}{T_0} \quad (3.11)$$

The elastic behavior can be written as:

$$\mathbf{t} = \begin{Bmatrix} t_n \\ t_s \\ t_t \end{Bmatrix} = \begin{bmatrix} E_{nn} & E_{ns} & E_{nt} \\ E_{ns} & E_{ss} & E_{st} \\ E_{nt} & E_{st} & E_{tt} \end{bmatrix} \begin{Bmatrix} \varepsilon_n \\ \varepsilon_s \\ \varepsilon_t \end{Bmatrix} = \mathbf{E}\boldsymbol{\varepsilon} \quad (3.12)$$

The elasticity matrix provides fully coupled behavior between all components of traction and strain vectors. By default, an uncoupled traction-separation law is given with off-diagonal terms set to zero in elasticity matrix. All the terms in the matrix must be defined if a couple behavior is desired, in which shear separations could lead to normal stresses and normal stresses could give rise to shear stresses. The material parameters, e.g. interfacial elastic stiffness for traction-separation model could be better understood by studying displacement of a truss [100]. The elasticity E_c , stiffness K_c and density $\bar{\rho}_c$ of the interface is given by

$$E_c = K_c T_0 = \frac{E_a}{T_c} T_0, \quad \bar{\rho}_c = \rho_c T_c \quad (3.13)$$

where E_a , T_c and ρ_c represent adhesive material elasticity, geometrical thickness and density. The density represents mass per unit area instead of mass per unit volume. The constitutive thickness T_0 is by default equal to one regardless of the geometric thickness of cohesive elements. This default value is motivated by the fact that the geometric thickness of cohesive elements is usually close to zero for the application of traction-separation-based constitutive response. The default choice ensures that nominal strains are equal to the corresponding separations. It's also possible to specify the constitutive thickness directly or compute it based on nodal coordinates. The characteristic element length of cohesive elements is equal to its constitutive thickness. The above equations imply the stiffness K_c tends to infinity and density $\bar{\rho}_c$ tends to zero. This stiffness is often chosen as a penalty parameter, while large penalty stiffness is detrimental to the operator in Abaqus/Standard.

3.3.2.2 Damage initiation

Damage initiation refers to the beginning of stiffness degradation. There are four ways to define the damage initiation criterion in Abaqus [100]:

- Maximum nominal stress criterion

$$\max \left\{ \frac{\langle t_n \rangle}{t_n^0}, \frac{t_s}{t_s^0}, \frac{t_t}{t_t^0} \right\} = 1 \quad (3.14)$$

- Maximum nominal strain/separation criterion

$$\max \left\{ \frac{\langle \varepsilon_n \rangle}{\varepsilon_n^0}, \frac{\varepsilon_s}{\varepsilon_s^0}, \frac{\varepsilon_t}{\varepsilon_t^0} \right\} = 1 \quad \text{or} \quad \max \left\{ \frac{\langle \delta_n \rangle}{\delta_n^0}, \frac{\delta_s}{\delta_s^0}, \frac{\delta_t}{\delta_t^0} \right\} = 1 \quad (3.15)$$

- Quadratic nominal stress criterion

$$\left\{ \frac{\langle t_n \rangle}{t_n^0} \right\}^2 + \left\{ \frac{t_s}{t_s^0} \right\}^2 + \left\{ \frac{t_t}{t_t^0} \right\}^2 = 1 \quad (3.16)$$

- Quadratic nominal strain/separation criterion

$$\left\{ \frac{\langle \varepsilon_n \rangle}{\varepsilon_n^0} \right\}^2 + \left\{ \frac{\varepsilon_s}{\varepsilon_s^0} \right\}^2 + \left\{ \frac{\varepsilon_t}{\varepsilon_t^0} \right\}^2 = 1 \quad \text{or} \quad \left\{ \frac{\langle \delta_n \rangle}{\delta_n^0} \right\}^2 + \left\{ \frac{\delta_s}{\delta_s^0} \right\}^2 + \left\{ \frac{\delta_t}{\delta_t^0} \right\}^2 = 1 \quad (3.17)$$

where t_n^0 , t_s^0 and t_t^0 refer to normal, slip and tear traction respectively; ε_n^0 , ε_s^0 and ε_t^0 represent normal, slip and tear strain in cohesive element respectively; δ_n^0 , δ_s^0 and δ_t^0 denote normal, slip and tear separation respectively.

3.3.2.3 Damage evolution

The damage evolution law describes the degrading of the cohesive stiffness once the initiation criterion is reached. A scalar damage variable D is used to describe the overall damage extent. Once the damage initiates, the damage variable D monotonically evolves from 0 to 1. Dependent on the step time, the traction tensor is calculated by [100]:

$$t = (1 - D)\bar{t} \quad (3.18)$$

where \bar{t} represents the stress vector predicted by the elastic traction-separation behavior for the current separations without damage. For the damage under a combination of normal and shear deformation, i.e. in mix-mode, the effective separation δ_m is introduced as [138]:

$$\delta_m = \sqrt{\langle \delta_n \rangle^2 + \delta_s^2 + \delta_t^2} \quad (3.19)$$

Damage evolution could be defined based on effective separation or based on fracture energy. For evolution based on effective separation, linear, exponential and tabular damage evolutions could be used for customized softening curves in application, see Figure 3.6. Damage evolution is defined with damage variable D in Abaqus. Both linear and exponential damage evolution have their own damage variable expressions as a function of the effective separation beyond damage initiation, i.e. $\delta_m^{max} - \delta_m^0$. Alternatively, damage variable D could be specified directly as a tabular function.

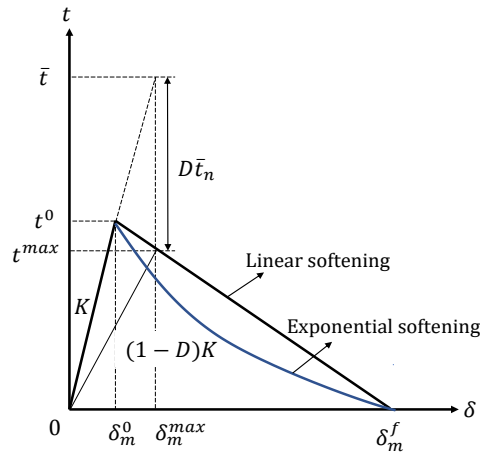


Figure 3.6 Illustration of traction-separation with linear and exponential damage evolution in Abaqus

The damage variable D expression as function of effective separation after damage initiation $\delta_m^{max} - \delta_m^0$ for linear and exponential damage evolutions as well as their corresponding traction-separation expressions are given as follows:

- Linear damage evolution

$$D = \frac{\delta_m^f(\delta_m^{max} - \delta_m^0)}{\delta_m^{max}(\delta_m^f - \delta_m^0)} \quad (3.20)$$

$$t^{max} = \begin{cases} \frac{t^0}{\delta_m^0} \cdot \delta_m^{max}, & \text{for } \delta_m^{max} \leq \delta_m^0 \\ \frac{t^0}{\delta_m^0 - \delta_m^f} \cdot (\delta_m^{max} - \delta_m^f), & \text{for } \delta_m^0 < \delta_m^{max} < \delta_m^f \end{cases} \quad (3.21)$$

- Exponential damage evolution

$$D = 1 - \frac{\delta_m^0}{\delta_m^{max}} \left(1 - \frac{1 - e^{-\alpha \frac{\delta_m^{max} - \delta_m^0}{\delta_m^f - \delta_m^0}}}{1 - e^{-\alpha}}\right) \quad (3.22)$$

$$t^{max} = \begin{cases} \frac{t^0}{\delta_m^0} \cdot \delta_m^{max}, & \text{for } \delta_m^{max} \leq \delta_m^0 \\ -\frac{t^0 \cdot e^{-\alpha}}{1 - e^{-\alpha}} + \frac{t^0}{1 - e^{-\alpha}} \cdot e^{-\frac{\alpha}{\delta_m^f - \delta_m^0}(\delta_m^{max} - \delta_m^0)}, & \text{for } \delta_m^0 < \delta_m^{max} < \delta_m^f \end{cases} \quad (3.23)$$

Only the quantity of effective separation at complete failure δ_m^f relative to the one at damage initiation δ_m^0 , i.e. $\delta_m^f - \delta_m^0$ needs to be specified for linear damage evolution, whereas a non-dimensional exponential parameter α describing the rate of damage evolution is additionally required in the exponential damage evolution. Damage evolution could also be defined based on fracture energy for linear and exponential damage evolution. Similar with effective separation approach, damage variable D is calculated as function of fracture energy, which refers to the area under the traction-separation curve. However, it's not possible to involve tabular function for energy based damage evolution.

Abaqus also offers three measures to specify the relative proportions of normal and shear separation in mix-mode, where two are based on energies and one based on tractions in tabular form for damage evolution defined with traction. For damage evolution defined with energy, additional two approaches are available for definition of dependence of the fracture energy in mix-mode, i.e. Power law form and Benzeggagh-Kenane form [139].

3.3.3 Contact interaction

Abaqus/Standard provides three different algorithms to simulate contact behavior: 1) general contact; 2) contact pairs and 3) contact elements. General contact and contact pairs both use surfaces to define contact, while contact elements are provided when contact between two bodies cannot be simulated with surface-based contact approaches. Generally, it's suggested to use surface-based approaches if possible and the two approaches could be simultaneously used. In this thesis, surface-based approaches are used and will be mainly discussed later. The general contact approach could be used by general contact interaction type in Abaqus/CAE, while contact pairs approach could be defined by surface-to-surface or self-contact interaction type in Abaqus/CAE. An overview of contact interaction in Abaqus/Standard is displayed in Figure 3.7.

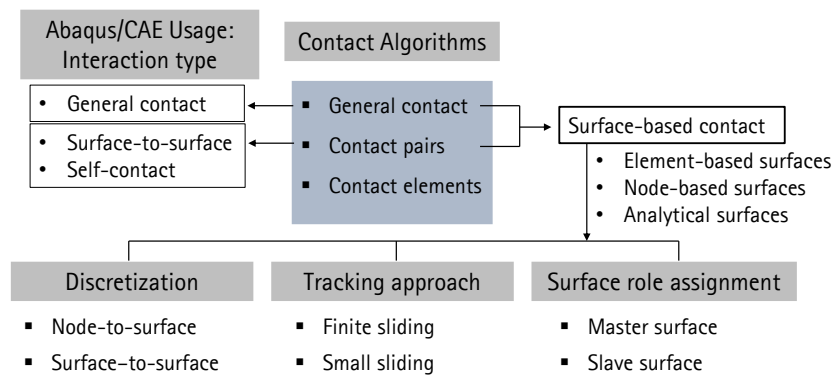


Figure 3.7 Overview of contact interaction in Abaqus/Standard

Surface pairings or self-contact surface need to be specified for general contact and contact pairs approaches. Abaqus/Standard has three categories of contact surfaces:

- Element-based deformable and rigid surfaces
- Node-based deformable and rigid surfaces
- Analytical rigid surfaces

For general contact, the default is to define a single self-contacting surface for all bodies involved in contact, which allow an easy and powerful method to define contact. Self-contact in this algorithm is not limited to contact of a single body itself but contacts between the bodies as well as contact of each body with itself. General contact could alternatively be defined by specifying surface pairings. Self-contact will be modeled only in the overlapping region. On the other hand, contact pairs should be defined by specifying two separate interacting surfaces or a single self-contact surface. In contact interaction definition, the following points should be noticed: a) at least one surface must be a non-node-based surface; b) at least one surface must be a non-analytical rigid surface.

Several contact formulations are provided for the surface-based approaches based on:

- Contact discretization: node-to-surface and surface-to-surface discretization
- Tracking approach
 - Finite sliding: most general case for arbitrary motion of surface
 - Small sliding: despite the state of motions little sliding between contact pairs
- Surface role assignment: master and slave surface roles

In the node-to-surface discretization, each slave node interacts with a point of projection on the master surface on the opposite side of contact interface and thus a single slave node interacts with a group of nearby master nodes from which values are interpolated to the projection point. On the other hand, surface-to-surface discretization takes the shape of both slave and master surfaces in the region of contact constraints into consideration. Therefore, surface-to-surface discretization provides in general more accurate results than node-to-surface discretization. A comparison of the characteristics of these two discretizations is listed in the following Table 3.4.

Table 3.4 Comparison of node-to-surface and surface-to-surface discretizations

	Node-to-surface	Surface-to-surface
Contact condition enforcement	Each individual slave node	In an average sense over regions nearby slave nodes, i.e. predominantly consider one slave node but also consider adjacent slave nodes.

Penetrations	Slave nodes are constrained from penetrating master surface but master surface can penetrate into slave surface.	Some penetration may be observed at individual nodes but large, undetected penetrations of master nodes into slave surface don't occur.
Contact direction	Based on normal of master surface	Based on an average normal of slave surface in the region surrounding a slave node
Application scope	Slave surface definition only needs the location and surface area associated with each node. Thus, slave surface can be defined as a group of nodes, i.e. a node-based surface. It's also available even if a node-based surface is not used in a contact pair definition.	It's not applicable if a node-based surface is used in the contact pair definition.
Default constraint enforcement method	(1) Finite sliding: Augmented Lagrange method for 3D self-contact; otherwise, direct method. (2) Small sliding: direct method	(1) Finite sliding: penalty method (2) Small sliding: direct method

For two separate surfaces, the master or slaver surface role must be assigned in contact pairs. In comparison, the master and slaver roles are automatically assigned, for self-contact in contact pairs as well as general contact approach. The following rules are given for an appropriate choice of master and slave role [100]:

- Analytical rigid or rigid-element-based surfaces must always be the master surface.
- A node-based surface can act only as slave surface and use node-to-surface contact.
- Slave surfaces must always be attached to deformable bodies or deformable bodies defined as rigid.
- Both surfaces in a contact pair cannot be rigid surfaces with the exception of deformable surfaces defined as rigid.

Generally, the smaller surface should be chosen as slave surface; for similar size surfaces, the stiffer body should be chosen as master surface; when two surfaces have comparable stiffnesses, master surface should be chosen as surface with coarser mesh. The choice of master and slave roles has much less effect on the results with a surface-to-surface contact formulation than node-to-surface contact formulation. However, the solution of surface-to-surface contact formulation can become quite expensive when the slave surface is much coarser than the master surface. Figure 3.8 demonstrates characteristics and influences of different contact formulations.

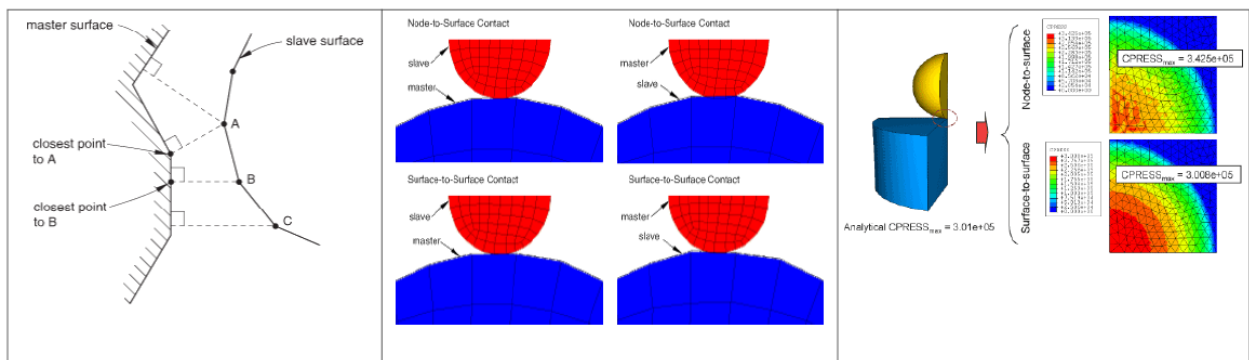


Figure 3.8 Node-to-surface contact discretization (left); Comparison of contact enforcement for different master-slave assignments with node-to-surface and surface-to-surface contact discretizations (middle); and Comparison of contact pressure accuracy for node-to-surface and surface-to-surface contact discretizations (right) [100]

A summary of available contact formulations for general contact and contact pairs algorithms in Abaqus/Standard are shown in the following Table 3.5.

Table 3.5 Available contact formulations for surface-based approaches in Abaqus/Standard

Contact approach	Contact type	Contact formulations
General contact		<ul style="list-style-type: none"> Finite sliding + surface-to-surface discretization
	Two separate surfaces	<ul style="list-style-type: none"> Finite sliding + node-to-surface discretization Finite sliding + surface-to-surface discretization Small sliding + node-to-surface discretization Small sliding + surface-to-surface discretization
Contact pairs	Self-contact	<ul style="list-style-type: none"> Finite sliding + node-to-surface discretization Finite sliding + surface-to-surface discretization
	Contact cohesive behavior	<ul style="list-style-type: none"> Finite sliding + node-to-surface discretization Small sliding + node-to-surface discretization Small sliding + surface-to-surface discretization

The mechanical behaviors of the interaction between contacting bodies, such as contact pressure-overclosure relationship, damping, friction, debonded surfaces, are defined by assigning a contact property model to a contact interaction. Debonded surfaces would be simulated with traction-separation behavior adopting CZM, i.e. contact cohesive behavior. In this thesis, pressure-overclosure behavior, friction behavior and contact cohesive behavior are utilized and will be discussed in detail.

3.3.3.1 Pressure-overclosure behavior

In Abaqus/Standard, four types of pressure-overclosure relationships could be defined in the contact interaction, which are 1) "hard" contact; 2) "softened" contact with a linear law; 3) "softened" contact with an exponential law and 4) "softened" contact with tabular piecewise-linear law. In a "hard" contact, any contact pressure can be transmitted between two contacting surfaces when they are in contact. The contact pressure reduces to zero when the surfaces separate, i.e. the clearance between two surfaces is zero. This kind of zero-penetration condition may or may not be strictly enforced depending on the constraint enforcement methods. On the other hand, the surfaces transmit pressure when the overclosure between them is greater than a specified value in a "softened" contact. The ways that the contact pressure increases as the clearance continues to diminish could be defined as linear, exponential and tabular piecewise-linear law. The linear pressure-overclosure relationship is identical to a tabular relationship with two data points, where the first point locates at origin. Different pressure-overclosure relationships are demonstrated in Figure 3.9.

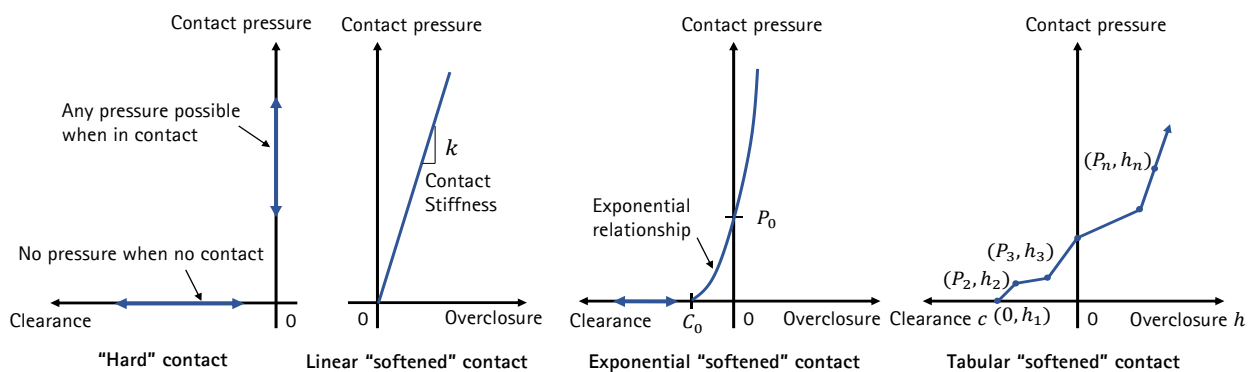


Figure 3.9 Pressure-overclosure relationships in Abaqus/Standard

A "hard" contact pressure-overclosure relationship is by default used for both surface-based and element-based contact. The "softened" contacts might be used to model a soft and thin layer on one or both surfaces. For contact involving element-based surfaces, the "softened" contact relationships are specified in terms of overclosure/clearance vs. contact pressure, while for node-based surfaces the "softened" contact is specified in terms of overclosure/clearance vs. contact force. In Abaqus/Standard, it's sometimes easier to resolve the contact conditions with "softened" contact relationships for numerical reasons. Special caution should be paid when using softened contact in implicit dynamic simulation, where a perfect elastic collision instead of impact algorithm is used, leading to convergence problems and small time increments. However, softened contact may work well in implicit dynamic calculations where impact effects are not important [100].

In order to appropriately simulate a pressure-overclosure relationship, effective contact algorithms are needed. Firstly, the contact issues will be explained. In Figure 3.10 (a), a spring with stiffness k is loaded with a force F . A rigid obstacle locates Δx from the free end of the spring. As long as $g = \Delta x - u > 0$, the relationship between displacement and force could be expressed as

$$k \cdot u = F \tag{3.24}$$

However, when the force F is so great that it leads to $g < 0$, the validity for the contact must be enforced to $g = 0$. Abaqus offers four constraint enforcement algorithms: 1) *Penalty* method; 2) *Lagrange Multiplier* method; 3) *Augmented Lagrange* method and 4) direct method, also known as *Multi-Point Constraint* (MPC). The Lagrange Multiplier method is not directly listed as a separate method in Abaqus, but embedded in direct and Augmented Lagrange methods. It would automatically activate under certain conditions, which will be discussed later.

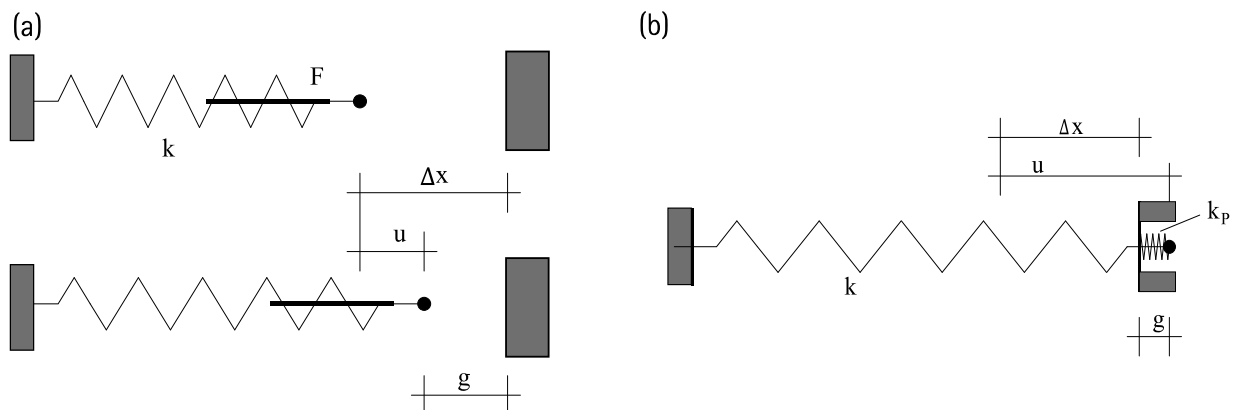


Figure 3.10 Contact conditions: (a) contact model problem; (b) penalty stiffness [140]

Penalty method is one of the oldest algorithms for solving constrained optimization problems, which replaces a constrained optimization problem by a series of unconstrained problems whose solutions converge to the original constrained problems. The unconstrained problems are formed by adding a term, called *penalty function*. It's known that the static equilibrium is obtained when the minimum of potential energy is reached. When the contact is open ($g > 0$), the potential energy of the system is [140]

$$W = \frac{1}{2}ku^2 - uF \rightarrow Min. \tag{3.25}$$

However, when the contact condition is violated ($g < 0$), a penalty term is added to increase the energy. The optimization problem now is

$$W = \frac{1}{2}ku^2 - uF + \frac{1}{2}k_p g^2 \rightarrow Min. \quad (3.26)$$

where k_p is a penalty parameter. Figure 3.10 (b) shows that the term $\frac{1}{2}k_p g^2$ has the same value with the energy of a spring with stiffness k_p . Thus, the penalty parameter could also be interpreted as a penalty stiffness.

The penalty method gives a stiff approximation of "hard" contact, with which the contact force is proportional to the penetration distance. Abaqus offers linear and nonlinear variations of penalty methods. The penalty stiffness keeps constant resulting a linear pressure-overclosure relationship in the linear penalty method. In comparison, the penalty stiffness in the nonlinear penalty method increases linearly from a lower constant stiffness region to a higher constant stiffness region, resulting a nonlinear pressure-overclosure relationship, see Figure 3.11. The penalty stiffness k_{lin} in linear penalty method is by default set to 10 times a representative underlying element stiffness. On the other hand, the default lower initial stiffness k_i is equal to the representative underlying element stiffness and final higher stiffness k_f is the same as 100 times the representative underlying element stiffness.

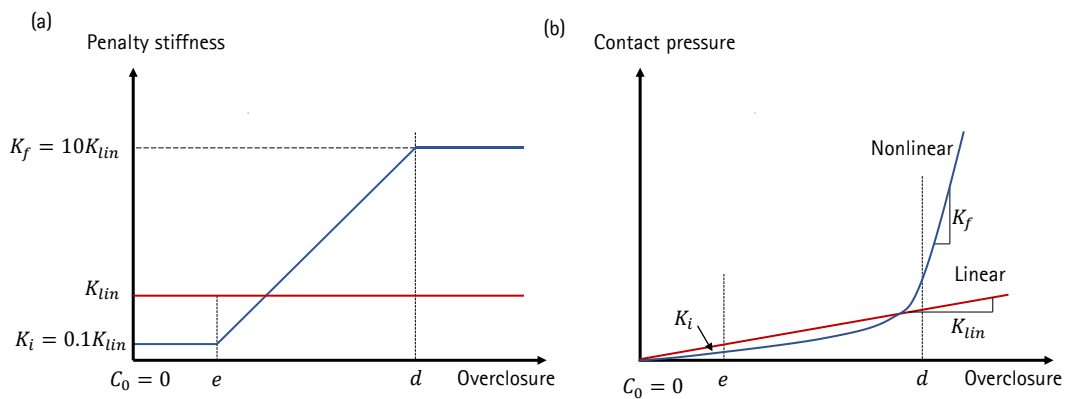


Figure 3.11 Comparison of linear and nonlinear penalty methods

Lagrange Multiplier method uses the term $\lambda g(u)$ instead of penalty term to add into the potential energy. Thus, the modified energy could be expressed as

$$W = \frac{1}{2}ku^2 - uF + \lambda g(u) \rightarrow Min. \quad (3.27)$$

where λ is the so called Lagrange multiplier. To satisfy the contact condition, the Lagrange multiplier is equal to the contact forces [140]. This method is automatically used when a "hard" contact is simulated with direct method and when the penalty stiffness exceeds 1000 times representative underlying element stiffness.

Augmented Lagrange method uses the linear penalty method with an augmentation iteration, which applies only to "hard" contact. This approach firstly finds a converged solution with penalty method. When a slave node penetrates the master surface more than the penetration tolerance, the contact pressure is "augmented" and another series of iterations is executed to find the corresponding converged solution until the actual penetration is less than the tolerance. This method could make the resolution of contact conditions easier and avoid problems with overconstraint meanwhile keeping penetrations small.

The **direct method** strictly enforces a given pressure-overclosure behavior for each constraint, without approximation or use of augmentation iterations. It's the only method to enforce "softened" contact regardless of the contact formulation types. Due to its strict interpretation of contact constraints, "hard" contact with

direct enforcement is susceptible to overconstraint issues. Thus, the following situation is not available with direct method:

- Finite-sliding, surface-to-surface formulation;
- 3D self-contact using node-to-surface discretization.

The default constraint enforcement methods for different contact formulations are listed in Table 3.4.

3.3.3.2 Friction behavior

Abaqus provides friction models to simulate shear transmission across the interface. Classic isotropic and anisotropic Coulomb friction models as well as an introduction of a shear stress limit τ_{max} are available. The Coulomb friction model, also called Amontons-coulomb friction model, refers to the work done by Guillaume Amontons and Charles-Augustin de Coulomb in 1699 and 1785 respectively, describing two contacting surfaces carrying shear stresses up to a certain magnitude (critical shear stress) τ_{crit} until they start sliding relative to each other. The Coulomb model could be represented as the following:

$$\tau = \begin{cases} \tau_{crit} \cdot Sgn(\delta_s), & \text{when } \delta_s \neq 0 \\ \tau_{app}, & \text{when } \delta_s = 0 \text{ and } \tau_{app} < \tau_{crit} \end{cases} \quad (3.28)$$

where δ_s is slip rate, τ_{app} is applied shear stress. When $\tau_{app} < \tau_{crit}$, there is no slip between two contact surfaces and friction stress is equal to the applied shear stress. This state is known as sticking state. When the applied shear stress reaches the critical shear stress, i.e. $\tau_{app} \geq \tau_{crit}$, the two surfaces slip relative to each other and the friction stress is equal to the critical shear stress. The critical shear stress is defined as

$$\tau_{crit} = \mu\sigma \quad (3.29)$$

where μ refers to Coulomb friction coefficient. In some cases such as very large contact pressure stress, a shear stress limit $\bar{\tau}_{max}$ could be specified, so that sliding occurs when equivalent shear stress reaches this value regardless of the magnitude of contact pressure. Figure 3.12 shows the stick and slip regions in Coulomb friction model without and with max. shear stress limit.

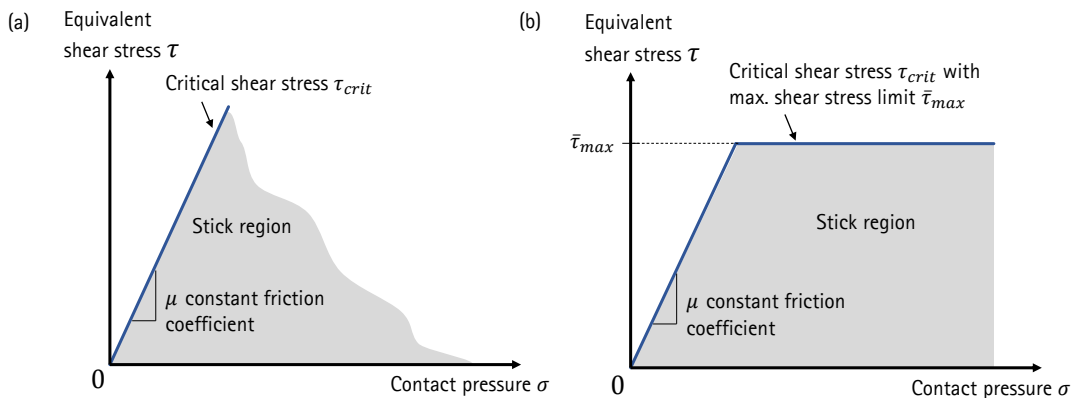


Figure 3.12 Stick and slip regions in friction models [100]

In the classical Coulomb friction model, the friction coefficient is constant from sticking state to sliding state, see Figure 3.13 (a). However, experimental results show that static friction for initiation of slipping from a sticking condition (i.e. friction at zero sliding speed) is larger than the friction at an established slipping state,

see Figure 3.13(b) by Morin in 1833. Thus, the static friction coefficient μ_s is larger than the kinetic friction coefficient μ_k . Abaqus provides two ways to define the friction coefficient:

- Specify the friction coefficient as a function of slip rate, contact pressure, temperature and field variables with Penalty or Lagrange Multiplier constraint enforcement formulations;
- Specify the static and kinetic friction coefficients directly with Static-Kinetic Exponential Decay constraint enforcement formulation.

In the first approach, if a friction coefficient is defined independent from any of the above mentioned factors, a classical Coulomb friction is modeled. When a friction coefficient is defined as a function of slip rate, then the difference between static and kinematic friction coefficient could be considered. In the second approach, an exponentially decay of friction coefficient is assumed. Thus, static coefficient μ_s , kinetic coefficient μ_k and decay coefficient should be provided.

In Coulomb friction, no slip exists in sticking state, which refers to an infinite sticking stiffness. However, incremental slip may occur even in the sticking state, implying a finite sticking stiffness, see Figure 3.13 (c). In this case, elastic slip could be specified during sticking in Penalty and Static-Kinetic Exponential Decay constraint enforcement methods. Lagrange Multiplier method could be used for imposing an infinite sticking stiffness, where no relative motion occurs in sticking state. However, this method increases the computational cost of analysis and may even cause convergence problems, especially if many points are iterating interaction between slipping/sticking conditions.

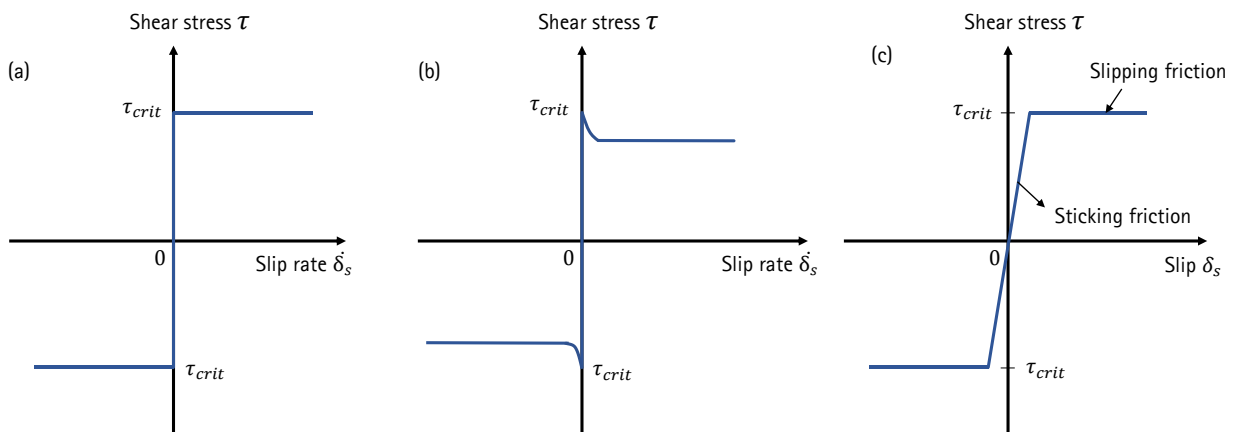


Figure 3.13 Representative friction models

Additional friction models are also available, such as "frictionless" model where no friction stress exists and "rough" model where no slip occurs regardless of contact pressure. User defined friction model for a more customized application could also be simulated with subroutines.

By default, if the friction coefficient is less than 0.2, Abaqus/Standard uses the symmetric solver while unsymmetric solver is invoked when the friction coefficient is higher than 0.2. In general, unsymmetric solver is more expensive than symmetric solver for each iteration, it could however reduce the iteration numbers and achieve faster rate of convergence.

3.3.3.3 Contact cohesive behavior

Cohesive contact behavior provides a simplified way to model traction-separation behavior with negligibly small interface, which is defined as surface interaction property. The linear elastic behavior in contact is defined similar with the cohesive elements approach. However cohesive contact uses interface stiffness K and interface separation δ directly:

$$\mathbf{t} = \begin{Bmatrix} t_n \\ t_s \\ t_t \end{Bmatrix} = \begin{bmatrix} K_{nn} & K_{ns} & K_{nt} \\ K_{ns} & K_{ss} & K_{st} \\ K_{nt} & K_{st} & K_{tt} \end{bmatrix} \begin{Bmatrix} \delta_n \\ \delta_s \\ \delta_t \end{Bmatrix} = \mathbf{K}\boldsymbol{\delta} \quad (3.30)$$

The damage initiation criteria and damage revolution definitions are almost the same for both approaches. Only the cohesive elements use strains whereas cohesive contact use contact opening and sliding as separation vector. A comparison in detail of cohesive element and cohesive contact is illustrated in Table 3.6.

Table 3.6 Comparison of cohesive element and cohesive contact with traction–separation behavior

	Cohesive elements	Cohesive contact
Thickness	Very small	zero
Definition of cohesive constitutive behavior	Material property specification	Interaction property specification
Elastic constitutive matrix	Material elasticity E	Interface stiffness K
Traction	Element stress t	Contact stress t
Separation	Element strain ϵ	Contact opening & sliding δ
Constitutive calculation	Calculated at integration points of elements	Calculated at contact constraint location primarily associated with slave nodes
Approach for more accurate results	Mesh refinement for the cohesive elements relative to the adjacent bodies	Mesh refinement for the slave surface relative to the master surface
Initial bond–state	Must be bonded at the start	No need to be bonded at beginning and could be re-bonded when surfaces are in contact afterwards for sticky contact behavior
Re-bond ("sticky") ability	No re-bond after failure	Could be re-bonded with sticky contact and not re-bonded with non-sticky contact, by default not sticky
Mass	In the material definitions	No mass in the model

3.3.3.4 Interaction of traction–separation behavior with compression and friction

In the contact normal direction, the pressure overclosure relationships govern the compressive behavior when a slave node is in contact with master surface, i.e. "closed", while the cohesive behavior contributes to normal stress only when a slave node is not in contact with master surface, i.e. "open". The two behaviors don't interact with each other, since they each describe the interaction between the surfaces in a different contact regime.

In the contact shear direction, the situations could be divided into three stages [100]:

1. **Cohesive stiffness undamaged:** the cohesive model is active and the friction model is dormant. Shear stress is only contributed from cohesive behavior.
2. **Cohesive stiffness degrading:** both cohesive and friction model are active. The elastic stick stiffness of the friction model increases in proportion to the degradation of the elastic cohesive stiffness. Shear stress is a combination of both cohesive and friction contribution.
3. **Cohesive stiffness fully damaged:** only friction model works. Shear stress only comes from friction.

Consequently, the constitutive relation for shear stress is given as:

$$\tau = \begin{cases} K\delta, & \text{for } D = 0 \ (0 \leq \delta \leq \delta_m^0) \\ (1 - D)K\delta + D\tau_f, & \text{for } 0 < D < 1 \ (\delta_m^0 < \delta < \delta_m^f) \\ \tau_f, & \text{for } D = 1 \ (\delta \geq \delta_m^f) \end{cases} \tag{3.31}$$

where K is the original interface stiffness, δ is interface separation, D refers to damage variable and τ_f denotes the shear contributed from pure friction. An overview of the interaction is displayed in Figure 3.14.

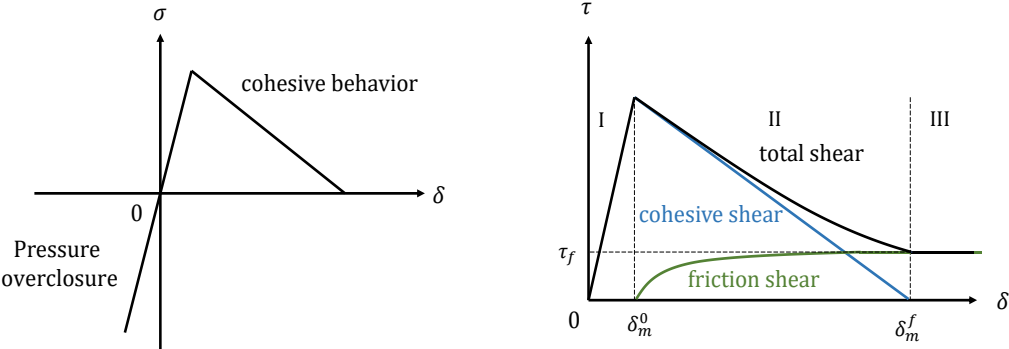


Figure 3.14 Schematic of interaction between cohesive behavior and compressive or friction behavior

4. Experimental determination of interface fracture parameters

The load bearing behavior of a structure is significantly influenced by the nonlinear material behavior of the concrete and the nonlinear interaction of both components. An efficient and sustainable structural design therefore requires consideration of both mentioned phenomena. The nonlinearities are demonstrated by mathematical equations or functional relationships that approximate the real behavior. The material models establish the correlation of forces and displacement in numerical simulation. Suitable model parameters should be specified for the materials and real BC. On the other hand, the proposed physical models have to be validated by experiments. And the numerical results should be calibrated by experiment results, which in return determines the model parameters. The determination of experimental parameters involves both high costs and time consumption as well as demanding testing conditions. The number and type of required parameters determine the efficiency of the simulation as well the experimental scope. The mathematical model and the model parameters have a direct impact on the quality and meaningfulness of the simulation calculation. The correlation between material model, simulation and experiment is schematically illustrated in Figure 4.1.

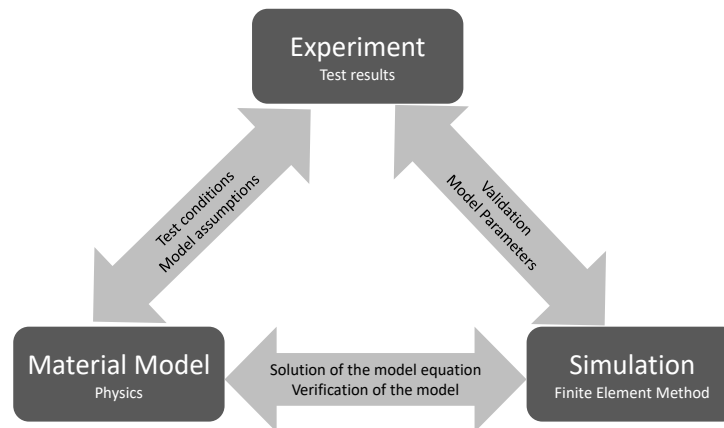


Figure 4.1 Correlation between material model, experiment and numerical simulation [141]

In order to have more accurate simulation results, proper material parameters should be given. Thus, experiment program is implemented to determine the material parameters. Since in this thesis the main focus lays on the interface damage, the material properties of concrete and CAM are assumed as linear while the bonding behavior between concrete and CAM is considered as nonlinear.

4.1 Objectives of the interface experiments

Composite structures such as continuous slab track, which consists of cast-in-situ concrete, prefabricated concrete slabs and a cast-in-situ cementitious mortar filling layer, exhibit much lower interfacial strength at the top interface than at the bottom interface. The prefabricated slabs are fixed with position setups on the cast-in-situ concrete slabs, then the filling material is poured down through holes in the prefabricated slab to the bottom concrete slab. After hardening of the filling layer, the position setups are removed and a three-layer composite structure is formed. The phenomenon of different properties at two interfaces may be due to the pouring method that leads to material inhomogenities, especially air voids in the mortar filling layers. When designing the experiments, two interfaces have been taken into consideration in order to be able to investigate the differences between top and bottom interface. In these preliminary tests, two similar interfaces are firstly tested to study the influence of experiment methods itself. Filling layer is poured from side instead of from top for both shear and tensile specimens, see Figure 4.2.

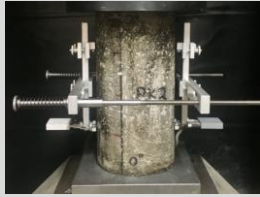



The main objectives of the experiment are:

(1) to obtain the interface material damage model between concrete and cement-asphalt mortar (CAM) for further use of numeric study. Fractural properties of both normal (Mode I) and tangential (Mode II) directions should be investigated;

(2) Preliminary investigation on feasibility of interface bonding tests.

Besides the interfacial properties between concrete and CAM, the material characteristics of concrete as well as CAM were also tested according to the corresponding codes. General review of the experiment programme is summarized in Table 4.1.

Table 4.1 General review on the experiment program

Specimen	Type A-1	Type A-2	Type B-1	Type B-2	Type C	Type D
Material	C40/50	CAM	Cement mortar	CAM	C40/50 + CAM	
Demonstration						
Size [mm]	D/H: 150/300	D/H: 100/200	L/B/H: 160/40/40		See later description	
Testing parameters	<ul style="list-style-type: none"> Elastic modulus Compressive strength 		<ul style="list-style-type: none"> Flexural strength Compressive strength 		<ul style="list-style-type: none"> Stress-slip curve at interface Surface roughness 	
Testing age	28d		1d, 7d and 28d		≥ 28d	
Codes	<u>Compressive strength:</u> EN 12390-3 (2017) [142] <u>Elastic modulus:</u> EN 12390-13 (2014) [143]		<u>Flexural and compressive strength:</u> EN 196-1(2016) [144] <u>CAM:</u> Tentative Specification of CAM for CRTS II (2008) [145]		<u>Surface roughness:</u> EN 13036-1(2010) [57]	

4.2 Preparation of the material and specimens

The two concrete parts are made of C40/50 concrete, while the filling material in between is made of CAM which is similar to the material used in continuous slab track. The cement used in the experimental tests is CEMI 52.5R. Water-cement ratios for concrete and CAM are 0.53 and 0.5 respectively, moreover CAM has an asphalt-cement ratio of 0.3. In order to insure the quality of CAM, additional testing of the cement mortar, which has the same cement and sand mixture as well as water-cement ration by mass with CAM, is also required. The Material mix proportions are listed in Table 4.2.

Table 4.2 Material mix proportions (kg/m³)

	Cement	Aggregate	Sand	water	Water reducer
C40/50	415	780	900	220	2.13
	Cement and sand mixture* ¹	Anionic asphalt emulsion* ²	Water	Antifoamer	Water reducer
CAM	1552	280	168	0.05	2.2

Cement mortar* ³	Cement	Sand	Water	Water reducer
	671	1193	355.5	2.2

*¹: Cement and sand mixture consists of 36% cement and 64% fine sand by mass

*²: Anionic asphalt emulsion consists of 60% asphalt and 40% water by mass

*³: Cement mortar has the same cement-sand mixture and water-cement ratio by mass with CAM

According to the *Tentative Specification of CAM for CRTS II (2008)*, technical requirements such as sand particle size distributions and mortar strength should be satisfied. The main requirements are summarized in Table 4.3.

Table 4.3 Technical requirements for CAM

Cement and Sand mixture			Cement mortar	CAM	
Sieve size [mm]	Passing rate [%]	Testing results [%]	Compressive strength [MPa]	Flexural strength [MPa]	Compressive strength [MPa]
1.18	100	100	1d \geq 12	1d \geq 1	1d \geq 2
0.6	90-100	96.16	7d \geq 30	7d \geq 2	7d \geq 10
0.3	55-70	65.44	28d \geq 35	28d \geq 3	28d \geq 15
0.15	45-55	42.40			
0.075	31-45	36			

The particles of cement and sand mixture, that are smaller than 0.075 mm, mainly consist of cement particles. In the material preparation, sands were sieved and then remix to make a satisfactory particle size distribution. The final particle size distribution results are also shown in Table 4.3. It could be seen that besides small deviation, the general particle size distribution of the cement and sand mixture is qualified. Testing results of mechanical material properties are listed in Table 4.4.

Table 4.4 Testing results of material parameters

Material	C40/50 (Type A-1)	CAM (Type A-2)	Cement mortar (Type B-1)		CAM (Type B-2)	
E Modulus [GPa]	25.478	1.757	-	-	-	-
Compressive strength [MPa]	42.23	3.97	1d	13.10	1d	2.29
			7d	38.47	7d	4.60
			28d	55.36	28d	5.49
Flexural strength [MPa]	-	-	1d	3.37	1d	1.08
			7d	7.59	7d	1.60
			28d	9.22	28d	1.64

The cement mortar fulfills the requirements in Table 4.3, while CAM has much less strength than required. Since it's not possible now to get the original CAM mixture used in CRTS II, additional components such as aluminum powder and anti-foaming agent are also absent. The interaction between cement mortar and asphalt emulsion is also very complex, it's not easy to make a fully qualified CAM in a short time. Nevertheless, the CAM is still used in further experiments to obtain a similar interfacial behavior between concrete and CAM in CRTS II. The 28d compressive strength of cuboid CAM is higher than the cylinder, which is also reasonable due to the small size of cuboid.

For the manufacture of the composite structure which consists of concrete and CAM layers, a silicone mould was used to create the same rough concrete surface at each specimen to make the roughness of the specimen surfaces similar to each other and also to practical CRTS II, see Figure 4.2 - a). The two concrete parts were firstly manufactured. After 28 days, the filling layer of CAM was poured between the two concrete parts from the side. With this casting direction instead of from top to bottom, the two interfaces should have similar characteristics. Finally, the specimens are prepared.

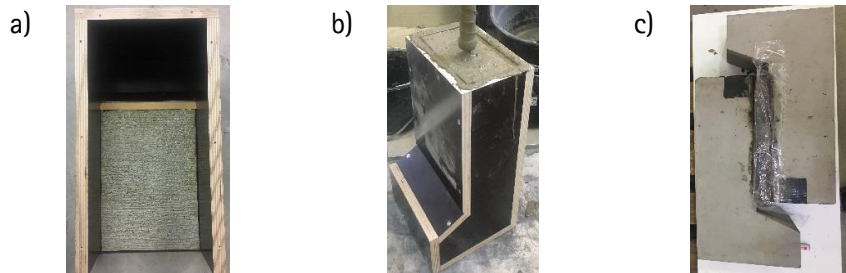


Figure 4.2 Manufacture of the specimen type D: a) formwork of the concrete part with silicone mould, b) casting of concrete part, c) casting of CAM

Before the casting of CAM, the average macrotexture depth (MTD) of the concrete surfaces are measured with sand patch method according to EN 13036-1: 2010 [57]. The measured surface roughness for each concrete part are presented in Figure 4.3. The MTD vary from 0.56 mm to 0.69 mm with a mean value of 0.61 mm. According to Model Code 2010, these concrete surfaces belong to "smooth" category for surface roughness smaller as 1.5 mm.

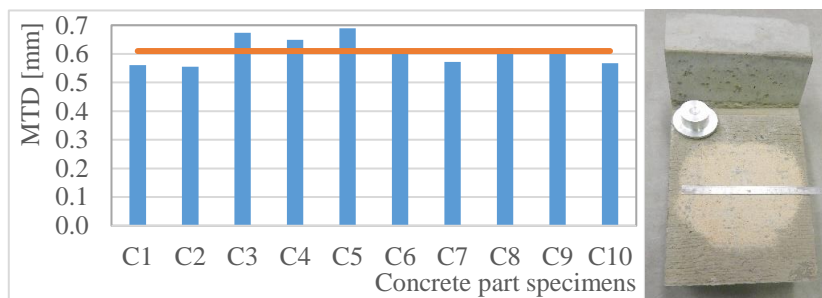


Figure 4.3 Average macrotexture depth (MTD) of concrete part specimens

In this preliminary experiment, direct tensile test was chosen to investigate the fracture mechanism for crack opening Mode I. Since one specimen was unfortunately damaged before testing, two tensile specimens (marked as TPK1 and TPK2) were available for the experiments. Although evidence showed that (presented in chapter 4.4) it's practically impossible to carry out a pure shear interface testing, push-off test was selected to study the crack propagation in Mode II. Three specimens (marked as SPK1, SPK2 and SPK3) were used to implement the push-off test.

4.3 Direct tensile test

4.3.1 Testing setup and instrumentation

Tension specimens consist of two cubic concrete parts and a CAM layer in between. In order to measure the relative displacement at interface, four linear variable displacement transducers (LVDT) are used to record the displacements at bottom interface. What's more, four omega sensors are used to measure the total displacements of the two interfaces. Since the expected loading force is very small, tensile force is recorded by an external force transducer with higher accuracy, see Figure 4.4.

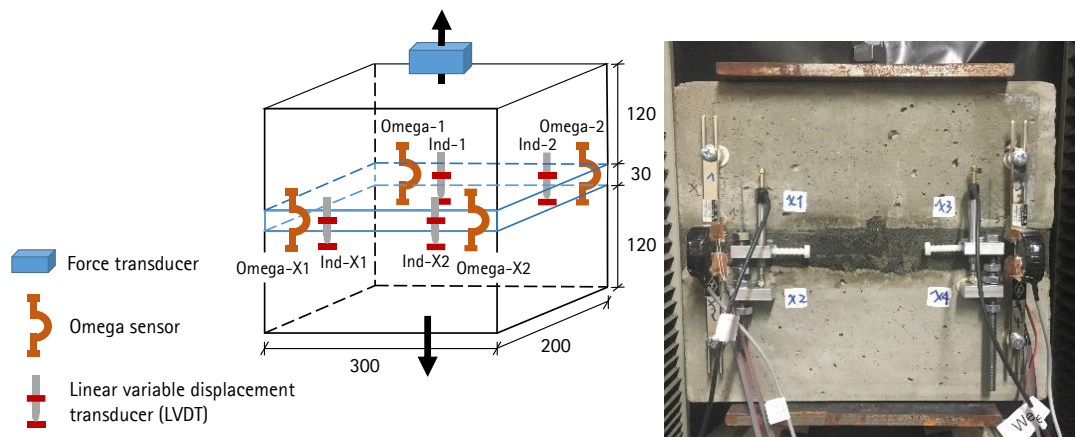


Figure 4.4 Geometry of direct tensile specimen and test setup configuration

A 250 kN capacity electromechanical testing machine was used to carry out the experiments. In order to conduct tensile forces, steel plates were anchored with the concrete parts and connected with the machine. The experiments were displacement controlled with a speed of 0.0005 mm/min. All the sensor data were recorded with a frequency of 10 Hz.

4.3.2 Testing results

The general results of the interface direct tensile tests are described in Figure 4.5. Typical tensile softening behaviour was found for interface between concrete and CAM. The machine loads reached the maximum forces of 535.32 N and 517.16 N for TPK1 and TPK2 respectively and then fell down to a relatively constant forces of about 249.19 N and 286.81 N respectively. The residual constant forces refer to the self-weight of specimen and setup. As a result, the differences between maximum loads and residual constant loads are the interfacial adhesion forces, which are 286.13 N for TPK1 and 230.35 N for TPK2. Omega sensors at the same surface showed quite similar displacements, while the omega sensors at two different surfaces deformed in opposite direction. This phenomenon showed a tilt of the specimen, which refers to a non-uniform stress state at interface. Same results are also demonstrated by LVDTs. The reasons for this tilt phenomenon are (a) inevitable difficulties in the centric loading alignment; (b) additional DOF (rotation) at the loading point caused by the joint of force transducer in the testing setup. For an optimization of the direct tensile test, rotation at two sides of specimen should be strictly restrained.

Comparing the results of omega sensor and LVDT at same position, the differences between the two kinds of sensors are partly due to the tiny displacements at undamaged interfaces but mainly caused by different measurement concepts of these two sensors. Omega sensor measures the relative displacements between two fixed points, while the LVDT is only fixed on one point and measures the displacements in one certain direction. In other word, the measured direction is isolated for LVDT but not for omega sensor. When the specimen tilts, the measured displacements for these two sensors differ. The differences between the two sensors are about 6%.

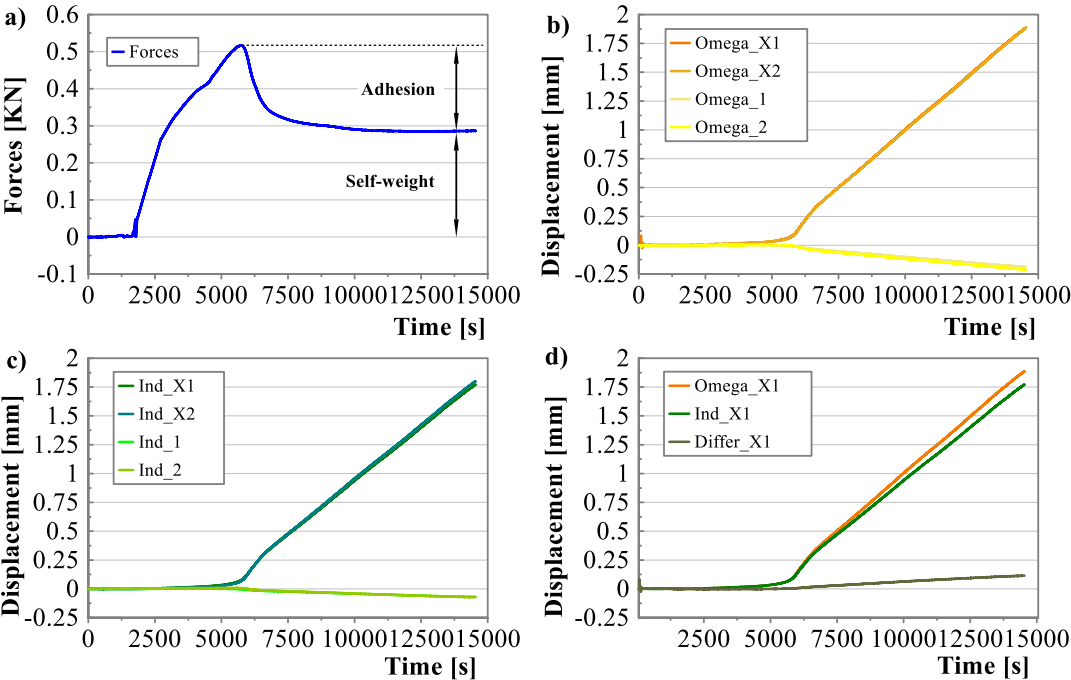


Figure 4.5 Time-related tensile testing results: a) machine force, b) displacements of four omega sensors, c) displacements of four LVDTs, d) comparison of omega sensor and LVDT at same position

In order to obtain a force-displacement relationship, the mean value of four LVDTs is used as interface displacements. The correlation curves for TPK1 and TPK2 are displayed in Figure 4.6. Maximum tensile forces of 0.535 kN and 0.517 kN are obtained at displacements of 0.0401 mm and 0.0368 mm for TPK1 and TPK2 respectively. The resulting maximum adhesion stresses (i.e. maximum adhesion forces divided by the interface area) were 4.87 kPa and 3.90 kPa for each specimen. The adhesion stresses are quite small but the results are in the same range with other research regarding similar material [146]. An observation in detail at the damaged interface showed that the damage is a combination of adhesion and cohesion. The same characteristics have been seen for both tensile and push-off test specimens. Other researchers [33] also mentioned this phenomenon.

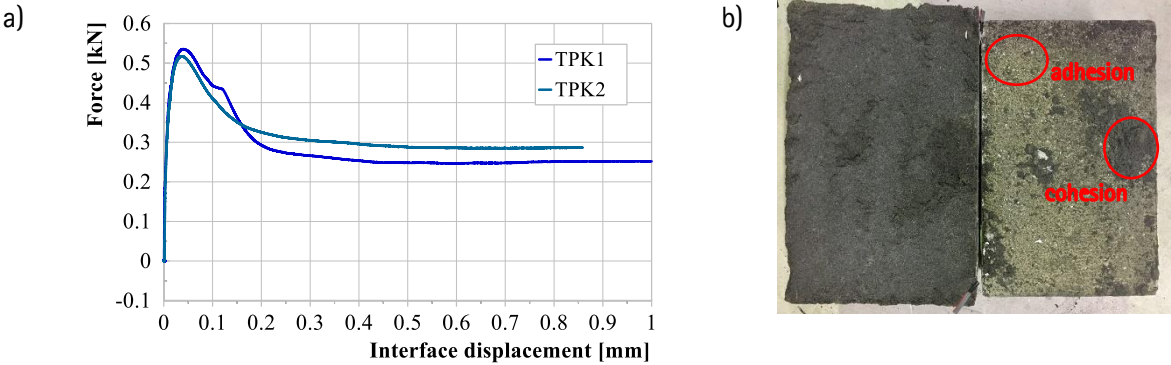


Figure 4.6 Direct tensile testing results: a) tensile force-slip curves for TPK1 and TPK2, b) picture of damaged interfaces

4.4 Push-off test

4.4.1 Test setup and instrumentation

Push-off test specimens consist of two L-shape concrete parts and a middle layer of CAM. One concrete part is placed on the "rigid" foundation, while the other concrete part is loaded with compression force of the electromechanical machine, see Figure 4.7. Since there is no reinforcement across the interface, the fracture mechanism in this case is actually a tension-shear mix mode. Previous experiences with push-off tests showed that without compression at interface, the softening phase of the crack propagation is very difficult to record. This phenomenon also means that push-off test could be used to conduct a compression-shear mix mode, but not it's suitable for tension-shear mix mode. As a result, two steel plates were used to induce constraint forces (or clamping forces) at interface. The constraint forces were controlled and monitored with four thread steel bars on which strain gauges were applied. The steel plate pressing concrete part sitting on foundation directly contacted with concrete part, since very limited vertical displacements were expected at this side. On the other hand, steel rollers were used to transfer the compression forces of the steel plate pressing on the loaded concrete part. Since the loaded concrete part has much bigger displacements, the rolls could significantly reduce the friction between steel plate and loaded concrete part. What's more, normal interface displacements would generate additional forces in the thread steel bars, which produces increasing clamping stresses at interface. Therefore, four springs with stiffness of about 3.8 N/mm were used to reduce stress changes in the thread steel bars caused by horizontal deformations.

Four LVDTs were used to measure the tangential interface deformations at two sides, meanwhile two LVDTs for normal interface displacements. Original clamping force in each tread steel bar was about 100 N, and the clamping forces were monitored during the whole experimental tests. The tests were displacement controlled with a speed of 0.001 mm/min with a testing frequency of 10 Hz.

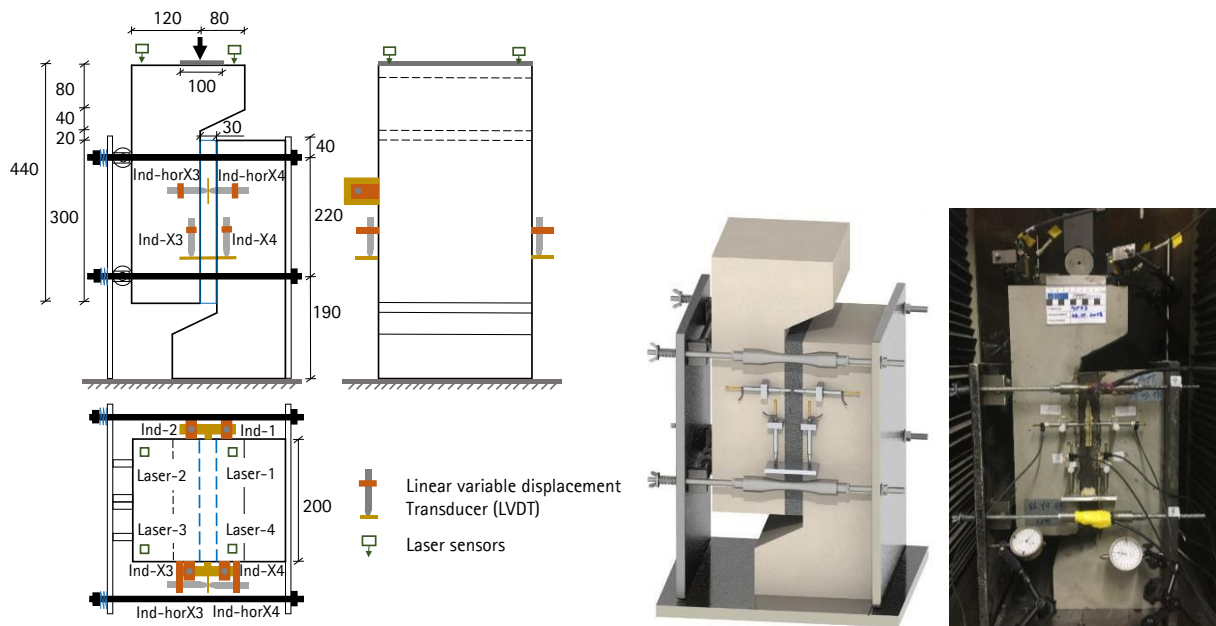


Figure 4.7 Geometry of push-off specimen and test setup configuration

4.4.2 Testing results

Machine forces also showed a softening behaviour under displacement controlled push-off tests. However, the ultimate forces were much bigger than direct tensile experiments, with the values of 2.023 kN, 2.737 kN and 1.966 kN for SPK1, SPK2 and SPK3 respectively. It's because aggregate interlock and friction play an

important role in the interface shear resistances. The force then dropped down to a relative constant force, which refers to the residual friction at interface. The measured residual frictions were approximately 350.44 N, 447.78 N and 322.34 N respectively. What's more, the self-weight of the specimen should also be taken into consideration when calculating the frictional forces. Taking the self-weight of the loaded L-shaped concrete part (26.43 kg) into consideration, the friction coefficients could be determined as 1.34, 1.64 and 1.33 for SPK1, SPK2 and SPK3 respectively, based on the ratio of residual friction forces to clamping forces at thread steel bars. It should be noticed here that the total clamping force increases after interface is undermined. To get the actual friction coefficient, the latest clamping force should be used instead of original one. Friction coefficient is influenced by the roughness, and the concrete surfaces' roughness used here are similar. Although the concrete surfaces belong to "smooth" category, the friction coefficients are much higher than expected and belong to "very rough" category according to Mode Code 2010 [45]. This may be due to the material characteristic of CAM, since asphalt component has a much stickier behaviour than normal concrete. More experiments are needed to find conclusions from the results. Interface between direct loaded concrete part and CAM is marked as Interface I and interface between CAM and sitting on foundation concrete part is marked as Interface II. For SPK1 and SPK3, damage occurred at Interface I, while specimen failed at Interface II for SPK2. When damage occurs at one interface, the crack grows in the damaged interface while other interface stays undamaged. This could be seen from the results that the damaged interface had much bigger tangential and normal displacements than the undamaged interface. As tangential interface displacements increased, the normal interface displacements also rose. The normal interface displacements could also be observed by the increased clamping forces at the thread steel bars. These indicate a mix mode fracture mechanism for push-off test. The measured displacements of four laser curves at four corners of the loaded concrete part also showed a tilt of the loading specimens, which again means the existence of normal stresses besides shear stresses at interface. The reasons for this phenomenon may be due to (a) volume dilatancy after interface damage occurs; (b) technical difficulty to load perfectly at interface line; (c) self-weight of the loading concrete part leading to bending forces at interface. Example of general results of push-off tests are displayed in Figure 4.8.

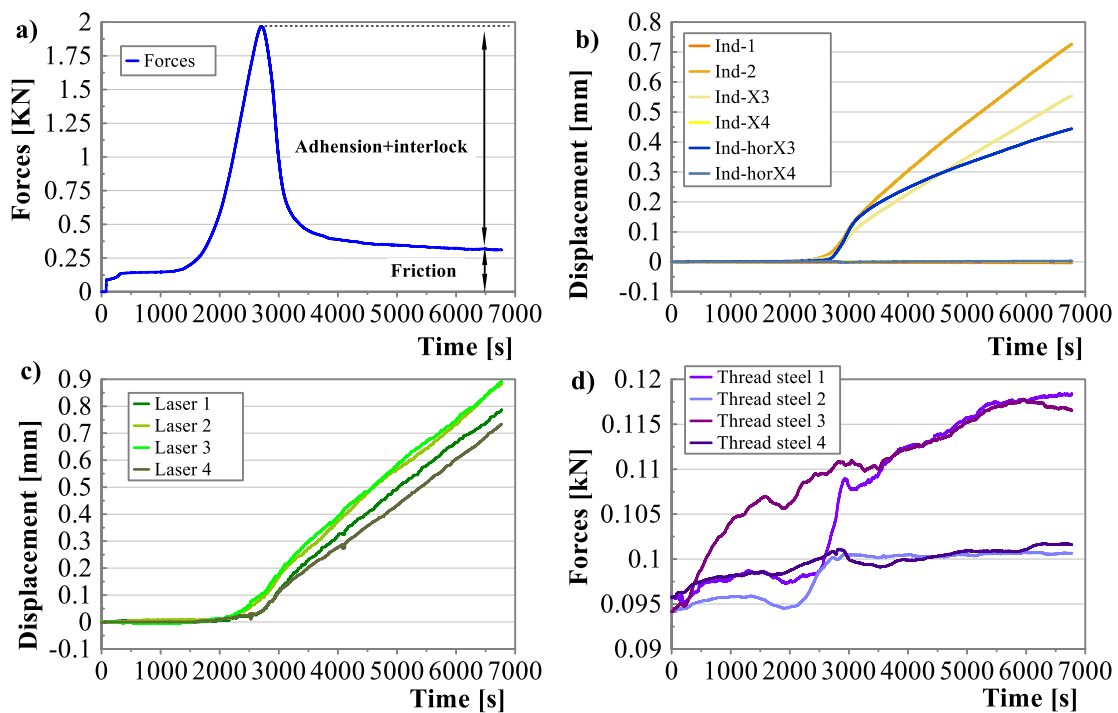


Figure 4.8 Time related push-off testing results: a) machine forces, b) displacements of six LVDTs, c) displacements of four lasers, d) constraint forces of four thread steels

Same as tensile tests, mean value of two vertical LVDTs at the damaged interface are used to get the force-slip curves, see Figure 4.9. Maximum Forces of 2.023 kN, 2.737 kN and 1.966 kN are obtained at tangential displacements of 0.0184 mm, 0.041 mm and 0.026 mm for SPK1, SPK2 and SPK3 respectively. Testing results for SPK1 and SPK3 are much more similar with the one for SPK2. This may be because the damaged interface is different for SPK2 and the stress state is then also different. It still requires further investigation to verify this assumption. The interlock phenomenon could also be demonstrated by the comparison of damaged and undamaged interface. Small cementitious fragments were observed at damaged interface, which corresponds the interlock crack model.

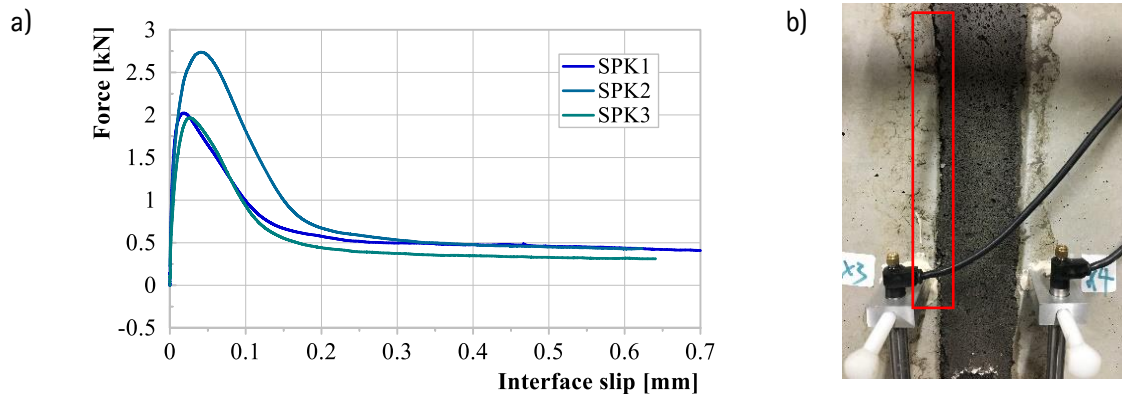


Figure 4.9 Push-off testing results: a) force-slip curves for SPK1, SPK2 and SPK3, b) comparison of damaged (left) and undamaged (right) shear interfaces

4.5 Simulation of the experiments

The direct determination of fracture mechanical parameters of cementitious material is only possible with centric direct tensile test, which has very high requirements on the experiment facilities and is also somehow erroneous due to the inevitable strain gradients [96]. In contrast, other experiment methods provide an alternative to determine the fracture characteristics with inverse analysis. Inverse analysis means the identification of the local fracture material parameters from the global behavior of a test specimen, e.g. a bending tensile test. Most experiments in fracture mechanics can be simulated with a numerical model, specifying fracture mechanical material parameters. In reverse, the fracture-mechanical material parameters can also be deduced from a measurement curve using the numerical model. Figure 4.10 shows the process of an inverse analysis. An original fracture parameter set is assumed for the material in step 1 and input in step 2 to simulate the experiment. A comparison of the calculated results with the experiment results is then implemented in step 3. When the total error measure reaches the accepted minimum, then the inverse analysis is complete (step 5). Otherwise, the input fracture parameter set is optimized by an evolutionary algorithm in step 4, which leads to a loop to step 1. Within the simulation of experiments in this thesis, manual optimization of the parameters is used instead of a complex algorithm.

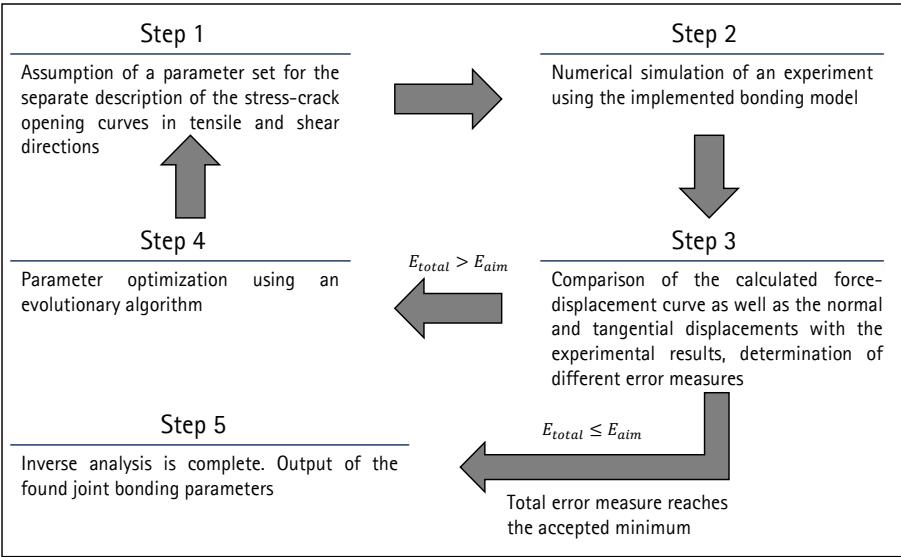


Figure 4.10 Overview of the inverse analysis concept [33]

4.5.1 Material parameters and FE discretization

The observation of the experiment results indicates that at the failure of bonding interface between concrete and CAM, no crack exists in the material. Thus, the material properties of concrete and CAM are assumed as linear elastic in the simulation. Table 4.5 shows the input parameters for C40/50 and CAM, where E and ν refer to elastic modulus and Poisson's ratio respectively, ρ and g denote density and gravitational acceleration.

Table 4.5 Material parameters in FEM

Material	E [N/mm ²]	ν	ρ [kg/mm ³]	g [N/kg]
C40/50	25478	0.2	2.247×10^{-6}	9.807
CAM	1757	0.2	1.26×10^{-6}	9.807

Both 2D and 3D simulations are implemented for the efficiency of calculation. The 8-node quadratic shell elements with reduced integration, i.e. CPS8R, are used in the 2D models. Meanwhile, linear brick elements with reduced integration (i.e. C3D8R) are utilized in 3D model for higher calculation efficiency, since the bending stresses are very small here.

The bonding properties between concrete and CAM are simulated with surface-to-surface contact interaction, which are summarized Table 4.6.

Table 4.6 Contact definition between concrete and CAM

	Discretization	Track approach	Master & slaver surfaces
Contact interaction	Surface-to-surface	small sliding	Master: C40/50 Slaver: CAM
	Normal behavior	Tangential behavior	Surface-based cohesive behavior
Contact properties	"Hard" contact (Lagrange Multiplier by default)	Friction coefficient (Penalty)	<ul style="list-style-type: none"> Linear elastic Damage initiation Damage evolution

As described in chapter 3.3.3, the master surface should be assigned to a stiffer surface with more coarse mesh size compared to the slave surface.

There are different types of track-separation law based on fictitious crack model (or CZM). In Abaqus, only linear elastic law for the track-separation relationship is available. After damage initiation, linear, exponential and tabular curves could be defined for the damage evolution (or softening curves). Assuming a constant fracture energy, a comparison of different softening curves is illustrated in Figure 4.11.

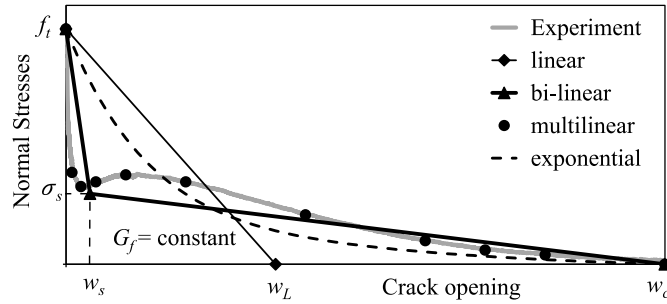


Figure 4.11 A comparison of different softening curves with same fracture energy [33]

The mathematical expressions of the curves are summarized in Table 4.7.

Table 4.7 Expressions for different softening curves

Softening types	Stress-displacement expression	Fracture energy expression
Linear	$\sigma(w) = \begin{cases} f_t \cdot \left(1 - \frac{w}{w_L}\right), & 0 \leq w \leq w_L \\ 0, & w > w_L \end{cases}$	$G_f = \frac{f_t \cdot w_L}{2}$
Bilinear	$\sigma(w) = \begin{cases} f_t - (f_t - \sigma_s) \frac{w}{w_s}, & 0 \leq w \leq w_s \\ \sigma_s \cdot \frac{w_c - w}{w_c - w_s}, & w_s \leq w \leq w_c \\ 0, & w > w_c \end{cases}$	$G_f = \frac{f_t \cdot w_s + \sigma_s \cdot w_c}{2} = \frac{\alpha_s + \beta_s}{2} \cdot f_t w_c$ <p style="text-align: center;"> $(\alpha_s = \frac{w_s}{w_c} \text{ and } \beta_s = \frac{\sigma_s}{f_t})$ </p> $\sigma_s = \frac{2G_f}{w_c} - \frac{f_t}{w_c} \cdot w_s$
Exponential	$\sigma(w) = \begin{cases} A + (f_t - A) \cdot e^{-\lambda w}, & 0 \leq w \leq w_c \\ 0, & w > w_c \end{cases}$	$G_f = \int_0^{w_c} [A + (f_t - A) \cdot e^{-\lambda w}] dw = Aw_c + \frac{f_t}{\lambda}$

For a given fracture energy G_f and maximal stress f_t , it's easy to calculate and give the maximal separation w_L for linear damage evolution in Abaqus. On the other hand, exponential parameter α should be determined in an exponential damage evolution, which needs more interpretation on the measurement datum. Comparing the above listed stress-displacement expression for exponential softening curves with equation (3.23), it could be seen that

$$A = -\frac{t^0 \cdot e^{-\alpha}}{1 - e^{-\alpha}}, \quad \lambda = \frac{\alpha}{\delta_m^f - \delta_m^0} \tag{4.1}$$

where $t^0 = f_t$ that denotes the maximal stress and $\delta_m^f - \delta_m^0 = w_c$ which refers the maximal separation after damage initiation. Substituting equation (4.1) into the fracture energy expression for exponential softening curves listed in Table 4.7, the following equation is obtained:

$$G_f = t^0(\delta_m^f - \delta_m^0)\left(\frac{1}{\alpha} - \frac{e^{-\alpha}}{1 - e^{-\alpha}}\right) \quad (4.2)$$

Thus, given specific values for fracture energy G_f , maximal stress t^0 and maximal separation after damage initiation ($\delta_m^f - \delta_m^0$), the exponential parameter α is then determined.

With regard to the bilinear as well as multilinear softening curves, tabular damage evolution is adopted where a list of damage scalar D in relationship with displacement after damage initiation should be inputted as a table. Figure 3.6 shows the definition of traction–separation curves in Abaqus. It could be seen that

$$D = 1 - \frac{t^{max}}{\bar{t}} = 1 - \frac{t^{max}}{K \cdot \delta_m^{max}} = 1 - \frac{\delta_m^0}{t^0} \cdot \frac{t^{max}}{\delta_m^{max}} \quad (4.3)$$

For every chosen measurement point (δ_m^{max}, t^{max}), the value of ($D, \delta_m^{max} - \delta_m^0$) could be inputted. As a result, arbitrary softening curves including bilinear curve could be simulated with tabular damage evolution in Abaqus.

In both direct tensile tests and push-off tests, only one interface is damaged, while the other one has only very tiny displacements. The reasons could be that:

- (1) Even though the two interfaces are manufactured to have the same bonding ability by pouring the CAM from side to side instead from top to bottom, small variations still exist between two interfaces due to material inhomogeneity, different concrete surface characteristics, etc. Fluctuations in the bonding behavior of interfaces are quite common.
- (2) Once the relative "weaker" interface starts to damage, the resulting external force also falls down, which keeps the force always smaller than the damage initiation criterion of the "stronger" interface.
- (3) The BC in direct tensile tests are also a little different for two interfaces. The rotation at lower side of the composite specimen is restrained while the upper side of the specimen is not, due to the additional joint of force transducer at loading point. The damage is therefore more prone to occur at lower interface than the upper interface in the experiments.

When the same cohesive contact behavior (i.e. same interface stiffness) is given to the two interfaces, both of them will be damaged in the simulation, which contradicts with the reality. The reaction force at loading point is influenced by the stiffness at two interfaces. The stiffer the undamaged interface is, the larger the contribution proportion of the damaged interface to the reaction forces at loading point. When the undamaged interface stiffness is 20 times greater than the damaged interface, the resulting force–displacement curve is similar with the model that the undamaged interface is tie constrained (i.e. infinite large interface stiffness). Moreover, this value drops to only 2.7 times in the push-off test, so that the results is similar with the model of tie constraint at undamaged interface. For a simplification, the damaged interface will be modeled with surface-based cohesive behavior (Table 4.6) and the undamaged interface will be simulated with tie constraint in both direct tensile test and push-off test.

4.5.2 Direct tensile test

Both 2D and 3D FEM are built to study the direct tensile test, see Figure 4.12. A reference point is utilized to simulate the loading point of the experiment. The upper interface is restrained with tie constraint so that no damage will happen here in the model. Otherwise, the lower interface is defined with surface-based cohesive behavior (Table 4.6), which could lead to damage under tension. The bottom surface of the specimen is fully restrained with encastre BC.

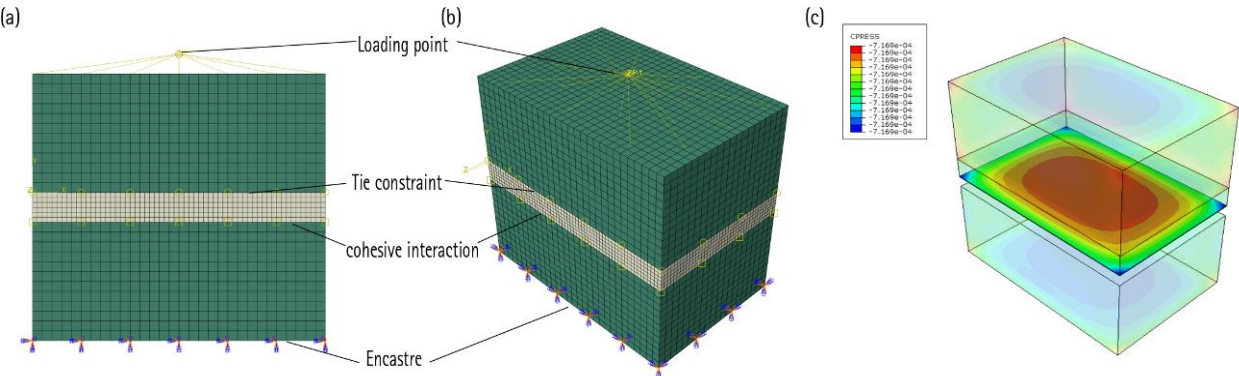


Figure 4.12 Modelling of direct tensile test: (a) 2D FEM, (b) 3D FEM, (3) modelling results of 3D FEM

4.5.2.1 Centric loading

As described above, a centric direct tensile test could determine the interface fracture properties directly. In practice, it's however somehow inevitable to produce the eccentricity. In the first step of the direct tensile test simulation, a centric loading is assumed during the experiments, which means the stresses at interface are uniform. Mean value of the four LVDTs at corners is taken as the general interface displacement. Thus, the fracture parameters for the simulation could be directly identified from the experiment results and different kinds of softening curves could be compared and studied.

The input parameters of different softening curves for direct tensile test under centric loading are listed in the following Table 4.8.

Table 4.8 Parameters (Mode I) of contact cohesive behavior under centric tensile loading

K_{nn} [MPa/mm]	δ_m^0 [mm]	δ_m^f [mm]	G_f [N/mm]	w_L [mm]	w_s [mm]	α
0.10625	0.0368	0.5752	3.9496×10^{-4}	0.202	0.114282	5.1738

A comparison between the FE results in 2D and 3D indicates almost no differences in this case, see Figure 4.13 a). This is because the specimen has much higher material stiffness than the interface stiffness, making the concrete part almost "rigid" compared to the bonding interface. Thus, 2D FEM was used to study different softening curves for a better calculation efficiency. As shown in Figure 4.13 b), linear, bilinear, exponential and multilinear softening curves with same fracture energy could be simulated. Multilinear curve has the best accordance with the measurement data and exponential curve takes the second place. Bilinear curve could better represent the real damage evolution than linear curve but it is inferior to the exponential curve. Because multilinear curve requires additional work on data sampling, the exponential softening curve is chosen for the further experiment simulations.

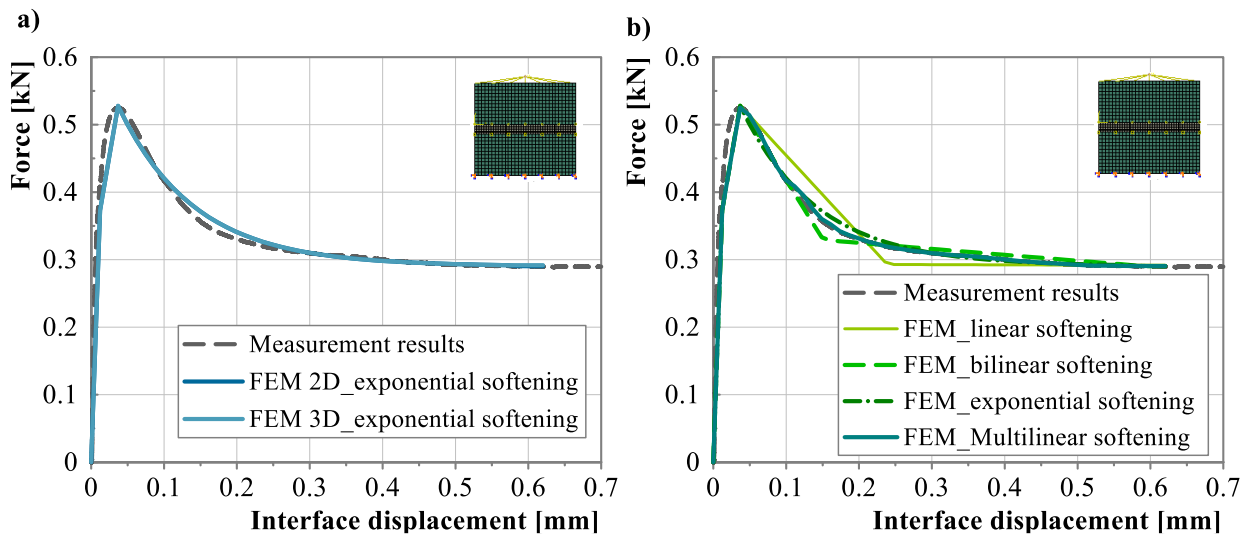


Figure 4.13 Comparison of measurement results with FEM results for TPK2

The contact compression and damage scalar are studied to make a close scrutiny at the damaged interface, shown in Figure 4.14. The interface is initially under compression due to self-weight and then turns to tension as interface opens. Since Abaqus only offers a linear elastic model for elastic phase of CZM, the cohesive elastic stiffness K_{nn} could easily be seen from the figure, which is identical for all the softening curves. After damage initiation, the damage develops with different softening curves. It could also be observed that the damage scalar decreases dramatically between the interface displacement from 0.036 mm to 0.2 mm for all the softening curves, which indicates a mainly interface damage happening in this phase, although a full damage goes to the interface displacement with 0.575 mm for all the curves except linear softening. The damage scalar decreases then gradually to zero with very small variations after that. What's more, the variation of damage scalar decreases with increasing interface opening.

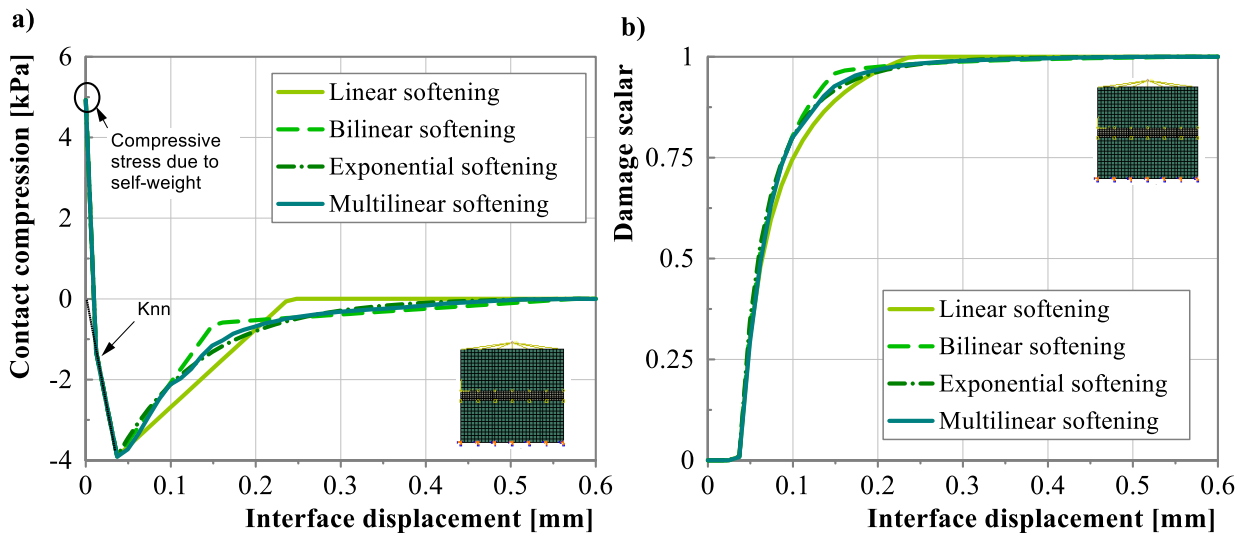


Figure 4.14 Contact compression and damage scalar of different softening curves

4.5.2.2 Eccentric loading

By deviating the loading point at top the specimen, eccentricity could be introduced in the model. The stresses at damaged interface are therefore not uniform any more but under different stress states, leading to different

resulting force-displacement curves at loading point, see Figure 4.15 a). The larger the eccentricity is, the smaller the maximal resulting force at loading point. As a result, an inverse analysis is required to obtain the true fracture characteristics at the interface. By manually optimizing the inputted bond parameters (Figure 4.10), the resulting force-displacement curve could then fit to the one without eccentricity (i.e. in accordance with the measurement results), see Figure 4.15 b). In this way, the optimized bond parameters are found.

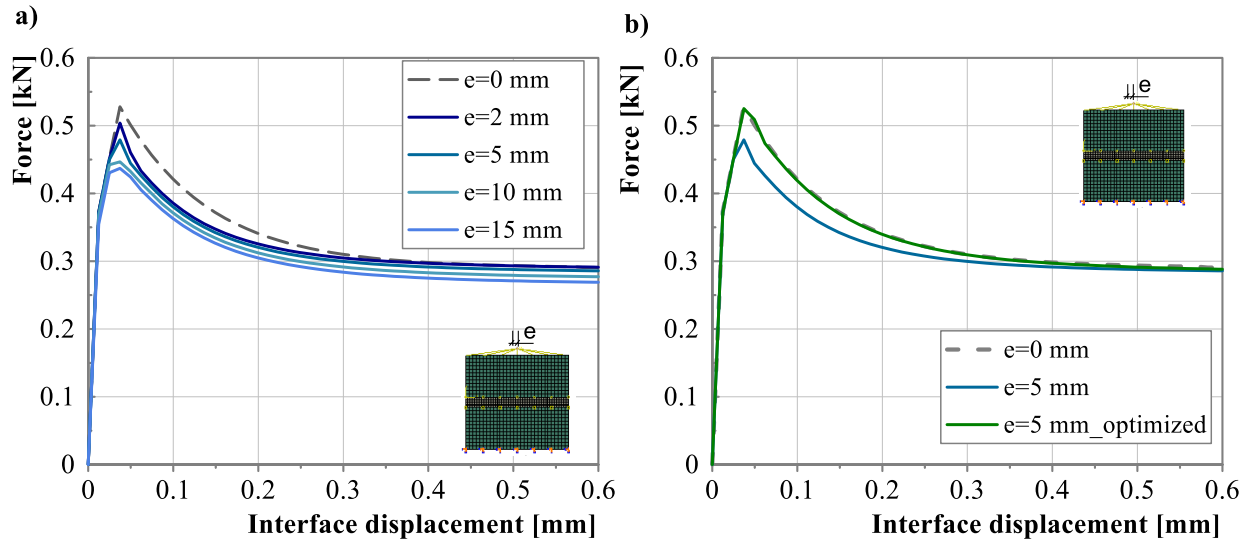


Figure 4.15 Resulting force-displacement curves at loading point with consideration of eccentricities

The bond behavior of the interface is modelled with CZM, in which all the necessary parameters could be found in Figure 3.6. Table 4.9 summarizes the optimized parameters after inverse analysis under different eccentricities. Only the displacement for damage initiation δ_m^0 and exponential parameter α were changed, while the stiffness K_{nn} and maximal separation after damage initiation $(\delta_m^f - \delta_m^0)$ remained the same.

Table 4.9 Optimized CZM parameters in Mode I at interface with the consideration of eccentricities

Eccentricity e [mm]	0	2	5	10	15
δ_m^0 [mm]	0.0368	0.039	0.045	0.05	0.054
α	5.173	4.05	4.6	4.9	5.0
K_{nn} [MPa/mm]	0.1063				
$(\delta_m^f - \delta_m^0)$ [mm]	0.5384				

Calculated according to equations (3.23) and (4.2), the constitutive model of traction-separation law as well as the corresponding fracture energy under different loading eccentricities could be displayed in Figure 4.16. It could be seen that the damage initiation displacement δ_m^0 increases with the augment of loading eccentricities. Once the eccentric loading exists, the fracture energy increases dramatically from $e=0$ mm to $e=2$ mm. After that, the fracture energy grows almost in linear proportion to the eccentricity. Linear regression for the fracture energy G_f in relationship with eccentricity e leads to

$$G_f = 0.499 + 0.006475 \cdot e \tag{4.4}$$

On account of the difficulties to get a convergent FE result for eccentricity smaller than 2 mm, the value of minimal fracture energy under eccentric loading could be determined as 0.499 N/m.

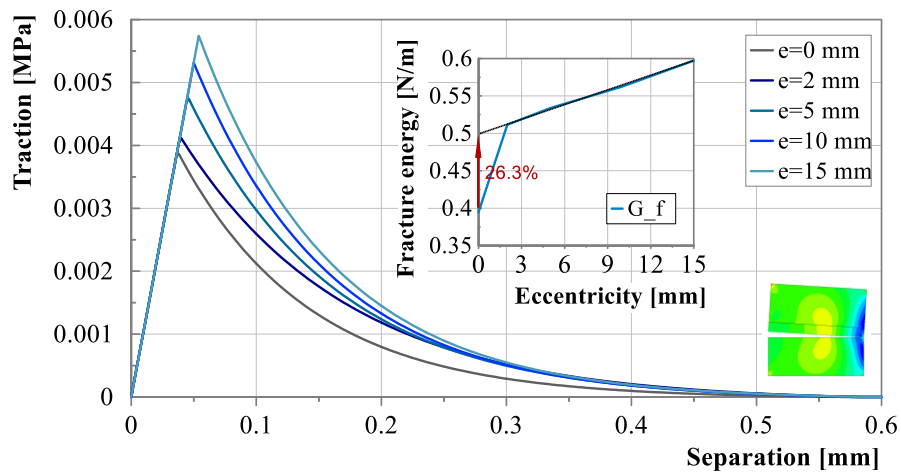


Figure 4.16 Optimized traction-separation law with the consideration of eccentric loading

Assuming an infinite small eccentricity, the determined fracture energy in an eccentric loading experiment is 26.3% higher than the one in a centric loading experiment. Keeping δ_m^0 , K_{nn} and $(\delta_m^f - \delta_m^0)$ unchanged, the exponential parameter is then adjusted to 3.8721 instead of 5.1738 for a larger fracture energy.

4.5.3 Push-off test

Besides the fracture characteristics of interface in Mode I, the damage properties in Mode II and Mode III should also be determined. The interface is considered as isotropic, therefore the characteristics are the same in Mode II and Mode III. Push-off tests are then implemented to determine to fracture characteristics in Mode II and Mode III.

Similar with direct tensile tests, 2D and 3D FEM of push-off test are built to obtain the interface fracture characteristics with inverse analysis, see Figure 4.17. Interface I (i.e. interface between the loaded concrete and CAM) is modeled with exponential cohesive contact, while Interface II (i.e. interface between the sitting on ground concrete and CAM) is modeled with tie constraint. Axil connector elements are used to simulate the clamping forces at the four thread steel bars. The interaction between specimen and steel plates at two sides are set as frictionless contact.

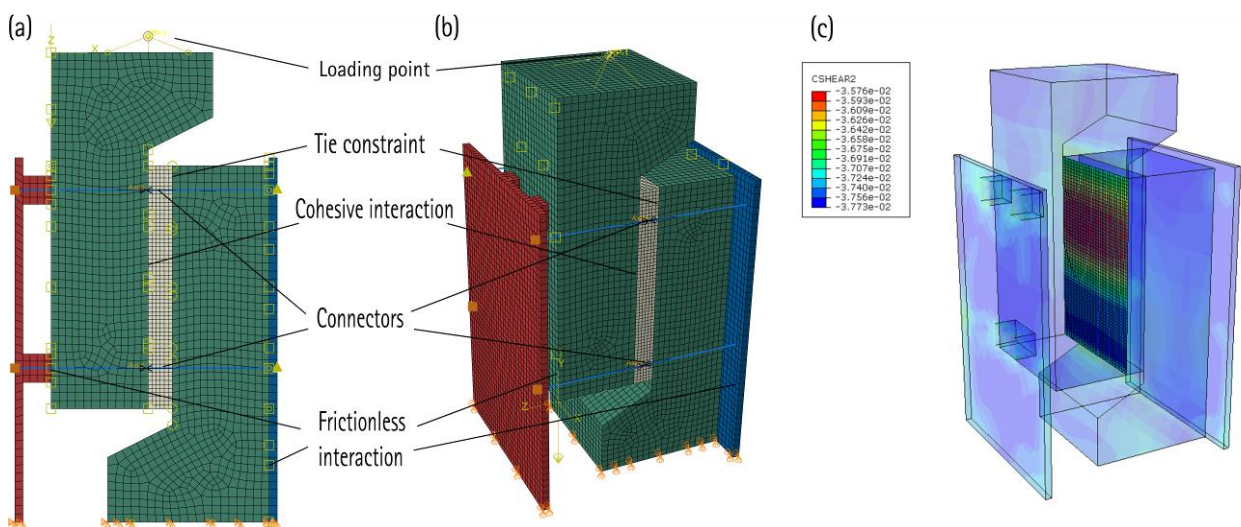


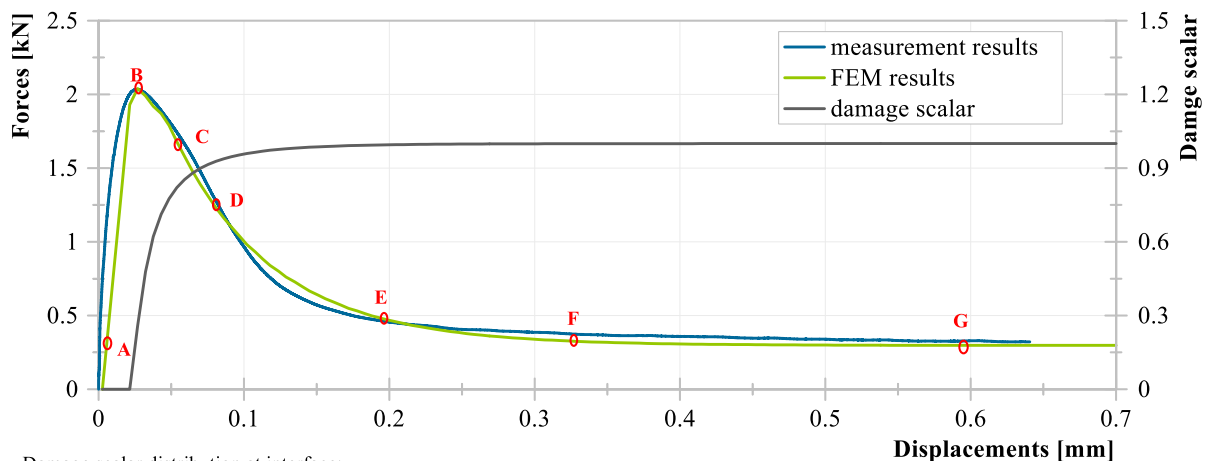
Figure 4.17 Modelling of push-off test: (a) 2D FEM, (b) 3D FEM, (3) modelling results of 3D FEM

Push-off test exhibits a mix-mode fracture behavior. Due to the presence of compression stresses at interface, the damage could only occur in Mode II. Nevertheless, minor normal displacements (i.e. contact opening) still exist in the simulation, the determined fracture parameters of Mode I from direct tensile test are used here. Assuming a uniform stress state at interface, the original inputted parameters are listed in Table 4.10.

Table 4.10 Original inputted parameters of contact cohesive behavior for push-off test

K_{nn} [MPa/mm]	K_{ss}/K_{tt} [MPa/mm]	δ_m^{n0} [mm]	$\delta_m^{t0}/\delta_m^{s0}$ [mm]	δ_m^f [mm]	α	μ
0.10625	1.475	0.0368	0.0261	0.6214	9	0.8

The inverse analysis was firstly carried out with 2D FEM for a quick calculation and then implemented by 3D FEM for a refined optimization. The final force-displacement curve of the 3D FEM comparing with measurement results as well as the damage scalar at interface midpoint in relationship with displacements are displayed in Figure 4.18. It could be observed that interface damage already exists at the maximum loading force and develops dramatically in the first 0.1 mm, i.e. damage scalar varying from 0 to 0.92. In comparison, the damage scalar from point E to point G has a variation only from 0.99 to 1. The smaller the damage scalar is, the larger scatter the damage scalar distribution at interface has. For example, the interface damage scalar distribution at point B has a maximum deviation of 0.0517, while the values drop to 0.0210, 0.0071, 0.0005 and 0.0001 at points C, D, E, and F respectively. This phenomenon indicates that, with the rising interface displacements, the damage scalar also increases, and meanwhile its distribution at interface gets more uniform.



Damage scalar distribution at interface:

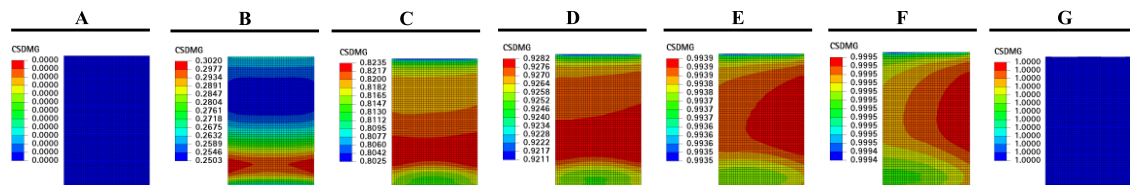


Figure 4.18 FEM results of push-off test: loading force and damage scalar at interface in relationship of loading displacements

The optimized interface fracture parameters are listed in Table 4.11. The calculated friction coefficient is different than the one from testing results. Because the dilatancy is ignored in the simulation, the clamping forces go back to the original value after interface undermines, which is not the case in reality. What's more, the measured self-weight of concrete part is also different from the calculated one on account of the specimen geometry variations in the experiments.

Table 4.11 Optimized inputted parameters of contact cohesive behavior for push-off test

K_{nn} [MPa/mm]	K_{ss}/K_{tt} [MPa/mm]	δ_m^{n0} [mm]	$\delta_m^{s0}/\delta_m^{t0}$ [mm]	δ_m^f [mm]	α	μ
0.10625	3	0.0368	0.0125	0.6214	8.5	1.475

In the experiments, damage at interface II was also observed, where the specimen has a much larger strength than the other two specimens with damage at interface I, see Figure 4.9. It was assumed that this may be caused by different stress states at two interfaces. However, numerical simulation shows no big difference of the force-displacement curve between the damage at interface I and interface II, given the same cohesive contact behavior at respective interfaces. Thus, the variation of force-displacement curves for different specimens belongs to experimental fluctuation.

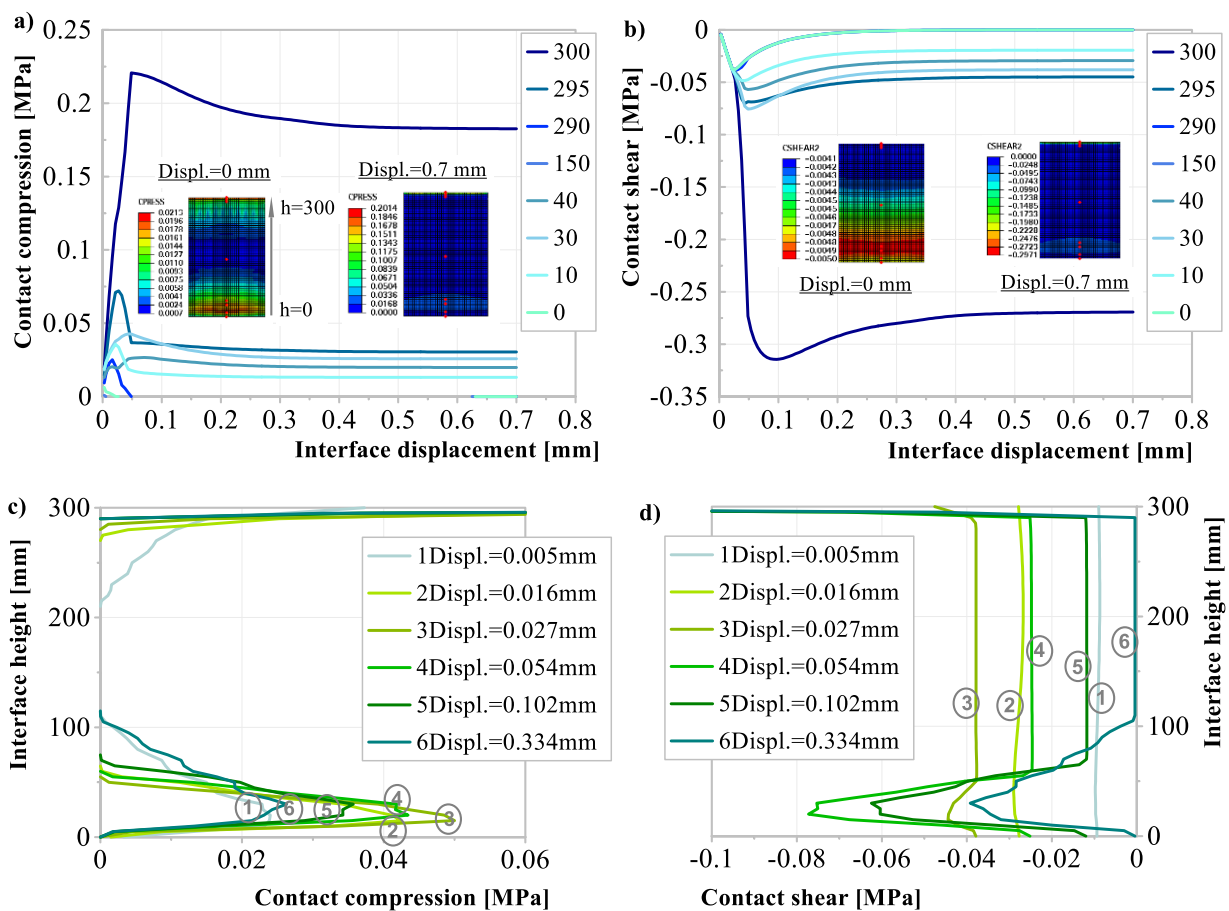


Figure 4.19 FEM results of push-off test: a) contact compression and b) contact shear

The contact compression and contact shear in relationship with interface displacement as well as the stress distributions along the interface height are demonstrated in Figure 4.19. The stress-displacement curves of the points with a distance of 300 mm, 295 mm, 290 mm, 150 mm, 40 mm, 30 mm, 10 mm and 0 mm to the bottom of interface are plotted. For the sake of clamping forces at the thread steel bars, the interface is originally in compression. The top edge of the interface is then under large compression with increasing displacement as a result of the constraint equipment and tilt of the specimen, whereas the compression is smallest in the middle of the interface. After interface damage initiation, minimal tensile stresses even occur by reason of contact opening. The compressive stresses gradually increase in the area where the clamping

forces are applied (i.e. position of the two bottom thread steel bars) and decrease again at the bottom edge of interface.

Contact shear stresses are a combination of cohesive shear stresses and frictional stresses. The shear values are then influenced by the compressive stresses. Similar with contact compression, the top edge of the interface is under largest shear stresses (mainly composed of friction). In the middle and bottom edge of the interface, the shear stresses mainly come from cohesive stresses and gradually decrease to zero when interface damages. The shear stresses in the area of applied clamping forces have a dual influence of cohesive shear and friction. The stresses decrease to a constant residual value after interface is fully undermined.

As shown in Figure 4.19, the stresses have a non-uniform distribution at interface in the push-off test. Both compressive and shear stresses exist, leading to a mix-mode interface damage. As a result, a reverse analysis is inevitable in push-off test to obtain the true fracture parameters.

4.6 Summary

In this chapter, experimental determination of interface fracture parameters is carried out. Direct tensile test for mode I and push-off test for mode II and mode III are chosen in the experiments. In general, the following points could be summarized:

- (1) Force-displacements curve with typical damage softening behaviour is obtained by the displacement-controlled direct tensile test. The ultimate adhesion forces of 286.13 N and 230.35 N are gained at displacements of 0.0401 mm and 0.0368 mm for TPK1 and TPK2 respectively. Interface damage is a combination of both adhesion and cohesion. However, tilts of the specimen were observed, which leads to non-uniform stress state at interface and inaccurate results.
- (2) Force-displacements curves obtained from push-off tests are a result of interface resistance from adhesion, aggregate interlock and residential friction. Maximum shear forces of 2.023 kN, 2.737 kN and 1.966 kN are obtained at tangential displacements of 0.0184 mm, 0.041 mm and 0.026 mm for SPK1, SPK2 and SPK3 respectively. The ultimate shear strength is much higher than the tensile strength due to the contribution of aggregate interlock and friction. Friction coefficients could be determined as 1.34, 1.64 and 1.33, which are much higher than expected values for "smooth" category in MC2010 [45]. This may be due to the sticky behaviour of asphalt component in CAM. Both tangential and normal interface displacements at damaged interface were measured. The normal interface displacements could also be observed by the increased clamping forces at the thread steel bars. These indicate a mix mode fracture mechanism for push-off test. The reasons for this phenomenon may be due to a) volume dilatancy after interface damage occurs; b) technical difficulty to load perfectly at interface line; c) self-weight of the loading concrete part leading to bending forces at interface.
- (3) Numerical simulation with inverse analysis was implemented to obtain the actual fracture parameters at interface. A comparison between the FE results in 2D and 3D indicates almost no differences in this case. This is because the specimen has much higher material stiffness than the interface stiffness, making the concrete part almost "rigid" compared to the bonding interface. Thus, 2D FEM was used to study different softening curves for a better calculation efficiency. For the direct tensile test, centric loading with different softening curves (linear, bilinear, exponential and multilinear) was simulated in the first step. Multilinear curve has the best accordance with the measurement data and exponential curve takes the second place. Bilinear curve could better represent the real damage evolution than linear curve but it is inferior to the exponential curve. Because multilinear curve requires additional work on data sampling, exponential softening curve was then chosen for further simulation because of its optimum in both accordance with experiment results and time consuming in preparation of inputted parameters. Eccentric

loading was then studied in simulation of direct tensile test. A linear relationship between fracture energy and the eccentricity is then obtained in equation (4.4).

- (4) Push-off test exhibits a mix-mode fractural behaviour and non-uniform stress distribution at interface, thus reverse analysis is necessary. Interface damage already exists at the maximum loading force and develops dramatically in the first 0.1 mm, i.e. damage scalar varying from 0 to 0.92. On the other hand, the damage scalar at displacements from 0.3 mm to 0.6 mm has a variation only from 0.99 to 1. With the rising interface displacements, the damage scalar also increases and meanwhile its distribution at interface gets more uniform. Numerical simulation shows no big difference of the force-displacement curve between the damage at interface I and interface II, given the same cohesive contact behavior at respective interfaces. Both compressive and shear stresses distribution at interface have big scatter. The top edge of the interface has maximum compressive and shear stresses while the middle and bottom edge of the interface has minimal values. The interface stress state is influenced by the constraint setup as well as position of induced clamping forces. Compared to the middle of the interface, increased compressive and shear stresses could be observed in the area where the clamping forces are applied, i.e. position of the two bottom thread steel bars. A suggested fracture parameter set for interface between concrete and CAM with an exponential softening behavior is listed in Table 4.11.
- (5) The direct tensile test setup needs to be optimized in order to eliminate the phenomenon of specimen tilts. Smaller-sized specimens that are fully connected with the rigid steel plate and meanwhile avoid hinges in testing system, could be a solution for that. Alternative methods such as splitting experiments could also be used, which requires reverse analysis to gain the material constitutive model.
- (6) Interface damage in practical engineering is usually an interaction of shear and tension. A proper feasible testing method to investigate interface behaviour including the damage evolution under tension and shear forces should be designed in further steps.

5. Longitudinal interface behavior under uniform temperature variations

In EN 1992-3 Annex M, two kinds of restraint based on practical problems are addressed, which are restraint at ends and restraint along one edge, see Figure 5.1. The first one occurs when a new section of concrete is cast between two pre-existing sections, while the second one is particular common when a wall is cast onto a pre-existing stiff base. The restraint at ends has been extensively studied and is reasonably well understood. On the other hand, the restraint along one edge has not been researched so systematically and there appears to be little published guidance.

The continuous slab track of Bögl system (or CRTS II in China) is actually a combination of these two kinds of restraint. The vertical joints between two prefabricated slabs create restraints at ends, while the horizontal joints due to interface bonding between prefabricated concrete slab and CAM lead to the second kind of restraint, i.e. restraint along one edge. When temperature increases, the vertical joints close and movements at horizontal interface joints are then limited. However, when temperature decreases, the vertical joints open and the system is then only restraint by the interface bonding of horizontal joints between prefabricated concrete slab and CAM, see Figure 5.1.

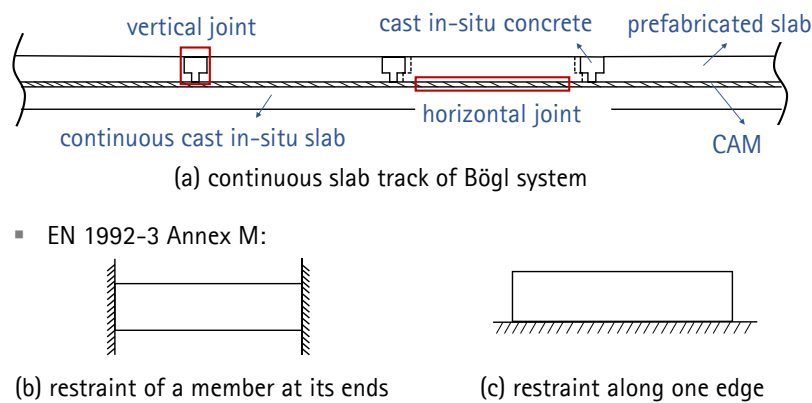


Figure 5.1 Continuous slab track of Bögl system and types of restraint in EN 1992-3

As a result, the second kind of restraint is chosen to study the longitudinal interface damage in the first step. Experiment results [147] show that the top interface bonding between prefabricated concrete slab and CAM is much weaker than the bottom interface bonding between CAM and continuous cast-in-situ substrate concrete slab. The bottom interface shows no relative displacement until the full damage of the top interface. Thus, only top interface damage between prefabricated and CAM is studied in the model. Since the prefabricated concrete slab is much stiffer than the interface bonding meanwhile the slab thickness is much smaller than the width and length, the prefabricated concrete slab is considered as a Euler-Bernoulli beam. External forces and interface resistance load axially on the beam. The continuous cast-in-situ concrete slab and CAM layer shows negligible deformation compared to the prefabricated beam and are thus considered as rigid for simplification.

Uniform temperature variations cause longitudinal deformations of the prefabricated beam that induce longitudinal displacements at interface, while temperature gradient variations lead to flexural deformations of the beam which arouse vertical displacements at interface. The normal and tangential interface resistances are uncoupled in this model. Pure longitudinal interface displacement doesn't contribute to vertical interface stresses and pure vertical displacement at interface gives no rise to tangential interface stresses.

In sum, the following hypotheses are assumed in the analytical model:

- (1) The prefabricated concrete slab is considered as a Euler-Bernoulli beam;

- (2) The continuous cast-in-situ concrete slab combined with CAM layer is considered as rigid;
- (3) The interface resistance reacts centrally at beam axis;
- (4) The normal and tangential interface resistances are uncoupled.

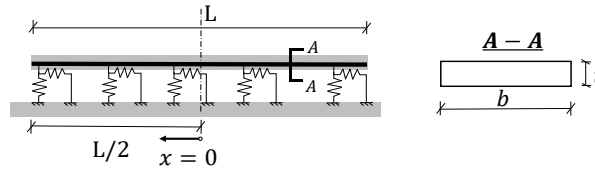


Figure 5.2 Analytical model of interface damage

Since the thermal deformation is symmetric about the mid axis, the symmetric axis is taken as $x = 0$ and half of the system is investigated in the model, see Figure 5.2.

5.1 Analytical models

Longitudinal relative displacement at interface arouse interface resistance forces in the longitudinal direction. Typical kinds of horizontal interface resistance are displayed in Figure 5.3.

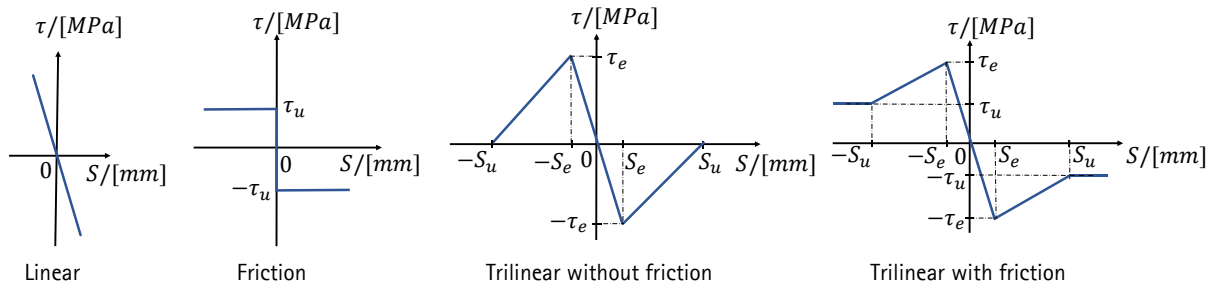


Figure 5.3 Typical stress-slip relationship for longitudinal interface resistance

In practical cases, residential friction forces still contribute to the longitudinal resistance after fully damage of interface bonding. Thus the trilinear stress-slip relationship could most appropriately describe the interface resistance. Linear elastic, damage evolution and friction phases of interface under shear stresses could be simulated with the trilinear stress-slip relationship. In order to study the interface behavior step by step, a linear elastic interface resistance is first studied. Then, interface with pure friction resistance is investigated. Finally, the trilinear interface resistance under uniform temperature variation is modelled.

5.1.1 Linear longitudinal interface behavior

The resistance forces are linear proportional to relative displacements at interface with linear interface behavior

$$\tau(x) = -k \cdot S(x) \quad (5.1)$$

where $\tau(x)$ is the interface shear stress along the slab length and $S(x)$ refers to the relative longitudinal interface displacements. Relative displacements at interface could be expressed as deformation differences between two layers

$$S(x) = U_1(x) - U_2(x) \quad (5.2)$$

Since in this case, the deformation of the bottom layer is comparably neglectable, relative interface displacement is thus equal to the deformation of the slab

$$S(x) = U(x) \quad (5.3)$$

where $U_1(x)$, $U_2(x)$ and $U(x)$ denote longitudinal deformation of the top slab, substrate slab and Euler-Bernoulli beam respectively. The stresses equilibrium in an infinitesimal unit is described in Figure 5.4.

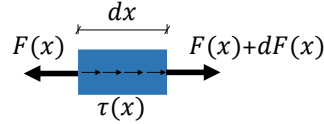


Figure 5.4 Differential element of length dx under uniform temperature

This equilibrium leads to the following equations

$$dF(x) = -\tau(x) \cdot dx \quad (5.4)$$

$$\frac{dF(x)}{dx} = -\tau(x) \quad (5.5)$$

On the other hand, the relationship between deformation, strain and force is

$$\frac{dU(x)}{dx} = \varepsilon(x) = \frac{F(x)}{EA} \quad (5.6)$$

Making a differential of the above equation leads to

$$\frac{d^2U(x)}{dx^2} = \frac{1}{EA} \cdot \frac{dF(x)}{dx} \quad (5.7)$$

Substitute the equations (5.1), (5.3) and (5.5) to equation (5.7)

$$\frac{d^2S(x)}{dx^2} = \frac{k}{EA} \cdot S(x) \quad (5.8)$$

Transform the above equation to the following format

$$\frac{d^2S(x)}{dx^2} - \frac{k}{EA} \cdot S(x) = 0 \quad (5.9)$$

Assume

$$\lambda = \sqrt{\frac{k}{EA}} \quad (5.10)$$

Substitute the equation (5.10) to equation (5.9)

$$\frac{d^2S(x)}{dx^2} - \lambda^2 \cdot S(x) = 0 \quad (5.11)$$

This is a homogeneous differential equation, the general solution could be described as

$$S(x) = C_1 \cdot e^{\lambda x} + C_2 \cdot e^{-\lambda x} \quad (5.12)$$

Since no deformation exists at symmetric axis, the BC could be expressed as

$$S(0) = C_1 + C_2 = 0 \quad (5.13)$$

As a result

$$C_1 = -C_2 \quad (5.14)$$

Substitute the equation (5.14) to equation (5.12)

$$S(x) = C_1 \cdot (e^{\lambda x} - e^{-\lambda x}) = 2C_1 \cdot \sinh \lambda x \quad (5.15)$$

Differential of the above equation leads to

$$\varepsilon(x) = \frac{dS(x)}{dx} = \lambda C_1 \cdot (e^{\lambda x} + e^{-\lambda x}) = 2\lambda C_1 \cdot \cosh \lambda x \quad (5.16)$$

Considering there is no external force at beam ends, so the strain at beam end is equal to thermal strain without restraint

$$\varepsilon(L/2) = \lambda C_1 \cdot \left(e^{\frac{\lambda L}{2}} + e^{-\frac{\lambda L}{2}} \right) = \alpha_T \cdot \Delta T \quad (5.17)$$

So that the two unknown factors are solved as

$$C_1 = \frac{\alpha_T \Delta T}{\lambda \left(e^{\frac{\lambda L}{2}} + e^{-\frac{\lambda L}{2}} \right)} \quad (5.18)$$

$$C_2 = -\frac{\alpha_T \Delta T}{\lambda \left(e^{\frac{\lambda L}{2}} + e^{-\frac{\lambda L}{2}} \right)} \quad (5.19)$$

Finally, the relative displacements at interface and stresses in slab are expressed as follows

$$S(x) = \frac{\alpha_T \Delta T}{\lambda \left(e^{\frac{\lambda L}{2}} + e^{-\frac{\lambda L}{2}} \right)} \cdot (e^{\lambda x} - e^{-\lambda x}) = \frac{\alpha_T \Delta T \cdot \sinh \lambda x}{\lambda \cdot \cosh \frac{\lambda L}{2}} \quad (5.20)$$

$$\varepsilon(x) = \frac{\alpha_T \Delta T}{\left(e^{\frac{\lambda L}{2}} + e^{-\frac{\lambda L}{2}} \right)} \cdot (e^{\lambda x} + e^{-\lambda x}) = \frac{\alpha_T \Delta T \cdot \cosh \lambda x}{\cosh \frac{\lambda L}{2}} \quad (5.21)$$

The strains in beam consist of two components, which are strain due to stresses ε_σ and strain due to temperature ε_T

$$\varepsilon = \varepsilon_\sigma + \varepsilon_T \quad (5.22)$$

Thus, the stresses in the beam could be determined as

$$\sigma = E \cdot \varepsilon_\sigma = E(\varepsilon - \varepsilon_T) = E(\varepsilon - \alpha_T \Delta T) \quad (5.23)$$

A result comparison between FEM and analytical model under uniform temperature variation $\Delta T = 10\text{ K}$ is demonstrated in the following Figure 5.5. The results of these two kinds of models are in agreement with each other. The end side of the beam has the largest interface displacements and stresses, while the interface displacements and stresses at symmetric axis (mid axis) are equal to zero. The beam stress induced from restraint has a negative correlation with beam strain, see equation (5.23). Hereby, the beam end is free from interface restraint, thus the beam stress at the end side is zero meanwhile the end side has the largest beam strain. On the other hand, symmetric axis is most restrained from the interface and has therefore the smallest beam strain and the largest beam stress. It could also be found that, the beam stresses are in compression due to the positive uniform temperature variation and restraint from interface.

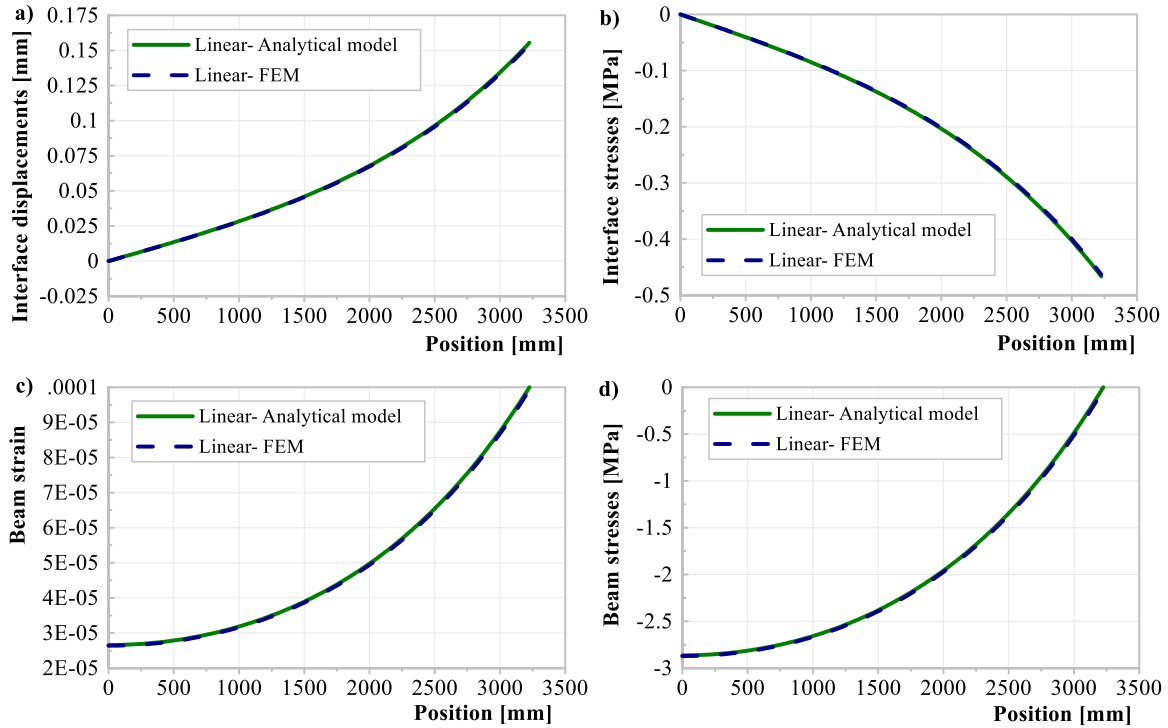


Figure 5.5 Comparison of analytical model and FEM of linear longitudinal interface behavior

5.1.2 Longitudinal interface with pure friction resistance

Considering interface resistance with pure friction, the shear stresses at interface could be expressed as

$$\tau(x) = -\text{sgn}(\Delta T) \cdot \tau_u = -\text{sgn}(\Delta T) \cdot \mu \cdot F_N \quad (5.24)$$

It should be noticed, that a positive uniform temperature variation causes elongation of the beam, while negative variation leads to shortening. Thus, the frictional stresses have reverse directions under positive and negative temperature variations. $\text{Sgn}(x)$ refers to the signum function and is defined as

$$\text{sgn}(x) = \frac{x}{|x|} \quad (5.25)$$

Substitute the equations (5.3), (5.5) and (5.24) into equation (5.7)

$$\frac{d^2 S(x)}{dx^2} = -\frac{\tau(x)}{EA} = \text{sgn}(\Delta T) \frac{\tau_u}{EA} \quad (5.26)$$

The general solution of the above equation is

$$S(x) = \operatorname{sgn}(\Delta T) \frac{\tau_u}{2EA} \cdot x^2 + C_1 \cdot x + C_2 \quad (5.27)$$

Based on the equations (5.3) and (5.6), the beam strain could be described as below:

$$\varepsilon(x) = \operatorname{sgn}(\Delta T) \frac{\tau_u}{EA} \cdot x + C_1 \quad (5.28)$$

Similar with previous linear elastic interface behavior, the BCs in this case are:

$$\begin{cases} S(x=0) = C_2 = 0 \\ \varepsilon(x=L/2) = \operatorname{sgn}(\Delta T) \frac{\tau_u}{EA} \cdot \frac{L}{2} + C_1 = \alpha_T \cdot \Delta T \end{cases} \quad (5.29)$$

As a result,

$$S(x) = \operatorname{sgn}(\Delta T) \frac{\tau_u}{2EA} \cdot x^2 + \left[\alpha_T \cdot \Delta T - \operatorname{sgn}(\Delta T) \frac{\tau_u L}{2EA} \right] \cdot x \quad (5.30)$$

$$\varepsilon(x) = \operatorname{sgn}(\Delta T) \frac{\tau_u}{EA} \cdot x + \left(\alpha_T \cdot \Delta T - \operatorname{sgn}(\Delta T) \frac{\tau_u L}{2EA} \right) \quad (5.31)$$

$$\sigma(x) = E[\varepsilon(x) - \alpha_T \Delta T] = \operatorname{sgn}(\Delta T) \frac{\tau_u}{2A} (2x - L) \quad (5.32)$$

The comparison between analytical model and FEM under uniform temperature variation $\Delta T = 10 \text{ K}$ is shown in Figure 5.6. The two models have good accordance. Interface stresses due to friction are constant along the beam. Same with linear interface behavior, the beam end has the largest interface displacements and stresses as well as the biggest beam strain. Beam stress at end is zero and it reaches maximum value at the symmetric axis.

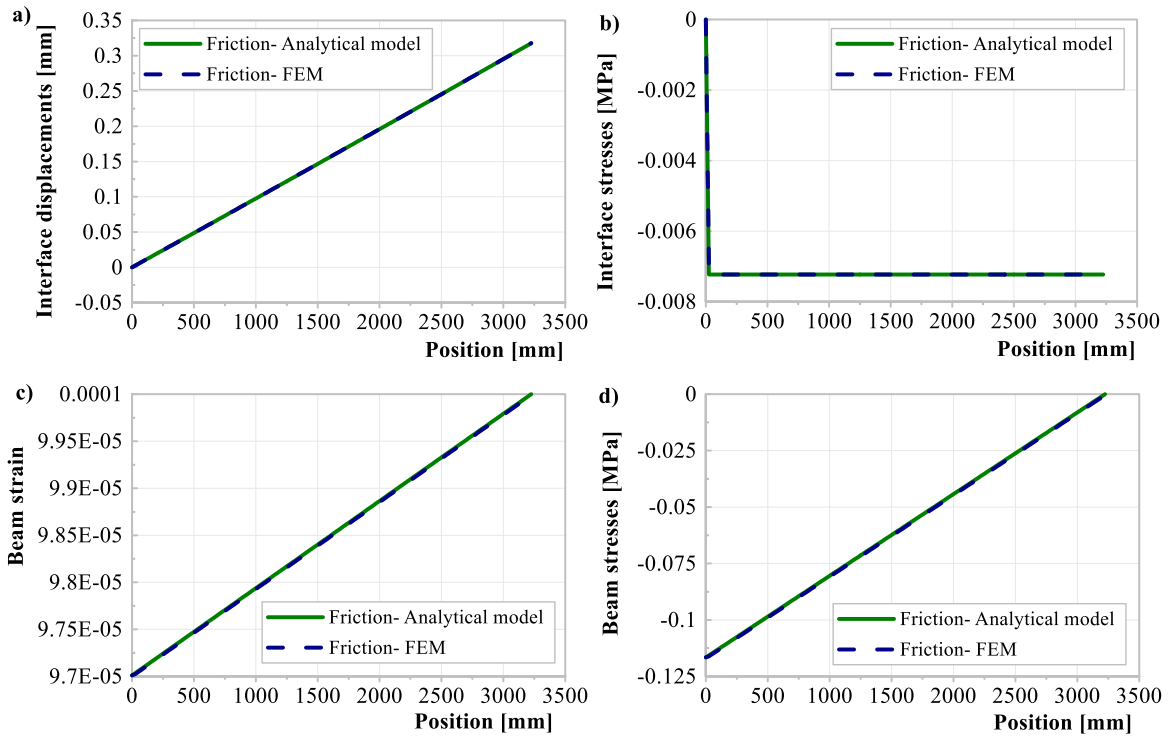


Figure 5.6 Comparison of analytical model and FEM of longitudinal interface with pure friction

5.1.3 Trilinear longitudinal Interface behavior

When the interface damage is considered in the linear elastic model, the trilinear longitudinal interface behavior is then introduced. In this model, the interface could be divided into three phases:

- Phase I: linear elastic behavior
- Phase II: damage evolution with linear softening curve
- Phase III: friction

The shear stresses in three phases could be described as below:

$$\tau(x) = -\text{sgn}[S(x)] \cdot \begin{cases} \frac{\tau_e}{S_e} \cdot |S(x)|, & 0 \leq |S(x)| < S_e \\ \tau_e - \frac{\tau_e - \tau_u}{S_u - S_e} \cdot [|S(x)| - S_e], & S_e \leq |S(x)| < S_u \\ \tau_u, & |S(x)| \geq S_u \end{cases} \quad (5.33)$$

Assume:

$$k_1 = \frac{\tau_e}{S_e}, \quad k_2 = \frac{\tau_e - \tau_u}{S_u - S_e} \quad (5.34)$$

According to the equations (5.3) and (5.7), the equilibrium equation for linear damage evolution phase (i.e. phase II) could be described as

$$\frac{d^2 S(x)}{dx^2} = \frac{1}{EA} \cdot \text{sgn}[S(x)] \cdot [\tau_e - k_2(|S(x)| - S_e)] \quad (5.35)$$

The above equation could be transformed as

$$\frac{d^2 S(x)}{dx^2} + \frac{k_2}{EA} \cdot S(x) = \text{sgn}[S(x)] \cdot \frac{\tau_e + k_2 S_e}{EA} \quad (5.36)$$

Assume

$$\beta = \sqrt{\frac{k_2}{EA}} \quad (5.37)$$

The homogeneous solution of the equation (5.36) is

$$S_h(x) = C_1 \cdot \cos \beta x + C_2 \cdot \sin \beta x \quad (5.38)$$

Assume a particular solution of the equation (5.36) is

$$S_p(x) = P \quad (5.39)$$

Substitute P into the equation (5.36)

$$0 + \frac{k_2}{EA} \cdot P = \text{sgn}[S(x)] \cdot \frac{\tau_e + k_2 S_e}{EA} \quad (5.40)$$

As a result

$$P = \text{sgn}[S(x)] \cdot \left(\frac{\tau_e}{k_2} + S_e \right) \quad (5.41)$$

When $\Delta T > 0$, the beam expands and $S(x) > 0$, resulting $\text{sgn}[S(x)] = 1$; on the other hand, when $\Delta T < 0$, the beam shrinks and then $S(x) < 0$, leading $\text{sgn}[S(x)] = -1$. Considering only half of the system where $x > 0$, the above equation could be substituted with the following expression

$$P = \text{sgn}(\Delta T) \cdot \left(\frac{\tau_e}{k_2} + S_e \right) \quad (5.42)$$

The solution for the equation (5.36) is a sum of the homogeneous and particular solutions

$$S(x) = S_h(x) + S_p(x) = C_1 \cdot \cos \beta x + C_2 \cdot \sin \beta x + P \quad (5.43)$$

Based on the equations (5.3) and (5.6), beam strain for damage phase could be expressed as

$$\varepsilon(x) = \dot{S}(x) = \beta(C_2 \cdot \cos \beta x - C_1 \cdot \sin \beta x) \quad (5.44)$$

As long as the interface slip in linear elastic phase (Phase I) reaches maximum elastic slip S_e , the interface turns into damage evolution phase (Phase II). The position where linear elastic phase turns into linear damage evolution phase is defined as x_{se} . Similarly, position where linear damage evolution phase (Phase II) turns into friction phase (Phase III) is defined as x_{su} . As a result, interface displacements with trilinear behavior under uniform temperature could be expressed in three phases as

$$S(x) = \begin{cases} C1 \cdot e^{\lambda x} + C2 \cdot e^{-\lambda x}, & 0 \leq x < x_{se} \text{ (Phase I);} \\ C3 \cdot \cos \beta x + C4 \cdot \sin \beta x + P, & x_{se} \leq x < x_{su} \text{ (Phase II);} \\ \operatorname{sgn}(\Delta T) \frac{\tau_u}{2EA} \cdot x^2 + C5 \cdot x + C6, & x_{su} \leq x < L/2 \text{ (Phase III).} \end{cases} \quad (5.45)$$

The beam strain could then also be displayed in three phases as

$$\varepsilon(x) = \begin{cases} \lambda(C1 \cdot e^{\lambda x} - C2 \cdot e^{-\lambda x}), & 0 \leq x < x_{se} \text{ (Phase I);} \\ \beta(C4 \cdot \cos \beta x - C3 \cdot \sin \beta x), & x_{se} \leq x < x_{su} \text{ (Phase II);} \\ \operatorname{sgn}(\Delta T) \frac{\tau_u}{EA} \cdot x + C5, & x_{su} \leq x < L/2 \text{ (Phase III).} \end{cases} \quad (5.46)$$

In order to solve the undetermined parameters, the following BCs are given in this case

$$2 \text{ Phases} \begin{cases} S(0) = 0 \\ S_I(x_{se}) = \operatorname{sgn}(\Delta T) S_e \\ S_{II}(x_{se}) = \operatorname{sgn}(\Delta T) S_e \\ \varepsilon_I(x_{se}) = \varepsilon_{II}(x_{se}) \\ \varepsilon_{III}(L/2) = \alpha_T \cdot \Delta T \end{cases} \quad \text{and} \quad 3 \text{ Phases} \begin{cases} S(0) = 0 \\ S_I(x_{se}) = \operatorname{sgn}(\Delta T) S_e \\ S_{II}(x_{se}) = \operatorname{sgn}(\Delta T) S_e \\ \varepsilon_I(x_{se}) = \varepsilon_{II}(x_{se}) \\ S_I(x_{su}) = \operatorname{sgn}(\Delta T) S_u \\ S_{II}(x_{su}) = \operatorname{sgn}(\Delta T) S_u \\ \varepsilon_{II}(x_{su}) = \varepsilon_{III}(x_{su}) \\ \varepsilon_{III}(L/2) = \alpha_T \cdot \Delta T \end{cases} \quad (5.47)$$

The unknown parameters have the same amount with the equations of BCs. Thus, the undetermined parameters could be solved. All the parameters in equation (5.45) are summarized in Table 5.1.

Table 5.1 Summary of the calculation parameters for longitudinal interface behavior

$k_1 = \frac{\tau_e}{S_e}$	$k_2 = \frac{\tau_e - \tau_u}{S_u - S_e}$
$\lambda = \sqrt{\frac{k_1}{EA}}$	$\beta = \sqrt{\frac{k_2}{EA}}$
$P = \operatorname{sgn}(\Delta T) \cdot \left(\frac{\tau_e}{k_2} + S_e\right)$	$C1 = \frac{\operatorname{sgn}(\Delta T) S_e}{2 \sinh(\lambda x_{se})} = A(x_{se})$
$C2 = -A(x_{se})$	$C3 = \frac{\beta [\operatorname{sgn}(\Delta T) S_e - P] \cot(\beta x_{se}) - \lambda \operatorname{sgn}(\Delta T) S_e \coth(\lambda x_{se})}{\beta [\cos(\beta x_{se}) \cot(\beta x_{se}) + \sin(\beta x_{se})]} = B(x_{se})$
$C4 = \frac{\operatorname{sgn}(\Delta T) S_e - P - B(x_{se}) \cos(\beta x_{se})}{\sin(\beta x_{se})} = C(x_{se})$	$x_{su} = \frac{1}{\beta} \left[\arccos \frac{\operatorname{sgn}(\Delta T) S_u - P}{\sqrt{B(x_{se})^2 + C(x_{se})^2}} + \arctan \frac{C(x_{se})}{B(x_{se})} \right] = D(x_{se})$
$C5 = \alpha_T \cdot \Delta T - \operatorname{sgn}(\Delta T) \frac{\tau_u L}{2EA}$	$C6 = \operatorname{sgn}(\Delta T) S_u - C5 \cdot D(x_{se}) - \operatorname{sgn}(\Delta T) \frac{\tau_u}{2EA} D(x_{se})^2 = E(x_{se})$

In Table 5.1, all the unknown parameters except C5 are described as a function of x_{se} . The position x_{se} where interface turning from Phase I into Phase II could be resolved using equation $\varepsilon_{II}(x_{su}) = \varepsilon_{III}(x_{su})$:

$$\beta \{C(x_{se}) \cdot \cos[\beta D(x_{se})] - B(x_{se}) \cdot \sin[\beta D(x_{se})]\} = \operatorname{sgn}(\Delta T) \frac{\tau_u}{EA} D(x_{se}) + C5 \quad (5.48)$$

Thus, all the unknown parameters could be determined. Substituting the equation (5.45) to equation (5.33), stresses at interface are determined. The stresses and strains in the beam can then be expressed according to the equations (5.5) and (5.22) as follows

$$\sigma(x) = \frac{1}{A} \int -\tau(x) dx \quad (5.49)$$

$$\varepsilon(x) = \alpha_T \Delta T + \frac{\sigma(x)}{E} \quad (5.50)$$

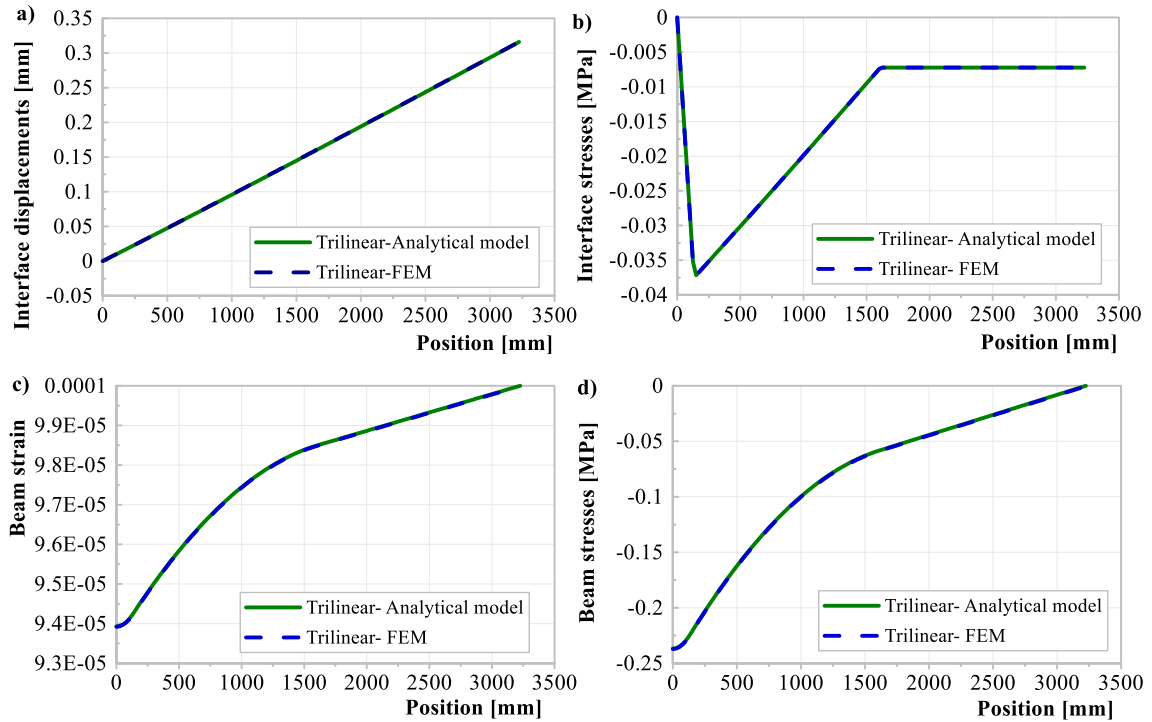


Figure 5.7 Comparison of analytical model and FEM of trilinear longitudinal interface

The result comparison between FEM and analytical model under uniform temperature variation $\Delta T = 10 K$ is presented in Figure 5.7. Same as above, the two models agree with each other. The interface displacement increases monotonously along the beam length from symmetric axis to beam end. Meanwhile, compared to the linear interface behavior, the maximum interface displacement at slab end of the trilinear interface behavior increases from 0.15 mm to 0.32 mm due to the interface damage and its restraint diminish. The interface stress exhibits nevertheless a trilinear variation along the length because of interface damage.

5.1.4 Calculation algorithms with Matlab

Different amplitude of uniform temperature variations could lead to different interface states, i.e. the whole interface could in a linear elastic state, trilinear with 2-phases state or trilinear with 3-phases state. For interface under uniform temperature variations, the maximum longitudinal interface displacement occurs at beam end. Thus, the deformation of the beam end could be used to determine the interface state under a certain uniform temperature variation. The following Figure 5.8 summarized the calculation algorithms for longitudinal interface behavior under uniform temperature variations. Various BCs are also given in the figure for corresponding interface states.

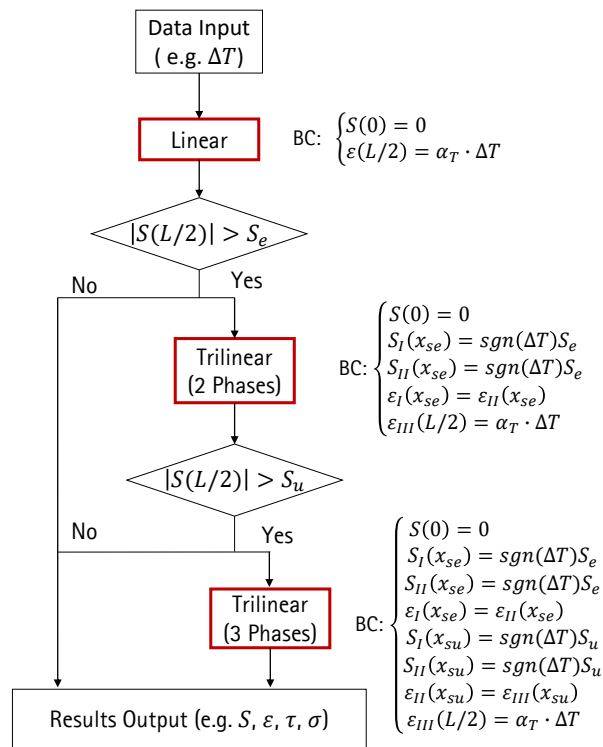


Figure 5.8 Flowchart of algorithms for longitudinal interface behavior under uniform temperature variations

5.2 Finite element models

In this thesis, the example of continuous slab track (i.e. CRTS II) is chosen for the interface analysis under temperature variations. The geometry of the prefabricated slab of CRTSII in is used in the analysis. Linear elastic properties are applied to concrete and CAM.

Table 5.2 Geometry and material properties of the prefabricated slab of CRTSII

Length (L) [mm]	Width (b) [mm]	Thickness (t) [mm]	Density (ρ) [kg/m ³]	Elastic modulus (E) [MPa]	Thermal coefficient (α_T) [K ⁻¹ or °C ⁻¹]
6450	2550	200	2500	39000	1×10 ⁻⁵

As described in chapter 4.5, the interface fracture parameters could be determined with inverse analysis based on experiments. Table 4.11 gives a suggested fracture parameters for interface between concrete and CAM with exponential softening behavior. To simplify, these parameters could be recalculated into ones with linear softening (given the same fracture energy) meanwhile the corresponding stress-slip relationship for longitudinal interface resistance could also then be determined in Table 5.3.

Table 5.3 Suggested fracture parameters for interface between concrete and CAM with linear softening behavior in Mode II/III and corresponding stress-slip relationship for longitudinal interface resistance

K_{SS} [MPa/mm]	δ_m^0 [mm]	δ_m^f [mm]	G_f [N/mm]	μ
3	0.0125	0.1555	2.68×10 ⁻³	1.475
τ_e [MPa]	τ_u [MPa]	S_e [mm]	S_u [mm]	
0.0375	0.00723	0.0125	0.1555	

It's easy to find that

$$\tau_e = K_{ss} \cdot \delta_m^0 \quad \text{and} \quad \tau_u = \rho g t \cdot \mu \quad (5.51)$$

The maximal elastic displacement $S_e = \delta_m^0$ and maximal elastic-damage displacement $S_u = \delta_m^f$.

5.2.1 1D models

In the 1D FEM, the interface behavior is modeled with Cartesian connector elements in Abaqus/Standard. The connector elements are discretely joined to the beam, while representing the continuous interface resistance. Thus, the mesh size of the beam has to be considered when specifying the linear or nonlinear properties of the connectors, so that one connector element imitates the interface behavior of its nearby area dependent on the mesh size. The connector stiffness of 1D FEM in longitudinal direction (denoted as k_1^{1D}) and vertical direction (denoted as k_2^{1D}) are thus expressed as

$$k_1^{1D} = K_{ss} \times b \times Meshsize = \tau_e \times b \times Meshsize / \delta_m^0 \quad (5.52)$$

$$k_2^{1D} = K_{nn} \times b \times Meshsize = \sigma_{max} \times b \times Meshsize / \delta_m^0 \quad (5.53)$$

The centric loading models, where the interface resistance reacts along the beam axis, have same results with analytical models developed in chapter 5.1. Nevertheless, the interface actually gives resistance only at bottom edge, which produces an eccentric loading of the beam. Euler-Bernoulli beam with element type B33 and Timoshenko beam with element type B31 are available in Abaqus. Timoshenko beam could provide a more accurate results due to its shear flexibility. In this case, no big difference between Euler-Bernoulli beam and Timoshenko beam is found. Timoshenko beam is still chosen to use in the 1D FEM. Rigid beams, whose two ends are tied to the Timoshenko beam and Cartesian connector elements respectively, are used to simulate the eccentric loading of interface resistance, see Figure 5.9.

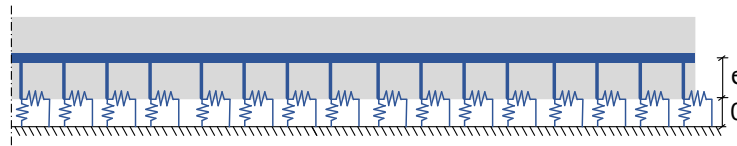


Figure 5.9 Presentation of the 1D eccentric FEM (half system)

Unlike analytical models which only have longitudinal beam deformations under uniform temperature variations, the Timoshenko beam in the 1D eccentric FEM not only deforms longitudinally but also exhibits a flexural deformation for the sake of eccentric loading. The overall longitudinal interface behavior of the beam is then not only influenced by the longitudinal interface resistance but also by the vertical interface resistance. It's easy to assume that the stiffer the vertical interface resistance, the bigger the longitudinal deformation and the closer deformation results of the 1D eccentric FEM to analytical model (or centric loading FEM). Since a stiffer vertical interface stiffness provides a larger restraint in the vertical direction, the deformations caused by volume changes due to temperature would thus be released more in the longitudinal direction instead of vertical direction, vice versa. The longitudinal and vertical interface displacements of the 1D linear eccentric loading FEM (linear longitudinal interface stiffness $K_{ss} = 3 \text{ MPa/mm}$) under uniform temperature variation $\Delta T = 10 \text{ K}$ with consideration of different vertical interface stiffness are demonstrated in the following Figure 5.10.

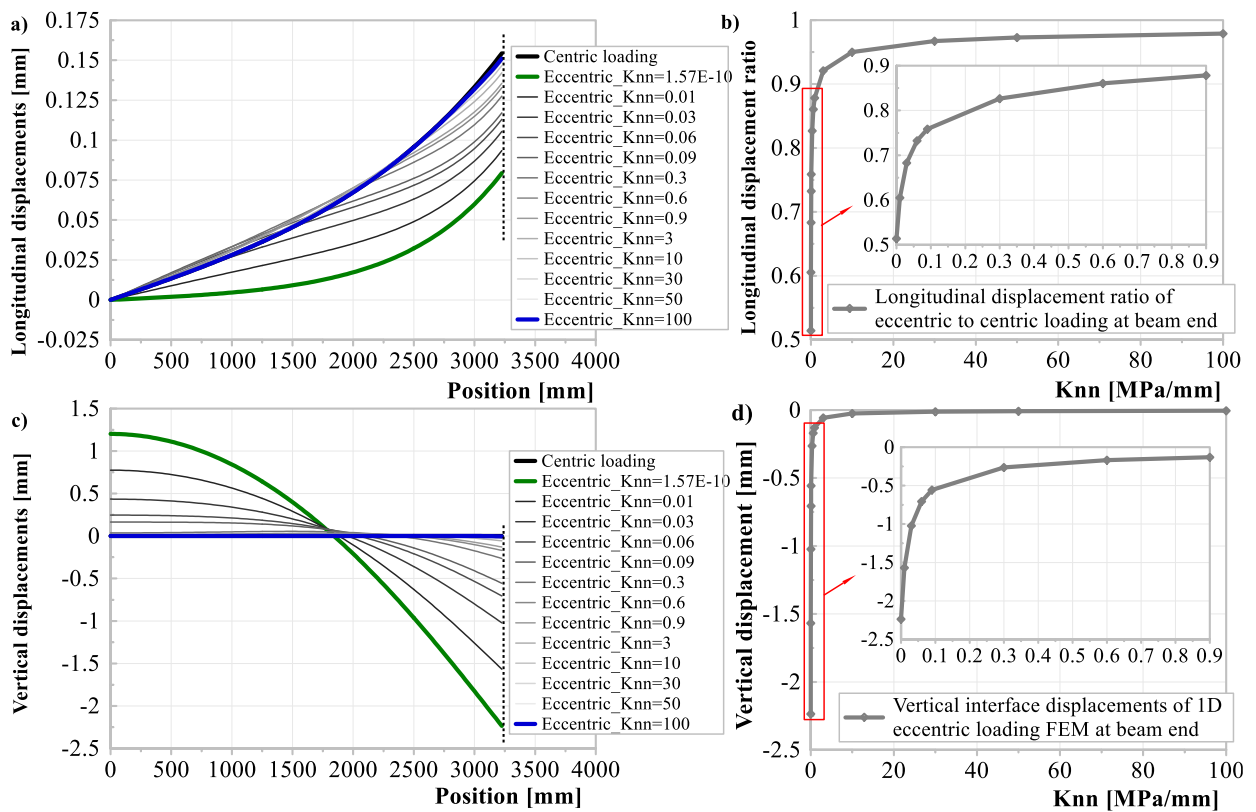


Figure 5.10 Longitudinal and vertical interface displacement of the 1D linear eccentric loading FEM with consideration of various vertical interface stiffness K_{nn} ($\Delta T = 10 K$)

Centric loading model has the largest longitudinal interface displacements without any vertical interface displacements. Due to the eccentricity, bending deformation of the beam and vertical interface displacements occur in the 1D eccentric FEM, which reduces the longitudinal interface displacements. With increasing vertical interface stiffness K_{nn} , the vertical interface displacements decrease and longitudinal interface displacements increase, see Figure 5.10 (a). However, this deformation variation is much more sensitive for the vertical stiffness smaller than 0.9 MPa/mm. The longitudinal displacement ratio of eccentric to centric loading FEM at beam end dramatically increases from 0.51 to 0.88 within the vertical interface stiffness K_{nn} not more than 0.9 MPa/mm, whereas the augmentation of this ratio only increase from 0.88 to 0.98 for K_{nn} from 0.9 to 100 MPa/mm, see Figure 5.10 (b). Similar phenomenon is also found in the vertical direction. Increasing K_{nn} leads to decrease of the vertical displacements and the alteration is much bigger in the range where K_{nn} is smaller than 0.9 MPa/mm, see Figure 5.10 (c) and (d).

The corresponding beam strain and beam section forces (i.e. axial forces, shear forces and moment) are presented in Figure 5.11. The centric loading FEM has the largest beam strain and axial forces, while the beam shear forces and bending moment are equal to zero. Eccentric loading FEM with minimal vertical interface stiffness K_{nn} has in general the smallest beam strain as well as axial forces. With increasing K_{nn} , the beam strain and axial forces also grow, approaching to the results of centric loading. However, the beam shear forces are positively correlated to vertical interface stiffness. The eccentric loading beam with minimal K_{nn} has the smallest shear forces, nevertheless it has the biggest bending moment, also indicating a largest flexural deformation of the beam. Bending moment decreases as the K_{nn} increases.

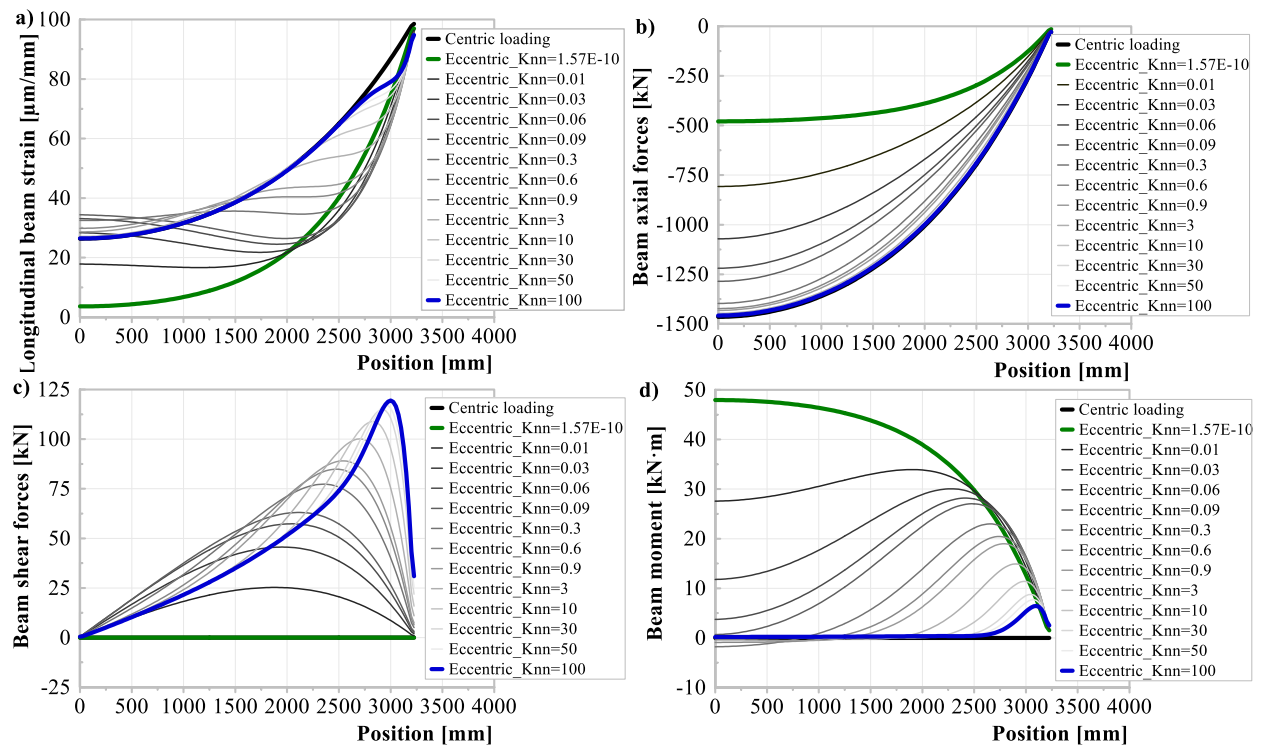


Figure 5.11 Beam strain and section forces of the 1D linear eccentric loading FEM with consideration of various vertical interface stiffness K_{nn} ($\Delta T = 10 K$)

The above discussions are based on linear interface behavior in both longitudinal and vertical directions, where no damage is considered. In reality, interface would deteriorate upon certain criterions. Therefore, the influence of eccentricity on trilinear longitudinal interface behavior should be argued. Figure 5.12 shows the longitudinal and vertical interface displacement of 1D eccentric FEM with trilinear longitudinal behavior under uniform temperature variation $\Delta T = 10 K$ taken into consideration of various interface vertical stiffness K_{nn} . The longitudinal interface parameters are listed in Table 5.3.

It could be seen that the interface vertical stiffness K_{nn} has a much smaller impact on the longitudinal displacements of trilinear interface model than linear interface model. The longitudinal displacement ratio of eccentric to centric loading FEM at beam end increases from 0.928 to 0.995 within the vertical interface stiffness K_{nn} not more than 0.10625 MPa/mm, whereas the variation of this ratio is from 0.514 to 0.769 for linear interface model. In general, the longitudinal displacements increase and vertical displacements decrease in trilinear interface model compared with linear interface model. It's because that the interface degradation reduces the restraint in longitudinal direction and the deformation would thus release more in the longitudinal direction instead vertical direction. In another word, when the longitudinal interface damages, the vertical interface stiffness is then relatively "increases", resulting more deformation in longitudinal direction. Thus, the phenomenon in the trilinear interface model has actually the same mechanism background with the linear interface model. Moreover, the longitudinal interface displacement is much less sensitive to vertical stiffness K_{nn} in trilinear interface model than in the linear one.

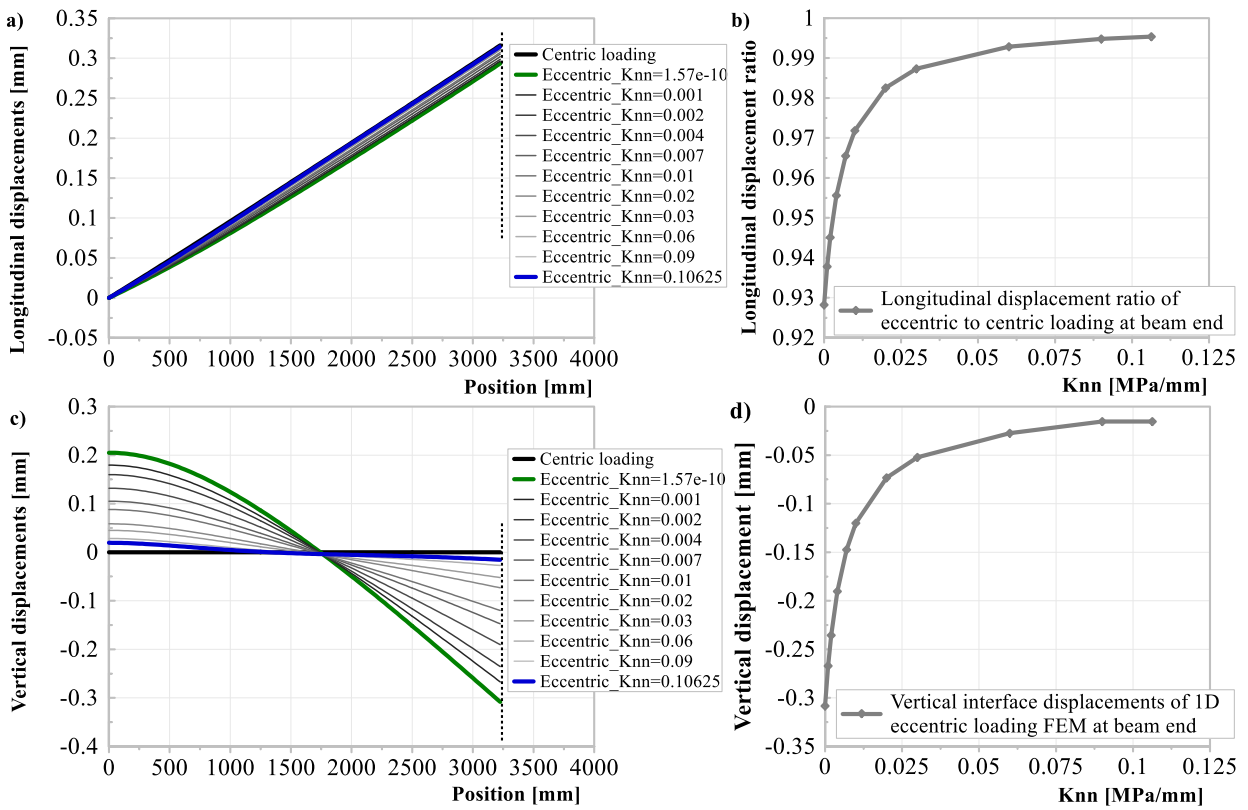


Figure 5.12 Longitudinal and vertical interface displacement of the 1D eccentric loading FEM with trilinear longitudinal behavior taken into consideration of various vertical interface stiffness K_{nn} ($\Delta T = 10 K$)

5.2.2 2D models

For the simulation of a 2DFEM, there are two ways to simulate the interface behavior, i.e. with connector elements same as in 1DFEM or with contact based CZM, see Figure 5.13.

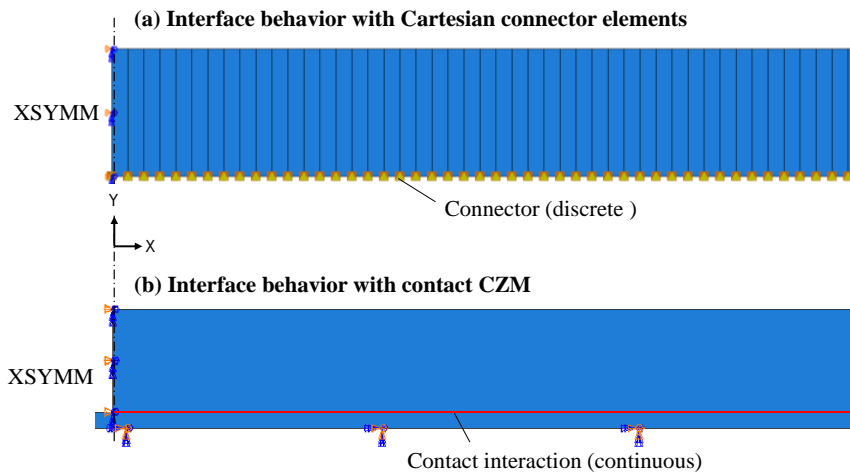


Figure 5.13 Simulation methods of interface behavior in 2DFEM (half system)

Same with 1DFEM, the interface behavior could be defined by linear or nonlinear elastic behavior of the Cartesian connector elements in longitudinal and vertical directions. An alternative is to simulate the interface

behavior with contact CZM. The biggest difference is that the interface behavior with connector elements could only be discretely modeled while the CZM has a continuous characteristic. Thus, proper mesh sizes should be considered in the model with connector elements.

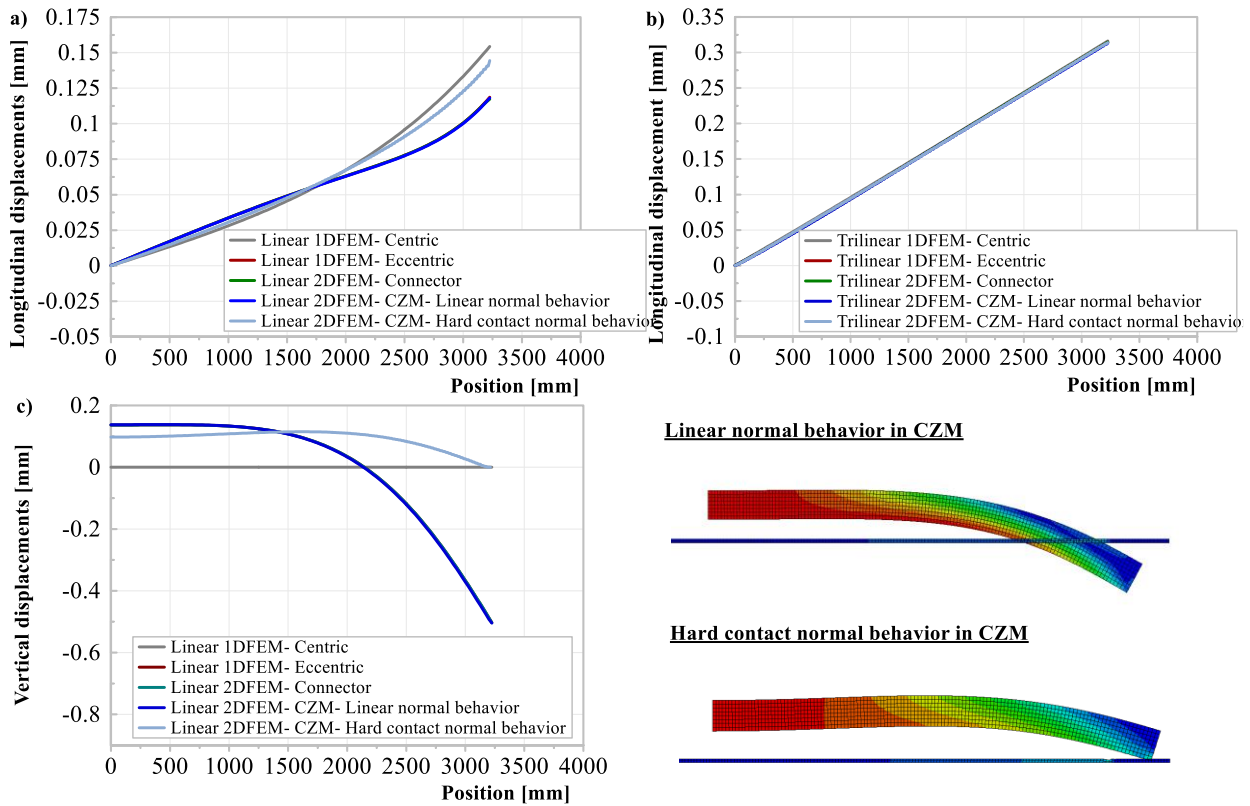


Figure 5.14 Longitudinal and vertical displacements of linear and trilinear 2DFEM ($\Delta T = 10K$)

The longitudinal and vertical displacements of 2DFEM are demonstrated in Figure 5.14. It could be seen that the linear 2DFEM with connector elements has almost the same results as the eccentric loading 1DFEM where the connector elements are also used to discretely simulate the interface behavior. In the linear 2DFEM with CZM, the cohesive stiffness K_{nm} in Mode I represents the vertical interface stiffness when the contact is "open". The interface behavior under compression are defined by contact normal behavior when the contact is "close" (see chapter 3.3.3.4). To make a linear vertical interface behavior in both tension and compression of CZM same as the one with linear connector elements, the linear contact normal behavior should be defined with a very small stiffness such as $K_{norm} = 0.00001 \text{ MPa/mm}$, while the cohesive stiffness in Mode I K_{nm} equals to 0.10625 MPa/mm which corresponds to the linear vertical stiffness of the FEM with connector elements. The interface displacement results in this case are then same with the 2DFEM with connector elements.

In reality, the sub-plate could provide a supportive foundation for the upper-plate, which prevents large negative vertical displacements. The stiffer the sub-plate material, the smaller the negative vertical interface displacements. When the hard contact normal behavior is chosen, the vertical interface displacements will generally decrease and longitudinal displacements could thus increase. However, when interface damage in longitudinal direction is considered, the interface displacements are almost the same in all the above discussed models, see Figure 5.14 b). This is because that vertical interface stiffness relative to longitudinal interface stiffness becomes bigger in this case compared to the undamaged interface, the vertical displacements are so small that it has almost no influence on the longitudinal displacements.

5.2.3 3D models

The study based on 1D and 2D models shows slab deformation in longitudinal and vertical directions. However, the slab deformations or interface displacements deform also in horizontal direction, i.e. along slab width. This may have an interactive influences on the longitudinal and vertical deformations. Thus 3D models are needed to learn the whole slab deformation information. For the sake of symmetry, quarter of the slab system is simulated in the model. Figure 5.15 displays the simulation results of the linear 3DFEM with cohesive stiffness in Model I $K_{nn} = 0.10625 \text{ MPa/mm}$ and cohesive stiffness in Mode II $K_{ss} = 3 \text{ MPa/mm}$ under uniform temperature variation $\Delta T = 10^\circ\text{C}$. In this case, the linear normal behavior of CZM is used in the 3DFEM.

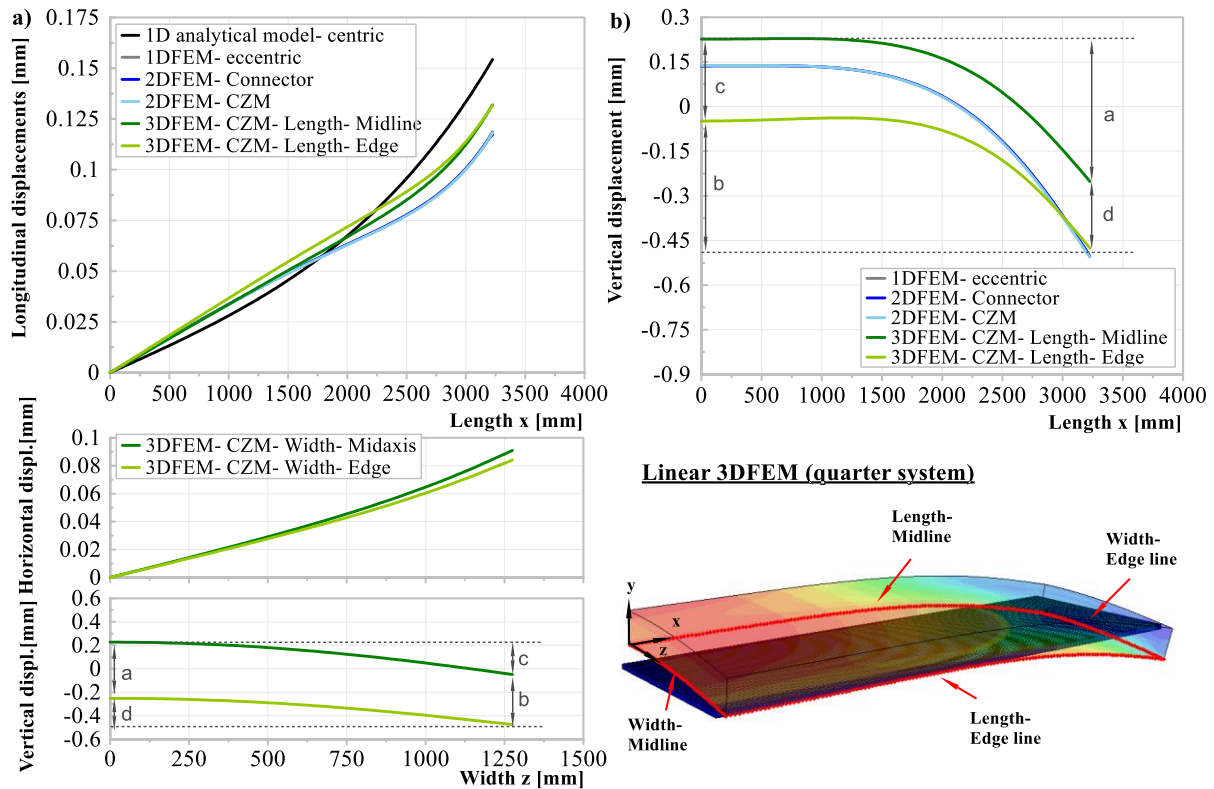


Figure 5.15 Longitudinal, vertical and horizontal interface displacements of linear 3DFEM ($\Delta T = 10\text{K}$)

The four edges of the contact surface of the quarter system (i.e. midline and edge line of the slab along length as well as midline and edge line of the slab along width) are chosen to study the interface displacements. It could be observed that the longitudinal deformation of the midline and edge line along the length are ultimately the same despite of the small scatter. What's more, they are larger than the final total longitudinal displacements in 2DFEM with CZM, while the midline has a very close result with the 2DFEM in the middle area and scatter gets larger at end of the slab.

The vertical interface displacement curve of 2DFEM along the length lays in the middle of the midline and edge line curves of 3DFEM. The vertical displacement differences of the midline along the length $a=0.478 \text{ mm}$ [Figure 5.15 b)] corresponds to the displacement differences between midline and edge line along width at symmetric axis $z=0 \text{ mm}$ [Figure 5.15 c) - bottom diagram]. And the vertical displacement differences of the midline along the width $c=0.274 \text{ mm}$ [Figure 5.15 c) - bottom diagram] corresponds to the displacement differences between midline and edge line along length at symmetric axis $x=0 \text{ mm}$ [Figure 5.15 b)]. The same correlation goes also for the vertical displacement difference of edge line along length $b=0.427 \text{ mm}$ or along

width $d=0.224$ mm. It could also be found that the vertical displacements of the midline are larger than the edge line along both length and width. This may be because that the longitudinal restraint degree at midline is higher than the edge line and the deformations are somehow more restraint along midline in longitudinal direction, thus go to the vertical direction. Details about restraint degree will be discussed in chapter 5.3.

Since the width of the slab is considered in 3DFEM, there exists also a horizontal displacements along slab width [Figure 5.15 c) - upper diagram]. Despite small scatter, the horizontal displacement curves of the midline and edge line along width are generally the same. Here the midline along width has larger displacements in both horizontal and vertical direction. It may owe to the limitation of longitudinal displacements at this axis that the deformations here could only go to horizontal and vertical direction, while the deformations at edge side have the possibility in three directions.

5.3 Parameter study

In the above analysis, analytical models with consideration of linear, pure friction and trilinear interface behavior are developed and the results of analytical models have a very good accordance with the 1D centric FEM. However, the interface reacts only at the bottom side of the slab and thus introduces an eccentricity in the system. Therefore, 1D eccentric FEM are used to study the eccentricity. The connector elements are utilized in 1DFEM to mimic the interface behavior. 2DFEM with connector elements are firstly studied and compared with 1D eccentric FEM. Their results are in accordance with each other. Since the connector elements could only discretely simulate the interface behavior and also cost much trivial work in setting the connector elements at corresponding points, CZM provides a very good alternative to connector elements. Thus 2DFEM with CZM is studied and compared with 2DFEM with connector elements. Finally, 3DFEM with CZM is modelled, see Figure 5.16.

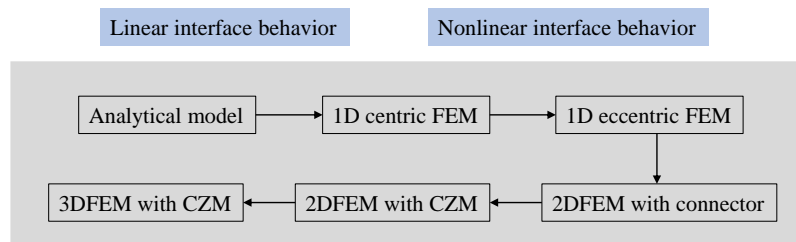


Figure 5.16 Analysis models for concrete-to-concrete interface behavior

It could be found that the eccentricity could produce vertical interface displacements but reduce the longitudinal interface displacements. With increasing vertical interface stiffness, the longitudinal displacements of eccentric models approach to the centric models (Figure 5.10). What's more, the models of nonlinear interface behavior with consideration of damage have much smaller scatter between centric loading model and eccentric loading model with various vertical interface stiffnesses (Figure 5.12). 2DFEM with CZM could slightly increase the longitudinal interface displacements relative to the one with connector elements. 3DFEM with CZM also has slightly larger longitudinal displacements than 2DFEM meanwhile the midline of the slab along length in 3DFEM have closer results with the 2DFEM than the edge line in 3DFEM (Figure 5.15).

In general, the 1D centric model (i.e. analytical model) has the largest longitudinal deformation under uniform temperature variation and the centric models are actually the most unfavorable case with regard to the longitudinal displacements. Thus, for the study of longitudinal interface behavior, the analytical models with a centric loading are on the safe side for practical applications. The following analysis will thus mainly be based on analytical models.

5.3.1 Interface parameter study

In the following Figure 5.17, interface shear stress, beam axial stress, degree of restraint as well as interface damage scalar under various uniform temperature variations are displayed. Different phases (i.e. linear elastic, damage evolution and friction phases) of interface could be observed in the diagram of interface shear stresses. The positive temperature variation leads to elongation of the beam while the negative variation cause beam shortening. The absolute deformations are nevertheless the same under positive and negative temperature variations with same the absolute value, which goes the same for beam axial stress. The beam axial stress at end side equals to zero since the restraint at beam end is free and it reaches the maximum value at mid axis due to its largest restraint degree at this location. It could also be observed that the axial stresses at mid axis firstly increase with increasing temperature variation and then decrease due to the interface degradation. The total resistant forces at interface decrease when the damage occurs to a certain extent.

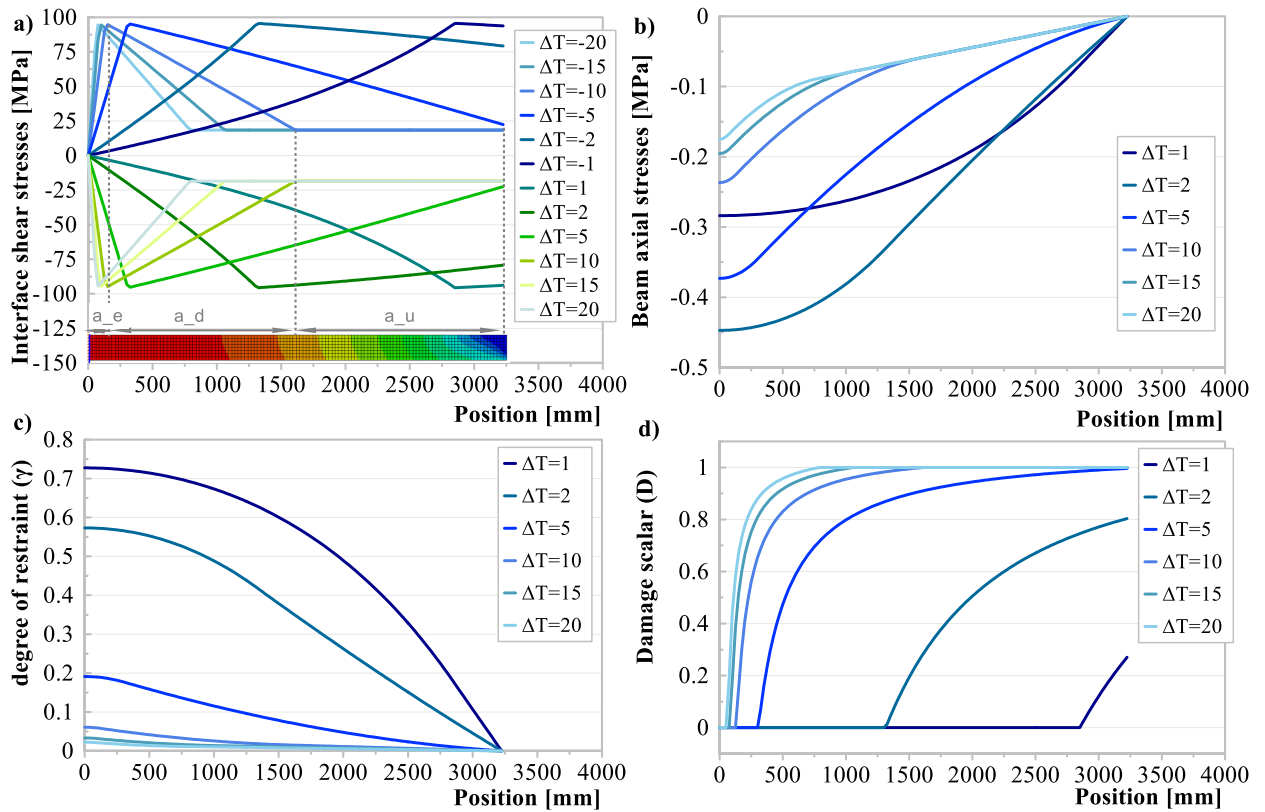


Figure 5.17 Longitudinal interface behavior under various uniform temperature variation

According to equation (2.19), the degree of restraint under in this case could be express as

$$\gamma(\sigma) = \frac{\sigma}{-E\alpha_T\Delta T} \quad (5.54)$$

While the interface damage scalar in an interaction of adhesive bonding and friction could be determined based on equation (3.31) as

$$D(S, \tau) = \frac{k_1 \cdot S - \tau}{k_1 \cdot S - \tau_u} = \frac{\tau_e S - \tau S_e}{\tau_e S - \tau_u S_e} \quad (5.55)$$

The restraint degree at beam end equals to zero owing to the free restraint at this location. Although there exists no deformation at mid axis, the beam strain here is not zero, thus restraint degree at mid axis could not be 1. Nevertheless, the degree of restraint amounts to a maximum value at mid axis, which may be caused by an "accumulated effects" of whole interface restraint. With increasing degree of restraint, the interface displacements (or beam deformation) decrease given the same temperature variation. On the other hand, interface damage scaler shows the stiffness degradation at a certain spot. In general, the severer the interface damages, the lower the degree of restraint. However, although the damage scalar at mid-axis keeps zero (i.e. undamaged), the restraint degree here could still decrease for the sake of whole interface damage effects. Thus, degree of restraint at mid-axis could somehow represent the restraint effect as well as resistance ability from whole interface. While the damage scalar reflects more about locally interface deterioration extent.

In order to study the influences of different interface parameters on the interface degradation, following stress-slip curves are applied in the model. Stress-slip relationships in Figure 5.18 (a) are used to learn the impacts of elastic stiffness k_e and maximum elastic slip S_e (or maximum elastic stress τ_e) while the curves in Figure 5.18 (b) are adopted to survey the influences of damage evolution rate k_d and maximum damage slip S_u (or residual friction stress τ_u).

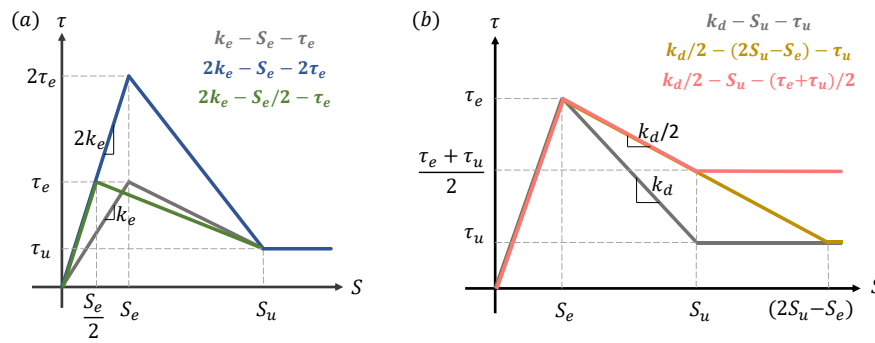


Figure 5.18 Presentation of studied longitudinal interface parameters

Figure 5.19 shows the influences of interface parameters on degree of restraint at mid-axis and length of different phases (i.e. length of elastic phase a_e , damage phase a_d and friction phase a_u) under increasing temperature variations. It could be found that elastic stiffness k_e decides the degree of restraint γ when the whole interface is elastic phase. Once damage occurs at interface, degree of restraint at mid-axis decreases. Strength τ_e has a more crucial influence on the degradation of the degree of restraint than interface stiffness k_e . Increasing the interface stiffness while keeping strength unchanged has insignificant impact on the interface damage, which even slightly aggravate the shortening of linear interface length a_e . Whereas, remaining stiffness while increasing strength would alleviate the degradation of degree of restraint. This is because that the maximum elastic slip S_e determines the initiation of damage and thus influences the resistance ability of the interface restraint. Keeping S_e unchanged, increasing stiffness k_e has a positive influence on the interface damage. However, even the stiffness k_e is increased, the maximum elastic slip S_e decreases given the same strength τ_e , which leads to a negative effects on the interface degradation. What's more, residual friction τ_u determines the end value, to which restraint degree approaches. The smaller the damage evolution rate k_d , the slower the degree of restraint γ approaches to the end value.

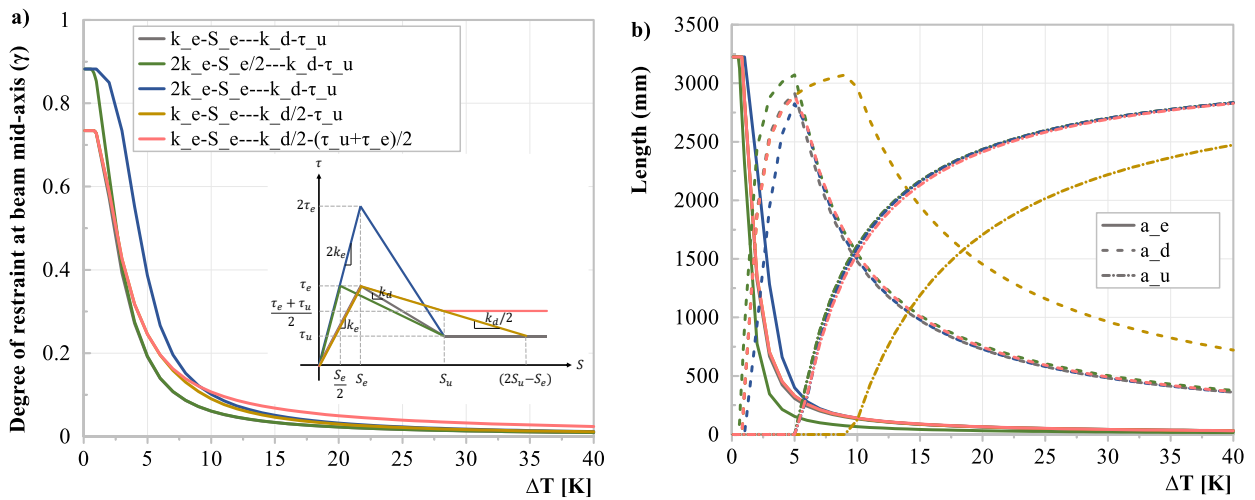


Figure 5.19 Influence of longitudinal parameters on degree of restraint and different phase lengths

With increasing temperature variation, interface length in linear phase a_e decreases monotonously, while damage length a_d increases first and then decreases when friction phases appears. Friction length a_u increases monotonously. The interface stiffness k_e and maximum elastic slip S_e together influence the reduction of elastic length. Whereas the maximum damage slip S_u mainly determines the initiation of friction phases.

5.3.2 Limit value study

For a safe application of interfacial bonded slab, the interface should be undamaged under external forces. In this case, the longitudinal interface behavior should stay in linear elastic phase under uniform temperature variation. In EN 1991-1-5 [148] chapter 6.1.3, the characteristic value of the maximum contraction ($\Delta T_{N,con}$) and expansion ($\Delta T_{N,exp}$) range of the uniform temperature component should be taken as

$$\begin{cases} \Delta T_{N,con} = T_0 - T_{e,min} \\ \Delta T_{N,exp} = T_{e,max} - T_0 \end{cases} \quad (5.56)$$

where T_0 refers to the initial temperature of a structure element and may be taken as 10°C if no information is available. The minimal ($T_{e,min}$) and maximum ($T_{e,max}$) uniform structure temperature components could be determined for concrete slab (Type 3) as

$$\begin{cases} T_{e,min} = T_{min} + 8 \\ T_{e,max} = T_{max} + 2 \end{cases} \quad (5.57)$$

where T_{max} and T_{min} denote maximum and minimum shade air temperature with an annual probability of being exceeded of 0.02 (equivalent to a mean return period of 50 years) based on the minimum hourly values recorded. In the national annex, T_{max} could be specified by 37°C and T_{min} by -24°C. As a results, the expansion range of uniform temperature component $\Delta T_{N,exp}$ with a value of 29 K is decisive here, see following:

$$\begin{cases} \Delta T_{N,con} = T_0 - T_{e,min} = 10 - (T_{min} + 8) = 2 - (-24) = 26 \text{ K} \\ \Delta T_{N,exp} = T_{e,max} - T_0 = (T_{max} + 2) - 10 = 37 - 8 = 29 \text{ K} \end{cases} \quad (5.58)$$

The whole interface should be in elastic phase under maximum uniform temperature variation, which means the interface displacement at slab end should be no bigger than maximum elastic slip S_e . Thus, the serviceability limit state of the interface could be expressed as

$$S\left(\frac{L}{2}\right) = \frac{\alpha_T \Delta T \cdot \sinh \frac{\lambda L}{2}}{\lambda \cdot \cosh \frac{\lambda L}{2}} = \frac{\alpha_T \Delta T}{\lambda} \tanh \frac{\lambda L}{2} = S_e(k, L) \quad (5.59)$$

The following Figure 5.20 demonstrates the lower limit surface curve of longitudinal interface behavior under uniform temperature variation. The longer the slab length L is and the smaller the interface stiffness k is, the larger the limit maximum elastic slip S_e is. For longer slab length, the interface stiffness has larger influence on the limit maximum elastic slip. For example the limit S_e with stiffness 2.9 and 10 MPa/mm for a 1 m slab length are 0.141 mm and 0.131 mm, whereas the limit S_e for 7 m slab length are 0.460 mm and 0.256 mm respectively. The limit maximum elastic slip scatter is bigger for longer slab. However the differences between $S_e - k$ curves of various slab lengths become smaller with increasing slab length.

For a slab length of 6.45 m with a shear interface stiffness of 3 MPa/mm in this case, the lower limit maximum elastic slip S_e should be 0.451 mm. Therefore, reinforcements across the interface should be used in order to obtain the enough resistance. Obviously, the increase of interface stiffness could reduce the required S_e .

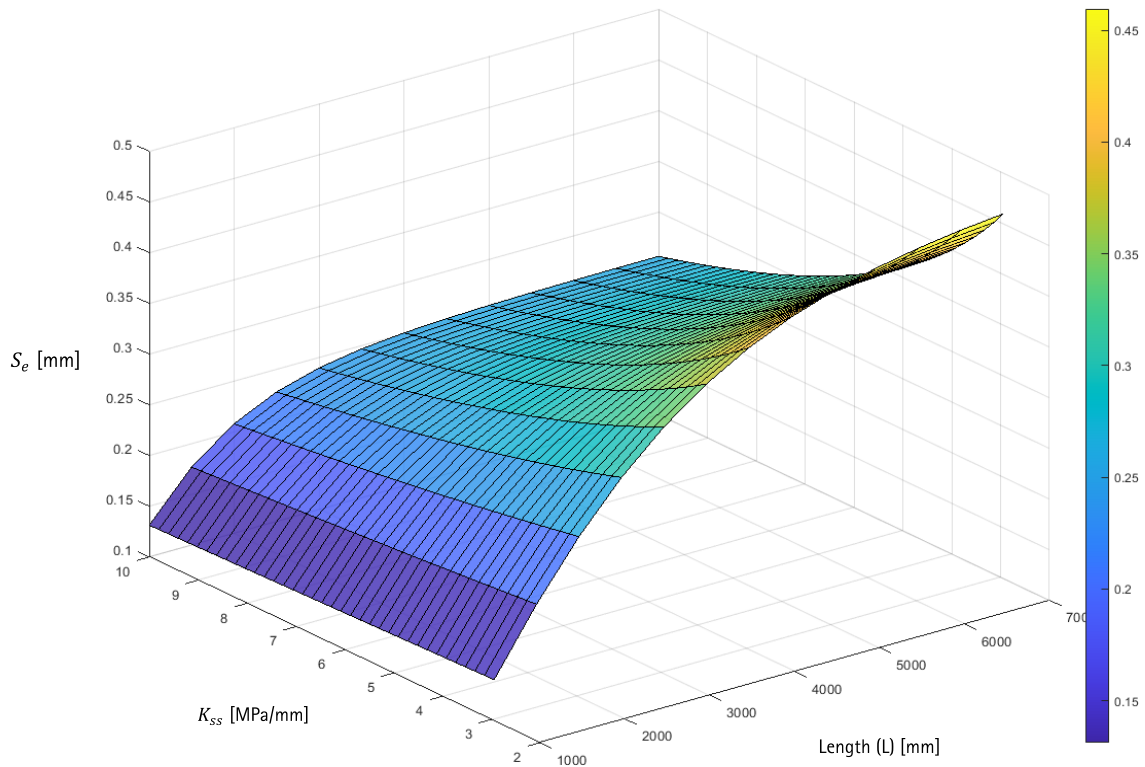


Figure 5.20 The lower limit surface for a fully linear longitudinal interface behavior under uniform temperature variation $\Delta T = 29 K$ (maximum linear displacement S_e as a function of interface shear stiffness K_{ss} and slab length L)

5.4 Summary

In this chapter, longitudinal interface behavior under uniform temperature variations is studied. Analytical models as well as 1D, 2D and 3DFEM are used to investigate the interface behavior. At last, parameter studies are also implemented to learn the influences of different interface parameters as well as to explore the interface limit state.

(1) Analytical models

- (a) Analytical models with consideration of linear, pure friction and trilinear interface behavior are developed and the results of analytical models have a very good accordance with the 1D centric FEM.
 - (b) In the results of the model, the end side of the beam has the largest interface displacements. While the interface displacements and stresses at symmetric axis (mid axis) are equal to zero. The interface damage in trilinear behavior leads to a larger interface displacement at slab end compared to the one in linear interface behavior. This is because that the interface degradation causes reduction of restraint and thus increases the thermal deformation of slab.
 - (c) The beam stress induced from deformation restraint has a negative correlation with beam strain, see equation (5.23). Hereby, the beam end is free from interface restraint, thus the beam stress at the end side is zero meanwhile this restraint free side has the largest beam strain. On the other hand, symmetric axis is most restraint from the interface and has therefore smallest beam strain and largest beam stress.
- (2) 1D eccentric FEM
- (a) In the 1D eccentric FEM, rigid beams, whose two ends are tied to the Timoshenko beam and Cartesian connector elements respectively, are used to simulate the eccentric loading of interface resistance.
 - (b) Flexural deformation of the beam and vertical interface displacements occur in the 1D eccentric FEM, which reduces the longitudinal interface displacements. Thus, the overall longitudinal interface behavior of the beam is then not only influenced by the longitudinal interface resistance but also by the vertical interface resistance.
 - (c) The stiffer the vertical interface resistance K_{nn} , the smaller the vertical interface displacements and the bigger the longitudinal displacements as well as the closer deformation results of the 1D eccentric FEM to analytical model (or centric loading FEM). Since a stiffer vertical interface stiffness provides a larger restraint in the vertical direction, the deformations caused by volume changes due to temperature would thus be released more in the longitudinal direction instead of vertical direction, vice versa.
 - (d) However, for shear stiffness K_{ss} of 3 MPa/mm, these deformation variations are much more sensitive for the vertical stiffness smaller than 0.9 MPa/mm.
 - (e) What's more, the interface vertical stiffness K_{nn} has a much smaller impact on the longitudinal displacements of trilinear interface model than linear interface model. It's because that the interface degradation reduces the restraint in longitudinal direction and the deformation would thus release more in the longitudinal direction instead vertical direction. In another word, when the longitudinal interface damages, the vertical interface stiffness is then relatively "increases", resulting more deformation in longitudinal direction.
- (3) 2DFEM
- (a) Interface behavior in 2DFEM could be simulated either with connector elements or contact CZM. The former models the interface discretely while the later has a continuous characteristic.
 - (b) Linear 2DFEM with connector elements has almost the same results as the eccentric loading 1DFEM.
 - (c) To make a linear vertical interface behavior in both tension and compression of CZM same as the one with linear connector elements, the linear normal behavior should be specified by a very small stiffness such as $K_{norm} = 0.00001 \text{ MPa/mm}$, while the cohesive stiffness in Mode I K_{nn} should be defined corresponding to the linear vertical stiffness in FEM with connector elements. The interface displacement results in this case are then same with the 2DFEM with connector elements.
 - (d) In reality, the sub-plate could provide a supportive foundation for the upper-plate, which prevents large negative vertical displacements. The stiffer the sub-plate material, the smaller the negative

vertical interface displacements. In the 2DFEM with CZM (hard contact normal behavior), the vertical interface displacements will generally decrease and longitudinal displacements thus could increase.

- (e) However, when interface damage in longitudinal direction is considered, the interface displacements are almost the same in all the above discussed models. This is because that vertical interface stiffness relative to longitudinal interface stiffness becomes bigger in this case compared to the undamaged interface, the vertical displacements are so small that it has almost no influence on the longitudinal displacements.

(4) 3DFEM

- (a) Since the slab deformations or interface displacements deform also in horizontal direction, i.e. along slab width, this may have an interactive influence on the longitudinal and vertical deformations. Quarter of the slab system is simulated in 3DFEM with linear normal behavior of CZM to learn the whole slab deformation information.
- (b) The longitudinal deformation of the midline and edge line along the length are ultimately the same despite of the small scatter. What's more, they are larger than the final total longitudinal displacements in 2DFEM with CZM, while the midline has a very close result with the 2DFEM in the middle area and scatter gets larger at end of the slab.
- (c) The vertical interface displacement curve of 2DFEM along the length lays in the middle of the midline and edge line curves of 3DFEM.
- (d) The vertical displacements of the midline are larger than the edge line along both length and width. This may be because that the longitudinal restraint degree at midline is higher than the edge line and the deformations are somehow more restraint along midline in longitudinal direction, thus go to the vertical direction.
- (e) Since the width of the slab is considered in 3DFEM, there exists also horizontal displacements along slab width. Despite small scatter, the horizontal displacement curves of the midline and edge line along width are generally the same. Here the midline along width has larger displacements in both horizontal and vertical direction. It may owe to the limitation of longitudinal displacements at this axis that the deformations here could only go to horizontal and vertical direction, while the deformations at edge side have the possibility in three directions.

(5) Parameter study

- (a) The 1D centric model (i.e. analytical model) has the largest longitudinal deformation under uniform temperature variation and the centric models are actually on the beneficial side with regard to the longitudinal displacements. Thus, for the study of longitudinal interface behavior, the analytical models with a centric loading are on the safe side for practical applications and are thus used for parameter studies.
- (b) Different phases (i.e. linear elastic, damage evolution and friction phases) of interface could be observed in the diagram of interface shear stresses. The positive temperature variation leads to elongation of the beam while the negative variation cause beam shortening. The absolute deformations are nevertheless the same under positive and negative temperature variations with same the absolute value, which goes the same for beam axial stress.
- (c) The beam axial stress at end side equals to zero since the restraint at beam end is free and it reaches the maximum value at mid axis due to its largest restraint degree at this location. What's more, the axial stresses at mid axis firstly increase with increasing temperature variation and then decrease due to the interface degradation. The total resistant forces at interface decrease when the damage occurs to a certain extent.

- (d) The restraint degree at beam end equals to zero owing to the free restraint at this location. Although there exists no deformation at mid axis, the beam strain here is not zero, thus restraint degree at mid axis could not be 1. Nevertheless, the degree of restraint amounts to a maximum value at mid axis, which may be caused by an "accumulated effects" of whole interface restraint. With increasing degree of restraint, the interface displacements (or beam deformation) decrease given the same temperature variation.
 - (e) On the other hand, interface damage scaler shows the stiffness degradation at a certain spot. In general, the severer the interface damages, the lower the degree of restraint. However, although the damage scalar at mid-axis keeps zero (i.e. undamaged), the restraint degree here could still decrease for the sake of whole interface damage effects. Thus, degree of restraint at mid-axis could somehow represent the restraint effect as well as resistance ability from whole interface. While the damage scalar reflects more about locally interface deterioration extent.
 - (f) Elastic stiffness k_e decides the degree of restraint γ when the whole interface is elastic phase. Once damage occurs at interface, degree of restraint at mid-axis decreases.
 - (g) Strength τ_e has a more crucial influence on the degradation of the degree of restraint than interface stiffness k_e . Increasing the interface stiffness while keeping strength unchanged has insignificant impact on the interface damage, which even slightly aggravate the shortening of linear interface length a_e . Whereas, remaining stiffness while increasing strength would alleviate the degradation of degree of restraint. This is because that the maximum elastic slip S_e determines the initiation of damage and thus influences the resistance ability of the interface restraint. Keeping S_e unchanged, increasing stiffness k_e has a positive influence on the interface damage. However, even the stiffness k_e is increased, the maximum elastic slip S_e decreases given the same strength τ_e , which leads to a negative effects on the interface degradation.
 - (h) Residual friction τ_u determines the end value, to which restraint degree approaches. The smaller the damage evolution rate k_d , the slower the degree of restraint γ approaches to the end value.
 - (i) With increasing temperature variation, interface length in linear phase a_e decreases monotonously, while damage length a_d increases first and then decreases when friction phases appears. Friction length a_u increases monotonously. The interface stiffness k_e and maximum elastic slip S_e together influence the reduction of elastic length. Whereas the maximum damage slip S_u mainly determines the initiation of friction phases.
- (6) Limit state study
- (a) For a safe application of interfacial bonded slab, the longitudinal interface behavior should stay in linear elastic phase under uniform temperature variation, which means the interface displacement at slab end should be no bigger than maximum elastic slip S_e . Thus, the serviceability limit value of the interface could be expressed as the equation (5.59).
 - (b) The longer the slab length L is and the smaller the interface stiffness k is, the larger the limit maximum elastic slip S_e is. For longer slab length, the interface stiffness has larger influence on the limit maximum elastic slip. The limit maximum elastic slip scatter is bigger for longer slab. However the differences between $S_e - k$ curves of various slab lengths become smaller with increasing slab length.
 - (c) For a slab length of 6.45 m with a shear interface stiffness of 3 MPa/mm in this case, the lower limit maximum elastic slip S_e should be 0.451 mm. Therefore, reinforcements should be used across the interface in order to obtain the enough resistance. Obviously, the increase of interface stiffness could reduce the required S_e .

6. Vertical interface behavior under temperature gradients

6.1 Analytical models

Flexural deformation of the beam under temperature gradient variations leads to vertical relative displacement at interface. Typical kinds of vertical interface resistance are displayed in Figure 6.1. The linear vertical interface resistance, also known as Winkler's foundation, assume a proportional relationship between displacement and stress, while tensionless stress-displacement relationship expects no tension at interface. Bilinear vertical interface resistance demonstrates different stiffness in compression and tension, while trilinear relationship further employs a linear damage evolution at tension.

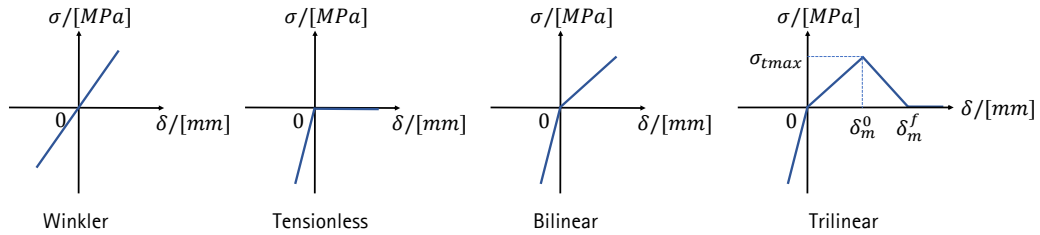


Figure 6.1 Typical stress-displacement relationship for vertical interface resistance

Practically, the trilinear stress-displacement relationship could best describe the vertical interface resistance. However, linear interface resistance is chosen for simplification in this analytical model firstly. Then a failure criterion with maximum tensile stress based on Winkler's foundation is assumed to simulate the interface damage. In the analysis of vertical interface behavior, longitudinal displacements are neglected at flexural deformation of the beam.

6.1.1 Interface as Winkler's foundation

The deflection of slab is a combination of temperature deformation and deformation under restraint forces

$$v = v_T + v_\sigma \quad (6.1)$$

where v denotes the actual deflection of the beam, v_T represents the deflection due to temperature and v_σ refers the deflection contributed from restraint forces. The equation (6.1) could also be transformed as

$$v_\sigma = v - v_T \quad (6.2)$$

According to differential equation of the deflection curve

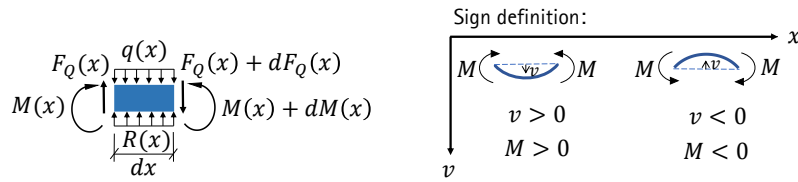
$$M(x) = -EIv_\sigma''(x) = -EI[v''(x) - v_T''] = -EI\left[v''(x) - \frac{\alpha_T \Delta T}{t}\right] \quad (6.3)$$

Based on differential equation of equilibrium for beams

$$\frac{d^2 M(x)}{dx^2} = \frac{dF_Q(x)}{dx} = P(x) \quad (6.4)$$

The load intensity $P(x)$ is equal to the differential of shear force $F_Q(x)$ meanwhile the shear force is equal to the differential of bending moment $M(x)$ at any section.

The stresses equilibrium in an infinitesimal unit is described in Figure 6.2.


 Figure 6.2 Differential element of length dx under temperature gradient

For linear elastic foundation with constant stiffness k_0 [MPa/mm]

$$P(x) = R(x) - q(x) = k \cdot v(x) - q \quad (6.5)$$

where $k = k_0 \cdot b$ [N/mm²] in 1D beam model, b denotes the width of the beam and q refers to load intensity due to gravity and $q = \rho g t b$ [N/mm] in this case.

Combining equations (6.3), (6.4) and (6.5) leads to the equilibrium expression as following

$$\frac{d^4 v(x)}{dx^4} + 4\eta^4 \cdot v(x) = \frac{q}{EI} \quad (6.6)$$

$$\eta = \sqrt[4]{\frac{k}{4EI}} \quad (6.7)$$

To solve this equation, assume the homogenous solution $v(x)^h = e^{rx}$ and substitute to equation (6.6)

$$(r^4 + 4\eta^4) \cdot e^{rx} = 0 \quad (6.8)$$

As a result

$$\begin{aligned} r^4 + 4\eta^4 &= 0 \\ (r^2 + 2\eta^2)^2 - (2r\eta)^2 &= 0 \\ (r^2 + 2\eta^2 + 2r\eta) \cdot (r^2 + 2\eta^2 - 2r\eta) &= 0 \\ [(r + \eta)^2 + \eta^2][(r - \eta)^2 + \eta^2] &= 0 \end{aligned} \quad (6.9)$$

The solutions of the above equation are

$$\begin{aligned} r_{1,2} &= -\eta \pm i\eta = -\eta(1 \pm i) \\ r_{3,4} &= \eta \pm i\eta = \eta(1 \pm i) \end{aligned} \quad (6.10)$$

The homogenous solution of the differential equation could then be expressed as

$$v(x)^h = e^{-\eta x} \cdot [C1 \cdot \cos(\eta x) + C2 \cdot \sin(\eta x)] + e^{\eta x} \cdot [C3 \cdot \cos(\eta x) + C4 \cdot \sin(\eta x)] \quad (6.11)$$

Assume the particular solution $v(x)^p = C$ and substitute to equation (6.6)

$$0 + 4\eta^4 \cdot C = \frac{q}{EI} \quad (6.12)$$

$$C = \frac{q}{4\eta^4 EI}$$

The general solution of equation (6.6) is then

$$\begin{aligned} v(x) &= v(x)^h + v(x)^p \\ &= e^{-\eta x} [C1 \cdot \cos(\eta x) + C2 \cdot \sin(\eta x)] + e^{\eta x} [C3 \cdot \cos(\eta x) + C4 \cdot \sin(\eta x)] \\ &\quad + \frac{q}{4\eta^4 EI} \end{aligned} \quad (6.13)$$

The angle of rotation is differential of deflection,

$$\begin{aligned} \theta(x) &= \eta e^{-\eta x} [(C2 - C1) \cdot \cos(\eta x) + (C1 + C2) \cdot \sin(\eta x)] \\ &\quad + \eta e^{\eta x} [(C3 + C4) \cdot \cos(\eta x) + (C4 - C3) \cdot \sin(\eta x)] \end{aligned} \quad (6.14)$$

According to equation (6.3) and (6.4)

$$\begin{aligned} M(x) &= -2EI\eta^2 \{e^{-\eta x} [-C2 \cdot \cos(\eta x) + C1 \cdot \sin(\eta x)] + e^{\eta x} [C4 \cdot \cos(\eta x) - C3 \cdot \sin(\eta x)]\} \\ &\quad + EI \frac{\alpha_T \Delta T}{t} \end{aligned} \quad (6.15)$$

$$\begin{aligned} F_Q(x) &= -2EI\eta^3 \{e^{-\eta x} [(C1 + C2) \cdot \cos(\eta x) + (C2 - C1) \cdot \sin(\eta x)] \\ &\quad + e^{\eta x} [(C4 - C3) \cdot \cos(\eta x) - (C3 + C4) \cdot \sin(\eta x)]\} \end{aligned} \quad (6.16)$$

Above solutions could also be expressed as

$$Sol = P0 \times D0 + E$$

$$P0 = \begin{bmatrix} C1 & C2 & C3 & C4 \\ \eta(C2 - C1) & -\eta(C1 + C2) & \eta(C3 + C4) & \eta(C4 - C3) \\ 2EI\eta^2 C2 & -2EI\eta^2 C1 & -2EI\eta^2 C4 & 2EI\eta^2 C3 \\ -2EI\eta^3(C1 + C2) & -2EI\eta^3(C2 - C1) & -2EI\eta^3(C4 - C3) & 2EI\eta^3(C3 + C4) \end{bmatrix} \quad (6.17)$$

$$Sol = \begin{bmatrix} v(x) \\ \theta(x) \\ M(x) \\ F_Q(x) \end{bmatrix} \quad D0 = \begin{bmatrix} e^{-\eta x} \cos(\eta x) \\ e^{-\eta x} \sin(\eta x) \\ e^{\eta x} \cos(\eta x) \\ e^{\eta x} \sin(\eta x) \end{bmatrix} \quad E = \begin{bmatrix} \frac{q}{4\eta^4 EI} \\ 0 \\ EI \frac{\alpha_T \Delta T}{t} \\ 0 \end{bmatrix}$$

Taking the BC into consideration, the system is symmetric with $v(x) = v(-x)$. This leads to following conclusions:

$$\begin{aligned} C1 &= C3 \\ C2 &= -C4 \end{aligned} \quad (6.18)$$

Substituting this BC into equation (6.17), shows that $\theta(0) = 0$ and $F_Q(0) = 0$. Meanwhile the solution could be simplified as

$$Sol = P \times D + E$$

$$P = \begin{bmatrix} 2C1 & 0 & 0 & -2C2 \\ 0 & 2\eta(C1 - C2) & -2\eta(C1 + C2) & 0 \\ 4EI\eta^2 C2 & 0 & 0 & 4EI\eta^2 C1 \\ 0 & 4EI\eta^3(C1 + C2) & 4EI\eta^3(C1 - C2) & 0 \end{bmatrix} \quad (6.19)$$

$$Sol = \begin{bmatrix} v(x) \\ \theta(x) \\ M(x) \\ F_Q(x) \end{bmatrix} \quad D = \begin{bmatrix} \cos(\eta x) \cosh(\eta x) \\ \cos(\eta x) \sinh(\eta x) \\ \sin(\eta x) \cosh(\eta x) \\ \sin(\eta x) \sinh(\eta x) \end{bmatrix} \quad E = \begin{bmatrix} \frac{q}{4\eta^4 EI} \\ 0 \\ EI \frac{\alpha_T \Delta T}{t} \\ 0 \end{bmatrix}$$

Since there are no external forces at beam end, other BCs are $M\left(\frac{L}{2}\right) = 0$ and $F_Q\left(\frac{L}{2}\right) = 0$. As a result, the parameters could be determined:

$$K1 = \frac{\sin\left(\frac{\eta L}{2}\right) \cdot \cosh\left(\frac{\eta L}{2}\right) + \cos\left(\frac{\eta L}{2}\right) \cdot \sinh\left(\frac{\eta L}{2}\right)}{\sin\left(\frac{\eta L}{2}\right) \cdot \cosh\left(\frac{\eta L}{2}\right) - \cos\left(\frac{\eta L}{2}\right) \cdot \sinh\left(\frac{\eta L}{2}\right)}$$

$$C1 = -\frac{\alpha \Delta T}{4\eta^2 t} \cdot \frac{1}{\sin\left(\frac{\eta L}{2}\right) \cdot \sinh\left(\frac{\eta L}{2}\right) + K1 \cdot \cos\left(\frac{\eta L}{2}\right) \cdot \cosh\left(\frac{\eta L}{2}\right)} \quad (6.20)$$

$$C2 = K1 \cdot C1$$

A result comparison between FEM and analytical model under uniform temperature gradient variation $\Delta T/t = -0.05 \text{ K/mm}$ (i.e. $\Delta T = -10 \text{ K}$) is demonstrated in the following Figure 6.3. The results of these two kinds models are in agreement with each other. It should be noticed that the "open" of interface is defined as positive displacement δ and "close" of interface is otherwise as negative, which has the same value with negative beam deflection v where positive one is assumed to be downwards. Under negative temperature gradients, the beam end has the largest positive vertical interface displacement and tensile interface stress, whereas the interface displacement at symmetric axis (mid axis) has negative value and interface stress here is in compression. The moment and shear force at beam end are equal to zero for the free of restraint at this spot, while the moment at mid axis reaches its maximum absolute value due to its largest restraint here. The result values reverse under positive temperature gradient with the same absolute value. In this case, beam end has negative vertical interface displacement and compressive interface stress, whereas the mid axis has positive interface displacement and tensile stress. Since the absolute values of interface displacement and stress at mid axis are smaller than the ones at beam end, the maximum tensile stress under positive temperature gradient is also smaller than the one under the negative temperature gradient with the same absolute value.

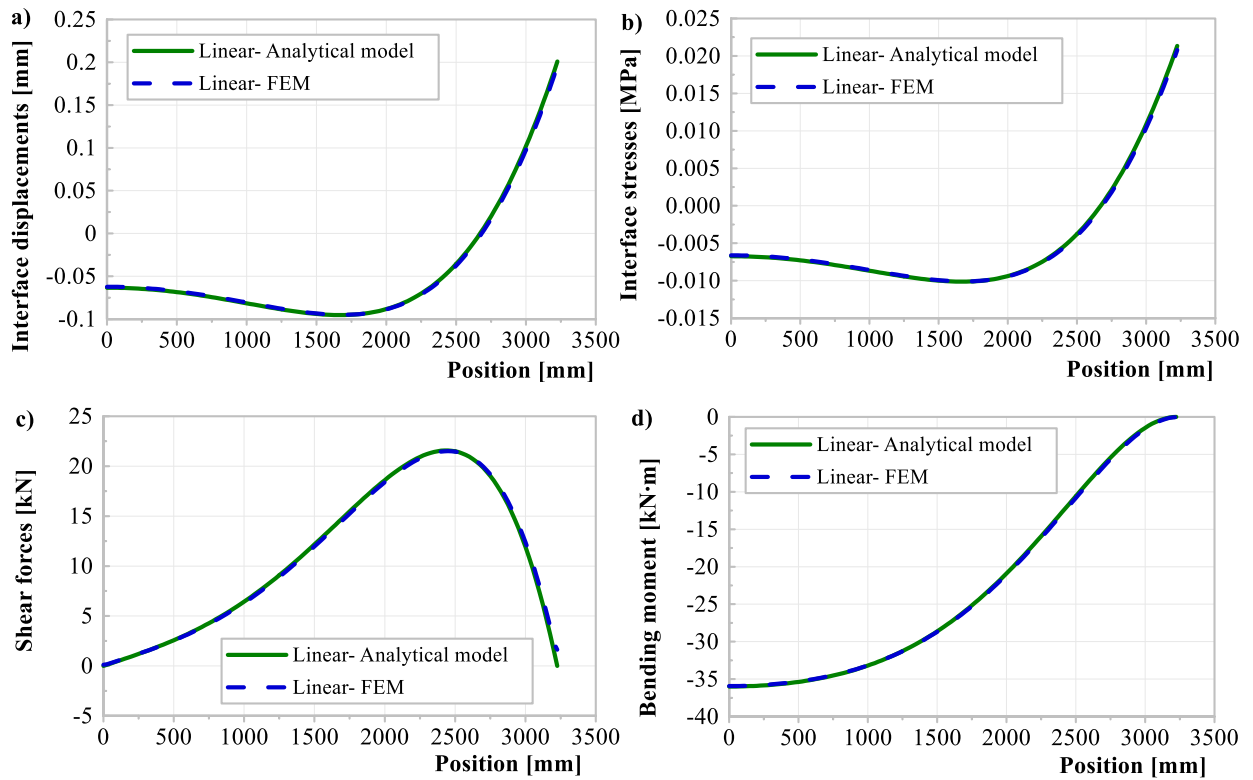


Figure 6.3 Comparison of analytical model and FEM of linear vertical interface behavior under negative temperature gradient ($\Delta T/t = -0.05 \text{ K/mm}$, $k_0 = 0.10625 \text{ MPa/mm}$)

6.1.2 Winkler's foundation with damage

Assuming a maximum tensile stress of the Winkler's foundation, interface could damage when reaching this criterion. Tensionless stress-displacement relationship with zero maximum tensile stress is a special case belonging to this condition. Interface damage begins from slab edge when negative temperature gradient is applied, while the damage starts from mid-axis of the slab when positive temperature gradient is loaded.

6.1.2.1 Negative temperature gradient

For interface damage under negative temperature gradients, debonding of the interface could be analyzed with shortening of the foundation-supported length. The stress and strain state of the beam is then divided into two phases, beam on Winkler's foundation and cantilever beam. The length of Winkler's foundation in the half-system is a , the stress and strain without foundation could be expressed as

$$F_Q(x) = q \left(\frac{L}{2} - x \right), \quad x \in [a, L/2] \quad (6.21)$$

$$M(x) = -\frac{q}{2} \left(\frac{L}{2} - x \right)^2, \quad x \in [a, L/2] \quad (6.22)$$

$$\begin{aligned} \theta(x) &= \theta_\sigma(x) + \theta_T(x), \quad x \in [a, L/2] \\ &= -\frac{1}{EI} \cdot \int M(x) dx + \int \frac{\alpha_T \Delta T}{t} dx = -\frac{1}{EI} \cdot \left[\frac{q}{6} \left(\frac{L}{2} - x \right)^3 + C_\theta \right] + \frac{\alpha_T \Delta T}{t} x \end{aligned} \quad (6.23)$$

$$\begin{aligned}
 v(x) &= v_\sigma(x) + v_T(x), \quad x \in [a, L/2] \\
 &= \int \theta_\sigma(x) dx + \int \theta_T(x) dx = -\frac{1}{EI} \cdot \left[-\frac{q}{24} \left(\frac{L}{2} - x \right)^4 + C_\theta \cdot x + C_v \right] + \frac{\alpha_T \Delta T}{2t} x^2
 \end{aligned} \tag{6.24}$$

where C_θ and C_v are variables that would be determined with deformation equilibrium at the turning point $x = a$. The stress and strain state within the Winkler's foundation remains similar with the expressions in Chapter 6.1.1. In order to solve the undetermined parameters a , $C1$ and $C2$, following BC are taken:

$$v(a) = 2C1 \cdot \frac{\cos(\eta a) \cosh(\eta a)}{A(a)} - 2C2 \cdot \frac{\sin(\eta a) \sinh(\eta a)}{B(a)} + \frac{q}{4\eta^4 EI} = -\delta_{emax} \tag{6.25}$$

$$M(a) = 4EI\eta^2 \cdot [C2 \cdot \frac{\cos(\eta a) \cosh(\eta a)}{A(a)} + C1 \cdot \frac{\sin(\eta a) \sinh(\eta a)}{B(a)}] + EI \frac{\alpha_T \Delta T}{t} = -\frac{q}{2} \left(\frac{L}{2} - a \right)^2 \tag{6.26}$$

$$F_Q(a) = 4EI\eta^3 \cdot [(C1 + C2) \cdot \frac{\cos(\eta a) \sinh(\eta a)}{C(a)} + (C1 - C2) \cdot \frac{\sin(\eta a) \cosh(\eta a)}{D(a)}] = q \left(\frac{L}{2} - a \right) \tag{6.27}$$

where δ_{emax} refers to the maximum interface displacements in Winkler's foundation (i.e. linear elastic phase). Derived from equation (6.25) and (6.26), variable $C1$ could be expressed as

$$C1 = \left[\frac{v_{max}}{2} - \frac{q}{2k} + C2 \cdot B(a) \right] / A(a) \tag{6.28}$$

$$C1 = \left[\frac{-q \left(\frac{L}{2} - a \right)^2}{8EI\eta^2} - \frac{\alpha_T \Delta T}{4\eta^2 t} - C2 \cdot A(a) \right] / B(a) \tag{6.29}$$

Combining the functions (6.28) and (6.29), variable parameter $C2$ becomes

$$C2 = \frac{A(a) \cdot [E(a) - P(\Delta T)] - P1 \cdot B(a)}{A(a)^2 + B(a)^2} \tag{6.30}$$

here the variable $C2$ is function of foundation length a . By substituting expression (6.30) into (6.28), variable $C1$ as a function of foundation length a is also found. Introducing $C1$ and $C2$ into equation (6.27), an equation of foundation length a is established and could be solved numerically. As a result, variables $C1$ and $C2$ are also determined.

To determine the variables C_θ and C_v , beam rotation and deflection are the same at limit point $x = a$ based on the expression in two phases, which are:

$$\begin{aligned}
 \theta(a) &= -\frac{1}{EI} \cdot \left[\frac{q}{6} \left(\frac{L}{2} - a \right)^3 + C_\theta \right] + \frac{\alpha_T \Delta T}{t} a = \frac{2\eta [(C1 - C2) \cdot C(a) - (C1 + C2) \cdot D(a)]}{\theta(a)} \\
 v(a) &= -\frac{1}{EI} \cdot \left[-\frac{q}{24} \left(\frac{L}{2} - a \right)^4 + C_\theta \cdot a + C_v \right] + \frac{\alpha_T \Delta T}{2t} a^2 = -\delta_{emax}
 \end{aligned} \tag{6.31}$$

The above equations lead to the determination of variables C_θ and C_v as:

$$C_\theta = -EI \cdot \left[\text{Theta}(a) - \frac{\alpha_T \Delta T}{t} a \right] - \frac{q}{6} \left(\frac{L}{2} - a \right)^3 \quad (6.32)$$

$$C_v = -EI \cdot \left[v_{max} - \frac{\alpha_T \Delta T}{2t} a^2 \right] + \frac{q}{24} \left(\frac{L}{2} - a \right)^4 - C_\theta \cdot a \quad (6.33)$$

A result comparison between FEM and analytical model under temperature gradient variation $\Delta T/t = -0.05 \text{ K/mm}$ is demonstrated in the following Figure 6.4. The results of these two kinds models are in agreement with each other. Similar with linear elastic model (i.e. model with Winkler foundation), the maximum interface displacement occurs at beam end, which has also a much larger value in this case with damage criterion than the one in linear elastic model. The interface damage could be observed in the interface stress diagram. The interface stress drops to zero once it reaches its damage criterion. The moment and shear force also equal to zero, while the maximum bending moment (absolute value) at mid axis reduces a little bit in this case compared to the one in linear elastic model. Since the damage of interface could reduce the interface restraint generally, the interface displacements would increase and bending moment of the beam would otherwise decrease.

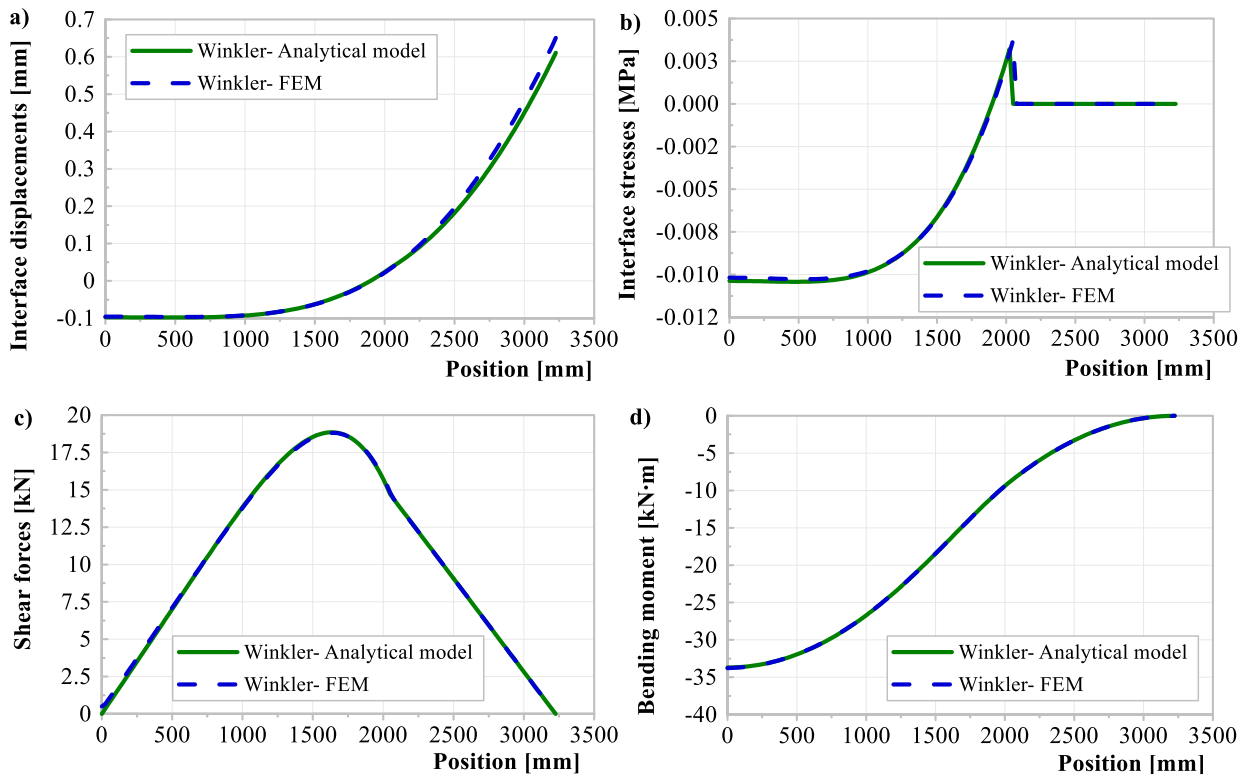


Figure 6.4 Comparison of analytical model and FEM of Winkler's foundation with damage under negative temperature gradients ($\Delta T/t = -0.05 \text{ K/mm}$, $k_0 = 0.10625 \text{ MPa/mm}$, $\delta_m^0 = 0.0368 \text{ mm}$)

6.1.2.2 Positive temperature gradient

When the beam is under positive temperature gradients, the interface debonding would otherwise start from the mid of the beam. In this case, the beam deformations and forces under the restraint of interface in linear elastic phase (denoted as Phase I) could be calculated by equation (6.17). Whereas, the beam deformations and forces without interface restraint caused by interface damage (denoted as Phase II) could be described as

$$\begin{cases} F_{Q-II}(x) = -qx + C5 \\ M_{II}(x) = -\frac{q}{2}x^2 + C5 \cdot x + C6 \\ \theta_{II}(x) = -\frac{1}{EI} \left[-\frac{q}{6}x^3 + \frac{C5}{2}x^2 + C6 \cdot x + C7 \right] + \frac{\alpha_T \Delta T}{t} x \\ v_{II}(x) = -\frac{1}{EI} \left[-\frac{q}{24}x^4 + \frac{C5}{6}x^3 + \frac{C6}{2} \cdot x^2 + C7 \cdot x + C8 \right] + \frac{\alpha_T \Delta T}{2t} x^2 \end{cases} \quad (6.34)$$

Assuming the turning point with the position a where the interface change from Phase I to Phase II, following boundary condition should be considered to determine the variables from C1 to C8 as well as turning point a

$$\begin{cases} \theta_I(0) = 0 \\ F_{Q-I}(0) = 0 \\ M_{II}(L/2) = 0 \\ F_{II}(L/2) = 0 \\ v_I(a) = -\delta_{emax} \\ v_I(a) = v_{II}(a) \\ \theta_I(a) = \theta_{II}(a) \\ F_{Q-I}(a) = F_{Q-II}(a) \\ M_I(a) = M_{II}(a) \end{cases} \quad (6.35)$$

The above equations besides $v_I(a) = -\delta_{emax}$ could transfer to a matrix-vector style as

$$\begin{bmatrix} A_{11} & A_{12} & \cdots & A_{19} \\ A_{21} & A_{22} & \cdots & A_{29} \\ \vdots & \vdots & \vdots & \vdots \\ A_{81} & A_{82} & \cdots & A_{89} \end{bmatrix} \begin{bmatrix} C1 \\ C2 \\ \vdots \\ C8 \end{bmatrix} = \begin{bmatrix} B_1 \\ B_2 \\ \vdots \\ B_8 \end{bmatrix} \quad (6.36)$$

in short:

$$A \cdot \vec{C} = \vec{B}$$

here the vector \vec{C} refers to the undetermined variables, matrix A denotes coefficients in the equations that should be multiplied by the undetermined variables whereas vector \vec{B} belongs to the coefficients that don't need to be multiplied by the undetermined variables. Both of matrix A and vector \vec{B} contain the undetermined variable a .

Unlike the above described method with regard to negative temperature gradients where the undetermined variables are directly calculated, the for-loop is used here to find the most precise position a that leading to the highest accurate result $v_I(a) = -\delta_{emax}$. In the for-loop, the program counts the loop index a from position $x = 0 \text{ mm}$ to $x = L/2 \text{ mm}$, and the undetermined variables could be calculated by $\vec{C} = A \setminus \vec{B}$. For each value of loop index a , a solution of beam deflection could be obtained. Among all the solutions, the one with highest accuracy of $v_I(a) = -\delta_{emax}$ is then chosen.

By calculating the inverse of the matrix A in Matlab, it is found that the condition number is very large for each value of the loop index. The condition number represents a measure that describes how inaccurate the solution x will be after approximation. If the condition number is infinite, the matrix is singular and not invertible. Since the condition number of A is much larger than 1, the matrix A is sensitive to the inverse calculation. Matrix A is a poorly conditioned matrix. The poorly conditioned matrix A means that when solving the linear system of equations $Ax = b$, a small perturbation Δa makes the solution of the equations $(A + \Delta a)x = b$ very different compared to the original solution $Ax = b$. The approximate solution x of the equations system is generally impossible to make $r = b - Ax = 0$, and when A is poorly conditioned, it is

still possible to get an approximate solution that is very different from the true solution even if $r = b - Ax$ is small. In this case, Singular Value Decomposition (SVD) is then used here. A singular value decomposition of a matrix describes its representation as the product of three special matrices. Similar to the eigenvalues, the singular value characterizes properties of the matrix. In this way, the almost singular linear equation systems can be adequately solved within the framework of computational accuracy.

Figure 6.5 shows the result comparison between FEM and analytical model under temperature gradient variation $\Delta T/t = 0.25 \text{ K/mm}$. The results of these two models are in consistent with each other.

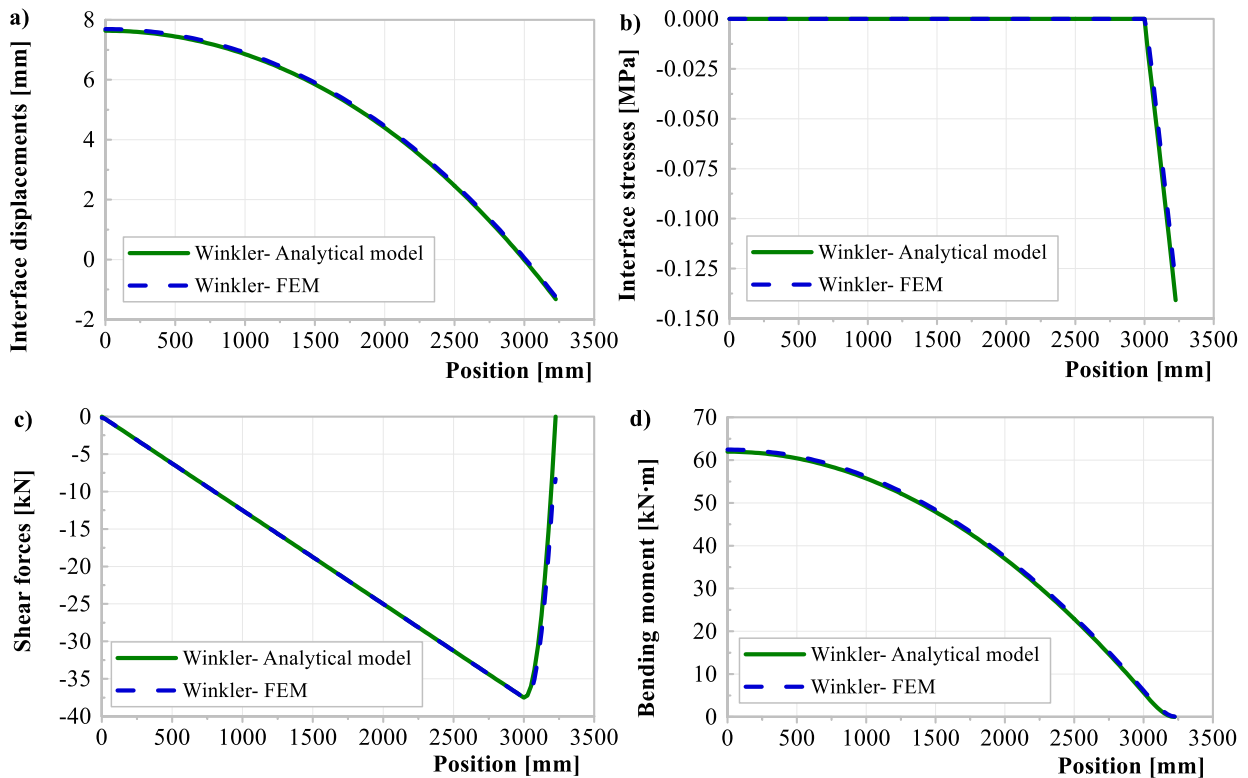


Figure 6.5 Comparison of analytical model and FEM of Winkler's foundation with damage under positive temperature gradients ($\Delta T/t = 0.25 \text{ K/mm}$, $k_0 = 0.10625 \text{ MPa/mm}$, $\delta_m^0 = 0.0368 \text{ mm}$)

During the calculation of interface damage under positive temperature gradients, it's found that the amplitude of positive temperature gradients leading the interface damage initiation is much bigger than the one of negative temperature gradients. This means that the interface under negative temperature gradients are much easier to damage compared with the case under positive temperature gradients, which also corresponds to practical experiences where most interface damage starts from edge to middle. Thus, the following analysis will focus on the interface vertical behavior under negative temperature gradients.

6.1.3 Bilinear vertical interface behavior

In most cases, the interface behaviors under compression and tension are different since the stiffness in compression is much larger than the one in tension. As a result, the bilinear vertical behavior is more practical and useful to learn the true interface performance in elastic phase.

Based on the equation (6.6), the governing equations of bilinear vertical interface behavior could be combined by two linear vertical behavior in compression and tension respectively

$$\frac{d^4 v(x)}{dx^4} + 2(\eta_1^4 + \eta_2^4) \cdot v(x) + 2(\eta_1^4 - \eta_2^4) \text{sgn}[v(x)] \cdot v(x) = \frac{q}{EI}, \left(\eta_1 = \sqrt[4]{\frac{k_1}{4EI}} \text{ and } \eta_2 = \sqrt[4]{\frac{k_2}{4EI}} \right) \quad (6.37)$$

where k_1 and k_2 in [N/mm²] denote the interface stiffness of compression and tension in 1D beam model respectively. Moreover $k_1 = k_{10} \cdot b$ and $k_2 = k_{20} \cdot b$, in which k_{10} and k_{20} refer to actual interface stiffness in [MPa/mm].

The solution of beam in linear vertical behavior is expressed in equation (6.17). To solve equations in bilinear behavior, it could then combine the solutions of two linear behaviors in compression (Phase I) and tension (Phase II) respectively. The undetermined variables could also be calculated by the following BCs

$$\begin{cases} \theta_{I}(0) = 0 \\ F_{Q_{I}}(0) = 0 \\ M_{II}(L/2) = 0 \\ F_{II}(L/2) = 0 \\ v_{I}(a) = 0 \\ v_{I}(a) = v_{II}(a) \\ \theta_{I}(a) = \theta_{II}(a) \\ F_{Q_{I}}(a) = F_{Q_{II}}(a) \\ M_{I}(a) = M_{II}(a) \end{cases} \quad (6.38)$$

in which the variable a refers to the position where interface transfer from compression to tension.

The calculation of the equations could either use the above described method in chapter 6.1.2.2 with for-loop or adopt the *vpasolve* or *fsolve* function in MATLAB. The difference between the two functions is that the former doesn't need the initial values while the later must be associated with initial values. Thus, to obtain the true solutions we need, the results range should be specified when using *vpasolve* function, e.g. specifying the variable a in the range of [0, L/2].

Figure 6.6 demonstrates the results in analytical model and FEM and both of them are accordant. It could also be found that despite the extensively increasing of compressive interface stiffness, the maximum interface displacement at beam end (i.e. 0.205 mm) has almost no variation compared with the one (i.e. 0.201 mm) in linear elastic behavior. What's more, with increasing compressive stiffness, the beam length in compression (i.e. ca 2050 mm) decreases and length in tension (i.e. ca 1175 mm) increases compared with the ones (i.e. ca 2650 mm in compression and ca 575 mm in tension) in linear vertical interface behavior. The bending moment in compression have much less variation scatter than the one in linear interface, which also corresponds to the beam deflection in compression. Meanwhile the absolute value of beam moment at mid axis also reduces a little bit (from 35.98 kN·m to 33.15 kN·m), indicating an equivalent degree of restraint reduction at this spot.

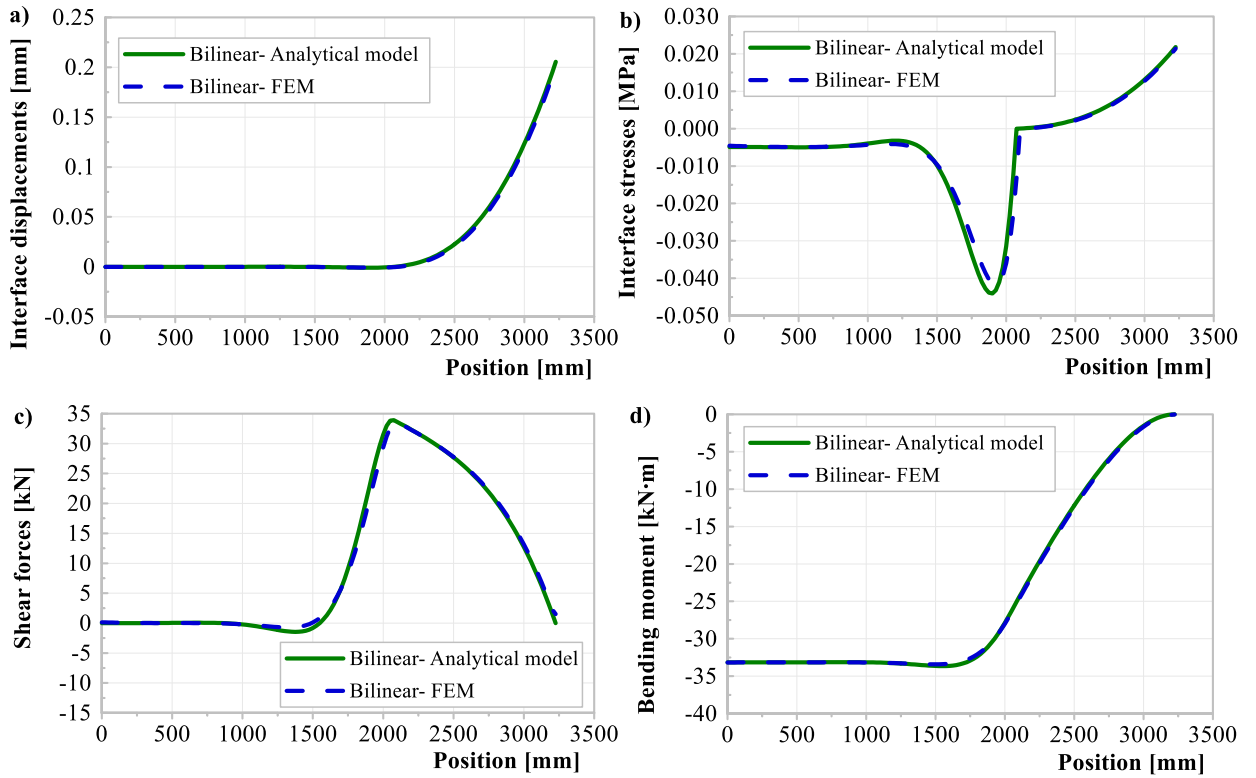


Figure 6.6 Comparison of analytical model and FEM of bilinear interface vertical behavior under negative temperature gradients ($\Delta T/t = -0.05 \text{ }^\circ\text{C}/\text{mm}$, $k_{20} = 0.10625 \text{ MPa}/\text{mm}$, $k_{10} = 45 \text{ MPa}/\text{mm}$)

6.1.4 Trilinear vertical interface behavior

When the interface damage is considered in the bilinear elastic model, the trilinear vertical interface behavior is then introduced. In this model, the interface could be divided into four phases:

- Phase I: elastic behavior in compression
- Phase II: elastic behavior in tension
- Phase III: damage evolution in tension
- Phase IV: free of interface restraint (i.e. fully damaged) in tension

The general solution of Phase I and Phase II are discussed above in equation (6.17), so does the general solution of Phase IV in equation (6.34). According to equation (6.5), the reactive distributed load $R(x)$ from interface in phase III is

$$\begin{aligned} R(x) &= -\sigma(x) = -\{\sigma_{tmax} - k_3[\delta(x) - \delta_m^0]\} = -\sigma_{tmax} + k_3[-v(x) + v_0] \\ &= -\sigma_{tmax} - k_3[v(x) - v_0] \end{aligned} \quad (6.39)$$

in which $\sigma(x)$ stands for the normal interface stress and the maximum tensile interface stress $\sigma_{tmax} = k_2\delta_m^0$, $v_0 = -\delta_m^0$ denotes the beam deflection where interface damage initiates and $v_f = -\delta_m^f$ refers to beam deflection where interface starts fully damaged.

$$k_3 = \frac{\sigma_{tmax}}{\delta_m^f - \delta_m^0} = \frac{-\sigma_{tmax}}{v_f - v_0} \quad (6.40)$$

Combining equation (6.4) and equation (6.39) leads to

$$\frac{d^2 M(x)}{dx^2} = P(x) = R(x) - q = -\sigma_{tmax} - k_3[v(x) - v_0] - q = -k_3 v(x) - \sigma_{tmax} + k_3 v_0 - q \quad (6.41)$$

Combining equations (6.3), and (6.41) leads to the equilibrium expression as following

$$\frac{d^4 v(x)}{dx^4} - \eta_3^4 \cdot v(x) = \frac{Q}{EI}, \quad \left(Q = q - k_3 v_0 + \sigma_{tmax} \text{ and } \eta_3 = \sqrt[4]{\frac{k_3}{EI}} \right) \quad (6.42)$$

To solve this equation, assume the homogenous solution $v(x)^h = e^{rx}$ and substitute to equation (6.42)

$$(r^4 - \eta_3^4) \cdot e^{rx} = 0 \quad (6.43)$$

As a result

$$\begin{aligned} r^4 - \eta_3^4 &= 0 \\ (r^2 + \eta_3^2)(r^2 - \eta_3^2) &= 0 \end{aligned} \quad (6.44)$$

The solutions of the above equation are

$$\begin{aligned} r_{1,2} &= \pm \eta_3 \\ r_{3,4} &= \pm i \eta_3 \end{aligned} \quad (6.45)$$

The homogenous solution of the differential equation could then be expressed as

$$v(x)^h = C1 \cdot e^{\eta_3 x} + C2 \cdot e^{-\eta_3 x} + C3 \cdot \cos(\eta_3 x) + C4 \cdot \sin(\eta_3 x) \quad (6.46)$$

Assume the particular solution $v(x)^p = C$ and substitute to equation (6.6)

$$\begin{aligned} 0 - \eta_3^4 \cdot C &= \frac{Q}{EI} \\ C &= -\frac{Q}{\eta_3^4 EI} = -\frac{Q}{k_3} \end{aligned} \quad (6.47)$$

The general solution of equation (6.42) is then

$$v(x) = v(x)^h + v(x)^p = C1 \cdot e^{\eta_3 x} + C2 \cdot e^{-\eta_3 x} + C3 \cdot \cos(\eta_3 x) + C4 \cdot \sin(\eta_3 x) - \frac{Q}{k_3} \quad (6.48)$$

The angle of rotation is differential of deflection,

$$\theta(x) = \eta_3 C1 \cdot e^{\eta_3 x} - \eta_3 C2 \cdot e^{-\eta_3 x} - \eta_3 C3 \cdot \sin(\eta_3 x) + \eta_3 C4 \cdot \cos(\eta_3 x) \quad (6.49)$$

According to equation (6.3)

$$M(x) = -EI\eta_3^2 [C1 \cdot e^{\eta_3 x} + C2 \cdot e^{-\eta_3 x} - C3 \cdot \cos(\eta_3 x) - C4 \cdot \sin(\eta_3 x)] + EI \frac{\alpha_T \Delta T}{t} \quad (6.50)$$

$$F_Q(x) = -EI\eta_3^3 [C1 \cdot e^{\eta_3 x} - C2 \cdot e^{-\eta_3 x} + C3 \cdot \sin(\eta_3 x) - C4 \cdot \cos(\eta_3 x)] \quad (6.51)$$

Above solutions could also be expressed as

$$\begin{bmatrix} v(x) \\ \theta(x) \\ M(x) \\ F_Q(x) \end{bmatrix} = \begin{bmatrix} C1 & C2 & C3 & C4 \\ \eta_3 C1 & -\eta_3 C2 & \eta_3 C4 & -\eta_3 C3 \\ -EI\eta_3^2 C1 & -EI\eta_3^2 C2 & EI\eta_3^2 C3 & EI\eta_3^2 C4 \\ -EI\eta_3^3 C1 & EI\eta_3^3 C2 & EI\eta_3^3 C4 & -EI\eta_3^3 C3 \end{bmatrix} \begin{bmatrix} e^{\eta_3 x} \\ e^{-\eta_3 x} \\ \cos(\eta_3 x) \\ \sin(\eta_3 x) \end{bmatrix} + \begin{bmatrix} -\frac{Q}{k_3} \\ 0 \\ EI \frac{\alpha_T \Delta T}{t} \\ 0 \end{bmatrix} \quad (6.52)$$

Similar with the method discussed above, BCs are applied to solve the undetermined variables. There are two kinds of cases here, namely the whole interface in 3 Phases (i.e. Phase I, II and III) and the whole interface in 4 Phases (i.e. Phase I, II, III and IV). Thus, the BCs could be summarized as following

$$\begin{array}{l} \text{3 Phases} \\ \left\{ \begin{array}{l} \theta_I(0) = 0 \\ F_{Q-I}(0) = 0 \\ M_{III}(L/2) = 0 \\ F_{III}(L/2) = 0 \\ v_I(a) = 0 \\ v_I(a) = v_{II}(a) \\ \theta_I(a) = \theta_{II}(a) \\ F_{Q-I}(a) = F_{Q-II}(a) \\ M_I(a) = M_{II}(a) \\ v_{II}(b) = -\delta_m^0 \\ v_{II}(b) = v_{III}(b) \\ \theta_{II}(b) = \theta_{III}(b) \\ F_{Q-II}(b) = F_{Q-III}(b) \\ M_{II}(b) = M_{III}(b) \end{array} \right. \end{array} \quad \text{and} \quad \begin{array}{l} \text{4 Phases} \\ \left\{ \begin{array}{l} \theta_I(0) = 0 \\ F_{Q-I}(0) = 0 \\ M_{IV}(L/2) = 0 \\ F_{IV}(L/2) = 0 \\ v_I(a) = 0 \\ v_I(a) = v_{II}(a) \\ \theta_I(a) = \theta_{II}(a) \\ F_{Q-I}(a) = F_{Q-II}(a) \\ M_I(a) = M_{II}(a) \\ v_{II}(b) = -\delta_m^0 \\ v_{II}(b) = v_{III}(b) \\ \theta_{II}(b) = \theta_{III}(b) \\ F_{Q-II}(b) = F_{Q-III}(b) \\ M_{II}(b) = M_{III}(b) \\ v_{III}(c) = -\delta_m^f \\ v_{III}(c) = v_{IV}(c) \\ \theta_{III}(c) = \theta_{IV}(c) \\ F_{Q-III}(c) = F_{Q-IV}(c) \\ M_{III}(c) = M_{IV}(c) \end{array} \right. \end{array} \quad (6.53)$$

in which a , b and c denote the positions where interface transfers from Phase I to Phase II, from Phase II to Phase III and from Phase III to Phase IV respectively.

Same as in chapter 6.1.3 discussed, the equations could be solve either with for-loop or with *vpasolve/fsolve* function in Matlab to specify all the undetermined variables in each phase as well as the turning position a , b and c . Figure 6.7 shows the result comparison between analytical model and FEM and they are in good accordance with each other. It could be found that, the maximum interface displacement at beam end here increase dramatically when interface damage is considered (i.e. 0.546 mm with damage in trilinear model and 0.205 mm without damage in bilinear model in Figure 6.6). However, this value is smaller than the one in the model of Winkle's foundation with damage (i.e. 0.611 mm in Figure 6.4), which indicating a positive influence of the damage evolution phase on the interface restraint ability. The different phases of interface could be observed in the interface stress diagram.

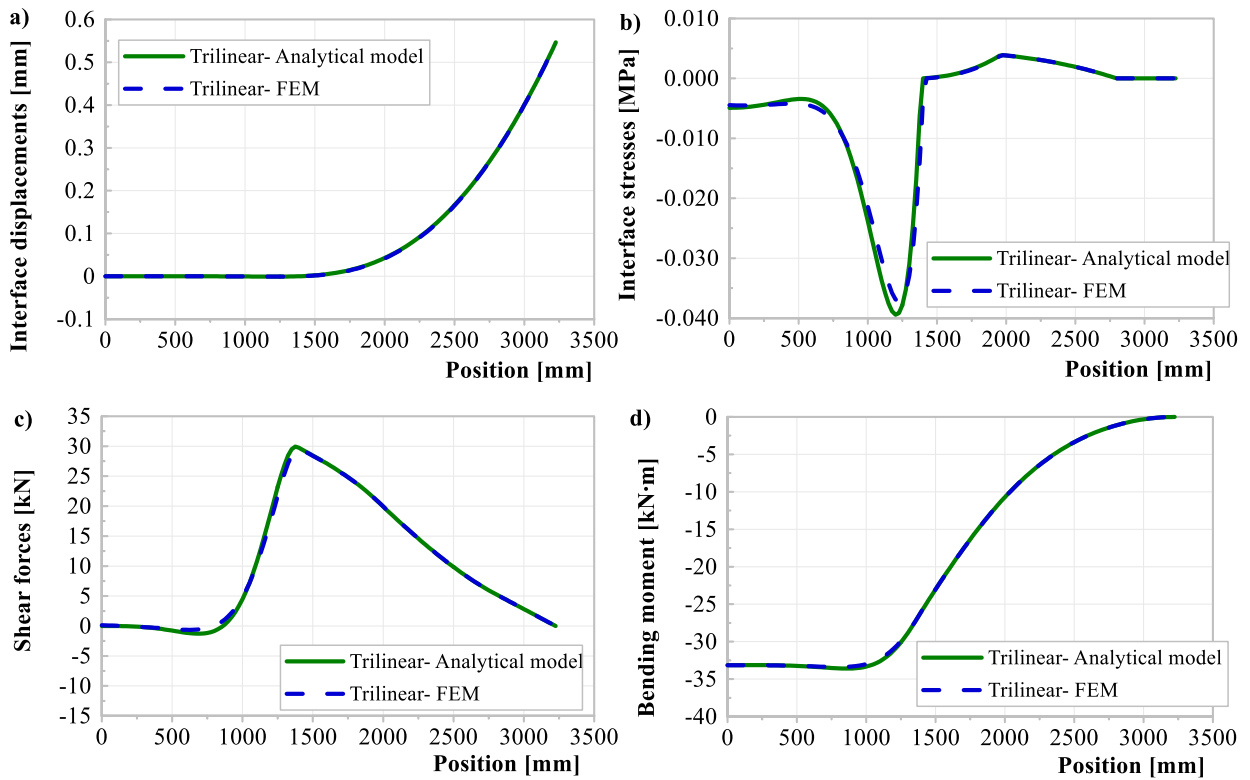


Figure 6.7 Comparison of analytical model and FEM of trilinear interface vertical behavior under negative temperature gradients ($\Delta T/t = -0.05 \text{ K/mm}$, $k_{20} = 0.10625 \text{ MPa/mm}$, $k_{10} = 45 \text{ MPa/mm}$, $\delta_m^0 = 0.0368 \text{ mm}$, $\delta_m^f = 0.292 \text{ mm}$)

6.1.5 Calculation algorithms with Matlab

Different amplitude of temperature gradients could lead to different interface state, i.e. the whole interface could in a bilinear elastic state, trilinear with 3-phases state or trilinear with 4-phases state. For interface under negative temperature gradients, the maximum vertical interface displacement occurs at beam end. The vertical interface displacements equal to negative beam deflections. Thus, the deflection of the beam end could be used to determine the interface state under a certain temperature gradient. The following Figure 6.8 summarized the calculation algorithms for vertical interface behavior under temperature gradients. Various BCs are also given in the figure for corresponding interface states.

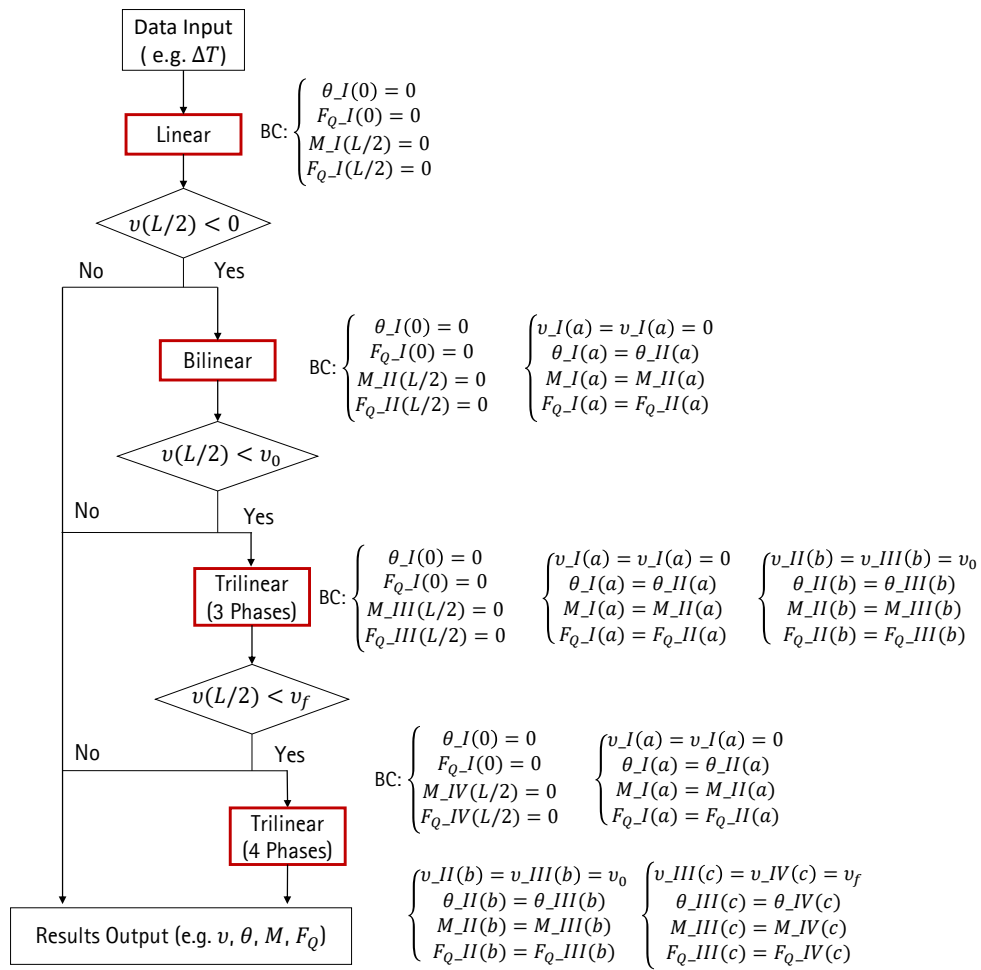


Figure 6.8 Flowchart of algorithms for vertical interface behavior under temperature gradients

6.2 Finite element models

In chapter 4.5.2 the fracture parameters are obtained from the inverse analysis of FEM based on the direct tensile tests. Table 4.9 offers the optimized CZM parameters with the consideration of eccentric loading. Meanwhile equation (4.4) gives the relationship between fracture energy and eccentricity. Thus, the fracture energy is 4.99×10^{-4} N/mm here assuming an infinite small eccentricity. The following Table 6.1 summarized all the parameters including CZM interface parameters and CAM layer parameters.

Table 6.1 Suggested fracture parameters for interface between concrete and CAM with linear softening behavior in Mode I as well as characteristic parameters of CAM layer

K_{nn} [MPa/mm]	δ_m^0 [mm]	σ_{max} [MPa]	δ_m^f [mm]	G_f [N/mm]	E_{CAM} [MPa]	t_{CAM} [mm]	v_0 [mm]	v_f [mm]
0.10625	0.0368	3.91×10^{-3}	0.292	4.99×10^{-4}	9000	30	-0.0368	-0.292

6.2.1 1D models

With regard to the vertical interface behavior under temperature gradients, there exist no difference between 1D centric loading and eccentric loading FEM. The above developed analytical model in chapter 6.1 shows that the results of analytical model have a very good accordance with the ones of 1DFEM. Thus, further studies based on 1D model would adopt either the analytical models or the centric loading 1DFEM.

6.2.2 2D models

Similar with the methods in chapter 5.2.2, connector elements and CZM could be used in the 2DFEM simulation. Hereby the linear, bilinear and trilinear interface behaviors are discussed in the following chapters.

6.2.2.1 Linear interface behavior

Figure 6.9 shows the 2DFEM results with different simulation methods and parameters. It could be found that, the 2DFEM with connector elements has almost the same results with the 1DFEM and it's also very easy to input the linear vertical stiffness in the models. In the FEM with CZM in contact interaction, the stiffness in tension and in compression are defined otherwise seperately. The cohesive stiffness K_{nn} in Mode I of CZM equals to the equivalent linear vertical stiffness in 1DFEM or 2DFEM with connector elements, see equations (5.52) and (5.53). However, unlike expected the stiffness K_{norm} in linear contact normal behavior needs to be very small compared to K_{nn} instead of equals to K_{nn} , in order to obtain the linear vertical interface behavior same as 1DFEM or 2DFEM with connector elements. It's also found that, the cohesive stiffness K_{ss} in Mode II has an influence on the vertical interface displacements. The increasing of K_{ss} would lead to decrease of vertical interface displacemen at beam end. Thus, the following studies on vertical interface behavior will neglect or set a very samll value of the shear stiffness K_{ss} in mode II, since it's the unfavourable case.

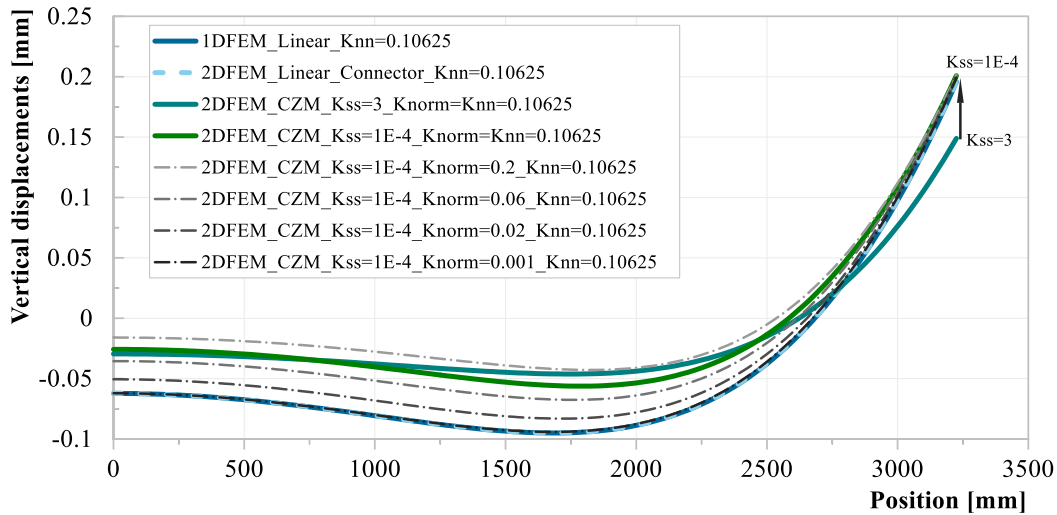


Figure 6.9 2DFEM results of linear vertical interface behavior ($\Delta T/t = -0.05 K/mm$)

6.2.2.2 Bilinear interface behavior

In practical, the interface behavior in compression and tension are usually very different since the foundation provides a much stiffer interface stiffness in compression. According to equation (3.13), the interface stiffness in compression could be expressed as

$$K_c = K_{norm} = \frac{E_{CAM}}{t_{CAM}} = \frac{9000 \text{ MPa}}{30 \text{ mm}} = 300 \text{ MPa/mm} \quad (6.54)$$

There are three ways to implements the bilinear vertical interface behavior in FEM:

- defining the bilinear connector stiffness in 1DFEM or 2DFEM;
- defining the stiffness K_{norm} of linear contact normal behavior and cohesive stiffness K_{nn} of CZM;
- defining a hard contact normal behavior and specify the cohesive stiffness K_{nn} of CZM.

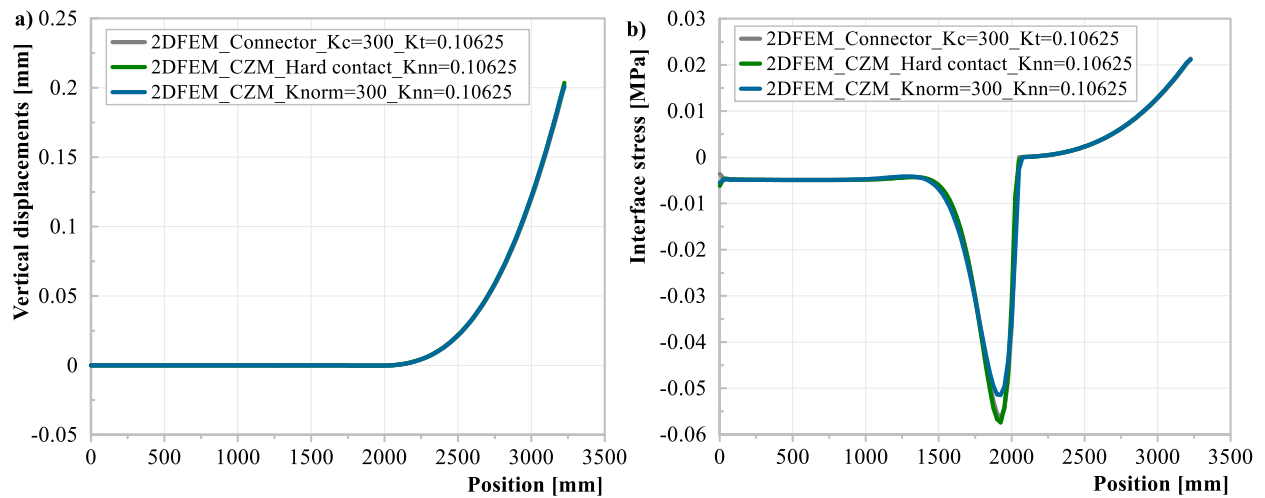


Figure 6.10 2DFEM results of bilinear vertical interface behavior ($\Delta T/t = -0.05 K/mm$)

Figure 6.10 demonstrates the result comparison of the above described simulation methods. It could be found that there exists almost no big difference between different models especially for the vertical interface displacements. Small scatter appears at the compressive interface stress peak, where the 2DFEM with connector elements and 2DFEM with hard contact normal behavior have much similar results than the rest of two models. In general, the difference between these models are very small and the results of them are in a good accordance.

6.2.2.3 Trilinear interface behavior

Introducing damage criterion into the bilinear vertical interface behavior leads to trilinear vertical interface behavior. In this case, the result differences between various models become bigger, see Figure 6.11. It could be seen that the 2DFEM with connector elements here has the largest difference with the other three models. The interface stress difference in compression is also larger than in tension. In the tension area, only the 2DFEM with connector has somehow differences with other three models, while the results of four models differentiate with each other in compression area. In general, the four models could all be used in simulation, while the 2DFEM with connector elements has the largest variation compared with the other three models.

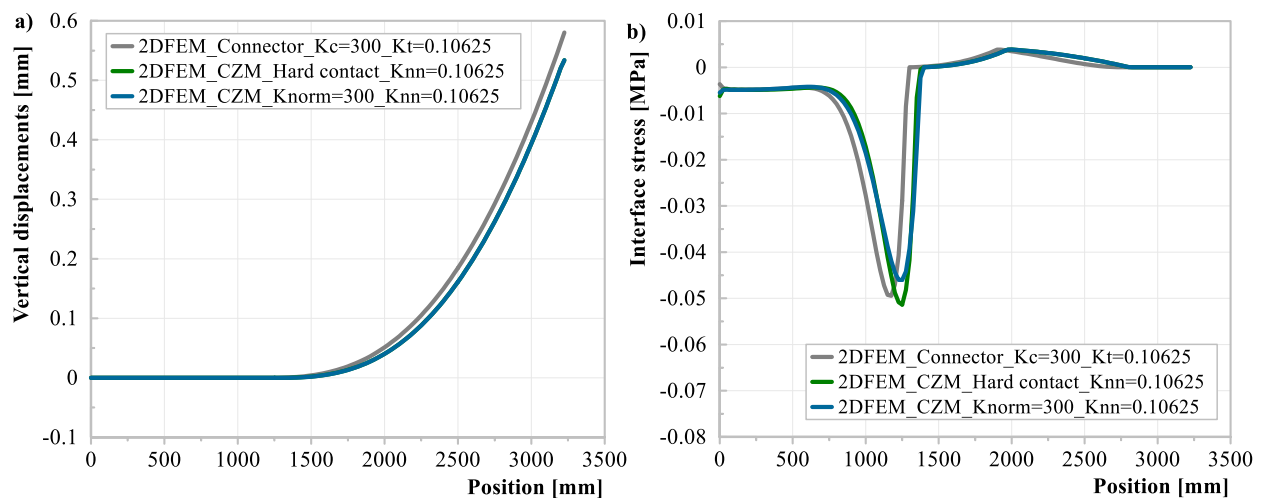


Figure 6.11 2DFEM results of trilinear vertical interface behavior ($\Delta T/t = -0.05 K/mm$)

6.2.3 3D models

The studies based on 1D and 2D models show slab vertical deformation along slab length under temperature gradients. However, the slab deformations or interface displacements deform also along slab width. This may have an interactive influence on the vertical deformations. Thus 3D models are needed to learn the whole slab deformation information. For the sake of symmetry, quarter of the slab system is simulated in the model. Figure 6.12 displays the simulation results of the linear 3DFEM with cohesive stiffness in Mode I $K_{nm} = 0.10625 \text{ MPa/mm}$, cohesive stiffness in Mode II $K_{ss} = 10^{-4} \text{ MPa/mm}$ and linear contact normal behavior with stiffness $K_{norm} = 10^{-6} \text{ MPa/mm}$ under temperature gradient $\Delta T/t = -0.05 \text{ K/mm}$.

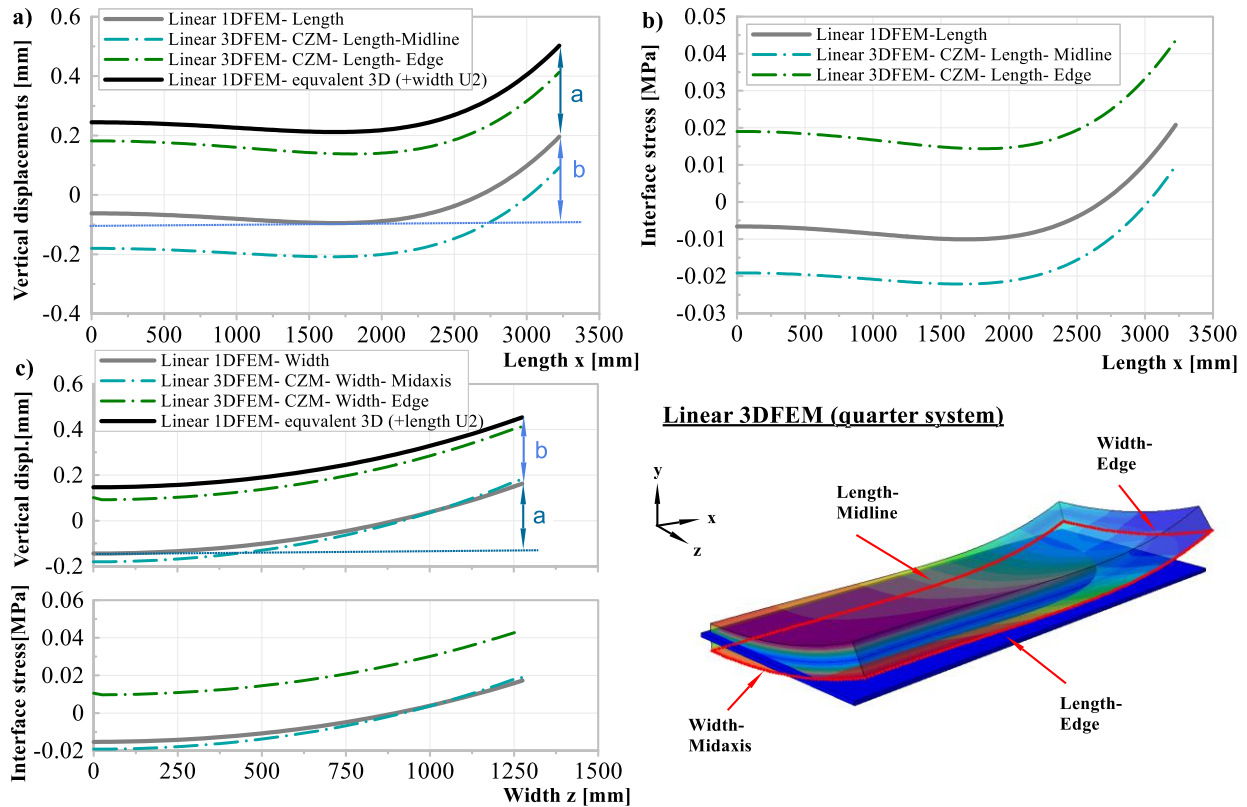


Figure 6.12 3DFEM results of linear vertical interface behavior

It could be seen from the above figure, that the actual vertical displacements of slab are a superposition of the vertical displacements along width and length. The vertical displacements of the midline along both length and width are smaller than the ones of edge line along length and width. The corner of the slab has thus the maximum vertical displacements. The vertical displacement curve of 1DFEM lays in between the vertical displacement curves of midline and edge line of 3DFEM meanwhile it's prone to be closer to the displacement curve of midline of 3DFEM especially for the curve along width. By adding the maximum vertical displacement difference along width [i.e. variable a in Figure 6.12 c)] to the vertical displacement curve along length in 1D model, gives a quasi-equivalent 3D vertical displacement curve in the 1D model [see Figure 6.12 a)]. Similarly, the quasi-equivalent 3D vertical displacement curve along width [see Figure 6.12 c)] could also be obtained by adding the maximum vertical displacement difference along length in 1D model [i.e. variable b in Figure 6.12 a)]. Since the recalculated equivalent vertical displacement curve of edge line has larger values than the one in 3DFEM, it could be used in the further limit state study for its unfavorable condition.

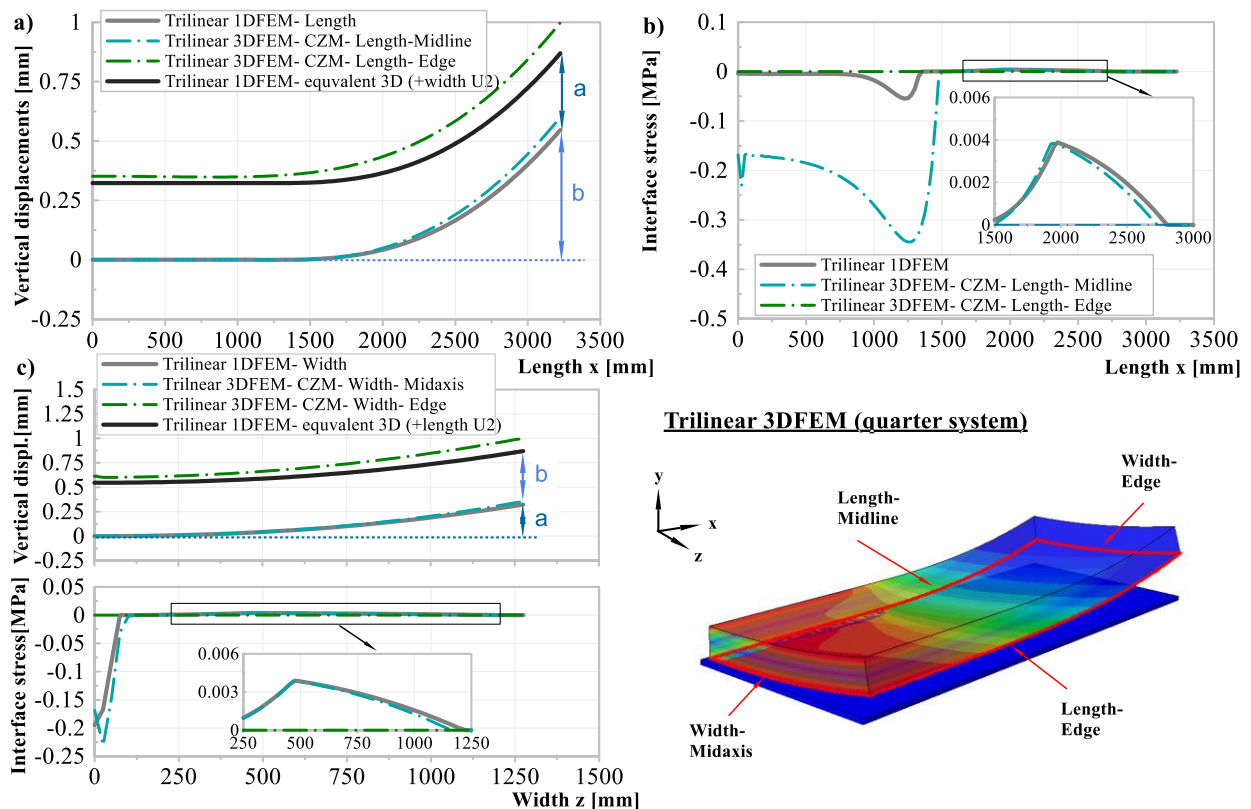


Figure 6.13 3DFEM results of trilinear vertical interface behavior

Figure 6.13 shows the simulation results of the trilinear 3DFEM with cohesive stiffness in Mode I $K_{nn} = 0.10625 \text{ MPa/mm}$, cohesive stiffness in Mode II $K_{ss} = 10^{-4} \text{ MPa/mm}$, maximum separation for damage initiation $\delta_m^0 = 0.0368 \text{ mm}$, effective damage separation at fully failure $\delta_m^f = 0.292 \text{ mm}$ and hard contact normal behavior under temperature gradient $\Delta T/t = -0.05 \text{ K/mm}$. The results are similar with the linear 3DFEM. The interface stresses in tension are however much smaller due to the damage while the interface stresses in compression are much larger since the compressive stiffness increases hugely. What's more, the maximum vertical displacements of midline and edge line along both length and width are bigger than the ones in linear 3DFEM. It should be noticed that the equivalent vertical displacement curve of edge line here has smaller value than the one in 3DFEM. Nevertheless, only the elastic model is used for limit state study, so that the equivalent curve could still be utilized in the further study for appropriate purposes.

6.3 Parameter study

Through the above analysis, it could be found that the results of 1D models (analytical model or FEM) have a good accordance with 2DFEM with connector elements or with CZM. Although the results of 1D models differ from 3DFEM, they could still represent the influences of each parameter in two dimensions. Thus, the 1D analytical models are used to study the influences of interface parameters. On the other hand, the maximum vertical displacement occurs at four corners in 3D models. Whereas, the equivalent vertical displacement curve of edge line in 1D models could be utilized to obtain the maximum vertical displacement at the corner. As a result, the equivalent 1D analytical models are adopted for limit state study under temperature gradients.

6.3.1 Interface parameter study

In the following Figure 6.14, interface shear stresses, beam bending moment, degree of restraint as well as interface damage scalar under various temperature gradients are displayed. Different phases (i.e. elastic

compression, elastic tension, damage evolution in tension and free of interface restraint) of interface could be observed in the diagram of interface normal stresses. The beam bending moment at end equals to zero since the restraint at beam end is free and it reaches the maximum value at mid axis due to its largest restraint degree at this location. It could also be observed that the bending moment at mid axis increases with increasing temperature gradient (absolute value). What's more, the bending moments in compression area increase while the ones in tension area increase firstly and then decrease with increasing temperature gradients. This is because that the interface in compression area exists no damage, whereas the interface in tension area damages more once it reaches its damage initiation criterion with increasing temperature gradients.

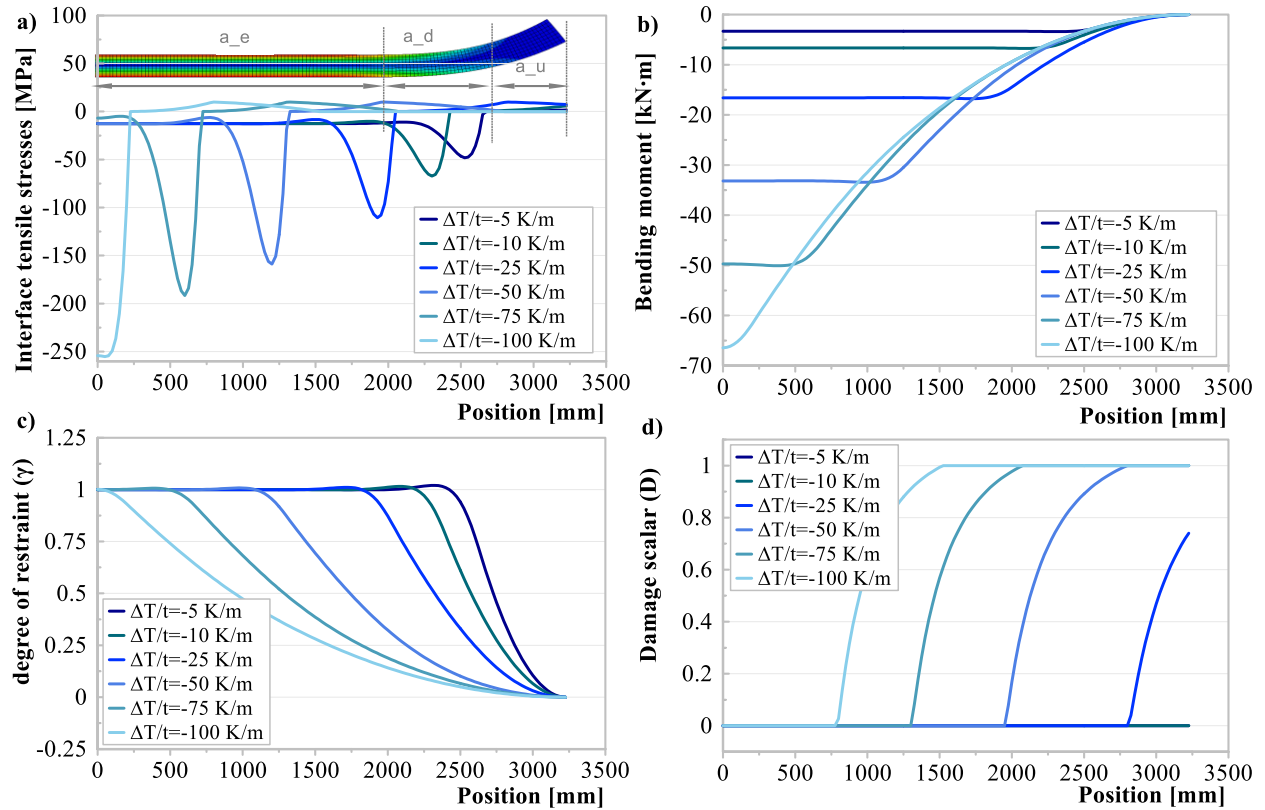


Figure 6.14 Vertical interface behavior under various negative temperature gradient variations

According to equation (2.19), the degree of restraint under temperature gradients could be express as

$$\gamma(M) = \frac{M}{EI\alpha_T\Delta T/t} \quad (6.55)$$

While the interface damage scalar in this case could be determined based on equation (3.20) as

$$D(v) = \begin{cases} 0, & v_0 \leq v \\ \frac{v_f(v - v_0)}{v(v_f - v_0)}, & v_f \leq v < v_0 \\ 1, & v < v_f \end{cases} \quad (6.56)$$

The restraint degree at beam end equals to zero owing to the free restraint at this location. For a slab under negative temperature gradients, the interface damages from edge to middle area. Meanwhile the interface at slab middle is under compression and interface at slab edge is under tension. The degree of restraints in most

compression area is around 1 due to the big restraint effect of large compressive interface stiffness. In some area near to the turning point where the compression turns into tension, the degree of restraint could even exceed 1, which indicates an over-restraint condition at this location. The interface degree of restraint then decreases to zero from the exterior compression area to the tension area. On the other hand, the interface damage scalar keeps zero in compression area where no damage exists and starts to decrease in tension area once the damage initiation criterion is satisfied.

Similar with analysis in chapter 5.3.1, stress-slip curves shown in Figure 6.15 are applied in the model to study the influences of different interface parameters on the interface degradation. The impacts of elastic compressive stiffness k_1 , tensile stiffness k_2 , damage initiation slip δ_m^0 (or maximum tensile stress σ_e) and slip for complete failure δ_m^f will be studied.

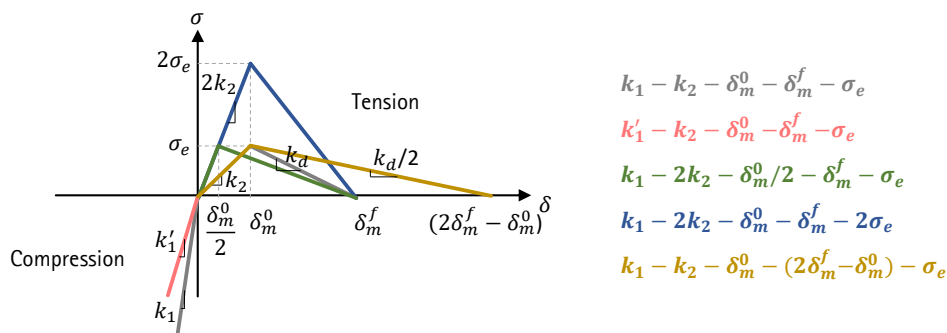


Figure 6.15 Presentation of studied vertical interface parameters

Figure 6.16 shows the influences of interface parameters on degree of restraint at mid-axis and length of different phases (i.e. the length of elastic phase a_e , damage evolution a_d and unrestraint phase a_u meanwhile in some cases the length of compression phase a_c and elastic tension phase a_t , what's more $a_e = a_c + a_t$) under increasing temperature gradient variations.

As we could find in the Figure 6.14, the degree of restraint at mid axis keeps around 1 by cause of large compressive stiffness meanwhile no damage in compression. Thus the degree of restraint at mid axis could not represent the restraint effect and resistance ability of the whole interface under temperature gradients so well as the cases under uniform temperature variations. In Figure 6.16 a) could also be observed that the degree of restraint at mid-axis firstly keeps constant around 1, then increases and finally decreases with increasing absolute values of the temperature gradients. Compressive stiffness k_1 (i.e. the grey curve) has the most significant influence on the degree of restraint at mid axis. The reduction of compressive stiffness could firstly decrease the degree of restraint a little bit, then increase and finally decrease the degree of restraint at mid axis compared to the one with larger compressive stiffness (i.e. the red curve). Keeping δ_m^0 unchanged meanwhile increasing tensile stiffness k_2 (i.e. the blue curve) as well as increasing the slip at failure (i.e. the violet curve) have a positive influence on the degree of restraint at mid axis since they retard the decrease of degree restraint. Whereas, increasing the interface tensile stiffness and keeping strength unchanged (i.e. the green curve) has insignificant impact on the degree of restraint at mid axis.

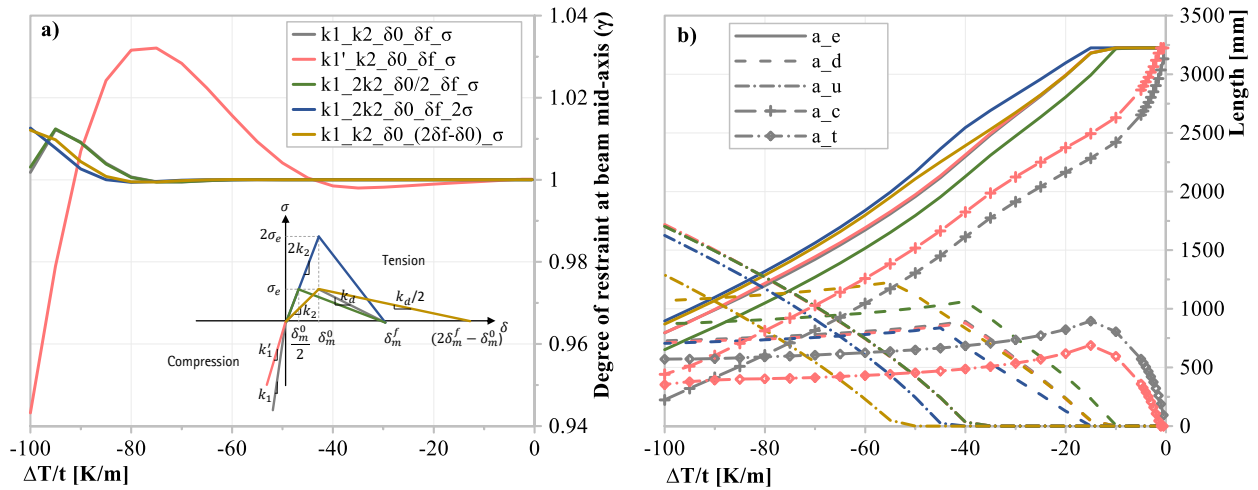


Figure 6.16 Influence of vertical parameters on degree of restraint and different phase lengths ($k_{10} = 300 \text{ MPa/mm}$, $k'_{10} = 6.7 \text{ MPa/mm}$, $k_{20} = 0.10625 \text{ MPa/mm}$, $\delta_m^0 = 0.0368 \text{ mm}$, $\delta_m^f = 0.292 \text{ mm}$)

The lengths of different phases with various interface parameters under temperature gradients are displayed in Figure 6.16 b). With increasing absolute values of temperature gradients, interface length in linear phase a_e decreases monotonously, while damage evolution length a_d increases first and then decreases when unrestraint phases appears. Unrestraint length a_u increases monotonously.

The compressive stiffness k_1 has almost no influence on the lengths of elastic, damage evolution and unrestraint. However, the decrease of compressive stiffness could increase the compressive length part and reduce the tensile part in the whole elastic length (see the gray and red curves). Keeping δ_m^0 unchanged meanwhile increasing tensile stiffness k_2 (i.e. the blue curve) could increase the elastic length and reduce the unrestraint length leading to a positive impact on the interface damage. Whereas increasing the interface tensile stiffness and keeping strength unchanged (i.e. the green curve) could reduce the elastic length and increase the damage evolution length, which results in a negative impact on interface damage overall. This is because in this case, the damage initiation slip reduces and thus the interface could start to damage under a relative smaller temperature gradient (absolute value) leading to a reduction of elastic length. On the other hand, increasing the slip at failure (i.e. the violet curve) could otherwise reduce the unrestraint length and increase the elastic and damage evolution lengths that in general alleviates the interface damage. The influences of various interface parameters on lengths of different phases are also mostly in accordance with the influence of parameters on degree of restraint at mid axis.

6.3.2 Limit value study

6.3.2.1 Under temperature gradient variation

The values of vertical linear temperature difference components are recommended in Table 6.1 of EN1991-1-5 [148], where the linear temperature difference for heating $\Delta T_{M,heat}$ and the linear temperature difference for cooling $\Delta T_{M,cool}$ are listed.

$$\begin{cases} \Delta T_{M,heat} = 15 \text{ K} \\ \Delta T_{M,cool} = -8 \text{ K} \end{cases} \quad (6.57)$$

As discussed before, given same absolute value, negative temperature gradients are more unfavorable than positive ones. In order to analyze the limit value of interface, the most unfavorable case should be used. Thus,

$\Delta T_{M,cool} = -15 \text{ K}$ is applied here. Considering the slab thickness $t = 200 \text{ mm}$, the loaded temperature gradient is $\Delta T/t = -75 \text{ K/m}$. The whole interface should be in elastic phase under maximum temperature gradient, which means the interface vertical displacement at the corner of slab should be no bigger than vertical damage initiation slip δ_m^0 . As a result, the lower limit δ_m^0 for serviceability here equals to the maximum vertical interface displacements at slab corner.

The following Figure 6.17 demonstrates the lower limit surface curve of a bilinear vertical interface behavior under temperature gradient. Figure 6.17 a) discusses the influence of slab length and width on the limit vertical damage initiation slip δ_m^0 . It could be found that with increasing the dimension in width or length could enlarge the lower limit δ_m^0 . However, when the slab width and length come to the values larger than 2500 mm, the dimensions would have a much smaller influence on the lower limit δ_m^0 . Figure 6.17 b) studies the influence of interface tensile stiffness and slab length on the lower limit δ_m^0 . It could be observed that increasing the tensile stiffness could reduce the lower limit δ_m^0 limit dramatically. For example, the slab with tensile interface stiffness $K_{nn} = 0.1 \text{ MPa/mm}$ and width 2500 mm has a lower limit $\delta_m^0 = 0.6549 \text{ mm}$ while the slab with tensile interface stiffness $K_{nn} = 1 \text{ MPa/mm}$ and width 2500 mm has a lower limit $\delta_m^0 = 0.2323 \text{ mm}$. The limit value reduces 64.5%. Obviously, the increase of tensile interface stiffness could reduce the required δ_m^0 . Same with the results in Figure 6.17 a), the influence of slab dimension would vanish once it reaches a certain value. With increasing tensile interface stiffness, this value also increases. When the tensile interface stiffness is 0.1 MPa/mm, the value goes to 3000 mm whereas when the tensile interface stiffness is 1 MPa/mm, the value goes to 2000 mm. For a slab in the case of CRTS II with tensile interface stiffness $K_{nn} = 0.10625 \text{ MPa/mm}$, slab width 2550 mm, length 6450 mm and thickness 200 mm, the lower limit δ_m^0 lays at 0.65 mm under temperature gradient -75 K/m .

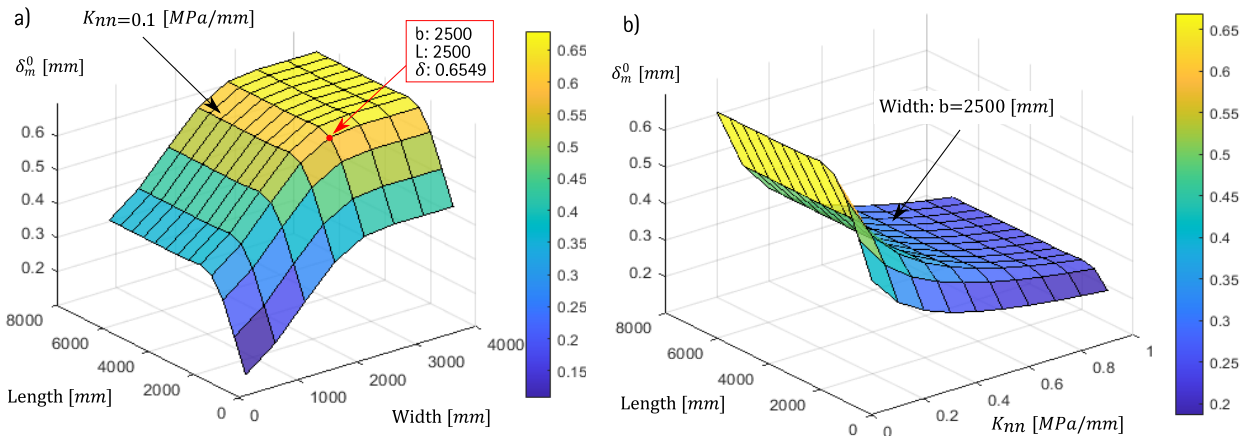


Figure 6.17 The lower limit surface for an elastic bilinear vertical interface behavior ($K_{norm} = 300 \text{ MPa/mm}$) under temperature gradient $\Delta T/t = -75 \text{ K/m}$: a) maximum vertical displacement of the slab δ_m^0 as a function of slab width b and length L with an interface tensile stiffness $K_{nn} = 0.1 \text{ MPa/mm}$; b) maximum vertical displacement of the slab δ_m^0 as a function of interface tensile stiffness K_{nn} and slab length L with a slab width $b = 2500 \text{ mm}$

6.3.2.2 Under uniform temperature variation

As discussed in chapter 5.2, the slab under uniform temperature variation could also arouse flexural deformation (i.e. vertical interface displacements) due to eccentric loading. As a result, it's also necessary to study the limit value of vertical interface behavior under uniform temperature variations. Equation (5.58) shows the recommended negative uniform temperature variation $\Delta T = -26 \text{ K}$.

Figure 6.18 shows the influence of interface tensile stiffness K_{nn} and shear stiffness K_{ss} on the lower limit vertical damage initiation slip δ_m^0 for a bilinear vertical interface behavior under uniform temperature

variation $\Delta T = -26\text{ K}$ based on 3DFEM. It could be discovered that the maximum vertical interface displacement at slab corner is an interactive result of interface tensile stiffness K_{nn} and shear stiffness K_{ss} . When the shear stiffness keeps the same, increasing tensile stiffness could reduce the lower limit δ_m^0 . However, when the tensile stiffness stays unchanged, increasing shear stiffness could otherwise increase the lower limit δ_m^0 . It could be found that it's the ratio of vertical and shear stiffness K_{nn}/K_{ss} that has the essential influence on vertical interface displacements under uniform temperature variations. It's because that higher vertical stiffness could restrain the slab deformation more, given the same shear stiffness. When the shear stiffness increases, the slab deformation would go to vertical direction given the same vertical stiffness.

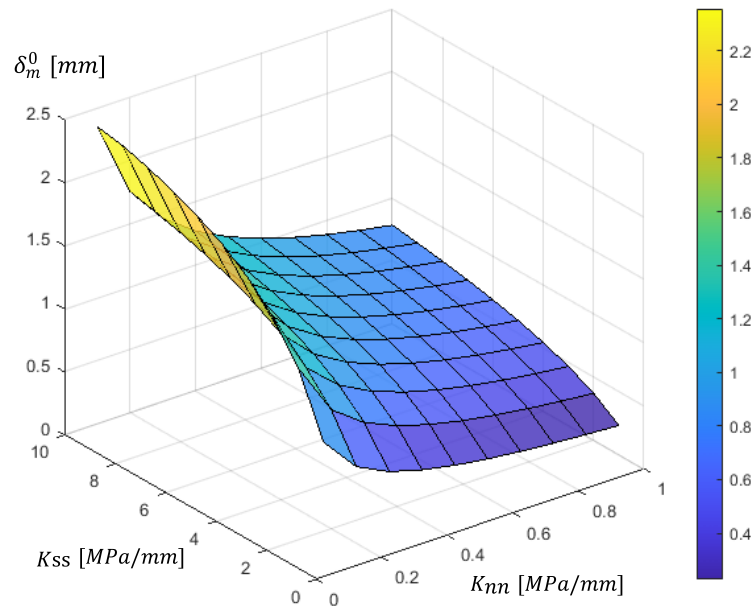


Figure 6.18 The lower limit surface for an elastic bilinear vertical interface behavior under uniform temperature variation $\Delta T = -26\text{ K}$ (maximum vertical displacement of the slab δ_m^0 as a function of interface tensile stiffness K_{nn} and interface shear stiffness K_{ss} with slab length $L = 6450\text{ mm}$ and width $b = 2550\text{ mm}$)

It could also be found that, the maximum vertical displacement at slab corner under uniform temperature variation $\Delta T = -26\text{ K}$ is actually much more unfavorable than the case under linear temperature difference $\Delta T_{M,cool} = -15\text{ K}$. For a slab in the case of CRTS II with tensile interface stiffness $K_{nn} = 0.1625\text{ MPa/mm}$, slab width 2550 mm , length 6450 mm and thickness 200 mm , the lower limit δ_m^0 lays at 1.60 mm under uniform temperature variation -26 K .

6.3.2.3 Influence of slab thickness

In the above discussion, the slab dimensions in width and length are studied. Nevertheless, the influence of slab thickness remains still unclear. Figure 6.19 shows the influence of slab thickness on the maximum interface displacements under various temperature load cases. It could be found that the increasing of slab thickness could lead to the increase of maximum longitudinal interface displacement at slab end under uniform temperature variation 29 K . Whereas the maximum vertical interface displacement at slab corner under uniform temperature variation -26 K would firstly increases until thickness goes to 300 mm and then decrease. For the maximum vertical interface displacement under temperature gradient, two cases should be studied. When the temperature gradient keeps the same, e.g. -75 K/m , the linear temperature difference increases with the thickness increase. In this case, the maximum vertical interface displacement is almost in linear proportion with the slab thickness. However, when the linear temperature difference stays the same

regardless of thickness increase, e.g. -15 K, the maximum vertical interface displacement also increases but the differences becomes smaller with increasing thickness. When the thickness is larger than 300 mm, the influence of thickness on the vertical interface displacement turns to be insignificant.

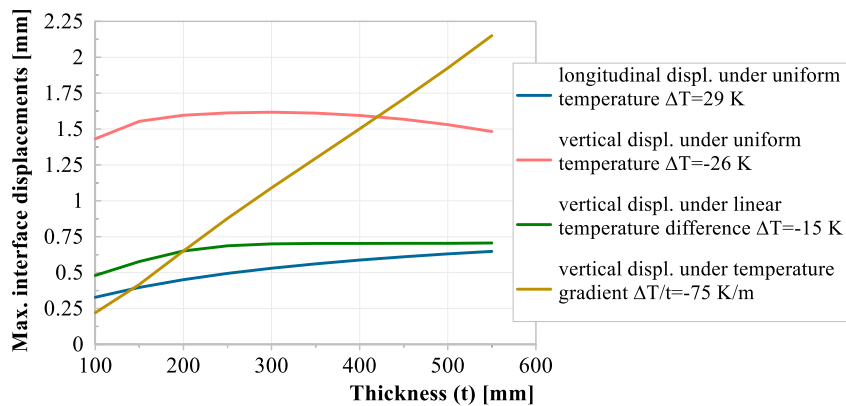


Figure 6.19 Influence of slab thickness on the maximum interface displacement under various temperature load cases ($L = 6450\text{mm}$, $b = 2550\text{mm}$, $K_{nn} = 0.10625\text{ MPa/mm}$, $K_{ss} = 3\text{ MPa/mm}$)

6.4 Summary

In this chapter, vertical interface behavior under temperature gradients is studied. Analytical models as well as 1D, 2D and 3DFEM are used to investigate the interface behavior. What's more, parameter studies are also implemented to learn the influences of different interface parameters as well as to explore the limit state.

(1) Analytical models and 1DFEM

- Analytical models with consideration of Winkler's foundation (i.e. linear elastic behavior), Winkler's foundation with damage, bilinear vertical interface behavior and trilinear vertical interface behavior are developed and the results of analytical models have a very good accordance with the 1DFEM. What's more, there exist no difference between 1D centric loading and eccentric loading FEM under temperature gradients.
- The beam end has the largest positive vertical interface displacement and tensile interface stress, whereas the interface displacement at symmetric axis (mid axis) has negative value and interface stress here is in compression under negative temperature gradients. The result values reverse under positive temperature gradient with the same absolute value. In this case, beam end has negative vertical interface displacement and compressive interface stress, whereas the mid axis has positive interface displacement and tensile stress. The moment and shear force at beam end are equal to zero for the free of restraint at this spot, while the moment at mid axis reaches its maximum absolute value due to its largest restraint here.
- When damage criterions in tension are considered, the interface stress would then reduce once it reaches its damage initiation criterion. The interface stress drops to zero when the damage criterion at complete failure is satisfied. Different phases of the interface could thus be observed in the interface stress diagram. Since the damage of interface could reduce the interface restraint generally, the interface displacements would increase and bending moment of the beam would otherwise decrease.
- It's found that the amplitude of positive temperature gradients leading the interface damage initiation is much bigger than the one of negative temperature gradients. This means that the interface under negative temperature gradients are much easier to damage compared with the case under positive temperature gradients, which also corresponds to practical experiences where most

concrete-to-concrete interface damage starts from edge to middle. Thus, the analysis for vertical interface behavior will focus on the case under negative temperature gradients.

- (e) The compressive interface stiffness has almost no influence on the maximum interface displacement at beam end. However, the maximum interface displacement at beam end increase dramatically when interface damage is considered. What's more, this value is smaller in trilinear model than the one in the model of Winkle's foundation with damage, which indicating a positive influence of the damage evolution phase on the interface restraint ability.
- (2) 2DFEM
- (a) The 2DFEM with connector elements has almost the same results with 1DFEM.
 - (b) In the FEM with CZM in contact interaction, the stiffness in tension and in compression are defined otherwise seperately. The cohesive stiffness K_{nn} in Mode I of CZM equals to equivalent the linear vertical stifnness in 1DFEM or 2DFEM with connector elements, see equations (5.52) and (5.53). However, the stiffness K_{norm} in linear contact normal behavior needs to be very small compared to K_{nn} , in order to obtain the linear vertical interface behavior same as 1DFEM or 2DFEM with connector elements. It's also found that, the increase of cohesive stiffenss K_{ss} in mode II leads to decrease of vertical interface displacement at beam end. Thus, the studies on vertical interface behavior will neglect or set with a very samll value of the shear stiffness K_{ss} in mode II for its unfavourable case.
 - (c) There are three ways to implements the bilinear vertical interface behavior in FEM: (i) define the bilinear connector stiffness in 1DFEM or 2DFEM; (ii) define the stiffness K_{norm} of linear contact normal behavior and cohesive stiffness K_{nn} of CZM; (iii) define a hard contact normal behavior and specify the cohesive stiffness K_{nn} of CZM. There exists almost no big difference between different models especially for the vertical interface displacements. Small scatter appears at the compressive interface stress peak. In general, the difference between these models are very small and the results of them are in a good accordance.
 - (d) Introducing damage criterion into the bilinear vertical interface behavior leads to trilinear vertical interface behavior. In this case, the result differences between various models become bigger. The 2DFEM with connector elements has the largest difference with the other three models. The interface stress difference in compression is also larger than in tension. In the tension area, only the 2DFEM with connector has somehow differences with other three models, while the results of four models differentiate with each other in compression area. In general, the four models could all be used in simulation, while the 2DFEM with connector elements has the largest variation compared with the other three models.
- (3) 3DFEM
- (a) The actual vertical displacements of slab are a superposition of the vertical displacements along width and length. The vertical displacements of the midline along both length and width are smaller than the ones of edge line along length and width. The corner of the slab has thus the maximum vertical displacements. The vertical displacement curve of 1DFEM lays in between the vertical displacement curves of midline and edge line of 3DFEM meanwhile it's prone to be closer to the displacement curve of midline of 3DFEM especially for the curve along width.
 - (b) By adding the maximum vertical displacement difference of the midline along width [i.e. variable a in Figure 6.12 c)] to the vertical displacement curve of midline along length in 1D model, gives a quasi-equivalent vertical displacement curve of edge line along length [see Figure 6.12 a)]. Similarly, the quasi-equivalent vertical displacement curve of edge line along width [see Figure 6.12 c)] could also be obtained by adding the maximum vertical displacement difference of midline along length in 1D model [i.e. variable b in Figure 6.12 a)]. Since the recalculated equivalent vertical displacement

curve of edge line has larger values than the one in 3DFEM, it could be used in the further limit state study for its unfavorable condition.

(4) Parameter study

- (a) The 1D analytical models are used to study the influences of interface parameters in two dimensions. Whereas, the equivalent vertical displacement curve of edge line in 1D models could be utilized to obtain the maximum vertical displacement at the corner. As a result, the equivalent 1D analytical models are adopted for limit state study under temperature gradients.
- (b) The bending moment at mid axis increases with increasing temperature gradient (absolute value). The bending moment in compression area increase while the ones in tension area increase firstly and then decrease with increasing temperature gradients. This is because that the interface in compression area exists no damage, whereas the interface in tension area damages more once it reaches its damage initiation criterion with increasing temperature gradients.
- (c) The restraint degree at beam end equals to zero owing to the free restraint at this location. The degree of restraints in most compression area is around 1 due to the big restraint effect of large compressive interface stiffness. In some area near to the turning point where the compression turns into tension, the degree of restraint could even exceed 1, which indicates an over-restraint condition at this location. The interface degree of restraint then decreases to zero from the exterior compression area to tension area. On the other hand, the interface damage scalar keeps zero in compression area where no damage exists and starts to decrease in tension area once the damage initiation criterion is satisfied.
- (d) The degree of restraint at mid axis keeps around 1 by cause of large compressive stiffness meanwhile no damage in compression. Thus the degree of restraint at mid axis could not represent the restraint effect and resistance ability of the whole interface under temperature gradients so well as the cases under uniform temperature variations.
- (e) The degree of restraint at mid-axis firstly keeps constant around 1, then increases and finally decreases with increasing absolute values of the temperature gradients. Compressive stiffness k_1 has the most significant influence on the degree of restraint at mid axis. The reduction of compressive stiffness could firstly decrease the degree of restraint a little bit, then increase and finally decrease the degree of restraint at mid axis compared to the one with larger compressive. Keeping δ_m^0 unchanged meanwhile increasing tensile stiffness k_2 as well as increasing the slip at failure have a positive influence on the degree of restraint at mid axis since they retard the decrease of degree restraint. Whereas, increasing the interface tensile stiffness and keeping strength unchanged has insignificant impacts on the degree of restraint at mid axis.
- (f) With increasing absolute values of temperature gradients, interface length in linear phase a_e decreases monotonously, while damage evolution length a_d increases first and then decreases when unrestraint phases appears. Unrestraint length a_u increases monotonously.
- (g) The compressive stiffness k_1 has almost no influence on the lengths of elastic, damage evolution and unrestraint. However, the decrease of compressive stiffness could increase the compressive length part and reduce the tensile part in the whole elastic length. Keeping δ_m^0 unchanged meanwhile increasing tensile stiffness k_2 could increase the elastic length and reduce the unrestraint length leading to a positive impact on the interface damage. Whereas increasing the interface tensile stiffness and keeping strength unchanged could reduce the elastic length and increase the damage evolution length, which results in a negative impact on interface damage overall. This is because in this case, the damage initiation slip reduces and thus the interface could start to damage under a relative smaller temperature gradient (absolute value) leading to a reduction of elastic length. On the other hand, increasing the slip at failure could otherwise reduce

the unrestraint length and increase the elastic and damage evolution lengths that in general alleviates the interface damage.

- (h) The influences of various interface parameters on lengths of different phases are also mostly in accordance with the influence of parameters on degree of restraint at mid axis.
- (5) Limit state study
- (a) The whole interface should be in elastic phase under maximum temperature gradient, which means the interface vertical displacement at the corner of slab should be no bigger than vertical damage initiation slip δ_m^0 . As a result, the lower limit δ_m^0 here equals to the maximum vertical interface displacements at slab corner.
- (b) With increasing the dimension in width or length could enlarge the lower limit δ_m^0 . However, when the slab width and length come to the values larger than 2500 mm, the dimensions would have a much smaller influence on the lower limit δ_m^0 , considering a tensile interface stiffness $K_{nn} = 0.1 \text{ MPa/mm}$.
- (c) Increasing the tensile stiffness could reduce the lower limit δ_m^0 limit dramatically. The influence of slab dimension would vanish once it reaches a certain value. With increasing tensile interface stiffness, this value also increases.
- (d) For a slab in the case of CRTS II with tensile interface stiffness $K_{nn} = 0.1625 \text{ MPa/mm}$, slab width 2550 mm, length 6450 mm and thickness 200 mm, the lower limit δ_m^0 lays at 0.65 mm under temperature gradient -75 K/m .
- (e) The maximum vertical interface displacement at slab corner is an interactive result of interface tensile stiffness K_{nn} and shear stiffness K_{ss} under uniform temperature variations. When the shear stiffness keeps the same, increasing tensile stiffness could reduce the lower limit δ_m^0 . However, when the tensile stiffness stays unchanged, increasing shear stiffness could otherwise increase the lower limit δ_m^0 .
- (f) It's the ratio of vertical and shear stiffness K_{nn}/K_{ss} that has the essential influence on vertical interface displacements under uniform temperature variations. It's because that higher vertical stiffness could restrain the slab deformation more, given the same shear stiffness. When the shear stiffness increases, the slab deformation would go to vertical direction given the same vertical stiffness.
- (g) For a slab in the case of CRTS II with tensile interface stiffness $K_{nn} = 0.1625 \text{ MPa/mm}$, slab width 2550 mm, length 6450 mm and thickness 200 mm, the lower limit δ_m^0 lays at 1.60 mm under uniform temperature variation -26 K .
- (h) The maximum vertical displacement at slab corner under uniform temperature variation $\Delta T = -26 \text{ }^\circ\text{C}$ is much more unfavorable than the case under linear temperature difference $\Delta T_M = -15 \text{ K}$.
- (i) The increasing of slab thickness could lead to the increase of maximum longitudinal interface displacement at slab end under uniform temperature variation 29 K. Whereas the maximum vertical interface displacement at slab corner under uniform temperature variation -26 K would firstly increases until thickness goes to 300 mm and then decrease.
- (j) For the maximum vertical interface displacement under temperature gradient, two cases should be studied. When the temperature gradient keeps the same, e.g. -75 K/m , the linear temperature difference increases with the thickness increase. In this case, the maximum vertical interface displacement is almost in linear proportion with the slab thickness. However, when the linear temperature difference stays the same regardless of thickness increase, e.g. -15 K , the maximum vertical interface displacement also increases but the differences becomes smaller with increasing thickness. When the thickness is larger than 300 mm, the influence of thickness on the vertical interface displacement turns to be insignificant.

7. Conclusion and outlook

7.1 Conclusion

This dissertation dealt with concrete-to-concrete interface damage mechanism under temperature loads. Direct tensile tests and push-off tests were designed and implemented to obtain the interface fracture parameters in mode I and mode II. A manual iterative inverse analysis based on FEM was used to calibrate the interface bond-slip relationships in both normal and tangential directions according to test results. The concrete interface restraint along one edge of the slab under temperature loads was investigated by the means of analytical solutions and numeric simulations. In the analytical solutions, 1D centric loading models for linear elastic interface behavior and trilinear interface behavior with consideration of damage criterions were developed step by step for structure under uniform temperature variations and temperature gradients. The analytical solutions were validated by the 1DFEMs. Furthermore, the 2DFEM with connector elements, 2DFEM with CZM in contact interaction as well as 3DFEM with CZM were employed to carry out simulations more precisely. Finally, investigations were implemented regarding interface parameter studies (e.g. interface stiffness, strength, damage initiation slip, slip at complete failure, etc.) with respect to the influences on the interface damage as well as slab geometric parameters (e.g. slab length, width and thickness) combined with interface parameters for limit state studies, in order to find out the proper design parameters for slab track systems. The main contents of the analysis in this thesis could then be summarized as follows:

- determination of interface characteristics based on laboratory experiments (i.e. direct tensile tests and push-off tests) and inverse analysis calibration procedure according to FEM;
- analytical solutions for interface behavior under uniform temperature variations in longitudinal direction and under temperature gradients in vertical direction;
- numerical simulations with connector elements and CZM in contact interaction for interface behavior under temperature loads;
- parameter studies on the interface damage and the serviceability limit state.

In the analysis, the following conclusions were obtained:

(1) Determination of interface characteristics

In the direct tensile tests, the tilt of the specimen occurs easily. However, the iterative inverse analysis based on FEM with the consideration of eccentricity could be implemented to calibrate the testing results and to obtain the actual interface bond-slip relationship in mode I. The optimized CZM parameters in Mode I at interface with the consideration of eccentricities were listed in Table 4.9. The relationship between fracture energy and the eccentricity was expressed in equation (4.4).

The push-off tests indicated a mix-mode fracture mechanism, since both tangential and normal interface displacements at damaged interface were measured. The reasons for this phenomenon may be due to a) volume dilatancy after interface damage occurred; b) technical difficulty to load perfectly at interface line; c) self-weight of the loading concrete part. The ultimate shear strengths of push-off tests were much higher than tensile strengths due to the contribution of aggregate interlock. The determined friction coefficients were also much higher than expected values for "smooth" category in Model Code 2010. This may be due to the sticky behaviour of asphalt component in CAM. Inverse analysis should also be used to gain the interface bond-slip relationship in mode II. A suggested fracture parameter set for interface between concrete and CAM with an exponential softening behavior was listed in Table 4.11.

(2) Longitudinal interface behavior under uniform temperature variations

The beam end has the largest interface displacements, while the interface displacements and stresses at symmetric axis (mid axis) are equal to zero for the structure restrained by one edge of bonding interface under uniform temperature variations. The interface damage in trilinear behavior leads to a larger interface displacement at slab end compared to the one in linear interface behavior. This is because the interface degradation causes reduction of restraint and thus increases the thermal deformation of slab. The beam stress induced from deformation restraint has a negative correlation with beam strain, see equation (5.23). Hereby, the beam end is free from interface restraint, thus the beam stress at the end side is zero meanwhile this restraint free side has the largest beam strain. On the other hand, symmetric axis is most restrained from the interface and has therefore the smallest beam strain and largest beam stress. Different phases (i.e. linear elastic, damage evolution and friction phases) of interface could be observed in the diagram of interface shear stresses. The positive temperature variation leads to elongation of the beam while the negative variation causes beam shortening. The absolute deformations are nevertheless the same under positive and negative temperature variations with the same absolute value, which goes the same for beam axial stress.

The restraint at one edge of the slab producing an eccentric loading of the structure leads also to a deflection beam and therefore vertical displacements at interface, which meanwhile reduces the longitudinal interface displacements under uniform temperature variations. Thus, the overall longitudinal interface behavior of the beam is then not only influenced by the longitudinal interface resistance but also by the vertical interface resistance. The stiffer the vertical interface resistance K_{nn} , the smaller the vertical interface displacements and the bigger the longitudinal displacements under uniform temperature variations. Since a stiffer vertical interface stiffness provides a larger restraint in the vertical direction, the deformations caused by volume changes due to temperature would thus be released more in the longitudinal direction instead of vertical direction and vice versa. Moreover, the interface vertical stiffness K_{nn} has a much smaller impact on the longitudinal displacements of trilinear interface model than linear interface model. Thus, when the longitudinal interface is damaged, the vertical interface stiffness is then relatively "increased", resulting in more deformation in longitudinal direction.

The 1D centric models (i.e. analytical models) have the largest longitudinal deformation under uniform temperature variation compared with the one in 1D eccentric FEM, 2D and 3D FEM. Thus the analytical models are actually on the safe side for practical applications with regard to the longitudinal displacements and could be used for parameter studies.

The restraint degree at beam end equals to zero owing to the free restraint at this location. Although there exists no deformation at mid axis, the beam strain here is not zero, thus restraint degree at mid axis could not be 1. Nevertheless, the degree of restraint amounts to a maximum value at mid axis, which may be caused by an "accumulated effect" of whole interface restraint. On the other hand, interface damage scalar shows the stiffness degradation at a certain spot. In general, the more severe the interface damages, the lower the degree of restraint. However, although the damage scalar at mid-axis remains zero (i.e. undamaged), the restraint degree here could still decrease for the sake of whole interface damage effects. Thus, degree of restraint at mid-axis could somehow represent the restraint effect as well as resistance ability from whole interface. In comparison, the damage scalar reflects more about local interface deterioration extent.

Elastic stiffness k_e decides the degree of restraint γ when the whole interface is elastic phase. Once damage occurs at interface, degree of restraint at mid-axis decreases. Strength τ_e has a more crucial influence on the degradation of the degree of restraint than interface stiffness k_e . Increasing the interface stiffness while keeping strength unchanged has insignificant impact on the interface damage, which even slightly aggravates the shortening of linear interface length a_e . On the other hand, remaining stiffness while increasing strength would alleviate the degradation of degree of

restraint. This is because the maximum elastic slip S_e determines the initiation of damage and thus influences the resistance ability of the interface restraint. Keeping S_e unchanged, increasing stiffness k_e has a positive influence on the interface damage. However, even when the stiffness k_e is increased, the maximum elastic slip S_e decreases given the same strength τ_e , which leads to a negative effect on the interface degradation. Residual friction τ_u determines the end value which restraint degree approaches. The smaller the damage evolution rate k_d , the slower the degree of restraint γ approaches the end value. With increasing temperature variation, interface length in linear phase a_e decreases monotonously, while damage length a_d increases first and then decreases when friction phases appears. Friction length a_u increases monotonously. The interface stiffness k_e and maximum elastic slip S_e together influence the reduction of elastic length, whereas the maximum damage slip S_u mainly determines the initiation of friction phases.

For a safe application of interfacial bonded slab, the longitudinal interface behavior should stay in linear elastic phase under uniform temperature variation, which means the interface displacement at slab end should be no bigger than maximum elastic slip S_e . Thus, the limit state of the interface could be expressed as the equation (5.59). The longer the slab length L is and the smaller the interface stiffness k is, the larger the limit value of maximum elastic slip S_e is. For longer slab length, the interface stiffness has larger influence on the limit value of maximum elastic slip. The scatter of the limit value of maximum elastic slip is also bigger for longer slab. However the differences between $S_e - k$ curves of various slab lengths become smaller with increasing slab length. For a slab length of 6.45 m with a shear interface stiffness of 3 MPa/mm in this case, the lower limit maximum elastic slip S_e should be 0.451 mm. Therefore, reinforcements should be used across the interface in order to obtain enough resistance. Obviously, the increase of interface stiffness could reduce the required S_e .

(3) Vertical interface behavior under temperature gradients

The beam end has the largest positive vertical interface displacement and tensile interface stress, whereas the interface displacement at symmetric axis (mid axis) has negative value and interface stress here is in compression under negative temperature gradients. The result values reverse under positive temperature gradient with the same absolute value. In this case, beam end has negative vertical interface displacement and compressive interface stress, whereas the mid axis has positive interface displacement and tensile stress. The moment and shear force at beam end are equal to zero for the freedom from restraint at this spot, while the moment at mid axis reaches its maximum absolute value due to its largest restraint here. When damage criteria in tension are considered, the interface stress would then reduce once it reaches its damage initiation criterion. The interface stress drops to zero when the damage criterion at complete failure is satisfied. Different phases of the interface could thus be observed in the interface stress diagram. Since the damage of interface could reduce the interface restraint generally, the interface displacements would increase and bending moment of the beam would otherwise decrease. The compressive interface stiffness has almost no influence on the maximum interface displacement at beam end. However, the maximum interface displacement at beam end increases dramatically when interface damage is considered. Moreover, this value is smaller in trilinear interface behavior than the one in the model of Winkler's foundation with damage, indicating a positive influence of the damage evolution phase on the interface restraint ability.

The amplitude of positive temperature gradients leading the interface damage initiation is much bigger than the one of negative temperature gradients. This means that the interface under negative temperature gradients is much easier to become damaged compared with the case under positive temperature gradients, which also corresponds to practical experiences where most concrete-to-concrete interface damage starts from edge to middle. Thus, the analysis for vertical interface behavior mainly focuses on the case under negative temperature gradients. The increase of cohesive

stiffness K_{ss} in mode II leads to decrease of vertical interface displacement at beam end. Thus, the studies on vertical interface behavior will neglect or set with a very small value of the shear stiffness K_{ss} in mode II for its unfavourable case.

There are three ways to implement the bilinear vertical interface behavior in FEM: (a) defining the bilinear connector stiffness in 1DFEM or 2DFEM; (b) defining the stiffness K_{norm} of linear contact normal behavior and cohesive stiffness K_{nn} of CZM; (c) defining a hard contact normal behavior and specifying the cohesive stiffness K_{nn} of CZM. There exists almost no difference between different models especially for the vertical interface displacements. Introducing damage criterion into the bilinear vertical interface behavior leads to trilinear vertical interface behavior. In this case, the result differences between various models become bigger. Nevertheless, the four models in general could all be used in simulation, while the 2DFEM with connector elements has the largest variation compared with the other three models.

The actual vertical displacements of slab are a superposition of the vertical displacements along width and length. The vertical displacements of the midline along both length and width are smaller than those of edge line along length and width. The corner of the slab has thus the maximum vertical displacements. The vertical displacement curve of 1DFEM lays in between the vertical displacement curves of midline and edge line of 3DFEM, meanwhile it's prone to be closer to the displacement curve of midline of 3DFEM. By adding the maximum vertical displacement difference of the midline along width [i.e. variable a in Figure 6.12 c)] to the vertical displacement curve of midline along length in 1D model, it gives a quasi-equivalent vertical displacement curve of edge line along length [see Figure 6.12 a)]. Similarly, the quasi-equivalent vertical displacement curve of edge line along width [see Figure 6.12 c)] could also be obtained by adding the maximum vertical displacement difference of midline along length in 1D model [i.e. variable b in Figure 6.12 a)]. Since the recalculated equivalent vertical displacement curve of edge line has larger values than that in 3DFEM, it could be used in the further limit state study for its unfavorable condition.

The bending moment at mid axis increases with increasing temperature gradient (absolute value). The bending moments in compression area increase while those in tension area increase first and then decrease with increasing temperature gradients. This is because the interface in compression area has no damage, whereas the interface in tension area is more damaged once it reaches its damage initiation criterion with increasing temperature gradients. With increasing absolute values of temperature gradients, interface length in linear phase a_e decreases monotonously, while damage evolution length a_d increases first and then decreases when unrestrained phases appears. Unrestrained length a_u increases monotonously.

The compressive stiffness k_1 has almost no influence on the lengths of elastic, damage evolution and unrestrained phases. However, the decrease of compressive stiffness could increase the compressive length part and reduce the tensile part in the whole elastic length. Keeping δ_m^0 unchanged while increasing tensile stiffness k_2 could increase the elastic length and reduce the unrestraint length, leading to a positive impact on the interface damage. Whereas increasing the interface tensile stiffness and keeping strength unchanged could reduce the elastic length and increase the damage evolution length, which results in a negative impact on interface damage overall. This is because in this case, the damage initiation slip reduces and thus the interface could start to damage under a relatively smaller temperature gradient (absolute value), leading to a reduction of elastic length. On the other hand, increasing the slip at failure could otherwise reduce the unrestraint length and increase the elastic and damage evolution lengths that in general alleviate the interface damage.

The whole interface should be in elastic phase under maximum temperature gradient, which means the interface vertical displacement at the corner of slab should be no bigger than vertical damage initiation slip δ_m^0 . As a result, the lower limit value of δ_m^0 here equals the maximum vertical interface

displacements at slab corner. Increasing the dimension in width or length could enlarge the lower limit value of δ_m^0 . However, when the slab width and length come to the values larger than 2500 mm, the dimensions have then an insignificant impact on the lower limit value of δ_m^0 , considering a tensile interface stiffness $K_{nn} = 0.1 \text{ MPa/mm}$. Increasing the tensile stiffness could reduce the lower limit value of δ_m^0 dramatically. The influence of slab dimension would vanish once it reaches a certain value. With increasing tensile interface stiffness, this value also increases. For a slab in the case of CRTS II with tensile interface stiffness $K_{nn} = 0.1625 \text{ MPa/mm}$, slab width 2550 mm, length 6450 mm and thickness 200 mm, the lower limit δ_m^0 lays at 0.65 mm under temperature gradient -75 K/m .

The maximum vertical interface displacement at slab corner is an interactive result of interface tensile stiffness K_{nn} and shear stiffness K_{ss} under uniform temperature variations. When the shear stiffness remains the same, increasing tensile stiffness could reduce the lower limit value of δ_m^0 . However, when the tensile stiffness stays unchanged, increasing shear stiffness could otherwise increase the lower limit value of δ_m^0 . It's the ratio of vertical and shear stiffness K_{nn}/K_{ss} that has the essential influence on vertical interface displacements under uniform temperature variations. This is because higher vertical stiffness could restrain the slab deformation more, given the same shear stiffness. When the shear stiffness increases, the slab deformation would go to vertical direction given the same vertical stiffness. For a slab in the case of CRTS II with tensile interface stiffness $K_{nn} = 0.1625 \text{ MPa/mm}$, slab width 2550 mm, length 6450 mm and thickness 200 mm, the lower limit value of δ_m^0 lays at 1.60 mm under uniform temperature variation -26 K . The maximum vertical displacement at slab corner under uniform temperature variation $\Delta T_N = -26 \text{ K}$ is much more unfavorable than the case under linear temperature gradient $\Delta T_M = -15 \text{ K}$.

In the most unfavorable case, the influence of uniform temperature variation is combined with linear temperature gradient ($\Delta T_N + \Delta T_M$), the lower limit value of δ_m^0 equals $1.60 \text{ mm} + 0.65 \text{ mm} = 2.25 \text{ mm}$. The vertical interface displacement is thus more crucial with respect to the interface damage, since it's effected by both uniform temperature variations and temperature gradients.

The increasing of slab thickness could lead to the increase of maximum longitudinal interface displacement at slab end under uniform temperature variation 29 K . In comparison, the maximum vertical interface displacement at slab corner under uniform temperature variation -26 K would firstly increase until thickness goes to 300 mm and then decrease. For the maximum vertical interface displacement under temperature gradient, two cases should be studied. When the temperature gradient stays the same, e.g. -75 K/m , the linear temperature difference increases with the thickness increase. In this case, the maximum vertical interface displacement is almost in linear proportion with the slab thickness. However, when the linear temperature difference stays the same regardless of thickness increase, e.g. -15 K , the maximum vertical interface displacement also increases but the differences become smaller with increasing thickness. When the thickness is larger than 300 mm, the influence of thickness on the vertical interface displacement turns out to be insignificant.

7.2 Outlook

The work on the interface damage mechanism between concrete layers in this thesis could be enhanced and extended in terms of the following aspects:

➤ Experiment approaches modification

The direct tensile test setup needs to be optimized in order to eliminate the phenomenon of specimen tilts. A solution for this could be to employ smaller-sized specimens that are fully connected with rigid steel plate meanwhile to avoid hinge in testing system. Alternative methods such as splitting experiments could also be used, which requires reverse analysis to gain the material constitutive model. What's more, Interface damage in practical engineering is usually an interaction of shear and tension. A proper feasible testing method (e.g. a modified slant shear test) to investigate interface

behaviour under tension and shear forces should be designed in further steps. What's more, in the further experiment programs, specimens with the reinforcement arrangement should also be taken into consideration.

- Long-term interface behavior under combination of shrinkage, creep and temperature variations

The interface stresses caused from deformation restraint could be induced not only by temperature loads but also by shrinkage and creep. Thus, the long-term interface behavior could also be considered in further studies. The shrinkage and creep effects may be considered as additional equivalent temperature variations in the models.

- Buckling of integrated structure under warming temperature loads

For an integrated CST system, the vertical joints under cooling temperature could be seen as open and the system is then only restrained by the interface bonding of horizontal joints between prefabricated concrete slab and CAM the structure, which is fully discussed in this thesis. However, even when the vertical joints under warming temperature are closed, limiting the movement at longitudinal interface joints, the warming temperature could lead to buckling in the integrated structure. The influence of interface restraint on the structural buckling could also be studied.

- Experimental and numerical study on interface behavior under dynamic/cyclic loading

Besides the interface behavior under monotonic loading, the interface behavior under dynamic loading is also very important in structural analysis such as vibration due to seismic or vehicle loads, etc.

- New material developments for a better interface bonding behavior

In order to obtain a better bonding interface behavior either for repair and strengthening or for new construction of concrete joints, new materials such as textile or fiber reinforced concrete could be developed combined with the considering of interface bonding behavior.

Bibliography

- [1] Randl (2013): Design recommendations for interface shear transfer in fib Model Code 2010. In: *Structural Concrete* 14.
- [2] Herbrand et al. (2017): Strengthening of Existing Bridge Structures for Shear and Bending with Carbon Textile-Reinforced Mortar. In: *Materials (Basel, Switzerland)* 10 (9).
- [3] Anant Bhosale (2017): Comparative Study of Prefabrication Constructions with Cast-in-Situ Comparative Study of Prefabrication Constructions with Cast-in-Situ Constructions. In: *International Journal of Advance Engineering and Research* 4 (3), S. 779–785.
- [4] Classen et al. (2020): Additive Manufacturing of Reinforced Concrete—Development of a 3D Printing Technology for Cementitious Composites with Metallic Reinforcement. In: *Applied Sciences* 10 (11), S. 3791.
- [5] Negro und Toniolo (2012): Design guidelines for connections of precast structures under seismic actions. Luxembourg: Publications Office (EUR Luxembourg, 25377).
- [6] Randl et al. (2008): Bemessung nachträglich ergänzter Betonbauteile mit längsschubbeanspruchter Fuge. Vergleichende Beurteilung aktueller Konzepte für die Baupraxis. In: *Beton- und Stahlbetonbau* 103 (7), S. 482–497.
- [7] Plank et al. (2015): Strukturoptimierte Türme für Offshore-Windenergieanlagen aus UHFFB in Segmentbauweise. In: *Forschungsbericht F 2935* Fraunhofer IRB Verlag, Stuttgart.
- [8] Guckenberger et al. (1980): Segmentäre Spannbetonträger im Brückenbau. DAFStb Heft. Berlin: Ernst (Deutscher Ausschuss für Stahlbeton, 311).
- [9] Lee: The Design of Bridges of Precast Segmental Construction. Technical Paper PCS 10 Sfb Df (91).
- [10] Philip W. Birkeland and Halvard W. Birkeland (1966): Connections in Precast Concrete Construction. In: *Journal Proceedings* 63 (3).
- [11] Loov und Patnaik (1994): Horizontal Shear Strength of Composite Concrete Beams With a Rough Interface. In: *pcij* 39 (1), S. 48–69.
- [12] Alan H. Mattock and Neil M. Hawkins (1972): Shear transfer in reinforced concrete - recent research. In: *Journal of the Precast/Prestressed Concrete Institut* 17(2), S. 55–75.
- [13] R.E. Loov (1978): Design of precast connections. Paper presented at a seminar organized by Compa International Pte, Ltd. Singapor.
- [14] EN 1992-1-1 (2004): Eurocode 2: Design of concrete structures - Part 1-1: General rules and rules for buildings. Brussels: European Committee for Standardization.
- [15] Joost Walraven, Jerome Frenay, Arjan Puijssers (1987): Influence of Concrete Strength and Load History on the Shear Friction Capacity of Concrete Members. In: *Journal of the Precast/Prestressed Concrete Institut* 32 (1), S. 66–84.
- [16] Tassios und Vintzeleou (1987): Concrete to Concrete Friction. In: *Journal of Structural Engineering, ASCE* 113 (4), S. 832–849.
- [17] Tsoukantas und Tassios (1989): Shear resistance of connections between reinforced concrete linear precast elements. In: *ACI Structural Journal* 86 (3), S. 242–249.
- [18] CEB-FIP (1993): Mode Code 1990. Design code. Lausanne: Telford (Bulletin d'information / Comité Euro-International du Béton, 213/214).

- [19] N. Randl (1997): Untersuchungen zur Kraftübertragung zwischen Alt- und Neubeton bei unterschiedlichen Fugenrauigkeiten. Dissertation. Institut für Betonbau der Leopold-Franzens-Universität Innsbruck, Innsbruck.
- [20] Randl und Wicke (2000): Schubübertragung zwischen Alt- und Neubeton. Experimentelle Untersuchungen, theoretischer Hintergrund und Bemessungsansatz. In: *Beton- und Stahlbetonbau* 95 (8), S. 461–473.
- [21] Randl et al. (2005): Verstärkung von Brückentragwerken durch Aufbeton. In: *Bauingenieur* (4), S. 207–214.
- [22] Silfwerbrand (1990): Improving concrete bond in repaired bridge decks. In: *Concrete International* 12 (9), S. 61–66.
- [23] Santos et al. (2007): Correlation between concrete-to-concrete bond strength and the roughness of the substrate surface. In: *Construction and Building Materials* 21 (8), S. 1688–1695.
- [24] Müller und Zilch (2008): New insights into mechanisms influencing the bond strength between old and new concrete. 37th Conference of Canadian Society for Civil Engineering. Quebec.
- [25] Walraven und Reinhardt (1981): Theory and experiments on the mechanical behavior of cracks in plain and reinforced concrete subjected to shear loading. Civil Engineering of the Delft University of Technology. 26 Bände. Delft, The Netherlands: HERON.
- [26] Franz (1959): Versuche über die Querkraftaufnahme in Fugen von Spannbetontägern aus Fertigteilen. In: *Beton- und Stahlbetonbau* 54 (7), S. 199–206.
- [27] Zelger und Rüschi (1961): Der Einfluss von Fugen auf die Festigkeit von Fertigteildecken. In: *Beton- und Stahlbetonbau* 56 (10), S. 234–237.
- [28] Daschner und Kupfer (1986): Literaturstudie zur Schubsicherung bei nachträglich ergänzten Querschnitten. DAFStb Heft. Berlin: Ernst, Verlag für Architektur u. Techn. Wiss (Deutscher Ausschuss für Stahlbeton, 372).
- [29] Nissen (1987): Rissverzahnung des Betons. gegenseitige Rissuferverschiebungen und übertragene Kräfte. Dissertation. München: Lehrstuhl für Massivbau der Technische Universität München.
- [30] Reinecke (2004): Haftverbund und Rissverzahnung in unbewehrten Betonschubfugen. Dissertation. München: Lehrstuhl für Massivbau der Technische Universität München.
- [31] Müller (2009): Zum Zug- und Schubtragverhalten von Betonfugen. Dissertation. München: Lehrstuhl für Massivbau der Technische Universität München.
- [32] Lenz (2012): Beton-Beton-Verbund-Potenziale für Schubfugen. Dissertation. München: Lehrstuhl für Massivbau der Technische Universität München.
- [33] Wagner (2016): Dauerhaftigkeitsrelevante Eigenschaften von dehnungsverfestigenden zementgebundenen Reparaturschichten auf gerissenen Betongründen. Dissertation. Unter Mitarbeit von Viktor Mechtcherine und Volker Slowik. Dresden: Technische Universität Dresden (Schriftenreihe des Institutes für Baustoffe, 2016, Heft 2).
- [34] Mohamed A. Ali and Richard N. White (1999): Enhanced Contact Model for Shear Friction of Normal and High-Strength Concrete. In: *Structural Journal* 96 (3).
- [35] Papanicolaou und Triantafyllou (2002): Shear transfer capacity along pumice aggregate concrete and high-performance concrete interfaces. In: *Mat. Struct.* 35 (4), S. 237–245.

- [36] Santos P.M.D. and Julio E.N.B.S (2010): Recommended improvements to current shear-friction provisions of model code. 3rd fib international congress. Washington DC.
- [37] P.M.D Santos (2011): Factors affecting bond between new and old concrete. In: *ACI Material Journal* 108(4), S. 449–456.
- [38] AASHTO (1996): Standard specifications for highway bridges. Adopted and published by the American Association of State Highway and Transportation Officials. 16th ed. Washington D.C.: American Association of State Highway and Transportation Officials.
- [39] DIN 1045-1 (2002): Tragwerke aus Beton, Stahlbeton und Spannbeton. Teil 1: Bemessung und Konstruktion. Berlin: Beuth Verlag GmbH.
- [40] Martin und Perry (2004): PCI design handbook. Precast and prestressed concrete / editor, Leslie D. Martin, Christopher J. Perry. 6th ed. Chicago: Precast/Prestressed Concrete Institute.
- [41] CSA (2004): Design of concrete structures. CAN/CSA-A23.3-04 : a National Standard of Canada. Mississauga, Ont.: Canadian Standard Association (CSA standard, A23.3-04).
- [42] AASHTO (2007): AASHTO LRFD bridge design specifications. 4th ed. Place of publication not identified: American Association of State Highway and Transportation Officials.
- [43] DIN 1045-1 (2008): Tragwerke aus Beton, Stahlbeton und Spannbeton. Teil 1: Bemessung und Konstruktion. Berlin: Beuth Verlag GmbH.
- [44] Wight (2008): Building code requirements for structural concrete (ACI 318-08) and commentary (ACI 318R-08). 1. print. Farmington Hills, Mich.: ACI.
- [45] FIB (2010): Model Code 2010. First complete draft. Lausanne: International Federation for Structural Concrete (Bulletin / International Federation for Structural Concrete Draft model code, 55).
- [46] China Institute of Building Standard Design & Research (2014): JGJ 1-2014: Technical specification for precast concrete structures. Beijing: Construction Press.
- [47] Trevino et al. (2004): Techniques and Procedures for Bonded Concrete Overlays. Report No. FHWA/TX-05/0-4398-2. Center for Transportation Research, University of Texas at Austin.
- [48] ISO 4287-1 (1984): Surface roughness. Terminology. Part 1: Surface and its parameters: International Organization for Standardization.
- [49] BS 1134-1 (1988): Assessment of surface texture. Part 1: Methods and instrumentation: British Standard Institute.
- [50] DIN 4762 (1989): Surface roughness. Terminology. Surface and its parameters (identical with ISO 4287-1): Deutsches Institut für Normung (DIN).
- [51] DIN 4768 (1990): Determination of roughness parameters Ra, Rz, Rmax by means of stylus instruments. Terms, measuring conditions: German Institute for Standardization.
- [52] JIS B 0601 (1994): Geometrical Product Specifications (GPS) - Surface texture: Profile method - Terms, definitions and surface texture parameters. Japanese Standards Association (JIS).
- [53] Thomas (1982): Rough surfaces. London: Longman Higher Education.
- [54] Mummery (1992): Surface texture analysis - the handbook. Thyssen: Hommelwerke GmbH.
- [55] Santos (2009): Assessment of the shear strength between concrete layers. Doctoral thesis. Coimbra, Portugal: University of Coimbra.

- [56] Kaufmann (1971): Das Sandflächenverfahren. Ein einfaches Verfahren zur Messung und Beurteilung der Textur von Fahrbahnoberflächen. In: *Straßenbau-Technik* (3), S. 131–135.
- [57] EN 13036-1 (2010): Road and airfield surface characteristics – Test methods – Part 1: Measurement of pavement surface macrotexture depth using a volumetric patch technique. Brussels: European Committee for Standardization.
- [58] American Society of Mechanical Engineers (1978): Surface Texture, Waviness and Lay. New York: American National Standard.
- [59] Santos P.M.D. and Julio E.N.B.S (2010): Comparison of Methods for Texture Assessment of Concrete Surfaces. In: *ACI Materials Journal* 107 (5).
- [60] Garbacz et al. (2005): Effect of concrete surface treatment on adhesion in repair systems. In: *Magazine of Concrete Research* 57 (1), S. 49–60. available online at: <http://dx.doi.org/10.1680/mac.2005.57.1.49>.
- [61] Courard und Nelis (2003): Surface analysis of mineral substrates for repair works: roughness evaluation by profilometry and surfometry analysis. In: *Magazine of Concrete Research* 55 (4), S. 355–366. available online at: <http://dx.doi.org/10.1680/mac.2003.55.4.355>.
- [62] Bissonnette et al. (2017): Development of specifications and performance criteria for surface preparation based on issues related to bond strength. Final report ST-2017-2886-1.
- [63] ACI Committee 555 (2001): Removal and reuse of hardened concrete. Farmington Hills, MI.: American Concrete Institute (ACI report, 555R-01).
- [64] Talbot und Pigeon (1995): Influence of Surface Preparation on Long-Term Bonding of Shotcrete. In: *ACI Materials Journal* 91 (6), S. 560–566.
- [65] Bissonnette et al. (2006): Concrete removal techniques: influence on residual cracking and bond strength. In: *Concrete International* 28 (12), S. 49–55.
- [66] Maintenance Group of CEN/TC 250/SC 2 (2008): Corrigenda to EN 1992-1-1. Document CEN/TC 250/SC 2 N 698.
- [67] Deutscher Ausschuss für Stahlbeton (2010): Erläuterungen zu DIN 1045-1. 2. überarbeitete Auflage 2010. DAFStb Heft. Berlin: Beuth Verlag GmbH (Deutscher Ausschuss für Stahlbeton, 525).
- [68] Ackermann und Burkhardt (1992): Tragverhalten von bewehrten Verbundfugen bei Fertigteilen und Ortbeton in den Grenzzuständen der Tragfähigkeit und Gebrauchstauglichkeit. In: *Beton- und Stahlbetonbau* 87 (7), S. 165–170. available online at: <http://dx.doi.org/10.1002/best.199200280>.
- [69] Zilch und Müller (2004): Experimentelle Untersuchung zum Ermüdungstragverhalten von unbewehrten Schubfugen an nachträglich ergänzten Betonbauteilen. Research report. München: Technische Universität München.
- [70] Zilch und Müller (2007): Grundlagen und Anwendungsregeln der Bemessung von Fugen nach EN 1992-1-1. Research report. München: Technische Universität München.
- [71] Beushausen (2005): Long-term performance of bonded concrete overlays subjected to differential shrinkage. Doctoral thesis. Cape Town: University of Cape Town.
- [72] Momayez et al. (2005): Comparison of methods for evaluating bond strength between concrete substrate and repair materials. In: *Cement and Concrete Research* 35 (4), S. 748–757.

- [73] RILEM (2011): Bonded cement-based material overlays for the repair, the lining or the strengthening of slabs or pavements. State-of-the-art report of the RILEM Technical Committee 193-RLS. Dordrecht, New York: Springer (RILEM state of the art reports, v. 3).
- [74] Zhang et al. (2019): Experimental studies on the interface between concrete and cement-asphalt mortar. fib Symposium 2019. fib Symposium. Krakow, Poland, 2019. Krakow, Poland.
- [75] EN 1542 (1999): Products and systems for the protection and repair of concrete structures – Test methods – Measurement of bond strength by pull-off. Brussels: European Committee for Standardization.
- [76], (2013): Test Method for Tensile Strength of Concrete Surfaces and the Bond Strength or Tensile Strength of Concrete Repair and Overlay Materials by Direct Tension (Pull-off Method). available online at: http://dx.doi.org/10.1520/C1583_C1583M-20.
- [77] EN 12390-6 (2009): Testing hardened concrete – Part 6: Tensile splitting strength of test specimens. Brussels: European Committee for Standardization.
- [78], (2017): Test Method for Splitting Tensile Strength of Cylindrical Concrete Specimens. available online at: http://dx.doi.org/10.1520/C0496_C0496M-17.
- [79] EN 12615 (1999): Products and systems for the protection and repair of concrete structures – Test methods – Determination of slant shear strength. Brussels: European Committee for Standardization.
- [80], (2018): Terminology Relating to Concrete Pipe and Related Products. available online at: <http://dx.doi.org/10.1520/C0822-20>.
- [81] Kuna (2010): Numerische Beanspruchungsanalyse von Rissen. Finite Elemente in der Bruchmechanik ; mit zahlreichen Beispielen. 2., verb. Aufl. Wiesbaden: Vieweg + Teubner (Studium).
- [82] Bazant (1992): Fracture mechanics of concrete structures. ACI Committee 446.
- [83] Anderson (2005): Fracture mechanics. Fundamentals and applications. Boca Raton, FL: Taylor & Francis.
- [84] Griffith (1920): The phenomena of rupture and flow in solids. In: *Philosophical Transactions of the Royal Society of London. Series A, Containing Papers of a Mathematical or Physical Character* 221, S. 163–198. available online at: <http://dx.doi.org/10.1098/rsta.1921.0006>.
- [85] Irwin (1956): Onset of fast crack propagation in high strength steel and aluminum alloys. In: *Sagemore Research Conference Proceedings* 2, S. 289–305.
- [86] Rice (1968): A Path Independent Integral and the Approximate Analysis of Strain Concentration by Notches and Cracks. In: *Journal of Applied Mechanics* 35 (2), S. 379–386. available online at: <http://dx.doi.org/10.1115/1.3601206>.
- [87] Westergaard (1939): Bearing pressures and cracks. In: *Journal of Applied Mechanics* 6, S. 49–53.
- [88] Irwin (1957): Analysis of stresses and strains near the end of a crack traversing a plate. In: *Journal of Applied Mechanics* 24, S. 361–364.
- [89] Brocks (2012): Plastizität und Bruchmechanik. Lecture script. Berlin: Institut für Mechanik der TU Berlin (Manuskripte zur Vorlesung).
- [90] Jenq und Shah (1985): Two Parameter Fracture Model for Concrete. In: *Journal of Engineering Mechanics* 111 (10), S. 1227–1241.
- [91] Bazant und Kazemi (1990): Determination of fracture energy, process zone length and brittleness number from size effect, with application to rock and concrete. In: *Int J Fract* 44 (2), S. 111–131.

- [92] Dugdale (1960): Yielding of steel sheets containing slits. In: *Journal of the Mechanics and Physics of Solids* 8 (2), S. 100–104.
- [93] Barenblatt (1962): The Mathematical Theory of Equilibrium Cracks in Brittle Fracture. In: *Mechanics* (7), S. 55–129.
- [94] Hillerborg et al. (1976): Analysis of crack formation and crack growth in concrete by means of fracture mechanics and finite elements. In: *Cement and Concrete Research* 6 (6), S. 773–781.
- [95] Saouma und Ingraffea (1981): Fracture mechanics analysis of discrete cracking. Advanced mechanics of reinforced concrete. Delft. International Association for Bridge and Structural Engineering (IABSE).
- [96] Bretschneider (2011): Inverse Analyse zur Ermittlung der bruchmechanischen Eigenschaften entfestigender und verfestigender zementgebundener Werkstoffe. Dissertation. Dresden: Technische Universität Dresden (Schriftenreihe des Institutes für Baustoffe, H. 2011,2).
- [97] Bažant und Oh (1983): Crack band theory for fracture of concrete. In: *Mat. Constr.* 16 (3), S. 155–177.
- [98] Petrangeli und Ožbolt (1996): Smeared Crack Approaches—Material Modeling. In: *Journal of Engineering Mechanics* 122 (6), S. 545–554.
- [99] Rots, Jan G. and Blaauwendraad, J. (1970): Crack models for concrete: discrete or smeared? fixed, multi-directional or rotating? TU Delft, Delft.
- [100] 3DS Dassault Systemes (2016): Abaqus documentation - user manual. Internet document. available online at: <http://130.149.89.49:2080/v2016/books/gsa/default.htm>.
- [101] Belytschko und Black (1999): Elastic crack growth in finite elements with minimal remeshing. In: *Int. J. Numer. Meth. Engng.* 45 (5), S. 601–620.
- [102] Jason et al. (2006): An elastic plastic damage formulation for concrete: Application to elementary tests and comparison with an isotropic damage model. In: *Computer Methods in Applied Mechanics and Engineering* 195 (52), S. 7077–7092.
- [103] Nguyen (2005): A thermodynamic approach to constitutive modelling of concrete using damage mechanics and plasticity theory. Dissertation. Oxford: University of Oxford.
- [104] Babu et al. (2005): Constitutive modeling of concrete: an overview. In: *Asian Journal of Civil Engineering* 6 (4), S. 211–246.
- [105] Kuna (2010): Schädigungsmechanik. Theorie, Numerik und Anwendung. Lecture script. Freiberg: Technische Universität Bergakademie Freiberg (Vorlesungsskript von Institut für Mechanik und Fluidodynamik).
- [106] Pölling (2001): Eine praxisnahe, schädigungsorientierte Materialbeschreibung von Stahlbeton für Strukturanalysen. Dissertation. Bochum: Ruhr-Universität Bochum (Forschungsarbeit aus dem Sonderforschungsbereich 398, Lebensdauerorientierte Entwurfskonzepte).
- [107] Meschke G. und Lackner R. and Mang H.A. (1998): An anisotropic elastoplastic-damage model for plain concrete. In: *Int. J. Numer. Meth. Engng.* 42 (3), S. 703–727.
- [108] Lee und Fenves (1998): A plastic-damage concrete model for earthquake analysis of dams. In: *Earthquake Engng. Struct. Dyn.* 27 (9), S. 937–956.
- [109] Yazdani S. und Schreyer H.L. (1990): Combined plasticity and damage mechanics model for plain concrete. In: *Journal of Engineering Mechanics* 116 (7), S. 1435–1450.

- [110] Han und Chen (1986): Strain-space plasticity formulation for hardening-softening materials with elastoplastic coupling. In: *International Journal of Solids and Structures* 22 (8), S. 935–950.
- [111] Bazant und Kim (1979): Plastic-fracturing theory for concrete. In: *ASCE J Eng Mech Div* 105 (3), S. 407–428.
- [112] Fardis und Buyukozturk (1980): Shear stiffness of concrete by finite elements. In: *Journal of the Structural Division* 106 (6), S. 1311–1327.
- [113] Walraven (1980): Aggregate interlock: A theoretical and experimental analysis. Dissertation. Delft: Delft University of Technology.
- [114] Foster et al. (2017): Shear Capacity of Reinforced Concrete Subjected to Tension. Experimental Results and Analysis. In: *J. Struct. Eng.* 143 (9), S. 4017085.
- [115] Jonasson (1977): Computer program for nonlinear computations in concrete with regard to shrinkage, creep and temperature. CBI Report No. 7:77. Stockholm: Swedish Cement and Concrete Research Institut.
- [116] Haardt (1991): Zementgebundene und kunststoffvergütete Beschichtungen auf Beton. Dissertation: TU Karlsruhe.
- [117] Birkeland (1960): Differential shrinkage in composite beams. In: *Journal Proceedings of American Concrete Institute* 56 (5), S. 1123–1126.
- [118] Silfwerbrand (1986): Differential shrinkage in composite concrete beams of old concrete and a new-cast concrete overlay. Bulletin No. 144. Stockholm, Sweden: Department of structural Mechanics and Engineering, Royal Institute of Technology.
- [119] Silfwerbrand (1997): Stresses and strains in composite concrete beams subjected to differential shrinkage. In: *ACI Structural Journal* 96 (4), S. 347–353.
- [120] Beushausen und Alexander M. (2004): Bonded concrete overlays subjected to differential shrinkage – an analytical model based on localized strain and stress. RILEM PRO 43. International RILEM Workshop on Bonded Concrete Overlays. Stockholm, Sweden, June 7–8, 2004. Swedish Cement and Concrete Research Institute (CBI).
- [121] Beushausen (2005): Long-term performance of bonded concrete overlays subjected to differential shrinkage. Doctoral thesis: University of Capetown.
- [122] Beushausen und Alexander M. (2006): Spannungen durch Verformungsbehinderung in gebundenen Aufbetonen. In: *Beton und Stahlbetonbau* 101 (6), S. 394–401.
- [123] Beushausen und Alexander M. (2007): Localised strain and stress in bonded concrete overlays subjected to differential shrinkage. In: *Materials and Structure* 40 (2), S. 189–199.
- [124] Al-Gburi et al. (2012): Simplified methods for crack risk analyses of early age concrete. Part 1: development of equivalent restraint method. In: *Nordic Concrete Research* 46, S. 17–38.
- [125] Japan Society of Civil Engineers (JSCE) (2007): Guidelines for Concrete No. 15. Standard specifications for concrete structures.
- [126] Knoppik-Wróbel und Klemczak (2015): Degree of restraint concept in analysis of early-age stresses in concrete walls. In: *Engineering Structures* 102, S. 369–386.
- [127] Nilsson (2000): Thermal cracking of young concrete. partial coefficients, restraint effects and influence of casting joints. master thesis. Luleå, Sweden: Luleå tekniska universitet.

- [128] Nilsson (2003): Restraint factors and partial coefficients for crack risk analyses of early age concrete structure. doctoral thesis. Luleå, Sweden: Luleå tekniska universitet.
- [129] ACI Report 207 (2007): Report on thermal and volume change effects on cracking of mass concrete. Farmington Hills, MI: American Concrete Institute.
- [130] EN 1992-3 (2006): Eurocode 2 – Design of concrete structures – Part 3: Liquid retaining and containment structures. Brussels: European Committee for Standardization.
- [131] Bamforth (2007): Early-age thermal crack control in concrete. London: CIRIA (CIRIA C, 660).
- [132] Wikipedia: Artical "Abaqus". Internet document. available online at: <https://en.wikipedia.org/wiki/Abaqus>.
- [133] Barth und Rustler (2013): Finite Elemente in der Baustatik-Praxis. Mit vielen Anwendungsbeispielen. 2., überarb. und erw. Aufl. Berlin, Wien, Zürich: Beuth (Bauwerk).
- [134] 3DS Dassault Systemes (2017): The Journey to Convergence. Seminar document for regional users' meeting. Braunschweig, Germany.
- [135] Fischer (2011): Finite-Elemente-Methode. Lecture script. Dortmund: Fachhochschule Dortmund (Skript zur Vorlesung des Wintersemesters 2011/12).
- [136] Nasdala (2012): FEM-Formelsammlung Statik und Dynamik. Wiesbaden: Vieweg+Teubner Verlag.
- [137] 3DS Dassault Systemes (2006): Connection Elements and Connection Library. Lecture 2. Tutorial document.
- [138] P.P. Camanho and C. G. Davila (2002): Mixed-mode decohesion finite elements for the simulation of delamination in composite materials. In: *NASA/TM-2002-211737*, S. 1–37.
- [139] Benzeggagh und Kenane (1996): Measurement of mixed-mode delamination fracture toughness of unidirectional glass/epoxy composites with mixed-mode bending apparatus. In: *Composites Science and Technology* 56 (4), S. 439–449. available online at: [http://dx.doi.org/10.1016/0266-3538\(96\)00005-X](http://dx.doi.org/10.1016/0266-3538(96)00005-X).
- [140] Rust (2009): Non-linear finite element analysis in structural mechanics. 1. Auflage. Cham: Springer (Engineering).
- [141] Keuser, M.; Meinhardt, M. (2018): Nichtlineare Berechnung von Stahlbetontragwerken mithilfe der Finite-Elemente-Methode. In: Konrad Bergmeister, Frank Fingerloos und Johann Dietrich Wörner (Hg.): *Beton-Kalender 2018: Bautenschutz, Brandschutz*. Berlin: Ernst & Sohn (Beton-Kalender (VCH) *).
- [142] EN 12390-3 (2017): Testing hardened concrete – Part 3: Compressive strength of test specimens. Brussels: European Committee for Standardization.
- [143] EN 12390-13 (2014): Testing hardened concrete – Part 13: Determination of secant modulus of elasticity in compression. Brussels: European Committee for Standardization.
- [144] EN 196-1 (2016): Methods of testing cement – Part 1: Determination of strength. Brussels: European Committee for Standardization.
- [145] Xie et al. (2008): Tentative Specification of Cement-Asphalt Mortar for CRTS II in High-speed Railway Lines. Beijing: Department of Science and Technology, Ministry of Railways of the People's Republic of China.
- [146] Su (2017): Deformation and stability of multi-layer partial connected structure system for bridge-ballastless track. Dissertation. Changsha, China: Central South University.

- [147] Su (2020): Bond-slip constitutive model of concrete to cement-asphalt mortar interface for slab track structure. In: *Structural Engineering and Mechanics* 74 (5), S. 589–600.
- [148] EN 1991-1-5 (2003): Eurocode 1: Actions on structures - Part 1-5: General actions - Thermal actions. Brussels: European Committee for Standardization.

Lebenslauf

Persönliche Angaben

Name	Sisi Zhang
Geburtsdatum	14. Juni 1989
Geburtsort	Hengyang, Hunan Provinz, Volksrepublik China
Familienstand	verheiratet, kein Kind

Schulische Ausbildung

09.1995-06.2001	Grundschule für Kinder der Arbeiter der Hengyang Traktor Fabrik
09.2001-06.2004	Hengyang Chuanshan experimentelle Mittelschule
09.2004-06.2007	Hengyang Nr.1 Oberschule

Akademischer Werdegang

06.2007	staatliche Aufnahmeprüfung für Chinesische Hochschulen und Universität in Hunan Provinz, China
09.2007-06.2011	Bachelor Studium an der Central South University of China Fachrichtung: Bauingenieurwesen
09.2011-06.2014	Master Studium an der Central South University of China Fachrichtung: Bauingenieurwesen
Seit 10.2014	Promovendin im Institut für Massivbau an Leibniz Universität Hannover